The Behaviour of Silica in Matt Water-based Lacquers

Christopher Patrick Royall
St Catharine's College
Cambridge

A dissertation submitted to the University of Cambridge
for the degree of
Doctor of Philosophy

5th December 2000

The behaviour of silica in matt water-based lacquers

Summary

The use of paint is ubiquitous, and the drive to develop more efficient and environmentally friendly products considerable. Here we examine the role of silica matting agent in clear water-based lacquers. These products vastly reduce the emission of organic compounds compared to traditional oil-based paints, but there are a number of problems to be overcome. In the case of matt products, the desired loss of specular reflection is frequently accompanied by poor transparency.

In order to address this optical behaviour, we consider the process of matting more fundamentally by determining the silica structure in the dried film, and during the drying process. We assume that there is no significant interaction between the polymer latex that forms the binder, and the micron-sized silica particles. We suggest that, at a critical concentration of silica, the air that lies between the silica particles in the dry powder is *exactly* replaced in the dried film by polymer. At this point we expect a percolating silica structure to be formed, similar to that found in the dry silica powder. This has implications for the surface properties, as we expect a considerable increase in surface roughness at this critical concentration.

These predictions are upheld, with a continuous silica structure being found at the concentration predicted, using confocal microscopy. Atomic force microscopy shows that surface roughness also increases significantly at this point. In addition, environmental scanning electron microscopy (ESEM) can image the surface of the lacquer during *in-situ* film formation, where we see a gradual transition from the liquid suspension to a dry polymer film. We find that for these clear lacquers, the matting is mainly dependent upon the surface roughness, and that there is a unique relationship between surface roughness and matting. We consider a variety of silicas, and correlate both microscopic and macroscopic properties to the nature of the silica particles used. Softer, lighter silicas produce films with more desirable properties. The silica behaviour is dominated by physical, rather than chemical properties, the most important being bulk density.

This work also considers the radiation damage of hydrated samples in ESEM by the electron beam. We simulate the radiation damage of a pure water sample by determining the concentrations of free radical and other reactive species. The results are consistent with experimental work relating higher radiation damage to a greater beam voltage and a hydrated environment. Here, the dominant reactive species is found to be the hydroxyl radical.

Declarations

This dissertation is the result of my own work and includes nothing which is the outcome of work done in collaboration.

I also declare that no part of this dissertation has been submitted for a degree, diploma or other qualification at any other University.

Part of this thesis has been submitted for publication:

C.P. Royall and A.M. Donald, "Confocal Microscopy and Environmental SEM Applied to Matting Water-based Lacquers", submitted to American Chemical Society Symposium Series, 790, chapter 11, 2001.

C.P. Royall, D.J. Stokes, I. Hopkinson and A.M. Donald, "Confocal Microscopy and Environmental SEM for polymers", submitted to Polymer News.

The length of this dissertation also lies within the word limit set by the Degree Committee of the Faculty of Physics and Chemistry, University of Cambridge.

Christopher Patrick Royall

Preface

The list of people to thank for their contribution to this project is far too long to include here, but here goes...

Firstly I'd like to thank Athene Donald for taking me on in the first place - and being a fantastic supervisor, to let me amuse myself for three years. Far too generous. My industrial sponsors, Gemma Morea-Swift, Derek Aldcroft and Robin Gibson for invaluable input on silica chemistry.

Brad Thiel for all things ESEM, especially how not to blow up paint in the ESEM and generally being an icon to us all. Geoff Soga for suggesting I write my own image analysis code. Unfortunately here Geoff shot himself in the foot, as he suffered an endless succession of 'c-questions' and was seldom able get on with his own work, let alone trade. Pietro Cicuta for happy hours spent watching paint dry, and what can only be described as exemplary care for apparatus.

Ian Hopkinson for risking the confocal in my hands. As far as I know the 63× lens has survived. Kari Dalnoki-Veress and Jamie Forrest for the use of the AFM in Sheffield. Fortunately I'd cut my teeth on the ESEM and confocal and the AFM got off relatively lightly.

I think it's fair to say that thanks to Paul, Big Gay Al, Jim, Johnny and Rudi, I will never be able to think of Cornwall in quite the same way. Alan must also be thanked for finally succeeding in explaining the difference between explicit and implicit finite difference schemes two years after the work was done.

Special thanks must be extended to Meg, for help in all manner of ways, from holiday (sorry, conference) arrangements and Pete, Frank and Roger for experimental support.

This work was supported by EPSRC and Crosfield Group.

Finally I'd like to thank Louisa Ferrier for putting up with the flip side of poorly microscopes/computers/bugs in the code...

'Nothing succeeds like excess', Oscar Wilde.

Contents

Abstract i

Declaration ii

Preface iii

1 Introduction 1

2 Background 4

2.1 Film Formation in Polymer Latices 4

2.2 Applied Water-Based Coatings 11

2.3 Silica Matting Agent 13

2.4 Pigmented Latices 18

2.5 Clear Matt Lacquers 19

3 Building the Silica Structure Model 22

3.1 Outline 22

3.2 Mathematical treatment 26

3.3 Porosimetry 28

3.4 Implications of the model 30

4 Experimental 34

4.1 Environmental SEM 35

4.2 Atomic Force Microscopy 46

4.3 Confocal Microscopy 52

5 Beam damage in ESEM **60**

5.1 Background 61

5.2 Experimental 62

5.3 Electron-Water Interactions 63

5.4 From one electron to a beam 66

5.5 Mean Concentration Model 68

5.6 Results and Discussion 72

5.7 Conclusions 80

5.8 Appendix: Diffusion Algorithm 82

6 Image Analysis **85**

6.1 Deconvolution in Confocal Microscopy 86

6.2 Numerical Analysis 91

6.3 Silica extraction for ESEM 97

6.4 Contrast enhancement in CLSM 104

6.5 Surface Roughness in AFM 106

6.6 Summary 107

7 ESEM characterisation **109**

7.1 Sample preparation 110

7.2 ESEM Experimental 112

7.3 Film formation results 119

7.4 Film thickness results 124

7.5 Conclusions 130

8 Testing the Silica Structure Model **132**

8.1 Model Predictions 132

8.2 Confocal Methodology 136

8.3 Results of confocal microscopy 139

8.4 Atomic force microscopy 150

8.5 Environmental SEM 158

8.6 Conclusions 166

9 Optical properties 169

9.1 Light scattering: Hazing 170

9.2 Confocal Microscopy: Hazing 172

9.3 Mechanisms for Hazing 176

9.4 Reflection 182

9.5 Reflection Mode CLSM 188

9.6 Conclusions 191

10 Summary and Conclusions 196

10.1 Developments in methodology 196

10.2 Matt lacquers 199

10.3 Future work 203

10.4 Conclusions 205

Bibliography 207

Appendices 215

Chapter 1

Introduction

This work intends to describe silica in matt water-based lacquers. We take a physical approach to this problem, developing a structural model which describes the silica behaviour. First we explain the nature of matt water-based lacquers and their place in the context of the paint industry. We then move on to outline our approach to study the matt water-based lacquer system that forms the subject of this thesis.

Traditional paints are based on a polymer dissolved in an organic solvent, which evaporates leaving a polymer layer on the substrate [1]. The last 20 years have seen a shift in the paint industry away from these traditional oil-based paints which involve the emission volatile organic compounds (VOC) in the form of the solvent, to low-emission, more environmentally friendly products [2]. This has been driven by consumer pressures and backed by legislation.

This change has brought about considerable technical innovation, and central to the reduction in VOC emission are water-based lacquers. For the purposes of this work, we regard the term lacquer as a synonym for paint [1]. Water-based products are largely developed from polymer latices, whose synthesis is based on the technique of emulsion polymerisation, originally developed in 1929 [3]. Unlike a conventional polymer solution, where the chains are free to move throughout the liquid, a latex confines the polymeric material to colloidal particles, which are then suspended in the continuous phase. By separating the polymer and fluid phases, we can use water as the continuous medium. This is a key development since we typically want to use hydrophobic, non water-soluble

polymers in lacquer applications.

Polymer latices can, under the right conditions, produce a continuous polymer film upon water evaporation, as described in more detail in chapter 2, section 2.1, so the VOC emission can be very low indeed. Latices have been extensively studied, beginning in 1953 with Bradford *et al.* [4], along with Brown [5], Vanderhoff *et al.* [6] and Sheetz [7] contributing further major mechanisms. Work on polymer latices has been extensively reviewed by Keddie [8] and Winnik [9].

However this more theoretical work has tended to focus on model systems. Here we focus on a specific product, a clear matt lacquer. The crucial difference here is the inclusion of silica (polymerised silicon dioxide, $(SiO_2)_n$). This most basic and abundant of minerals is very well understood [10]. In this work we concentrate on the interactions between synthetic amorphous silica and the polymer latex, and how silica may act as a 'matting agent', reducing the specular reflection (or 'gloss') of the lacquer [11].

Matting is associated with surface roughness on the lengthscale of light, introduced by the hard silica inclusions, which take the form of irregularly shaped particles on the 1-10μm lengthscale [11]. There is however a significant technological difficulty with matt lacquers. Inclusion of the matting agent can under certain conditions turn the otherwise transparent film white, indicating considerable light scattering, which we term 'hazing'. Although the silica and polymer are closely matched in refractive index (RI), we see this hazing in water-based products, whereas it is noticeably absent from oil based paints where the polymer chains are not confined to latex particles [12].

So our aim is to understand the matting process, and why it can introduce hazing. We focus on the influence of the silica, examining a number of different types, with a variety of surface and mechanical properties. The silicas in this work are based on fumed silica, precipitated silica and silica gel [10].

In chapter 3 we hypothesise and develop a volume-based model of the silica structure. We assume no significant interaction between the polymer latex that forms the binder and the micron-sized silica particles. We claim that at a critical concentration of silica, the air that lies between the silica particles in the dry powder is *exactly* replaced by polymer in the dried film. At this point we expect a percolating silica structure to be formed similar to that found in the dry silica powder. This has implications for the surface properties,

as we expect a considerable increase in surface roughness at this critical concentration.

This model is tested with the novel microscopy techniques of environmental scanning electron microscopy (ESEM) [13], confocal laser scanning microscopy (CLSM) [14] and atomic force microscopy (AFM) [15]. These structural probes enable imaging of both the bulk (CLSM) and surface (AFM and ESEM) of the film. We can map the spatial distribution of silica to a sub-micron resolution throughout the sample (see chapter 4). Image analysis builds a numerical interpretation of microscopy results. In chapter 6 we show how image analysis may be developed computationally to extract the numerical data to test our silica structure model in chapters 7-9.

The use of ESEM, is especially interesting as unlike conventional-SEM, it allows imaging of hydrated samples [13], so we can observe film-formation *in-situ*, and probe otherwise inaccessible predictions of our model. However prolonged experiments can result in considerable electron beam damage to aqueous samples. We develop a computational model to study damage to aqueous samples under ESEM conditions. The results from this work will enable us to reduce beam damage in future experiments by judicious selection of operating parameters (see chapter 5).

Matting can also be characterised by macroscopic optical properties, specular reflection and light scattering. In chapter 9 we compare these measurements with the ideas of our model, focusing on the relation between reflection and surface properties.

Finally we aim to draw these ideas together to build a comprehensive understanding of matt water-based lacquers. In this way, we seek to bridge the studies of latex film-formation in model systems with previous work on matt water-based lacquers.

Chapter 2

Background

Film formation in polymer latices has been extensively studied [8], but the literature has focussed on relatively pure systems, typically a fairly monodisperse latex suspension with some form of colloidal stabilisation. Here we are interested in a rather more complex system, with a silica matting agent and various other additives in addition to the latex. Although the inclusion of silica is known to introduce matting [11] [16] [17], relatively little has been done to understand the precise mechanism by which silica reduces specular reflection (matting).

We divide this chapter into four main parts, film formation in latices, amorphous silica matting agents and additives in matt lacquers, before moving onto work relevant to matt lacquers. In the next chapter we present our model of the structure adopted by the silica in matt lacquers.

2.1

Film Formation in Polymer Latices

We begin this section with an overview of film formation, before proceeding to give a historical outline of the various theories which have been advanced to describe the process.

Film formation from a latex suspension can be separated into four stages, as shown in figure 2.1 [18]. Initially the latex spheres are dispersed in the aqueous medium (stage I),

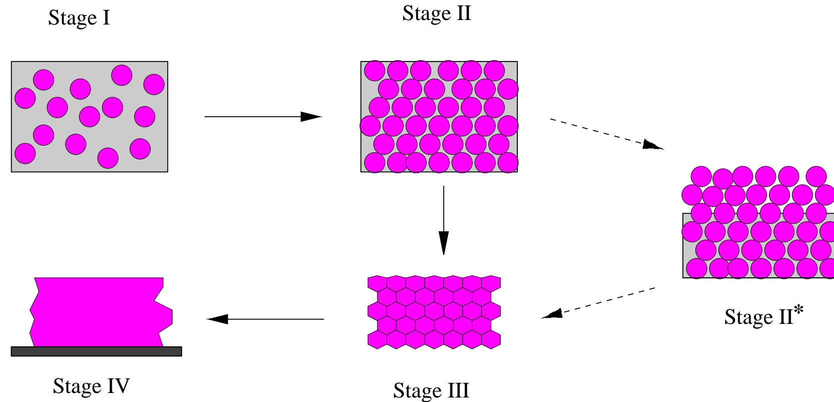

Figure 2.1: Film formation of latex. Water evaporates form the aqueous suspension (stage I) to form an array of latex spheres (stage II). Further evaporation of water is accompanied by deformation (stage III) and interdiffusion produces the final continuous polymer film (stage IV). The development of Keddie et al. *[18] [19] of stage II* where water evaporation precedes deformation is discussed below.*

before evaporation of water brings them together in a closely packed array (stage II). There is then deformation of the spheres and further water evaporation (stage III) to produce an optically transparent film. Interdiffusion of polymer chains across the interparticle boundaries results in the continuous polymer film of stage IV. The literature is reasonably agreed that stage I-II is driven by water evaporation [20]. The majority of the discussion has concerned the mechanisms of deformation in stage II-III [20]. Stage III-IV has also been studied [21] [22] [23] [24].

Historical Outline

The intention is not to provide a rigorous review of work in this area, rather to give a qualitative understanding of the processes at work. Various reviews of the field have already been published, [8] [9] [25].

Film formation in aqueous latices has been studied for half a century, with the first work by Bradford *et al.* [4]. That the mechanisms are still debated gives testimony to the complexity of the seemingly simple process of paint drying. The sticking point is the stage II-III transition, which we will term *deformation*, although it is also referred to as coalescence [20].

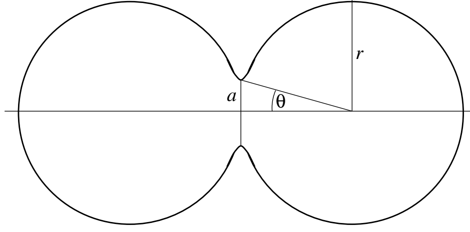

Figure 2.2: Dry sintering of Bradford et al. *[4]: θ evolves with time according to the Frenkel equation (2.1) as the spheres coalesce.*

There have really only been four mechanisms proposed [4] [5] [6] and [7], with other work modifying these fundamental models and providing experimental support for one or another. We consider each model in turn, before turning our attention to key subsequent work.

The first model, proposed by Bradford [4], is that of *dry sintering*. Bradford *et al.* drew heavily on the work of Frenkel [26], who described the coalescence of two colloidal metal spheres in terms of viscous flow (figure 2.2). Considering the polymer-air surface energy of two spheres, it is clear that the free energy is reduced by coalescence. Frenkel derived the following equation,

$$\theta^2 = \frac{3\sigma t}{2\pi\eta r}. \tag{2.1}$$

for spheres of radius r, surface tension σ and viscosity η. The angle θ, which describes the degree of coalescence, is defined in figure 2.2.

Brown [5] showed the shortcomings of the dry sintering model, by noting that it did not explain deformation and water evaporation occurring concurrently as observed, that lightly crosslinked polymers can film form but that they must deform without viscous flow, and the existence of a minimum film-forming temperature (MFT) below which a transparent film is not produced.

In order to address the problem, Brown identified the forces involved in deformation in his *capillary model*. Four promoted deformation, surface tension (F_s), gravity (F_{grav}), Van der Waals attraction (F_{vdw}) and the capillary force (F_c). F_c resulted from the interfacial

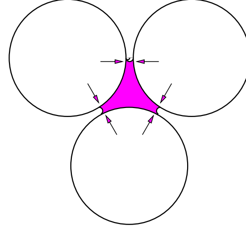

Figure 2.3: The capillary force resulting from interstitial water (shown in pink) acts normal to the latex sphere surfaces to bring the polymer spheres together via deformation

tension of the negative curvature of the water-air surface. This provides a force normal to the surface of each sphere, promoting deformation, as shown in figure 2.3 [5].

These forces are opposed by the resistance to deformation (F_g) and the electrostatic stabilisation (F_e). Brown stated that coalescence only occurred if

$$F_s + F_{grav} + F_{vdw} + F_c > F_g + F_e. \tag{2.2}$$

Arguing that all but F_c and F_g could be neglected, Brown reduced equation 2.2 to

$$F_c > F_g \tag{2.3}$$

as a criterion for deformation. He attempted to quantify each term, but some of his assumptions were flawed [7] [27] [28]. However, Brown's work is highly important in that it identifies the forces at work [20].

Lin and Meier [29] improved Brown's model considerably. Geometry led them to consider a ring of water around each pair of touching particles, instead of Brown's spherical meniscus. Crucially, this model showed that even tiny amounts of absorbed water (such as would occur in air with non-zero relative humidity) produced very considerable forces on the structure.

Another model was advanced by Sheetz [7]. He concluded that the models of Brown and Bradford were insufficient to drive deformation and also noted some weaknesses with

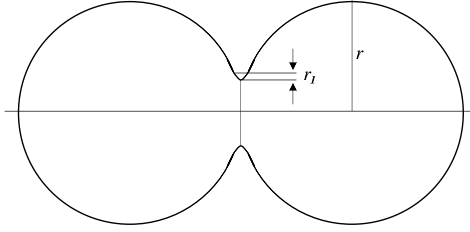

Figure 2.4: The radius of curvature between two spheres (r_1) is very small, which Vanderhoff et al. *[6] took as the driving force for the wet sintering model.*

Brown's model. Sheetz considered that film formation may not proceed uniformly throughout the whole system. He suggested that a coalesced layer could be formed on the surface, since upon reaching the end of stage I, the top layer of spheres would be pushed out of the surface. Capillary forces would then act to deform this layer, until it became coalesced. Water would evaporate from interstices lower down, with transport through the top layer having to occur by diffusion. Deformation was then driven by the compressive force exerted by the surface. Evidence for the Sheetz model is noted by Dobler and Holl who identified a dried layer at the film surface at an early stage of drying [30].

A return to surface energy driving deformation was made by Vanderhoff *et al.* [6]. They calculated the pressure differences on a pair of spheres bought together, noting that at the point of contact between the spheres, the surface had a very small radius of negative curvature, as shown in figure 2.4. The pressure difference induced by this small radius of curvature drove deformation, although they invoked water-air surface tension to bring the latex spheres into contact in the first place, at the end of stage I. This *wet sintering* theory assumed that the latex spheres are entirely immersed in water. There has been a considerable degree of debate concerning Vanderhoff's model [28] [30]. However, a more recent study by Dobler *et al.* [31] in which the latex was kept immersed in water (*ie* there was no evaporation) where deformation was observed appears to vindicate the wet sintering theory under these conditions. Eckersley and Rudin also tested the models of Brown and Vanderhoff [28]. According to their analysis, it was necessary to combine both models to provide sufficient work to deform the latex.

These four theories have been refined and developed since they were put forward [27] [28] [29]. At this point, we note another mechanism for completeness, advanced

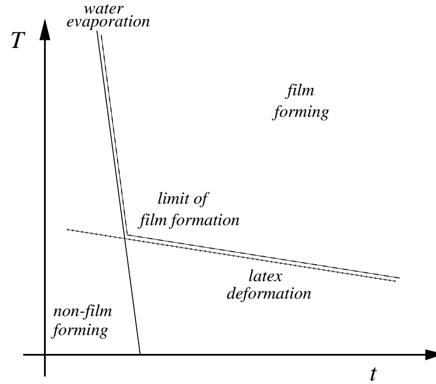

Figure 2.5: Temperature and time limits on film formation according to Sperry et al. *[33]. At high temperature, above the dotted line, film formation is governed by water evaporation, with latex deformation occurring concurrently. The time for film formation is given by the solid line. At lower temperatures, polymer diffusion is the rate-limiting step, with film formation time given by the dotted line.*

by Johnson, Kendall and Roberts, the JKR theory [32]. This treats deformation entirely elastically, under 'surface attractions' and an external load. Essentially, the JKR theory equates surface attractions and elastic forces [32]. It is limited by its assumption of elasticity, which appears not to be valid [20]. Certainly Dobler and Holl showed that the degree of deformation observed required surface tensions 100 times those usually assumed for polymer-water interfaces according to the JKR model [20].

T_g and minimum film-forming temperature

Sperry *et al.* [33] studied the minimum film-forming temperature (MFT), the lowest temperature at which a coherent film is produced for a wide range of latices. Unsurprisingly, given that the latex spheres must deform, they found that MFT correlated strongly with the glass transition temperature (T_g), with the MFT being typically several degrees lower. More interestingly, they found that films formed below the MFT (which are not transparent, due to interstices of air between non-deformed latex particles) did in fact become transparent after a time. This film formation time was consistent with polymer diffusion driving deformation according to the Williams-Landel-Ferry equation.

Film formation was thus decomposed by Sperry *et al.* [33] into the rate of water evaporation (which depended solely on temperature) and the rate of deformation, which

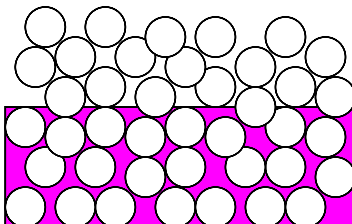

Figure 2.6: Stage II for 'hard' latices. Here water evaporation has occurred without concurrent deformation*

depended on the shear modulus of the polymer. Figure 2.5 shows the boundary between the film-forming and non-film-forming regimes. Below the dotted line in figure 2.5 evaporation occurs more quickly than deformation, and there is a considerable time lag before the film is transparent (stage III). Polymer diffusion was used to explain this time lag between water evaporation and coalescence as a function of particle size, with a simple diffusion model to account for the increased lag with larger particles. However to the right of the dashed line in figure 2.5 Sperry *et al.* found no particle size effect.

These observations of Sperry *et al.* along with those of Hwa [34] led Keddie *et al.* [18] [19] to introduce a new stage of film formation to figure 2.1, termed stage II*. Hwa had noted that a latex film typically dried from the outside in. The central region was generally turbid (stage I), whereas the dry exterior was clear (stage III). Between these two drying fronts there was a third region, in the case of relatively hard latices (MFT above the ambient temperature). This is shown schematically in figure 2.6, with air voids between the undeformed latex at the top of the film. Stage II* is included in figure 2.1 as an alternative route to stage III.

Keddie *et al.* analysed the change in refractive index associated with these drying fronts, and were able to predict the time taken for the closure of the interstitial voids formed in the case of the 'hard' latex, finding good agreement between theory and experiment.

Recent work by Routh and Russel [35] has unified the basic theories, and presented conditions under which we can expect each to apply. They characterise film formation conditions for a given latex in terms of evaporation time, capillary pressure, water-air surface tension, time for viscous collapse and shear viscosity, and derive limiting conditions

for the mechanisms of wet sintering and capillary deformation. Also incorporated in this unified model is the uniaxial compaction referred to by Lin and Meier [29] as opposed to two-particle sintering.

Interdiffusion

Here we consider stage III-IV in film formation. This interdiffusion was first proposed by Voyutskii [21], and has been verified in two ways. Hahn *et al.* used small angle neutron scattering (SANS) to obtain the radius of gyration of deuterated polymers as a function of time. Initially the deuterated chains are confined to single particles, but the increase in radius of gyration indicates polymer diffusion [22] [23].

Winnik *et al.* [24] developed an elegant technique using direct energy transfer (DET) by labelling two latices with fluorescent donor and acceptor molecules. On mixing these together, they interpretated the strength of the fluorescent signal as a measure of molecular mixing and interdiffusion. They showed that in the case of a poly-butyl-methacrylate (PBMA) latex, there is only 50 % volume fraction of mixing after 16 days, 27°C above the T_g. Hahn *et al.* also worked at elevated temperature, typically 50°C above the T_g. A further mechanism for this process was put forward by Winnik *et al.*: they suggested an entropic source. Polymer chains confined to latex particles can lower their entropy if they spread out. This effect is molecular weight dependent, in the opposite direction to diffusion, where small molecules diffuse more quickly [24].

We have seen that a number of theories have been proposed to describe film formation in polymer latices, one or more should be invoked, depending on the conditions and latex used. For a detailed review, the reader is directed to Keddie [8].

2.2

Applied Water-Based Coatings

The latex film-formation processes described above underpin all water-based coatings with a dispersed binder. Pure latices produce high quality films in the laboratory. However

practical water-based coatings have a number of further obstacles to overcome before commercial application [2]. A variety of additives are used in the water based coatings industry to provide the required performance.

Various additives are used here (see chapter 7, page 110). A rheology modifier improves the non-newtonian behaviour of water [2] [36] [37] [38]. A higher pH of around 9-10 also improves the rheology [39]. The surface behaviour is also improved with an anti-cratering agent [40] and high melting-point wax is used for surface enhancement [11]. A defoamer removes air bubbles introduced through high shear mixing [41] [42].

Coalescing Aid

The process from stage II to III of latex film formation can be enhanced by the addition of plasticisers [9]. These act to reduce the T_g of the latex, which we have already noted is strongly related to the MFT, so film formation can proceed at a lower temperature with respect to T_g [33]. The plasticiser is added to the formulation, and mixed with the aqueous phase. As the plasticiser is typically a solvent of the polymer binder, it increases chain mobility, thus effectively reducing the T_g, following water evaporation. Latices with higher T_g are often used because of superior hardness properties in the final film, as a T_g around room temperature will mean that the final film is somewhat tacky. Plasticisers enable polymers with T_g of up to 80°C to film form at ambient temperature [43]. To restore the polymer to its original T_g, the plasticiser is required to evaporate following film formation. Plasticisers which evaporate in this way are referred to as coalescing aids [43].

Coalescing aids are also known to increase interdiffusion by up to a factor of ten (stage III-IV). This both accelerates film formation and lowers the film formation temperature, so again we may use polymers with a higher T_g [9].

A further mechanism of coalescing aids is noted by Dobler *et al.* [30]. Addition of a water-soluble organic molecule such as a coalescing aid can reduce the rate of water evaporation. This in turn tends to reduce the temperature suppression due to the evaporating water, and the resulting higher temperature increases the rate of deformation.

Sufficient amounts of coalescing agent to promote film formation can result in a surface remaining tacky. A solution to this problem is to use two coalescing aids. One evaporates

quickly, reducing the length of time for which the product stays tacky. The other remains in the film for longer, enabling complete film formation [12].

2.3

Silica Matting Agent

At the heart of this work lies the silica matting agent. As mentioned in chapter 1, we seek to understand the way in which silica produces matting, and how the type of silica used influences its behaviour. In this section, we discuss the various types of silica used, and how their differing means of production give rise to a variety of physical and chemical properties.

We are primarily interested in two types of synthetic amorphous silica, fumed and precipitated silica, although some reference will be made to silica gel. All of these are used as powders, with a typical particle size of $1 - 10\ \mu m$, [12]. In each case, these *aggregate* particles are formed from rather smaller *ultimate* particles, with a typical size of $10 - 40$ nm, but can be up to 100nm [10]. The microstructure of precipitated silica is shown in figures 2.7, *(a)*showing aggregate particles and *(b)* showing ultimate particles. The porous nature of the silica is also evident from figure 2.7.

Formation

Fumed silica is made in a gas phase reaction. Essentially, a silica vapour is produced, and then condensed, usually by burning silicon tetrachloride in a hydrocarbon flame:

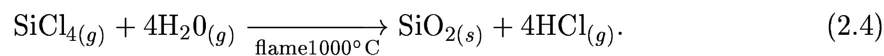

$$SiCl_{4(g)} + 4H_20_{(g)} \xrightarrow[\text{flame}1000^{\circ}\text{C}]{} SiO_{2(s)} + 4HCl_{(g)}. \quad (2.4)$$

The powder produced in this way is very pure [44] and has a low bulk density (see chapter 3) [10].

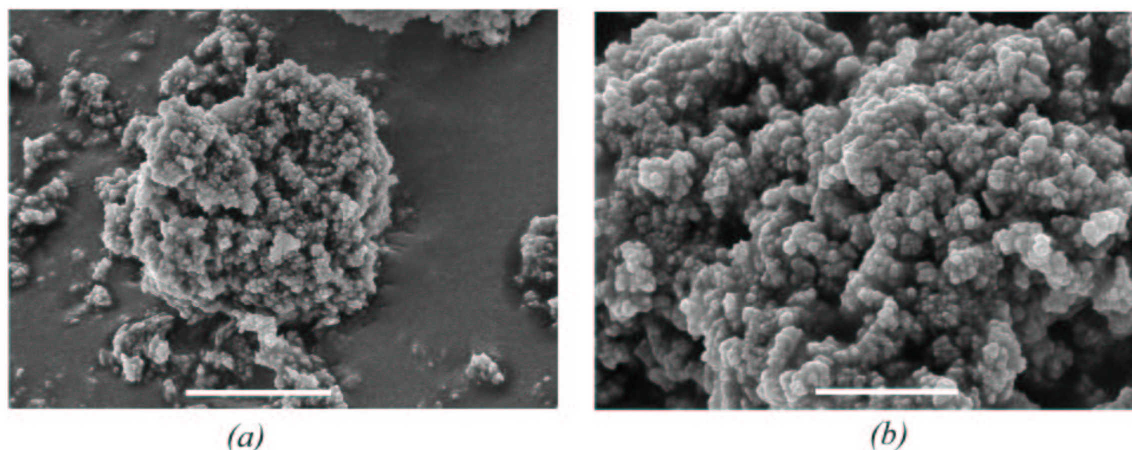

Figure 2.7: Conventional-SEM images of precipitated silica, (a) *showing aggregate particles (Scale bar=3μm), and* (b) *higher magnification showing ultimate particles (Scale bar = 1.2μm) [12].*

Precipitated silica and silica gel are both formed from aqueous solution in a similar way. The starting point is monosilicic acid solution ($Si(OH)_4$), typically produced from sodium silicate (Na_2SiO_3). Monosilicic acid can be polymerised according to the following equation:

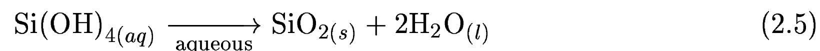

$$Si(OH)_{4(aq)} \xrightarrow[\text{aqueous}]{} SiO_{2(s)} + 2H_2O_{(l)} \quad (2.5)$$

The polymerisation is governed by pH and salt concentration (figure 2.8). At high pH, the silica particles are charged, producing colloidal stabilisation. This impedes aggregation, and the particles grow in size along the right-hand side of figure 2.8. Acidification or the addition of ions enables aggregation. In this way, a variety of ultimate particle sizes may be produced. Precipitation or gelation is also controlled by the reaction conditions, with higher salt concentration tending to favour precipitates [10].

Our distinction between gel and precipitate follows that of Iler [10]: A gel is a 3d network with uniform silica concentration, whereas a precipitate is formed from regions of higher silica concentration (and hence density) which precipitate out of solution. To

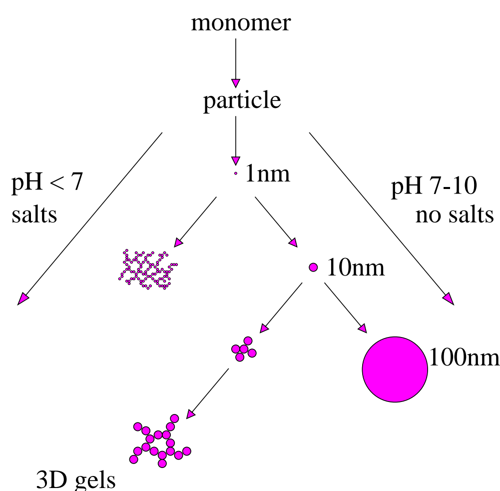

Figure 2.8: Polymerisation of silica in aqueous solution. High pH promotes growth of ultimate particles (right), but the addition of salts or reduction in pH causes aggregation.

produce a powder, gels are milled [10]. Gels tend to have a more tightly bound, robust structure than precipitates [10].

The most crucial difference between precipitates and gels compared to fumed silica lies in the bonds between the ultimate particles resulting from Ostwald ripening. Silica formed from aqueous solution has covalent bonds between the particles, whereas fumed silica has hydrogen bonding from adsorbed water [16]. The fumed silica does form aggregate particles as well, but these are necessarily weaker than precipitate or gel aggregate particles.

Surface Properties

The surface chemistry of silica is dominated by the adsorption of water, to form silanol groups ($\rangle$Si$-$OH), [10] [45]. In this section, we consider the behaviour of these silanol groups, paying attention to temperature, aqueous solution and pH. The implications for interactions with polymers are also mentioned.

In water, fumed silica ultimate particles (figure 2.9 *(a)*) can join through hydrogen-bonding of silanol groups to produce aggregates *(b)* and ultimately a gel-type network of ultimate particles *(c)*. The network is easily broken under the effects of shear *(d)*. This clearly effects the rheological properties of the dispersing medium, and fumed silica is

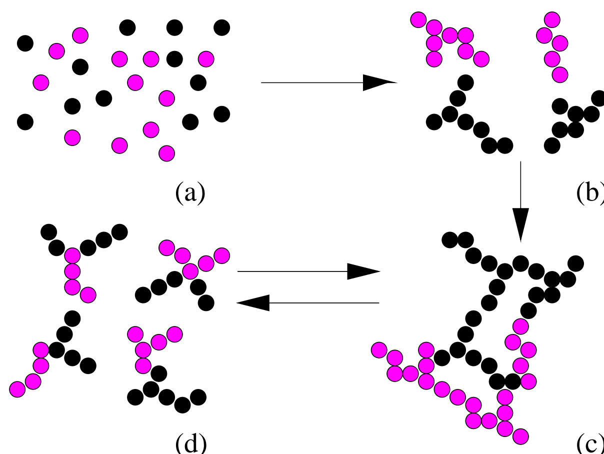

Figure 2.9: Formation and thickening effects of fumed silica. The ultimate particles (a) spontaneously produce aggregates through hydrogen bonding (b). At rest, a three dimensional network may build up (c), which is broken easily under shear(d).

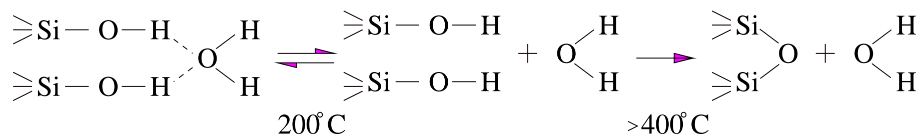

Figure 2.10: Water adsorption on the silica surface. By 200° C, water adsorbed via hydrogen bonding is lost, and above 400° C, covalently bound silanol groups are lost as well.

used as a thickening agent [16]. Precipitated silica and silica gel also exhibit spontaneous aggregation behaviour for particles of less than 100nm [10].

The concentration of $\rangle$Si–OH groups on the silica surface is typically $4.6 \pm 0.5\ nm^{-2}$ [10]. However, these are removed at elevated temperature. About 200°C is required to lose water molecules hydrogen-bonded to silanol groups, and the covalently bonded silanol groups are lost above 400°C, as shown in figure 2.10 [45]. The dehydroxylated state is somewhat irreversible. This temperature behaviour means that we would expect fumed silica (formed at elevated temperature) to have a surface dominated by siloxane (Si-O-Si) groups, compared to silanol groups for silicas formed from aqueous solution.

However, the second dehydroxylation step in figure 2.10 is not entirely irreversible. In aqueous solution (*ie* in a latex suspension), rehydration does occur, and Iler notes that the rate is increased in alkaline conditions, such as the latex suspension used here which has

a pH of 9-10. So the surface coverage of silanol groups is expected to be similar between the different silicas, although the fumed silica is initially more hydrophobic. There is more water bound internally in precipitated silicas and gels, which can result in an effective OH coverage of 6-8 nm^{-2}.

Porosity has a profound impact on the addition and removal of OH groups. It is remarkably hard to remove the OH groups from small pores, where the negative radius of curvature means that they are in closer contact, promoting hydrogen bonding. Conversely, on small ultimate particles, the positive curvature reduces the hydrogen bonding, and the OH groups are more easily lost [10].

In alkaline solution, silanol dissociates,

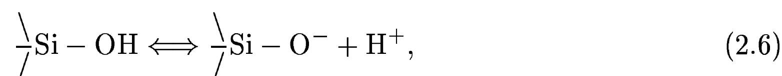

$$\rangle \mathrm{Si} - \mathrm{OH} \Longleftrightarrow \rangle \mathrm{Si} - \mathrm{O}^- + \mathrm{H}^+, \quad (2.6)$$

with about 1-1.5 $\rangle$Si–O$^-$ groups per nm^2 at pH 9. This dissociation has implications for adsorption of other species, in particular, the organic molecules found in the lacquers studied here. For pH < 7, hydrogen bonding between silanol and charged groups such as C-OH and C=O enables adsorption at these sites [10]. At higher pH, the surface charge from ionised $\rangle$Si–O$^-$ groups favours adsorption of cationic molecules. However the charge may be neutralised by sodium ions, which are frequently a by-product in silica gel and precipitated silica [10].

The silica particle structure has a considerable influence on polymer adsorption. The approach of a polymer chain to the silica surface is promoted by the more open structure of the fumed silica, compared to the precipitate, and hindered even more by the rather closed structure of the gel. This observation can also be applied to latex spheres, as will become evident in later chapters [10].

2.4

Pigmented Latices

Although relatively little work has been done on matt water-based lacquers (see next section), we can gain a significant understanding by considering pigmented latices. Like silica, pigments are typically hard, inorganic particles. Pigmentation affects latices in two principle ways: the pigment needs *dispersion*, which in turn requires wetting and breaking up of large pigment aggregates [46], and subsequent *colloidal stabilisation* [47]. Pigment-polymer interactions also differentiate pigmented latices. Crucial to the understanding of pigment behaviour is the critical pigment volume concentration (CPVC), introduced by Asbeck and Van Loo in 1949 [48].

Essentially, above a certain volume concentration, there is no longer enough polymer binder to wet the pigment particles or fill the interstices between them. So we find air voids in the dried film, a considerable increase in the permeability, and decrease in gloss [48]. This gloss decrease in pigmented (opaque) latices is associated with surface roughness, which we expand on in the next section.

More recently, permeability related to air voids has been detected well below the CPVC. This led Lu and Torquato [49] and Fishman *et al.* [50] to introduce the concept of coarseness, describing non-uniform pigment distribution. Well below the CPVC, it is possible for pigment particles to gather or agglomerate [47] such that the CPVC is exceeded locally. This leads to some voids and permeability. We discuss our treatment of CPVC for silica in matt lacquers in chapter 3, page 24.

A more fundamental study of interactions between latices and inorganic surfaces was carried out by Granier and Sartre [51]. They investigated adhesion between latex particles with varying amounts of surface acid groups and three inorganic substrates: calcium carbonate, mica and silica. These workers explained the adhesion in terms of acid-base interactions. More acidic latices adhered better to more alkaline surfaces. Silica was the least alkaline inorganic surface, and the adhesion was relatively poor. This suggests that for the lacquer studied here, the silica-polymer interactions are comparatively small, as it

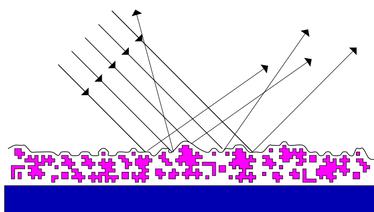

Figure 2.11: A matt coating: diffuse reflection from a rough surface. The roughness is achieved by particles on the same lengthscale as the wavelength of visible light.

has a 1% acid group content [52].

A novel study of silica in Poly(ethyl acrylate) latex was made by Espiard *et al.* [53] [54] [55]. They grafted polymer chains onto the silica and also encapsulated silica in latex particles. Where polymer chains were grafted twice onto silica particles, they found that the entangled polymers were effectively cross-linked, and the resulting stage IV film had rubber-like properties. The simple addition of silica into the latex which is analogous to the approach followed here increased the mechanical stiffness, but did not otherwise improve the mechanical properties.

2.5

Clear Matt Lacquers

We now turn to the system studied in this work, matt water-based lacquers. Schneider [11] has provided a general review of the application of silica in matt lacquers, but for more specific work, we turn to that of internal reports, particularly that of Franklin [17], which forms the precursor to this work.

Franklin described matt in terms of the loss of specular reflection (gloss), as shown schematically in figure 2.11. Light scattering was also measured in the form of haze, defined in figure 2.12. This is very important for clear (unpigmented) lacquers, as we require a high degree of transparency. In effect, this means that refractive index (RI) must be constant throughout the film.

Atomic force microscopy (AFM) (chapter 4, section 4.2 section) was used to determine

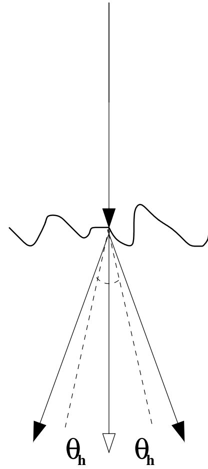

Figure 2.12: Haze is normally incident light scattered by more than 2.5°.

the surface roughness, which is characterised by the parameter R_a [56],

$$R_a = \frac{1}{N} \sum_{i=1}^{i=N} |h_i - \bar{h}|, \qquad (2.7)$$

where N is the number of points sampled, h_i is the height of each point, and $\bar{h}$ is the arithmetic mean of all the h_i.

Franklin was able to show that R_a was directly correlated with gloss reduction, for a variety of silicas, suggesting that gloss reduction is a purely surface phenomenon. Both R_a and gloss were functions of silica concentration by mass, with higher concentration reducing gloss and increasing R_a.

He also demonstrated that large angle light scattering, (haze), is dependent upon bulk properties. Furthermore, haze was dependent upon the type of silica used, with agglomerated fumed silica having low haze, and silica gels producing rather more, as shown in figure 2.13.

The postulated haze-producing mechanism stemmed from the fact that the diameter of the latex is typically larger than the pores in the silica particles. This would mean that the latex was unable to penetrate the pores, so the effective refractive index of the silica was then different, due to the air in the pores, to that of the film-formed latex. In effect,

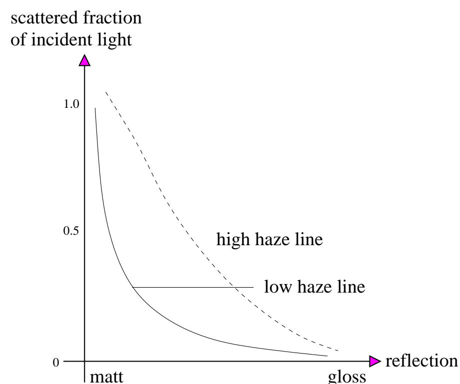

Figure 2.13: Schematic illustration of the reflection/haze behaviour of various matt water-based lacquers showing high and low haze lines [17].

this is a similar observation to that made by Iler [10] above concerning polymer approach to different types of silica, and one to which we shall return in chapter 9.

This work takes Franklin's observations as its starting point, and develops the themes he proposed. Two further techniques are used (see chapter 4 sections 4.1 and 4.3), environmental SEM and confocal microscopy, to characterise the silica structure in matt water-based lacquers. In the next chapter, we present our silica structure model for matt water-based lacquers.

Chapter 3

Building the Silica Structure Model

'If you wish to become really a man of science and not merely a petty experimentalist, I should advise you to apply to every branch of natural philosophy, including mathematics', Mary Shelley, in *Frankenstein*

In this chapter, we present our model of the structure assumed by the silica in the dried lacquer film. As can be seen from the preceding chapter, the system is rather complex. We therefore restrict ourselves to the simplest possible approach, based on the volumes occupied by the silica and the lacquer, which is outlined below. This is then developed more mathematically, and extended to take account of air in silica pores, as suggested by Franklin [17]. At the end of this chapter, we discuss the implications of the model. We also present the silicas which form the central topic of this work, and discuss how their behaviour may be influenced by density, mechanical properties and surface chemistry.

3.1 Outline

First we consider the dry silica powder in which the highly porous particles occupy a certain volume. Since the particles are porous and irregular in shape, air is found in both pores and interstices between the particles. The bulk density allows us to determine that fraction of space occupied by the silica which is silica itself and how much is air, by

comparison with the true density of silica.

In the case of lighter silicas, the bulk density is only a small fraction of the true density of around 2.18 gcm^{-3} (table 3.1) [10]. So only a tiny proportion of the volume occupied is silica, the majority being air. We also note that the silica particles must all be touching, to support themselves, so there is a continuous network of silica. Now, if the silica is incorporated into the lacquer, which is then dried, and the volume of air in the dry powder is exactly displaced by dry lacquer, the silica particles should again touch one another. Since this exact displacement occurs at a unique mass of silica added to the formulation (for a given volume of lacquer) we refer to it as the *critical mass*. It is related to the critical pigment volume concentration in pigmented lacquers (CPVC) [48] [57].

The model is illustrated schematically in figure 3.1. At lower silica concentration, the particles are separated, figure 3.1*(a)*. The silica network formed at the critical mass is shown schematically in *(b)*, where the silica particles touch to form a spanning structure. At higher silica concentration, our model suggests two possibilities: *(i)* The silica collapses under volume reduction in film formation driven by the evaporation of water and we see densification of the silica (figure 3.1*(c)*). Alternatively, *(ii)* the silica structure may be strong enough to resist collapse. In this second case, at the critical mass, we expect a transition from isolated silica held in a polymer phase to polymer adhered to a robust silica structure, which may produce air voids to as the film shrinks during drying, as shown in figure 3.1*(d)*.

We note at this point that *percolation* is required for the structure formed at the critical mass [58]. Percolation is a geometric phenomenon which can impart physical properties, as is the case here. Essentially, a percolating structure spans the system, whereas a non-percolating structure will have some smaller lengthscale [58]. Here if we populate the film with silica particles, at some critical *percolation threshold* the silica structure will span the film. Below the percolation threshold the silica particles will be isolated (figure 3.1*(a)*) but we assume a percolating silica structure such as that in *(b)* at the critical mass because the dry powder structure must percolate to support itself.

So at some point between isolated silica particles (figure 3.1*(a)*) and the critical mass *(b)* we expect to encounter this percolation threshold. Now percolation is necessary but not sufficient for the self-supporting structure shown in figure 3.1*(b)*. Because of the

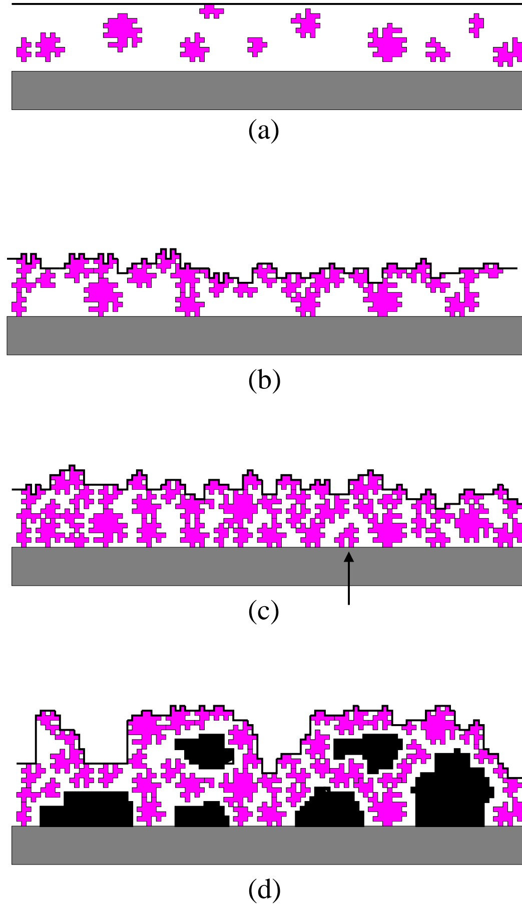

Figure 3.1: Schematic of the model of silica structure within dried lacquer. The low concentration regime (a) ($\frac{m_{sil}}{m_0} < 1$), critical mass of silica (b) ($\frac{m_{sil}}{m_0} = 1$), and two possibilities for $\frac{m_{sil}}{m_0} > 1$, with silica densification from collapse (c), or void formation with more robust silica (d). Note that (c) *and* (d) *do not exclude the possibility of isolated silica particles, for example that marked in* (c).

temporary bonds between ultimate particles mentioned in chapter 2, page 15 [16] the fumed silica in particular may form a percolating structure that is too weak too support itself. With precipitated silica, this is less likely due to permanent bonds between ultimate particles and aggregate particles larger than the 100nm maximum for self-aggregation [10]. Nonetheless we note that the formation of a self supporting structure associated with the critical mass requires percolation, but may not occur at the percolation threshold.

Figure 3.1*(c)* differentiates our approach from that of Asbeck and Van Loo [48], Lu and Torquato [49] and Fishman *et al.* [50]. They consider only hard particles, as in figure 3.1*(d)*. It is important to note that our approach is rather different. We focus on silica

Silica type	Bulk density ρ_{bulk} gcm^{-3}	m_0 from eq:3.6 (mass fraction)	m_0 from eq:3.8 (mass fraction)
Fumed	0.0645	0.0226	0.0243
Agglomerated fumed	0.0625	0.021875	0.0234
Precipitated	0.1378	0.0483	0.0548
Calcined precipitated	0.1017*	0.0356	0.0394†
Fine precipitated	0.0815	0.0285	0.0309
Coarse precipitated	0.2849	0.09972	0.139
Soft precipitated	0.18907*	0.0662	0.07462
Loose gel	0.1875	0.0656	0.0799†

Table 3.1: *Silica densities, measured compressing a known mass with a piston by Crosfield R&D [12], (Japanese industrial standards association number K6223-1976). The critical mass m_0 is given for the different silicas, according to equations 3.6 and 3.8. * Measured by tapping 25cm^3 measuring cylinder. † v^*_{pore} taken to be 0.5 cm^3g^{-1}.*

percolation. The correspondence to the critical pigment volume fraction CPVC depends on whether or not the silica collapses. A collapsed silica structure like figure 3.1*(c)* is effectively below its CPVC as there is still enough polymer binder to wet the silica [48], although there is more than enough silica to form a self-supporting structure as a dry powder, which we take as our starting point, so it is above the critical mass.

In fact our density measurement is different to the CPVC cell of Asbeck and Van Loo, as they determine the volume of the pigment after wetting. The voluminous fumed silica is massively compacted upon wetting, so we expect a rather different volume for our dry measurement for the same mass of silica. Our model is therefore not entirely analogous to the CPVC of Asbeck and Van Loo [48].

3.2

Mathematical treatment

We now derive expressions for the critical mass of silica. At the level of this work, we assume a uniform silica concentration, without extension to the local concentration fluctuations of Lu and Torquato [49] and Fishman *et al.* [50].

The bulk volume V_{bulk}, bulk density ρ_{bulk} and mass m_{sil} of silica are related by

$$V_{bulk} = \frac{m_{sil}}{\rho_{bulk}}. \tag{3.1}$$

Here V_{bulk} is the volume of silica and included air, both in pores and between particles. The volume of dry lacquer V_{dry} is given by

$$V_{dry} \approx C_{sol} V_{wet}, \tag{3.2}$$

with V_{wet} the volume of wet lacquer and $C_{sol} = 0.35$ [59] the solids content [1]. Equation 3.2 holds only if the densities of the wet and dry lacquers are equal. In fact both are approximately unity (see Appendix page 217). Our condition for the critical mass of silica requires that all air available to the polymer is displaced. The maximum volume available to the latex is the bulk volume occupied by the silica, V_{bulk}, yielding

$$V_{dry} = V_{bulk}, \tag{3.3}$$

but this neglects the volume that is silica itself, V_{sil} and those pores which are too small for the latex to access, V_{pore}. The volume required to displace the available air is then

$$V_{dry} = V_{bulk} - V_{sil} - V_{pore}. \tag{3.4}$$

Relating this to the volume of wet lacquer and the bulk and 'true' densities of silica, we have

$$V_{wet}C_{sol} = m_0 \left(\frac{1}{\rho_{bulk}} - \frac{1}{\rho_{sil}} \right) - V_{pore}, \tag{3.5}$$

where m_0 is the critical mass of silica required to satisfy equation 3.4. To solve equation 3.5 for m_0 requires the value of V_{pore}, which is dealt with in the next section. For now, we consider the simplest case. For a light silica, such that $\rho_{bulk} \ll \rho_{sil}$, we can neglect the contribution from ρ_{sil}. For a weakly bound silica, we expect that the pore structure will be disrupted by the drying latex, so that V_{pore} can also be neglected. This then yields

$$m_0 \approx \rho_{bulk} V_{wet} C_{sol}. \tag{3.6}$$

In the case where the silica is more dense, for example some of the heavier precipitates and the gels, we have

$$m_0 \approx \frac{V_{wet}C_{sol}}{\left(\frac{1}{\rho_{bulk}} - \frac{1}{\rho_{sil}} \right)}. \tag{3.7}$$

The volume of small pores V_{pore} is a constant for a certain mass of silica, so we can introduce a value for each silica, v^*_{pore}, the volume of pores inaccessible to the latex in 1g of silica. This gives

$$m_0 \approx \frac{V_{wet}C_{sol}}{\left(\frac{1}{\rho_{bulk}} - \frac{1}{\rho_{sil}} - v^*_{pore}\right)}. \tag{3.8}$$

We determine v^*_{pore} in the next section.

Now, there are air spaces between the silica particles in the dry powder, such that the volume fraction of the silica particles and their pores is

$$\phi = pV_{bulk}, \tag{3.9}$$

where p is the packing fraction [60]. Using equations 3.1-3.9, we have

$$\phi \approx p\frac{m_{sil}}{m_0}. \tag{3.10}$$

Equation 3.10 can be tested by measuring the silica volume fraction ϕ as a function of silica mass added to the lacquer during formulation. It may be valid for $\frac{m_{sil}}{m_0} \leq 1$ only, as two regimes of behaviour are expected at higher silica concentration, depending on whether or not the silica collapses (figure 3.1 *(c)* and *(d)*). If the silica collapses totally, then we expect ϕ to increase linearly beyond $\frac{m_{sil}}{m_0} = 1$. However we note that $\phi \leq 1$ by definition, so the linear behaviour must be limited.

3.3

Porosimetry

We turn now to the contribution to the volume made by small pores, from which the latex spheres are excluded. We seek a value v^*_{pore} as defined above. Now the determination of pore size and volume is a complex task of which only the briefest outline is presented here. For a more complete description, the reader is referred to Webb and Orr [61] and

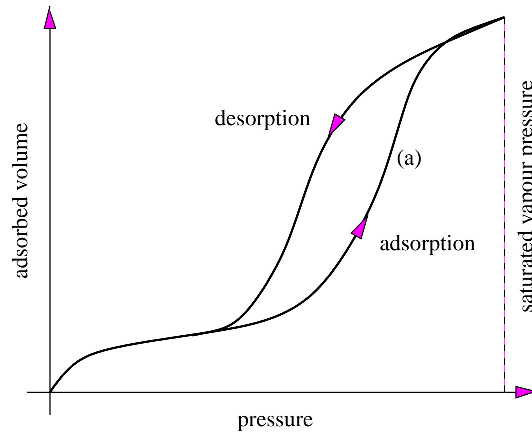

Figure 3.2: Hysteresis in gas adsorbed and desorbed as a function of pressure for a porous solid. The rapid increase in the adsorption branch at higher pressures, marked as (a)*, corresponds to condensation on the surface. Capillary forces in pores then inhibit desorption, causing the hysteresis shown.*

[62] The surface area of a solid may be found by adsorbing a layer of gas onto the surface. This adsorption results in a decrease in gas pressure, from which the surface area may be deduced, as the thickness of the layer of adsorbed gas may be determined for a given pressure. Eventually, upon approaching the saturated vapour pressure, the gas simply condenses onto the surface (figure 3.2).

This is conceptually straightforward, but the presence of small pores complicates matters. Pores may be filled with liquid adsorbant well before the saturated vapour pressure is reached [62]. The pressure at which the filling occurs is a function of pore radius, so the increase in adsorption due to condensation in the pores allows us to determine the pore radius.

During desorption, there is considerable hysteresis due to capillary forces in the pores suppressing evaporation (figure 3.2). The Barrett, Joyner and Halenda (BJH) method [61] is used here to determine pore radius from the adsorption measurements. The results of nitrogen porosimetry work carried out by the suppliers [12] are given in table 3.2.

Since we have the volume of gas adsorbed as a function of pressure, and we know the radius of the pores filled at each pressure, we can find the total volume of pores below a certain diameter. Here we assume that the latex cannot access any pores smaller than its diameter of 80nm (see chapter 8, figure 8.11). This gives us v^*_{pore} directly by integrating

Silica Type	BJH area m^2g^{-1}	BJH pore volume $cm^3g{-}1$	BJH pore diameter (nm)	$v^*_{pore} \leq 80nm$ cm^3g^{-1}
Fumed	175	1.103	25.2	0.504
AFS	180	0.951	21.1	0.574
Precipitated	110	1.086	39.4	0.468
Fine Precip.	112	0.978	49.0	0.509
Coarse Precip.	93	0.987	42.4	0.5459
Soft Precip	46.3	0.10	1.24	0.14
Loose gel	411	1.98	19.2	

Table 3.2: *Silica porosimetry data, for pore area, volume, characteristic diameter and volume of pores less than 80nm in diameter [61]. All porosimetry data is taken for the adsorption lines (see figure 3.2). This work was carried out by Crosfields R&D [12].*

the volume of nitrogen adsorbed in the appropriate pressure range, as given in table 3.2. It must be stressed that porosimetry is not an exact science. The BJH method makes a number of assumptions, in particular the adsorption values (used here) do not agree with desorption measurements, due to hysteresis (figure 3.2) [61]. However, from table 3.1, the effect of $v^* - pore$ on our calculated values for m_0 is not severe for any silica. In fact the use of equation 3.6 is reasonably accurate for all but the denser silicas. Nevertheless, we use m_0 values from equation 3.8 for experimental work.

3.4

Implications of the model

We have seen that the critical mass can be found by determining the bulk density of the dry powder, and then refined using the volume of small pores. In addition to the development of the percolating structure, we expect a considerable increase in surface roughness when $\frac{m_{sil}}{m_0} \approx 1$, as the silica structure can perturb the surface once a network is formed. This should be rather more marked in the case of the more robust silicas, which do not undergo collapse.

If Franklin's [17] view of matting is correct, then there should be a significant increase in matting associated with this development in surface roughness (see section 2.5). This

is in agreement with pigmented lacquers, where a decrease in gloss is found above the CPVC [48]. With the microscopies described in the next chapter, we can study this silica structure in detail. Confocal microscopy will enable three-dimensional imaging of the silica structure. The surface techniques of environmental SEM and atomic force microscopy should distinguish the collapsed (figure 3.1*(c)*) and non-collapsed *(d)* structures.

Silicas Studied

A variety of silicas are used here, whose properties are summarised in table 3.3, page 33. As noted by Franklin, the agglomerated fumed silica (AFS) exhibits little scattering of transmitted light (chapter 2, section 2.5). This fumed silica has a relatively high degree of aggregation, but it is still far more weakly bound than the precipitates or gels. Beyond repeating Franklin's experiments comparing precipitated silica and AFS, we have some variants which modify specific properties. In particular calcined precipitated silica is heated to 1000°C to remove any bound water, as discussed in chapter 2, page 16. In this way, the thermal history resembles that of fumed silica. So we expect that calcined precipitated silica will have the mechanical properties of precipitated silica, but the surface chemistry should be somewhat similar to fumed silica, as we infer from the loss of structurally bound water in table 3.3 [10] [12]. The mass loss at 1000°C is now more reminiscent of a fumed rather than precipitated silica (table 3.3). This should make it possible to isolate whether mechanical properties or surface chemistry are responsible for the lower haze in the case of AFS.

The precipitated silica has also been sieved, to provide coarse and fine fractions (CPS and FPS respectively). These are all chemically similar, but as can be seen from table 3.1, they have widely differing densities. In particular it seems that the larger coarse particles are either more closely packed than the smaller fine particles, or are themselves denser. The silica gel will also have similar chemical properties, but the aggregate particles should be more robust than precipitated silica and the pores are smaller (table 3.2).

The soft precipitated silica (SPS) has a rather larger ultimate particle size of around 100nm. These larger particles result in a weaker structure, as each ultimate particle is bound in a similar way to the normal precipitate, but there are far fewer bonds per unit

volume [10] [12]. So the mechanical properties of this silica bear more resemblance to AFS, whereas the surface is that of a precipitate. Note also that the pore volume of this structure is very small.

We conclude this chapter by noting the main points of our silica structure model:

(1) At a certain mass fraction of silica, $\frac{m_{sil}}{m_0} = 1$, incorporation of silica into the lacquer and subsequent film formation is equivalent to replacing air between silica particles as a dry powder with polymer.

(2) The silica volume fraction is linear in $\frac{m_{sil}}{m_0}$ at least up to the critical mass where it is equal to the packing fraction.

(3) Above $\frac{m_{sil}}{m_0} = 1$ we expect either structural collapse and silica densification or no collapse and a strong increase in surface roughness, depending on the mechanical properties of the silica.

Silica	Characteristic aggregate particle lengthscale	% Mass lost heating to 1000° C [12]	Comments
Fumed silica	0-40nm	2.0	Non-agglomerated fumed silica. High purity. Aggregates under H-bonding. Low bulk density.
Agglomerated fumed silica (AFS)	1μm some 10 μm	3.4	Fumed silica aggregates. Low bulk density, High purity.
Unseived precipitated silica (UPS)	1-10 μm	12.5	Precipitated silica. Wide particle size distribution. Moderate bulk density.
Fine precipitated silica (FPS)	3 μm	8.5	Fine fraction of UPS. Low bulk density.
Coarse precipitated silica (CPS)	10 μm	11.0	Coarse fraction of UPS. Dense.
Calcined precipitated silica	as UPS	2.2	UPS without bound water. Moderate bulk density.
Soft precipitated silica (SPS)	3 μm	N/A	Weakly bound precipitated silica. Large aggregate particle size of 100nm. Moderate bulk density. Low porosity
Silica gel	6.5 μm	9.0	Loose silica gel. Low pore diameter of 21nm. Dense.

Table 3.3: Silicas used in this work. Characteristic aggregate particle size is determined from ESEM work (chapter 8, section 8.5) except silica gel from light scattering [12] and fumed silica (where we quote typical *ultimate* particle size [10]).

Chapter 4

Experimental

This chapter is primarily devoted to a fairly detailed discussion of the microscopy techniques used. All are *scanning* microscopies, where we record the signal produced by a probe scanned across a specimen as a function of position. This gives an *image* of the specimen, where the brightness at each specimen point is related to the strength of the signal. Changes in brightness (contrast) in the image reveal the structure of the specimen.

The nature of the signal depends on the microscope. Environmental scanning electron microscopy (ESEM) measures electrons emitted from a sample irradiated with an electron beam [13], whereas atomic force microscopy (AFM) is sensitive to the force between the specimen and a fine tip [63]. Confocal laser scanning microscopy (CLSM) determines the distribution of fluorescent dye or refractive index variation in a sample [64]. The first two reveal information about the surface only but CLSM can image into the bulk of the lacquer film. Combining the different techniques, we can build up a comprehensive picture of the microscopic structure of the lacquer film. We now describe each of these techniques in turn, beginning in each case with a brief overview.

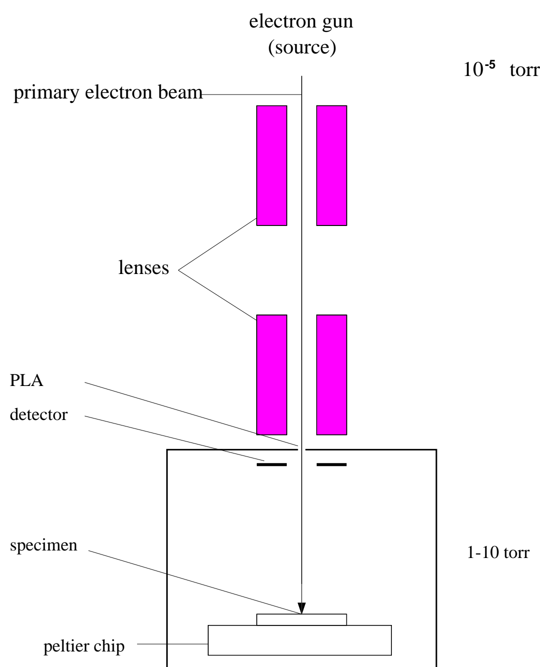

Figure 4.1: Schematic of an ESEM: the sample chamber is held at $1-10$ torr, while the electron optics are maintained at 10^{-5} torr.

4.1

Environmental SEM

ESEM was developed from conventional SEM in the 1980s [13]. The key difference lies in the sample chamber which, unlike conventional high-vacuum SEM, is only partially evacuated to a typical pressure of $1-10$ torr (760 torr = 1 atmosphere) as shown in figure 4.1.

The presence of this *imaging gas* above the sample has two main consequences. Insulating specimens may be imaged [65] and, if the gas used is water vapour then we can stabilise hydrated samples. This second effect is crucial here, as it enables us to observe drying of water based lacquers *in situ* [18] [19] [66] [67] [68]. We now explore the main components of ESEM, with reference to matt water-based lacquers.

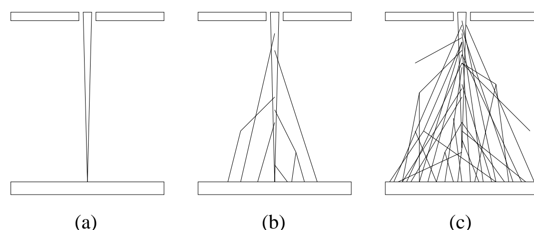

Figure 4.2: Variation in primary beam scattering as a function of pressure. In vacuo (a), there is negligible primary beam scattering (conventional-SEM). A partial pressure (b) of less than 20 torr produces 'oligo-scattering' (ESEM). At higher pressures (c) the primary beam is entirely lost.

Differential pumping system

Within the ESEM, the electron gun and optics are maintained in a moderately high vacuum. The presence of an imaging gas in the sample chamber produces a pressure gradient. The back-flow of gas is minimised with small pressure limiting apertures (PLA), and the pressure gradient is maintained via differential pumping (figure 4.1), [13]. This means that all but the specimen chamber is maintained at a vacuum of around 10^{-5} torr.

The electron optics are similar to a conventional SEM. The instruments used have either a tungsten hairpin (Electroscan 2010) or lanthanum hexaboride (Electroscan E3) thermionic source [69]. The primary electron beam is produced by accelerating electrons via an anode, and focussed using condenser and objective electron lenses. Stigmator coils provide a cylindrically symmetric beam, and scan coils produce the raster scan for image formation. A raster scan is typically a series of horizontal lines starting on the side of the scanned region to produce a 2D image. The electron optics are capable of producing a primary beam of a few nanometres in diameter, which governs the ultimate resolution of the microscope [69]. SEM electron optics are described in more detail in Goldstein *et al.* [70], chapter 2.

Probe beam scattering

When electrons pass through a gas, they interact with it and scatter. This changes the electron momentum, in a largely random way. Passing a highly focussed electron beam through a gas results in a very low electron density across a wide area, entirely inappro-

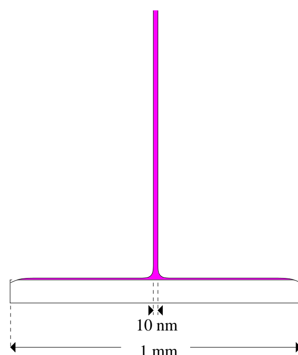

Figure 4.3: Electron intensity in ESEM. The electron intensity is very low across a wide region, giving rise to a uniform background. The central peak has the same width as the unscattered primary beam

priate for image formation. However, a short path through a partial pressure of less than ∼20 torr can be tolerated (figure 4.2). In this case a substantial proportion of the primary beam remains unscattered [13] [71]. Here we identify three regimes.

(1) In vacuo, there is no scattering (figure 4.2*(a)*), and the probe retains its shape.

(2) At high pressures (above ∼20 torr), the mean free path of the primary electrons in the beam (PE) is much less than the distance from the lowest PLA to the sample. Effectively all the electrons are scattered away from the beam and the shape is lost (figure 4.2*(c)*) [71].

(3) Between these two regimes, we have the *oligo-scattering* of ESEM. Here the PE mean free path exceeds the PLA-sample distance, so a significant proportion of the beam is unscattered. The scattered electrons are far removed from the beam, forming a uniform and low-intensity background signal, the *skirt* as shown in figure 4.2*(b)* [72]. So the only differences between mode *(b)* in figure 4.2 and conventional SEM are a loss of intensity in the primary beam and an additional uniform background signal from the skirt, as shown in figure 4.3.

Consequently ESEM can obtain a resolution of around 10 nm on a test sample [69]. Probe beam scattering is a function of pressure, and is discussed further below [71].

Electron-sample interactions

For the purposes of image composition, we consider the sample to be silica particles suspended in a polymer matrix, which may contain varying degrees of water. Electrons may scatter *elastically*, with no appreciable energy loss, or *inelastically* where a substantial amount of energy is lost. Primary beam electrons (PE) which are scattered elastically through a wide angle may re-emerge from the sample. These are termed backscattered electrons (BSE).

Inelastically scattered electrons interact with the sample in a variety of ways [70]:

(1) Ionisation of sample atoms to form secondary electrons (SE). These low-energy electrons are usually re-absorbed, but some escape and are detected [70].

(2) Formation of X-rays through Bremsstrahlung (deceleration of electrons by nuclei), and characteristic X-rays (X-rays emitted by electron transitions following inner shell ionisation) [70].

(3) Cathodoluminescence, lower energy photon emission from electron transitions in sample atoms [70].

(4) High-energy electrons generate phonons in the sample. Each excitation is small, transferring less than 1eV. Phonons cause heating of the sample, but since the irradiated region is usually in good thermal contact with its surroundings, most of the heat is conducted away, and large temperature rises are usually avoided [70] [73]

Of course, these interactions can cause considerable damage to the sample, particularly in the case of relatively fragile polymeric materials [73]. We consider electron-sample interactions in more detail in chapter 5, paying particular attention to mechanisms of sample damage.

The motion of each PE within the sample depends on probabilistic scattering events, so individual PE exhibit wide variations in their trajectories. However, the vast majority of scattering takes place within a region referred to as the interaction volume (figure 4.4). As the beam penetrates the sample it broadens, as electrons are scattered away from the central axis. Deeper in, electrons have lost sufficient energy that they are either absorbed

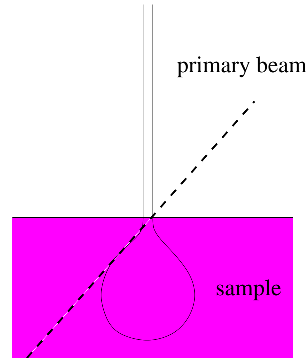

Figure 4.4: Approximate shape of the interaction volume. Primary beam electrons undergo scattering, into a broader region, before absorption as the electron range is reached, or backscattering. The dotted line represents a tilted surface.

or have already been backscattered. A typical interaction volume will have a shape shown in figure 4.4. The interaction volume is discussed in more detail in chapter 5, page 68, but for now we note that the lengthscale is of order 1-2μm for the samples we are interested in under typical operating conditions [70].

Backscattered electrons

BSE show a strong dependence on atomic number. Heavier atoms with larger nuclei have greater cross-sections for large-angle elastic scattering than light atoms with smaller nuclei. So the proportion of PE which are backscattered increases strongly with atomic number (Z) for ($Z < 60$). Since silicon backscatters more strongly than carbon on account of its higher atomic number, the BSE signal from silica is stronger than the surrounding polymer.

The BSE signal is not tremendously sensitive to beam energy. This is because although scattering is a function of beam energy, high energy electrons tend to lose energy through inelastic processes and then backscatter, whereas lower energy primary electrons typically backscatter after a shorter distance travelled through the sample. So for a given primary electron, the chances of it backscattering are not massively altered by its initial energy [70].

Secondary electrons

Secondary electrons (SE) have a far lower energy than BSE, typically a few eV. By comparison to BSE, SE are relatively insensitive to elemental composition in the sample, although carbon is known to produce a low SE signal. Although the BSE escape depth is of the same order as the electron range, the SE escape depth is much smaller. Low energy electrons are easily absorbed by the sample, and the SE mean free path is around 10nm for insulators [70]. The exponential decrease in escape probability with depth means that we assume a negligible contribution at depths greater than 5 times this mean free path, 50nm [70].

The SE component increases with decreasing beam voltage. This is due to the small escape depth. As the beam voltage is increased, the interaction volume enlarges, and a higher proportion of SE are produced deeper in the sample, and absorbed before emission [70].

We now consider the shape of the interaction volume (figure 4.4). If the primary beam is incident on the sample surface at an oblique angle, more of the interaction volume is close to the surface, and more SE can escape, since there is more interaction volume within the 10 nm escape depth (dotted line in figure 4.4). The angular distribution roughly follows a $\frac{1}{cos\theta}$ rule where θ is the angle of the probe beam to the normal. The case of BSE tilt dependence is more complicated and, although we observe the same overall behaviour BSE are less sensitive to surface topography [70]. So SE are the primary measure of surface topography (because of their small escape depth), whereas BSE contain more information about the elemental composition [70].

ESEM has revealed a further source of contrast with secondary electrons. Materials with different electronic structures have different SE emissions. This has been linked to the energy gap between the highest occupied molecular orbital and lowest unoccupied molecular orbital. Absorption of SE in this energy range is suppressed, so more escape from materials with larger energy gaps [74].

As water has a relatively large band gap, it produces a strong SE signal [74], so during drying of a latex film, we expect water-rich stage I latex to give a rather higher SE signal, which should decrease with the removal of water during drying.

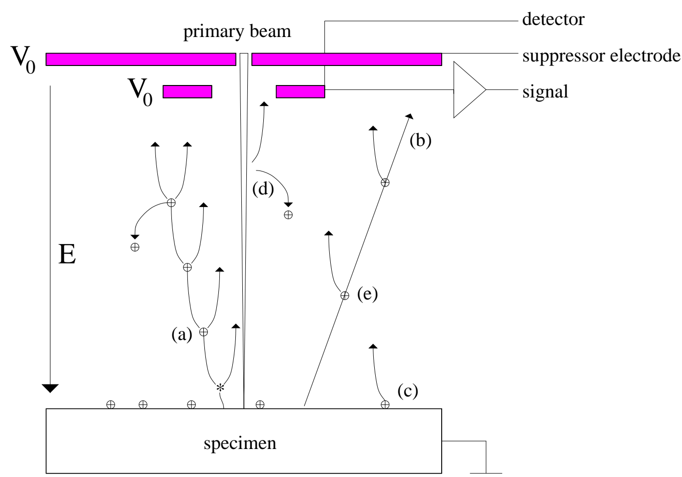

Figure 4.5: Signal amplification in the ESEM. The gaseous secondary electron detector is shown. Secondary electrons are accelerated in an electric field, and ionise the imaging gas. Successive ionisations initiate a cascade process amplifying the signal by a factor of up to 2000, process (a). The amplification process is complicated by further contributions (b) to (e).

Signal Amplification and Detection

The ESEM detector is based on SE amplification by the imaging gas [75]. Secondary electrons are attracted to the detector by an electric field by holding the detector at a bias of up to 500V. The secondary electrons emitted by the specimen are accelerated to ionise the gas, generating more *environmental* secondary electrons (ESE) at each ionisation. The resulting signal may be amplified by up to two thousand times [76] [77] (Process *(a)* in figure 4.5). BSE also produce environmental secondary electrons (process *(e)* in figure 4.5). Current from the detector is then amplified electronically to produce an image [69].

Secondary electron amplification is by no means the only process present in the ESEM sample chamber. The environmental secondary detector (ESD) is also sensitive to BSE through SE_{III} (which are produced by BSE striking the walls of the chamber, etc) [70] and BSE ionising water molecules and contributing to the SE cascade (process *(e)* in figure 4.5). SE_{IV} (produced by primary electrons in the optics column) also form a component of the signal. [70]. These unwanted contributions to the signal can be somewhat alleviated with the gaseous secondary electron detector (GSED), which has a suppressor electrode held at the same potential above it (figure 4.5). The suppressor electrode absorbs a large

proportion of BSE-produced ESE, SE_{III} and SE_{IV} before they reach the detector [69]. However the BSE contribution can also be a useful signal in itself, particularly with matt lacquers, increasing the contrast between silica and polymer/water matrix.

Positive ions are also produced by the amplification process. These are accelerated by the electric field, in this case towards the sample, (figure 4.5*(b)*). This is believed to influence sample charging from the primary beam and stabilise insulating samples. It is this charge neutralisation that enables ESEM to image insulating samples in their natural state. A further effect of positive ions is the release of electrons from the sample surface (process *(c)* in figure 4.5) [78], although this not significant if water is used as an imaging gas [79]. Primary beam ionisation (figure 4.5*(d)*) also deposits positive ions on the sample surface, and contributes to the signal received at the detector [78].

Signal Composition

ESEM predominantly uses a secondary electron signal [68], by utilising the gas amplification process described above. So far we have considered SE produced by the primary beam. However, BSE are also capable of ionising sample atoms. A secondary electron produced from a BSE ionisation is denoted SE_{II}, whereas a primary electron ionisation produces an SE_{I}. Further contributions to the secondary electron signal are SE_{III} and SE_{IV}(as mentioned above).

We can reduce SE_{III} and SE_{IV} with the suppressor electrode, and as the contribution is relatively small, we neglect it [76]. Not so with SE_{II}. Although SE_{II} have a much more indirect formation than SE_{I}, they can produce a very significant part of the signal [70].

We can determine the ratio of SE_{II} to SE_{I} [70]. Values for carbon give $\frac{SE_{II}}{SE_{I}}$ of 0.18. Silicon on the other hand produces rather more backscattering to yield a $\frac{SE_{II}}{SE_{I}}$ ratio of around 0.5 [70]. So the SE dominated ESEM signal contains a significant BSE contribution indirectly through the SE_{II} component.

In the matt lacquer, silica is expected to produce a high signal through both surface roughness (SE_{I}) and atomic number (SE_{II}). The polymer/water matrix should have a relatively low signal, although the absolute SE emission should depend on the water content.

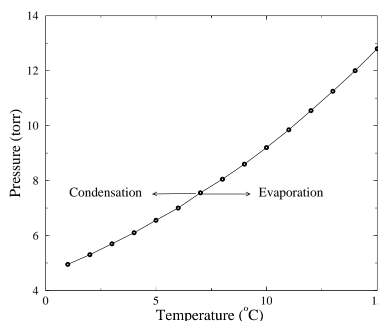

Figure 4.6: Saturated Vapour Pressure Line for water. The pressure range is shown for ESEM operation; hydrated samples must be chilled to less than 10^oC, to be stabilised at suitable chamber pressures for ESEM.

Resolution is limited by the transport of BSE through the sample. The PE range for the samples studied is around $1-2\mu m$ [70], so the place of SE$_{II}$ emission can be somewhat removed from the primary beam. This resolution degradation is compounded by the loss of primary beam intensity from beam scattering in the imaging gas [69].

Hydrated Samples

To image hydrated samples we must equalise evaporation and condensation rates. If water is used as the imaging gas, evaporation and condensation in a hydrated sample can be controlled. Fortunately, water behaves very well as an imaging gas, with a high ionisation cross-section producing a strong signal [76]. Equalisation of evaporation and condensation rates occurs at saturated vapour pressure (SVP) . Figure 4.6 shows the SVP line for water in the ESEM pressure range corresponding to temperatures of a few degrees Celsius. We chill the sample to the appropriate temperature with a Peltier chip controlled cooling stage [13].

The transition from air at room temperature and pressure to a few torr of water vapour and a few degrees Celsius involves both evaporation and condensation. An *optimised pumpdown procedure* for ESEM has minimised these effects [72]. Essentially we seek to prevent the water boiling, which occurs if the total pressure (water vapour and air) drops below the water vapour pressure. So we pump the chamber down to the SVP, and then flood with 4 torr of water vapour successively. After about nine cycles of pumping and

flooding, there is almost no air in the chamber. Relatively little evaporation and no condensation occurs with this method [72]. We develop the optimised pumpdown further in chapter 7.

Limitations

In order to use ESEM most effectively, it is important to appreciate its limitations. As noted above, it is a surface technique, so clearly little information concerning the bulk can be extracted. This can be circumvented to some extent, by imaging a vertical section of the specimen, as described later in chapter 9.

The further limitation, one that is fundamental to microscopy, is resolution. Ultimately, the resolution is limited by the width of the electron beam, which is of order 10nm. However considerations of radiation damage through beam-specimen interactions limit the magnification, since beam damage scales with the square of the magnification. This is because the area scanned is a square whose side is inversely proportional to the magnification, so a doubling in magnification causes a fourfold increase in PE density on the scanned region of the sample [70]. Beam damage is covered in chapter 5. Resolution also depends upon contrast within the specimen, the difference in electron emission between strongly and weakly emitting regions. For samples with low silica concentration (figure 3.1 *(a)* in chapter 3), we expect rather low contrast as the silica may be largely contained within the polymer matrix.

We now consider the signal-to-noise ratio. To obtain useful images, the noise contribution must be limited. Noise enters the system in a variety of ways, through electronic sources [70], counting statistics [14] and unwanted contributions to the cascade process [76] [78]. The primary beam scattering in the imaging gas reduces the signal strength, so although it does not strictly introduce noise, it nonetheless reduces the signal to noise ratio.

We have little control over electronic sources, and neglect them. Counting statistics are improved with a higher beam current, which may be achieved with a higher beam energy [70].

The probe beam skirt provides a significant and easily reducible background contribu-

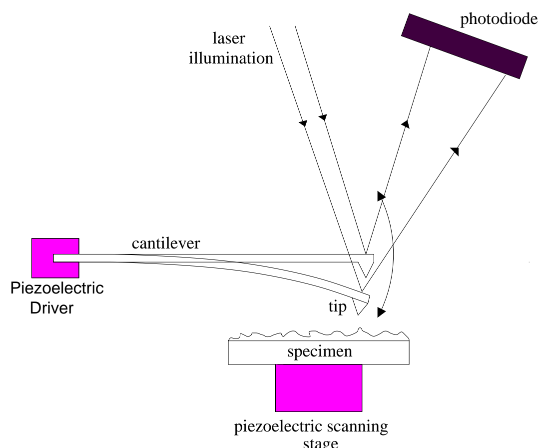

Figure 4.7: Schematic of an AFM in tapping mode. The piezoelectric driver oscillates the cantilever near resonance. Its amplitude is detected by the photodiode. The stage is adjusted to maintain a constant amplitude of oscillation during scanning.

tion to the signal which acts to reduce contrast. It is dependent upon chamber pressure [71], with higher pressures increasing the electron density in the skirt. The chamber pressure is also important in the gas cascade process, with higher pressures tending to promote the SE cascade, up to 4-5 torr, at which point the cascade operates most efficiently [78]. The effect of working distance (the length from the lowest PLA to the sample) is similar, although not equivalent to that of chamber pressure. A longer working distance promotes the gas cascade, but it also increases scattering in the primary beam. Higher beam energies also reduce the skirt, due to smaller scattering cross-sections at higher electron energy [80].

Effective use of the ESEM therefore requires control of the chamber pressure, working distance and beam energy to optimise the signal to noise ratio, while minimising sample damage. We shall return to these parameters in chapter 7 after we have considered beam damage in more detail.

4.2

Atomic Force Microscopy

The development of atomic force microscopy (AFM) from scanning tunnelling microscopy in the 1980s has enabled near-perfect mapping of surfaces at nanometre resolution [81] [82]. The idea behind AFM is to scan a very small tip across a surface, maintaining a constant force between tip and surface, and typically a constant distance between the two. By recording variations made to the height of the tip with respect to the stage, a surface map is produced. Although this is conceptually straightforward, the minute lengthscales involved require extreme precision in the relative positioning of the tip and surface, which we discuss below. A schematic of an AFM in tapping mode (see below) is shown in figure 4.7 [81] [83].

Surface Forces in AFM

We now describe AFM, developing the concepts behind the two imaging modes used here: topographic, producing the surface map [81], and phase contrast, which is sensitive to viscoelastic properties of the surface [84]. First, we consider the surface forces, which give rise to the tip-sample interaction.

The force experienced by the tip approaching the sample typically arises from a Lennard-Jones potential [15]. However the tip is held at the end of a flexible cantilever, which deflects under the tip-sample force. So moving the cantilever with respect to the surface causes it to bend, as the tip seeks out the potential energy minimum between the Lennard-Jones energy well and the well from the restoring force (figure 4.8) [15].

At large separations ($> 3\text{Å}$), the cantilever restoring force dominates, but closer to the surface, the tip moves to the Lennard-Jones minimum. Upon withdrawing the cantilever, there is considerable hysteresis, from at least two sources. Firstly, the Lennard-Jones well holds the tip until the deflection in the cantilever is sufficient to overcome the potential energy barrier to return to the restoring force minimum [15]. Secondly, in ambient conditions at non-zero relative humidity, the capillary forces associated with the adsorbed

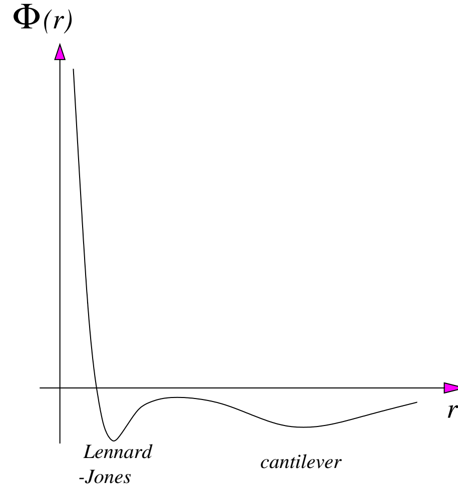

Figure 4.8: The potential felt by the tip is the superposition of the Lennard-Jones potential and the potential from the cantilever restoring force, so the potential $\phi(r)$ has two minima.

water layer increase the hysteresis further [83].

When the tip is in the Lennard-Jones potential well, the AFM is said to be in contact mode. Scanning in this mode, maintaining a constant deflection on the cantilever works well for hard materials, such as metals. More fragile polymers tend to be etched by the tip, so here we use tapping mode [82].

Tapping Mode

Tip-sample interactions are much reduced in tapping mode, so etching is no longer a problem [56]. Here the cantilever is oscillated near its resonance frequency such that it is only momentarily in contact with the sample (figure 4.7). Instead of the deflection of the cantilever, we measure the amplitude of oscillation.

The oscillations are at quite well described by the damped simple harmonic oscillator (SHO) approximation [84] [85],

$$m\frac{\partial^2 z}{\partial t^2} + \gamma\frac{\partial z}{\partial t} + k(z-u) = F(z), \tag{4.1}$$

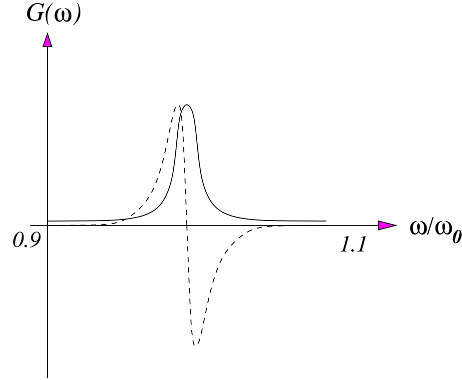

Figure 4.9: The amplitude $G(\omega)$ (solid line) and amplitude derivative $\frac{\partial G}{\partial \omega}$ (dotted line) plotted as a function of frequency in the vicinity of the resonance for the damped SHO.

with m the effective cantilever mass, z the tip height at time t, γ the dissipation, k the cantilever spring constant, u the driving displacement and $F(z)$ the tip-sample force.

In the simplest case, we assume that the tip-sample force is uniform [15]. It is straightforward to show that if u is harmonic, then z is also harmonic, with the same frequency ω and a phase shift of θ [15]. The normalised amplitude is then

$$G(\omega) = \frac{Q}{\sqrt{Q^2\left(1 - \frac{\omega^2}{\omega_0^2}\right)^2 + \frac{\omega^2}{\omega_0^2}}} \tag{4.2}$$

where the resonance frequency ω_0 and quality factor Q are defined as

$$\omega_0 = \sqrt{\frac{k}{m}} \tag{4.3}$$

and

$$Q = \frac{m\omega_0}{\gamma} \tag{4.4}$$

The amplitude $G(\omega)$ and amplitude derivative $\frac{\partial G}{\partial \omega}$ are plotted as a function of frequency in figure 4.9. As can be seen from the figure, the amplitude derivative peaks a little before the amplitude ($\omega \approx 0.93\omega_0$) [15]. At this frequency, we expect the maximum amplitude response to the tip-sample interaction. So we drive the cantilever a little below resonance, typically around 300 khz.

When the tip feels the force from the sample, the cantilever oscillation is moved off resonance and the amplitude falls. So if we maintain a constant amplitude of oscillation,

then we have a constant tip-sample interaction, although the tip only feels the effect of the surface at the downward extremity of its oscillation. Using this constant tip-sample interaction, we can obtain a height image in a similar way to contact mode. This oscillating cantilever method is termed tapping mode.

Phase Imaging and Instability

From the discussion above, we obtain [15] [86],

$$tan\theta = \frac{\omega\omega_0 m}{Q\left(\frac{k}{m} - \omega^2\right)} \tag{4.5}$$

At resonance, $\theta = \frac{\pi}{2}$. If, however the tip-sample interaction moves the cantilever away from resonance, then we may rewrite equation 4.5 to give the change in θ, $\delta\theta$ [86],

$$\delta\theta = \frac{\pi}{2} - tan^{-1}\left(\frac{k}{Q\sigma}\right) \approx \frac{Q\sigma}{k} \tag{4.6}$$

where the surface-tip interaction is treated to a first approximation by changing k to a new effective value $k^{eff} = k + \sigma(r)$ where $\sigma(r)$ is a measure of the local viscoelastic properties of the sample. This linear behaviour will hold for small perturbations only, but we see that equation 4.6 gives rise to phase contrast imaging [86]. Since σ is sensitive to the material properties of the sample, if we record a phase image, where θ is a function of lateral displacement, we obtain a measure of $\sigma(r)$. However, interpretation of phase contrast images is far from trivial.

The solution to the equation of motion of the oscillating cantilever is in practice rather more complex than we have described here. Bar *et al.* [84] have shown that, for a given set of parameters (sample viscoelasticity, amplitude of oscillation, driving frequency, etc), there may be multiple stable states of oscillation with differing phase angles. Furthermore, the oscillations can flip from one state to another, as a result of noise in the system, or surface irregularities. So two identical scans can produce widely differing phase images

[84].

Even during tapping-mode, a sharp tip becomes 'dull', as it is worn down by interaction with the sample surface. Changing the tip shape drastically affects the sample-tip interaction for polymeric materials [85] [87]. A sharp tip interacts weakly with soft polymers above their T_g, but more strongly with harder, lower T_g polymers. Conversely, a 'dull' tip interacts more strongly with softer polymers [85]. So the phase contrast depends on the sharpness of the particular tip used. Bearing these considerations in mind, at the level of this work, we interpret phase contrast images in a purely qualitative way.

AFM control

So far we have considered the theory of AFM image formation. Here we describe how the accuracy required is achieved in practice. To begin scanning, the oscillating cantilever is lowered towards the sample. As the tip-sample interactions increase, the amplitude reduces to some pre-determined value, and scanning is initiated. This amplitude set-point is a fraction of the undamped amplitude. A smaller fraction corresponds to a larger perturbation and hence greater interaction with the sample. The amplitude of oscillation is detected by the movement of a laser beam reflected off the end of the cantilever. The reflected laser beam is detected by a photodiode, as shown in figure 4.7 [88]. During scanning, a feedback loop is used to keep the location of the laser beam on the photodiode constant. The specimen height variations required to achieve this are recorded as a function of xy position [81].

The tiny displacements require the use of piezoelectric scanners, whose linear, reversible range is limited [83]. The Digital Instruments Multimode AFM used (at Sheffield) has a maximum lateral range of 100μm, which is quite sufficient for our purposes [56]. However the maximum vertical displacement is 5μm, which can be a problem with larger silica particles, of size $\sim 10\mu$m. Furthermore, the lateral scanning of the stage is not absolutely planar, as illustrated in figure 4.10 [83]. The stage is typically mounted on a piezoelectric tube, segmented into vertical quarters, $\pm x$, $\pm y$. The stage attached to the top of this tube describes an arc, as shown in figure 4.10, rather than a plane as would be desirable. This is referred to as cross-coupling [83]. It can be circumvented to some extent by image

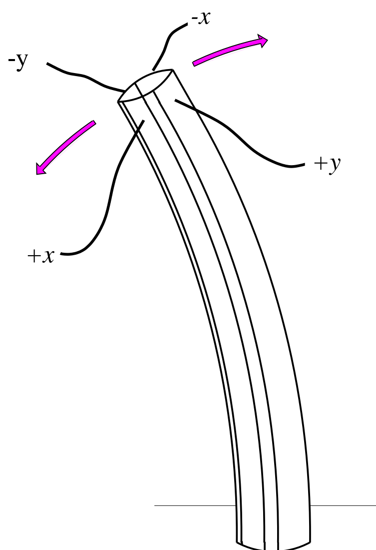

Figure 4.10: The piezoelectric tube supporting the stage means that xy scanning describes an arc, rather than absolute lateral displacement.

processing [56], as mentioned in chapter 6.

The cantilevers used here are etched from a single crystal of silicon, and have a spring constant k of 20-100 Nm^{-1}, and nominal radius 5-10nm [56].

AFM operation

We have seen that AFM, like ESEM, is subject to a number of experimental parameters. In addition to the amplitude set-point, the gain in the feedback loop controls the response of the stage height control to surface roughness. A sufficient gain is required to ensure that the tip remains in contact with the surface during scanning, but must be small enough to prevent damage to the surface, or electrical noise dominating the signal. This is easier at a slow scan speed, typically one or two lines of a 256×256 pixel image per second. Furthermore, although phase contrast images tell us about the material properties of the sample, their interpretation should be treated with caution. Essentially we look for contrast variation in phase imaging, which we associate with the different viscoelastic properties of the silica and polymer.

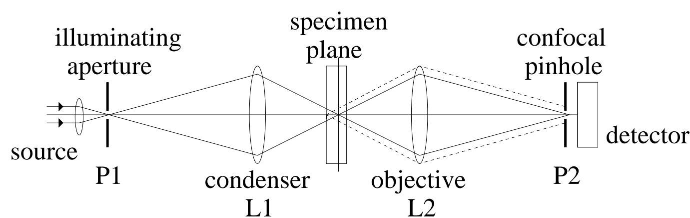

Figure 4.11: The principle of Confocal Microscopy, in transmission mode. Light is focussed into a point in the sample plane by the condenser lens. The confocal pinhole rejects all light except that from the point in focus (dotted lines show out-of-focus rejection) [64].

4.3

Confocal Microscopy

Despite being proposed as long ago as 1957 [89], the potential of confocal microscopy was not realised until the 1980s. In the meantime, laser light sources were developed to compensate for the low illumination inherent in the technique, along with image-processing software and the computer power required to run it. Confocal microscopy has two key advantages over conventional optical microscopy: improvement in resolution and rejection of out-of-focus blur, enabling 3D imaging of thick specimens [64] [90]. We can use confocal microscopy to complement ESEM and AFM surface analysis by imaging the bulk of the film. In this section, we give an overview of confocal microscopy and how it is distinguished from conventional optical microscopy, before proceeding to discuss the technique in more detail.

Image formation in the confocal microscope is unique because it uses both a point detector and source. Figure 4.11 shows such an instrument, in which light is transmitted through the sample. The figure shows that only a single point of light from the focal plane reaches the detector: the confocal pinhole discriminates against light from all other points of the focal plane, and from all out-focus planes [64].

The condition of a single point in focus requires that the specimen (or more usually, the probe beam and pinhole) are scanned to produce an image. The fact that only a single point contributes to the image at any one time means the overall intensity is very low.

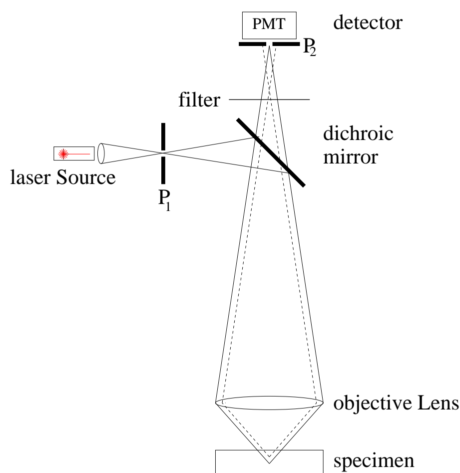

Figure 4.12: epi-*illumination in confocal mode. The objective and condenser lenses are the same, and the dichroic mirror allows the illuminating beam to pass through, while reflecting the returning beam to the detector. Again, the dotted lines show the rejection of out-of-focus light. [14].*

The intensity of each point (and hence the rate of scanning) can be increased enormously with the use of a laser light source. This is the confocal laser scanning microscope (CLSM) [14] [64] [1]. We see from figure 4.11 that if the confocal pinhole is removed, then all light transmitted by the sample is collected by the detector. If the source is then made uniform such that the entire field of view is illuminated, we have a conventional wide field (WF) microscope without the ability to reject out-of-focus light.

Returning to the CLSM, if the specimen is scanned in the z, as well as the x and y directions, a three-dimensional image may be constructed. This is not possible in a WF microscope because of out-of-focus contributions to the image. In WF microscopy, three dimensional images can only be indirectly produced from a number of thinly sliced specimens.

In practice the transmission mode of figure 4.11 is seldom used. *Epi*-illumination is used instead as shown in figure 4.12. Although this does not in principle effect the confocal optics, alignment of the various components is far easier, as L_1 and L_2 are replaced by a single lens. Here we use the CLSM in *epi-fluorescence* mode. Regions of interest in the specimen are labelled with a fluorescent dye, or *fluorophore*. These molecules are excited

[1] The CLSM referred to in this work is the Zeiss LSM 510

by a light source of appropriate wavelength, and then decay, releasing a photon of longer wavelength [14]. We use a filter to reject light that is simply reflected (figure 4.12), whereas fluorescent light is passed through to the detector. So the image produced is a map of the fluorescent dye in the specimen.

Removing the filter allows reflected light to reach the detector, which we can use as the signal. When operating in this *reflection mode*, the contrast comes from refractive index mismatch in the film. We consider reflection mode in chapter 9. We now proceed to discuss in more detail the key aspects of CLSM in the context of this work: image formation, aberrations, digitisation and photobleaching.

Image formation and Resolution

In all the microscopes used here, the image formed is the convolution of some *probe* with the specimen. In AFM, the probe is the cantilever tip [91], and in ESEM it is the primary electron beam [70]. The dimensions of these are well below the lengthscales we are interested in, so we may simply treat the probe as a δ-function, and neglect the convolution. Not so with confocal microscopy, as the size of the light probe is limited by diffraction [14] [92] [93]. Fortunately, since diffraction is well described, we can find the shape of the probe [93].

This shape is the point spread function (PSF) $h(x_0)$ [92]. We can then write the image as the convolution of the PSF and the specimen function $s(x_0)$ [94] [95],

$$i(x_i) = h(x_0) \oplus s(x_0) = \int_0 h(x_i - x_0) s(x_0) dx_0, \tag{4.7}$$

where $i(x_i)$ is the image function and $\oplus$ represents the convolution operation. x_0 is the object space, x_i is the image space. If we use a bright, sub-resolution object as a point source, then we can regard $s(x_0)$ as a δ-function [96]. An image of this point object is then simply the PSF.

So any image formed is the superposition of a large number of PSF, one for each point in the specimen. The resolution is then the smallest distance at which two point sources can

be distinguished. An idea of the lateral behaviour of the PSF can be obtained analytically [92] [93] [97]. From the work of Sheppard and Choudry [93], the lateral resolution in the CLSM is around 0.14μm and from Wilson in [14], the axial resolution is around 0.7μm.

Since $i(x_i)$ is the image which we measure, we can 'deconvolve' it with $h(x_0)$ to obtain the original specimen function $s(x_0)$. Although this operation is not mathematically defined, a variety of computational methods have been developed [95]. We explore the recovery of the specimen function $s(x_0)$ in more detail in chapter 6. One limitation of image reconstruction is that it requires a high-quality image to start with. Silicas which generate films of low clarity do not tend to result in high-quality images, as the intensity falls off with depth due to attenuation and spherical aberration.

Lens Aberrations

So far we have restricted ourselves to the diffraction-limited case. Real lenses exhibit deviation from this behaviour in the form of various aberrations. We classify these into two types, wavelength-dependent chromatic aberrations, and monochromatic aberrations which affect all light similarly. The most important form of aberration in confocal microscopy is spherical aberration, which occurs if we have refractive index mismatch between the sample and the lens. In the Zeiss planapochromat lens used, the effect of other aberrations, such as coma, astigmatism and chromatic aberration is rather small. The reader is referred to Pawley [14] for a more detailed discussion. We consider only the objective lens, as it is by far the most significant part of the optics of a CLSM in *epi*-illumination as far as aberration is concerned [14].

Spherical aberration is caused by non-spherical wavefronts produced by the objective lens. If the specimen refractive index differs from that for which the lens was designed, then we will find spherical aberration (figure 4.13). Oil-immersion lenses are designed for a refractive index of 1.518 (η_1 in the figure). The refractive index of water is 1.33, so a considerable shift in focal point occurs with aqueous specimens. This is exacerbated in confocal imaging of thick specimens, because the path length through the region η_2 in figure 4.13 is increased compared to conventional WF microscopy [14] [98]. The actual focal point z_a and the nominal focal point z_n are approximately related by

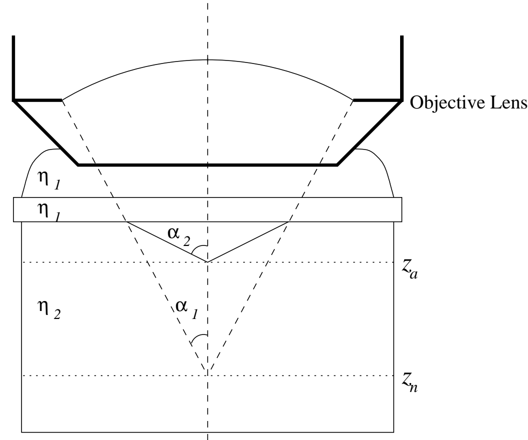

Figure 4.13: The shift in focus position caused by refractive index mis-match. The nominal focus position would be obtained in the case $\eta_1 = \eta_2$, but refraction at the interface moves this to the actual focus position.

$$z_n = \frac{tan\alpha_1}{tan\alpha_2} z_a = \frac{tan\left\{sin^{-1}\left(\frac{NA}{\eta_1}\right)\right\}}{tan\left\{sin^{-1}\left(\frac{NA}{\eta_2}\right)\right\}} z_a \tag{4.8}$$

where $\alpha_{1,2}$ are defined in figure and NA is the numerical aperture of the lens 4.13 [98].

This change in focus position is accompanied by a reduction in intensity, and a 'smearing out' of the axial intensity function. Hell *et al.* [98] showed that axial resolution in particular is much reduced, to $\sim 2\mu$m by imaging through 20 μm of water. However glycerol (η=1.47) shows relatively little loss of resolution, because at 1.47, the refractive index is far closer to that of the lens (1.518). There is some loss of lateral resolution, but it is rather less significant than the axial case. So the PSF is a function of imaging depth.

Here we expect the imaging of matt lacquers to tend more to the glycerol case, because refractive index matching of the lacquer with the silica produces a specimen with a refractive index similar to that of glycerol. Moreover, the appearance of the disordered silica structure is not expected to be hugely affected by the translation of the bottom of the image by a maximum of 1μm [98]. Any measurements of volume fraction (equation 3.10) will be unchanged, as the entire image is simply translated. Likewise percolation phenomena should also be unchanged. Of course, spherical aberration induced in this way

is a fundamental aspect of any experiment, as the refractive index of the system observed cannot in general be changed [14]. Therefore we do not treat spherical aberration and note that in any case, all the images are affected in the same way.

Digital Image Acquisition

All microscopes used here digitise images as the end product of the scanning process, so this discussion is relevant to AFM and ESEM as well. However, we consider CLSM because we operate at the limit of resolution, so the prospect of oversampling is significant.

These digital images are comprised of pixels, representing each point sampled. The digitisation process involves the loss of information, both in terms of the spatial dimensions of each pixel (which should in principle be a point), and in the intensity recorded. Intensity is recorded as an integer from 0 to 255, so turning a continuously varying analogue signal into one of 256 *grey levels* results in a loss of information [14]. We minimise this by ensuring that we use exactly the whole range from 0-255.

Since the resolution is limited, it is clear that having many pixels within a space smaller than the resolution will simply lead to many pixels with the same value. This is referred to as *over sampling*, and only results in more computer memory required to store the same information. So what is the ideal rate of sampling?

The Nyquist criterion states that for non-periodic data, the sampling frequency should be 2.3 times higher than the highest frequency in the data, to avoid any loss of information [14]. Here we require that the pixel size should be 2.3 times smaller than the resolution. In the case of 3D image acquisition, the discrepancy between lateral and axial resolution requires a different sampling rate in the lateral and vertical directions. The optimum lateral sampling rate is given by the Nyquist criterion and lateral resolution as $0.06\mu m\text{pixel}^{-1}$, and the axial sampling rate is $0.28\mu m\text{pixel}^{-1}$.

Noise

The low light levels inherent in confocal microscopy can result in noisy images. That is to say, the values assigned to pixels may be inaccurate because a rather small number of

photons have been counted to determine the grey level of the pixel. Photon counting is governed by Poisson statistics. If there are n photons per measurement, then the chance that the measurement lies within the range $(n - \sqrt{n})$ to $(n + \sqrt{n})$ is 63%. So if $n = 100$, there is a 63% chance that the error is less than 10%. However to improve the accuracy by a factor of ten, a hundred times as many measurements must be taken. Noise introduced by the fundamental process of photon counting is referred to as *intrinsic noise* [14].

Noise is also produced from the detector dark-current, electronic sources and stray out-of-focus light. This noise is referred to as *extrinsic* noise, and may be reduced by good instrument design and experimental procedure [14]. The detector used is a photomultiplier tube, which has a negligible dark-current. However, it has a fairly low quantum efficiency of around 13%. This means that noise from the Poisson statistics of data collection is increased compared to a detector with a higher quantum efficiency, such as a CCD [64]. So we would like to use a high laser power or long scan time, to maximise the counting statistics. Unfortunately, we are limited by photobleaching (see below).

The signal to noise ratio is also influenced by the width of the confocal pinhole. Practical CLSMs can only be partially confocal, since a true pinhole would let almost no light through. We can increase the signal by increasing the pinhole diameter up to one Airy unit, which maximises the useful signal reaching the detector, accepting the loss of some resolution [64].

Fluorescence Limitations

Fluorescence mode operation is limited by two factors:

(1) Photobleaching, which limits the total number of photons which can be counted to around 10^5 per molecule.

(2) Excited state saturation, the maximum rate of photon collection.

At the dye concentrations used here, we find experimentally photobleaching is the limiting factor.

Photobleaching is the irreversible loss of fluorescent activity which occurs from the reaction of excited-state fluorophore molecules to a non-fluorescent product [14]. Typically

this involves a route of decay to a non-fluorescent variant of the original ground state. Since the excited-state molecules can react with one another, a lower concentration of fluorophore may reduce photobleaching.

Bleaching is considerably worsened in CLSM, compared to WF fluorescence microscopy. This is because collecting a series of xy images to produce a 3D image requires that the probe beam be scanned laterally across the sample N_z times where N_z is the number of pixels in the z-direction. For WF fluorescence microscopy, the probe beam need only be passed across the sample once, so the effects of photobleaching are improved by a factor of N_z. Photobleaching depends on the rate of fluorophore excitation, and so may be reduced with a smaller laser power, although this will result in a reduced signal-to-noise ratio. We can also reduce photobleaching with a larger pixel size, retaining good counting statistics. So like AFM and ESEM, there are a number of parameters which we must optimise: laser power, scan time, pixel size and pinhole diameter. These we return to in chapter 8, and are listed in the appendix, page 218.

Chapter 5

Beam damage in ESEM

Electron microscopy of 'soft' materials is limited by structural and compositional damage from the electron beam. The information extracted from the specimen is thus limited by the maximum electron dose which can be tolerated. This radiation damage can severely restrict the size of structure which we can image since the dose increases with the square of the magnification. Different materials show widely varying susceptibility to the electron beam. Metals show little damage, but saturated polymers such as our poly-butyl methacrylate (PBMA) latex are very sensitive indeed [73]. In this chapter we investigate radiation damage in ESEM, both experimentally and using computer simulation.

The presence of liquid water is known to increase radiation damage in ESEM [99] [100], compared the conventional high-vacuum SEM. Radiation damage to hydrated specimens can be minimised by adjusting the operating parameters, especially beam energy, for each type of sample. This has been done for polypropylene by Kitching [100]. Like Kitching we investigate the effect of beam energy on our PBMA latex in the hydrated state.

At a more fundamental level, the electron beam-specimen system can be modelled numerically, to gain an improved understanding of beam damage, which is also followed here. This can enable us to devise experiments which are less susceptible to beam damage.

5.1

Background

The passage of the high-energy primary electrons (PE) from the beam imparts energy to the specimen through ionisation, excitation and displacement. The excited or ionised molecules may then undergo further ionisation or bond scission in the case of polymeric or biological specimens. Chain scission in polymers alters the molecular weight, and the smaller molecules produced may evaporate reducing the mass of the specimen. The free radicals produced by ionisation and bond scission can then attack the specimen [73].

Radiation damage involving water has been studied for conventional SEM. Biological specimens are frozen, and imaged at liquid nitrogen temperatures in *Cryo*-SEM. Under irradiation, ice acts as a source of small, highly mobile free radicals which provide more mechanisms for radiation damage [73]. Water in ESEM should behave in a similar way, only here the mobility of reactive species is substantially increased in the liquid medium. As a simplest case for a hydrated specimen, we consider pure water.

Electron-water interactions have been extensively studied through simulations [80] [101] [102] [103] and experimental work [104] [105]. This has enabled the free radical and ionic products to be quantified in the case of a single PE. The results of the simulations can be applied to ESEM conditions, where instead of a single incident electron, there is an electron *beam*. The number of reactive species is too large for individual particles to be considered, so instead an averaging approach is used to find their *concentration*. This is expected to determine the dominant damage-causing species produced in water, and also their mobility.

First we present our experimental results, before reviewing electron-water interactions, at the single-particle level. The application of these to ESEM conditions, with a many-electron beam is discussed, with particular attention paid to approximations made. Next, the model used here is constructed, and the main results are presented. It is worth pointing out at this stage that the object here is not to provide a highly accurate description of the system on the atomic level, but rather to determine main damage mechanisms and

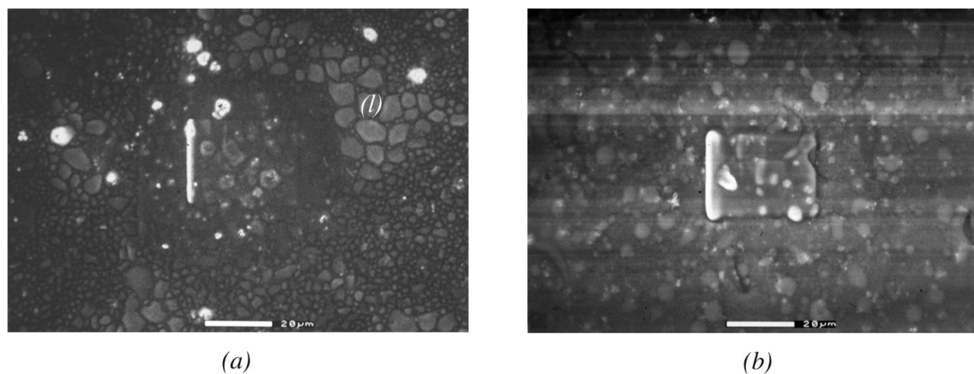

Figure 5.1: Beam-damaged hydrated films. The increase in beam damage from 8 keV (a) *to 12 keV* (b) *is clear. Bar=20 μm.*

identify how these may be minimised. We consider ESEM conditions to be a 5nA beam [77], and compare the effects of beam energies of 5 and 25 keV, representing typical limits of ESEM operation.

5.2

Experimental

We used an electroscan E-3 ESEM fitted with a LaB_6 filament to image matt water-based lacquer. This is a PBMA latex with silica inclusions, the components are listed in the appendix, page 216. The lacquer is held at 7°C and 7.5 torr chamber pressure to lie on the saturated vapour pressure line and remain hydrated, as discussed in chapter 4, page 43. The working distance was set to around 7mm.

To beam damage the lacquer, we scan at 4000× original magnification for five minutes, before imaging a larger region to compare damaged and non-damaged regions. Two such images are shown in figures 5.1*(a)* and *(b)* for beam energies of 8keV and 12keV respectively. In both images we see that the central region can be distinguished from the remainder, which we interpret as beam damage.

As expected from our considerations of backscattered and secondary electron (BSE and SE respectively) in chapter 4, section 4.1, the brighter features are taken to be silica

PE energy (keV)	Mean Free Path λ_{PE} (nm)	Mean range $\langle R \rangle$ (μm)	Normalisation constant 2A (dm^{-3})	$\frac{\partial}{\partial t}_{beam}\phi_\alpha(0,t)$ (Moldm^{-3}s^{-1})
5	15*	0.461**	1.29×10^{15} **	67.15
25	55*	7.0**	3.70×10^{11} **	0.0191

*Table 5.1: Parameters used for 5keV and 25 keV primary electrons. * from Hill and Smith [80], ** from La Verne and Mozumder [106].*

particles, with the exception of the line to the left of the central damaged region. This is increased damage because the beam lingers on the left during its raster scan.

There is some evidence of liquid on the surface, particularly in figure 5.1*(a)*, marked as *(l)*. This may be oil from the ESEM column, or condensed water. In either case, it is absent from the damaged region, so is not thought to contribute to the beam damage.

From the size of the white line and the difference between the central region and the undamaged remainder, it is clear that a 12keV beam energy damages the sample rather more than 8keV, for operating conditions which are otherwise the same. We now move on to a more theoretical perspective of beam damage.

5.3

Electron-Water Interactions

The passage of high-energy electrons through water has been studied through simulations involving one PE. This electron undergoes a number of inelastic scattering events by which it imparts energy to the water medium, and is eventually absorbed, after it has lost sufficient energy [80].

The inelastic scattering events result in ionisation or excitation of the water molecules,

$$e^- + H_2O \longrightarrow H_2O^+ + 2e^- \tag{5.1}$$

$$e^- + H_2O \longrightarrow H_2O^* + e^- \quad (5.2)$$

These excited state water molecules may then decay into free radicals or ions, for example,

$$H_2O^* \longrightarrow H\cdot + \cdot OH \quad (5.3)$$

$$H_2O^* \longrightarrow H^+_{aq} + OH^-_{aq} \quad (5.4)$$

where the dots represent unpaired electrons [73]. Each inelastic scattering event typically produces six reactive species in a space of a few nanometres [80]. These regions containing reactive species are termed *spurs*. For electrons with energy of order 5-25 keV, the average distance between these spurs (the mean free path) is large compared to their size as shown in table 5.1 [106].

The reactive species then either recombine in annihilation reactions (table 5.2) or diffuse away from the spur, where they are relatively unlikely to annihilate. Of course, reaction with water is possible (table 5.2), but this simply produces more reactive species. So to reduce the overall concentration reactive species must annihilate with one another. Decay within the spur tales place on a timescale of 10^{-10} to 10^{-9}s [80]. Those species that have not recombined at this time are termed the primary yield (table 5.3) [103]. The whole process is termed radiolysis.

	Reaction			Rate Constant $\times 10^{10} M^{-1}s^{-1}$
1	$\cdot OH + \cdot OH$	$\longrightarrow$	H_2O_2	0.45
2	$e^-_{aq} + e^-_{aq}$	$\longrightarrow$	$H_2 + 2OH^-_{aq}$	0.5
3	$H \cdot + H\cdot$	$\longrightarrow$	H_2	2.0
4	$OH + e^-_{aq}$	$\longrightarrow$	OH^-_{aq}	3.0
5	$H \cdot + OH\cdot$	$\longrightarrow$	H_2O	2.0
6	$H^+_{aq} + OH^-_{aq}$	$\longrightarrow$	H_2O	14.3
7	$H \cdot + H_2O_2$	$\longrightarrow$	$H_2O \cdot + \cdot OH$	0.016
8	$e^-_{aq} + H^+_{aq}$	$\longrightarrow$	$H\cdot$	2.3
9	$e^-_{aq} + H\cdot$	$\longrightarrow$	$H_2 + OH^-_{aq}$	2.5
10	$e^-_{aq} + H_2O_2$	$\longrightarrow$	$OH^-_{aq} + OH\cdot$	1.2
11	$e^-_{aq} + O_2$	$\longrightarrow$	$O_2^- \cdot$	1.9
12	$e^-_{aq} + O_2^- \cdot$	$\longrightarrow$	$OH^-_{aq} + HO_2^-$	1.3
13	$e^-_{aq} + HO_2\cdot$	$\longrightarrow$	HO_2^-	2.0
14	$H \cdot + O_2$	$\longrightarrow$	$HO_2\cdot$	1.9
15	$H \cdot + O_2^- \cdot$	$\longrightarrow$	HO_2^-	2.0
16	$H \cdot + HO_2$	$\longrightarrow$	H_2O_2	2.0
17	$H^+_{aq} + O_2^-$	$\longrightarrow$	HO_2^-	5.0
18	$OH \cdot + O_2^-$	$\longrightarrow$	$OH^-_{aq} + O_2$	1.2
19	$OH \cdot + HO_2$	$\longrightarrow$	$O_2 + H_2O$	1.2
20	$OH \cdot + OH^-$	$\longrightarrow$	$H_2O + O^- \cdot$	1.3
21	$H + OH^-$	$\longrightarrow$	$H_2O + e^-_{aq}$	0.0021
22	$OH \cdot + HO_2\cdot$	$\longrightarrow$	$O_2 + HO_2$	0.0033
23	$OH \cdot + O^- \cdot$	$\longrightarrow$	HO_2^-	1.8
24	$OH \cdot + HO_2^-$	$\longrightarrow$	$O_2^- \cdot$	0.75
25	$e^-_{aq} + HO_2^-$	$\longrightarrow$	$2OH^-_{aq} + H_2$	0.35
26	$e^-_{aq} + O^- \cdot$	$\longrightarrow$	$2OH^-_{aq}$	2.2
27	$H \cdot + O^- \cdot$	$\longrightarrow$	OH^-_{aq}	2.0
28	$H^+_{aq} + O^- \cdot$	$\longrightarrow$	$\cdot OH$	5.0
29	$H^+_{aq} + HO_2^-$	$\longrightarrow$	H_2O_2	5.0

Table 5.2: Reactions and rate constants [80]. The final products are water, hydrogen peroxide and hydrogen gas.

G_{eaq}	G_H	G_{OH}	G_{H+}	G_{OH^-}	G_{H2O2}	G_{HO_2}
2.0	0.8	1.6	2.6	0.6	1.4	0.11*

*Table 5.3: G-values for the primary yield. The G-value is the number of species produced per 100 eV of energy absorbed. Those used were obtained by Terrissol and Beaudre [103], for a PE energy of 10 keV. * denotes values obtained for PE energy = 1 Mev by Hill and Smith [80].*

5.4

From one electron to a beam

The essential task here is to apply the results for a single PE to a beam. Treating each PE and all its products individually is not practical, so some averaging approach is desirable.

Here we discuss the differences between the single PE and beam, and how they may be treated. We want to obtain a concentration for each species. As will be seen later, this is fairly straightforward to determine from the primary yields. Furthermore, we will seek to model the creation of reactive species as a smooth analytic function, giving concentrations as formed by radiolysis. This section will argue that each species may be treated by an average concentration, and that the spatial distribution in which they are formed is approximately Gaussian.

A continuous concentration

In the case of a single PE, following spur decay, the residual reactive species are isolated, as they have diffused away from the spurs into the bulk water. In this case, we expect the concentrations to become uniform eventually, and that the primary yields are a good starting point for further evolution.

Now these spurs are of finite size, and finite separation. So if enough PE are incident on the sample, we expect the spurs to overlap. That is, two or more elastic scattering events occur sufficiently close together that reactive species from different events can annihilate with each other. In this case, we expect a more complete annihilation than in the single PE case, as those species diffusing beyond the spur in which they were formed simply find another spur where there are other species with which to react. This contrasts with the reactive species produced by the single PE diffusing around the bulk, unlikely to find other species to annihilate with. In order for the primary yields to be valid, we need to show that spur overlap is not present, or at least not significant.

The highest beam current in ESEM is typically 5nA [77]. The timescale of spur decay is 10^{-10} to 10^{-9}s, and in this time 3-30 PE arrive. In order to crudely determine spur

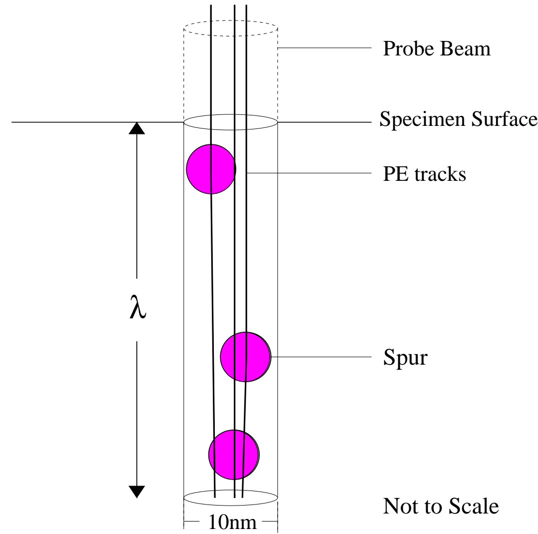

Figure 5.2: At the point of contact between the beam and the sample, the angular scattering of primary electrons is sufficiently small to be neglected, so the interaction volume may be modelled as a cylinder (not to scale). A calculation of spur overlap may be made by assuming each that incident electron (bold line) produces one spur (grey circle) within its mean free path.

overlap, we calculate the volume occupied by the spurs as a fraction of the total volume in the most irradiated region of the sample.

Clearly the most irradiated region is that directly below the electron beam. Since forward scattering dominates at the energies considered [80], we can model this region as a cylinder, whose diameter is equal to that of the electron beam, which is of order 10nm [70], as shown in figure 5.2. The height of the cylinder is the length in which we expect one scattering event, the mean free path. Within the volume of this cylinder, each PE should produce on average one spur. The mean free path λ_{PE} is determined from

$$\lambda_{PE} = \frac{1}{\sigma n_T} \tag{5.5}$$

where σ is the scattering cross-section (taken from Hill and Smith [80]) and n_T is the number of scattering targets. Each spur is assumed to be a sphere of radius 3nm, whose centre is located within the cylinder. This is consistent with the literature, which typically assumes a few nanometres [80] [106]. The volume of the cylinder shown in figure 5.2 is

equal to about 27 spur volumes, in the 5 keV case, and 98 for 25 keV PE, which suggests some spur overlap, although it is not expected to be dominant. At greater depths, angular scattering removes PE from the axial direction, so a treatment assuming no spur overlap is expected to be reasonable to first order. From this discussion we see that using primary yields (table 5.3) is appropriate for the level of this work.

The Gaussian interaction volume

The interaction volume is the region of the sample penetrated by the PE [70]. As mentioned above, PE scatter away from the initial trajectory, and a teardrop-shaped region is formed [70] [106]. So further into the sample the motion becomes more isotropic and tends towards a random walk. In fact the variation in mean PE range between the axial and other directions is only a factor of 0.03 [106]. For a Gaussian distribution, we expect no preferred direction. Since the axial direction is only slightly favoured, a treatment based on a spherical Gaussian distribution is indeed appropriate for the level of this work. The Gaussian interaction volume is centred on the point of contact between the sample and primary beam.

Of course the hemisphere lying above the sample surface is not part of the interaction volume, so we only treat the hemisphere below the surface, and normalise accordingly by a factor of two. The standard deviation of this Gaussian is then the mean PE range, $\langle R \rangle$, as determined by Laverne and Mozumder [106] (table 5.1). This introduction of spherical symmetry allows a vastly simpler one-dimensional approach to be followed.

5.5

Mean Concentration Model

Having discussed our assumptions, we now construct a model to describe the system, based on mean concentrations. The concentration profile of each species is produced in a Gaussian distribution, and normalised as shown below. Further radiolysis increases the concentration, which is evolved by the annihilation rate reactions listed in table 5.2.

Concentration-driven diffusion is also employed to investigate the spread of reactive species beyond the interaction volume. As mentioned above, we consider two beam energies, 5 and 25 keV and a current of 5nA.

The concentration of each species α is a function of time t and position $\mathbf{r}$, $\phi_\alpha(\mathbf{r},t)$. Spherical symmetry means $\mathbf{r}$ can be treated as a scalar, so the concentration is written $\phi_\alpha(r,t)$.

In order to determine the change in concentration produced by the primary beam, we take the Gaussian envelope of the interaction volume,

$$A\int_0^\infty\int_0^\pi\int_0^{2\pi}\exp\left(-\frac{r^2}{2\langle R\rangle^2}\right)r^2 dr sin\theta d\theta d\Phi = 1 \tag{5.6}$$

with the normalisation constant

$$A = \frac{1}{[\langle R\rangle(2\pi)^{\frac{1}{2}}]^3}. \tag{5.7}$$

This is doubled to take account of the fact that we only consider the hemisphere beneath the sample surface.

The molar rate of PE absorption is the beam current, divided by the electronic charge and Avogadro's number, normalised at $r=0$ by $2A$.

$$\frac{\partial}{\partial t_{beam}}\phi_\alpha(0,t) = 2A\frac{I_{beam}}{eN_a} \tag{5.8}$$

where I_{beam} is the beam current, e is the electronic charge and N_a is Avogadro's number. This is then multiplied by the Gaussian envelope to obtain the molar rate of PE absorption as a function of r,

$$\frac{\partial}{\partial t_{beam}}\phi_\alpha(r,t) = 2A\frac{I_{beam}}{eN_a}\exp\left(-\frac{r^2}{2\langle R\rangle^2}\right). \tag{5.9}$$

In order to obtain values for other species, we take the primary yields listed in table 5.3. Since these *G-values* give the yield per 100 eV absorbed, we multiply by 50 and 250 for 5 and 25 keV respectively. This then yields the concentration increase with respect to time. There is considerable discrepancy in the literature concerning G-values. Those used here

Species	Diffusion Coefficient $\times 10^{-5} cm^2 s^{-1}$
e^-_{aq}	4.5
H^+_{aq}	9.0
$H\cdot$	7.0
$\cdot OH$	2.8
OH^-_{aq}	5.0
O_2	2.1
$O_2^-\cdot$	2.1
$O^-\cdot$	2.8
H_2O_2	1.4
HO_2^-	1.4
$HO_2\cdot$	2.0

Table 5.4: Diffusion coefficients [80]

were obtained by Terrissol *et al.*, because they were calculated for a PE energy of 10 keV which is within the range used here, except HO_2 from Hill and Smith (table 5.3) [80].

The scheme of Hill and Smith is used to calculate the annihilation reactions, table 5.2. The reactions are all assumed to be first order in each reactant,

$$\frac{\partial}{\partial t_{react}}\phi_\alpha(r,t) = \frac{\partial}{\partial t_{react}}\phi_\beta(r,t) = -k\phi_\alpha(r,t)\phi_\beta(r,t), \tag{5.10}$$

where k is the rate constant (table 5.1). The evolution of the $\phi_\alpha(r,t)$ are advanced according to the reactions listed in table 5.2. A fourth-order Runge-Kutta method is used to find the change in concentration from annihilation reactions at each timestep [107].

Diffusion

The concentrations of the reactive species are not uniform, so they follow the diffusion equation,

$$\frac{\partial}{\partial t_{diff}}\phi_\alpha(r,t) = -D\nabla^2\phi_\alpha(r,t), \tag{5.11}$$

where D is the coefficient of diffusion, table 5.4, [108]. Since the system is spherically symmetric, we only need the $\phi_\alpha(r,t)$ in one dimension. From the central difference formula [109], we can obtain the following expression for $D\nabla^2\phi_\alpha(r,t)$, where the $\phi_\alpha(r,t)$ are defined on an axis passing through the origin of a spherically symmetric system.

$$
\begin{aligned}
\frac{\partial}{\partial t}_{diff}\phi_\alpha(r,t) \approx \\
& -\frac{D}{h^2}\Big(\phi_\alpha((n+1)h,0,0) - 2\phi_\alpha(nh,0,0) + \phi_\alpha((n-1)h,0,0)\Big) \\
& \quad -2\frac{D}{h^2}\Big(\phi_\alpha((n+1)h,0,0) - \phi_\alpha(n(h-1),0,0)\Big)\left(\sqrt{n^2+1}-n\right), \qquad (5.12)
\end{aligned}
$$

for the nth element where h is the spatial step size such that $r = nh$.

The detail of the derivation is given in the appendix to this chapter (section 5.8, page 82). The boundary conditions are chosen such that the origin is treated as a mirror through which there is no net diffusion, and at large values of r the concentration tends to its equilibrium value (see appendix).

The change in concentration is then found by

$$
\frac{\partial}{\partial t}_{total}\phi_\alpha(r,t) = \frac{\partial}{\partial t}_{beam}\phi_\alpha(r,t) + \frac{\partial}{\partial t}_{react}\phi_\alpha(r,t) + \frac{\partial}{\partial t}_{diff}\phi_\alpha(r,t), \qquad (5.13)
$$

which is numerically integrated to give the $\phi_\alpha(r,t)$ in a forward finite difference scheme. The length of the timestep is 10^{-9}s, and the spatial stepsize h is 0.2 μm. This values gave good stability in solving equation 5.13.

The time for which a particular part of the sample is irradiated is the *dwelltime*, t_d. This is dependent upon the area scanned (magnification), scan rate, and the size of the interaction volume (beam energy). Typical dwelltimes for ESEM are in the range 10^{-6}s to 10^{-2}s, which are considered here. A calculation following equation 5.13 is carried out where $\frac{\partial}{\partial t}_{beam}\phi_\alpha(r,t)$ is set to 0 for values of $t > t_d$, and the system is allowed to relax. The dwelltime is varied to simulate different operating conditions.

We model scanning as the beam dwelling on a succession of points for the dwelltime t_d. We consider each point in isolation, and assume complete relaxation between scans.

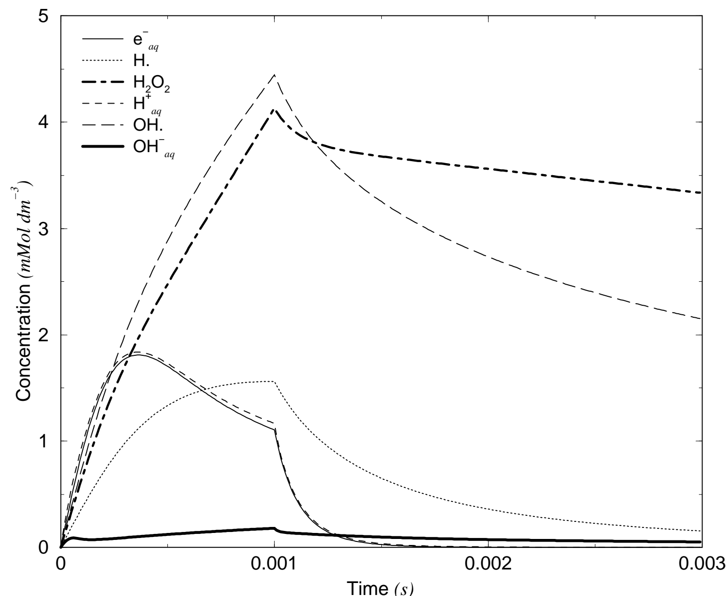

Figure 5.3: Generic behaviour of reactive species concentrations in a water sample, showing peaks for more reactive species, and continuous increase in H_2O_2 *and* OH. *25 keV, dwelltime* $= 10^{-3}s$

5.6

Results and Discussion

It is possible to give the results of this work in a variety of ways. Six dominant species are considered at two beam energies, for a variety of dwelltimes. An overview is presented, before attention is given to the effects of dwelltime, beam energy and particular species.

We begin by discussing the generic behaviour, for a 25 keV beam, with a moderate dwelltime of 10^{-3}s. At the point where the probe meets the sample ($r = 0$ for the spherical Gaussian), the maximum rate of creation is found (equation 5.9). The time evolution is shown in figure 5.3. As can be seen, the species evolve differently, but all decay for times greater than the dwelltime, as the system relaxes. More reactive species, the hydrated electron, hydrogen ion and hydrogen radical exhibit a peak concentration prior to the end of the dwelltime. Others, such as the hydroxyl radical and hydrogen peroxide only decay once irradiation ceases.

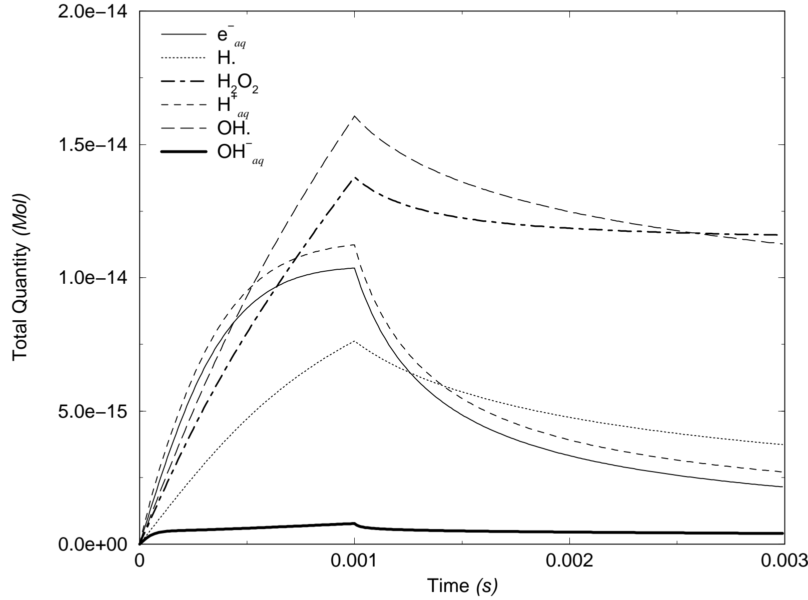

Figure 5.4: The total quantities show similar behaviour to central concentrations (figure 5.3), although the timescale is rather longer for the same dwelltime, 25 keV, dwelltime=10^{-3}*s.*

These peaks are due to competition between annihilation reactions, diffusion and creation. Initially, the concentrations are very small, so annihilation is negligible and creation dominates. After a certain time, the concentration is sufficient that the effects of annihilation and diffusion exceed creation. At this point, the concentration begins to fall. The time at which this happens depends on the particular species and beam energy.

The concentrations can be integrated throughout the system, so that an overall picture of total quantity can be built up. Figure 5.4 shows the same beam energy and dwelltime as that in figure 5.3. Comparison between the two shows a similar overall behaviour, however the total quantity plot (figure 5.4) has a somewhat broader time-evolution. This can be explained in terms of regions far from the centre. Fewer reactive species are produced here, and since the annihilation reactions are second order (equation 5.10), they are relatively less efficient. This means that it takes longer for the rate of annihilation to exceed creation (neglecting the effects of diffusion). So this broadening and delay of the peaks is not surprising. Further evidence can be seen from the rate of decay. The total quantity decays rather slowly, because annihilation is much slower far from the centre.

This is further demonstrated in figure 5.5, a plot of the concentration profile of the

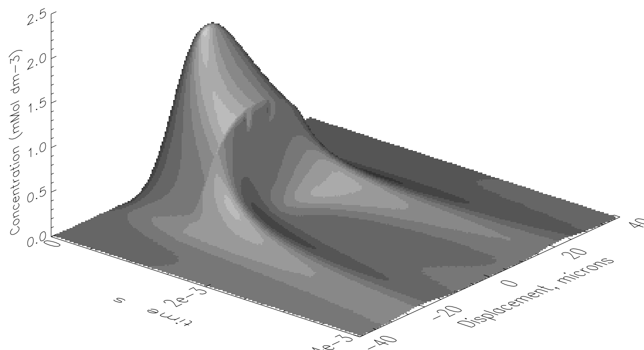

Figure 5.5: Time-evolution of the lateral profile of e^-_{aq}*, 25keV, dwelltime=*10^{-3}*s. Note the rapid decay in the centre, and much slower decay at low concentrations.*

hydrated electron, for the same dwelltime and beam energy (10^{-3}s and 25 keV). Here we see that after irradiation ceases, the concentration falls to zero, except at the edges, where two 'horns' are evolved. These represent very slow decay due to low concentrations.

Short dwelltimes

It has already been noted that at short dwelltimes the concentration is dominated by creation, so it should increase linearly. In other words, the contribution from the second and third terms in equation 5.13 can be neglected. This is shown to be true in the case of figure 5.6, for a dwelltime of 10^{-6}s, at 25 keV. The concentration of every species increases linearly with time, in proportion to its G-value for times less than the dwelltime. After irradiation there is negligible decay, as can be seen from the flat lines in figure 5.6.

Beam energy

For the same dwelltime as figure 5.3, the 5keV system shows a markedly different behaviour. The concentrations of all but hydrogen peroxide and the hydroxyl radical are small (figure 5.7). Longer dwelltimes are further discussed in a subsequent section. Suffice to say, the 5keV system evolves at a much faster rate than 25 keV, which we see in figures

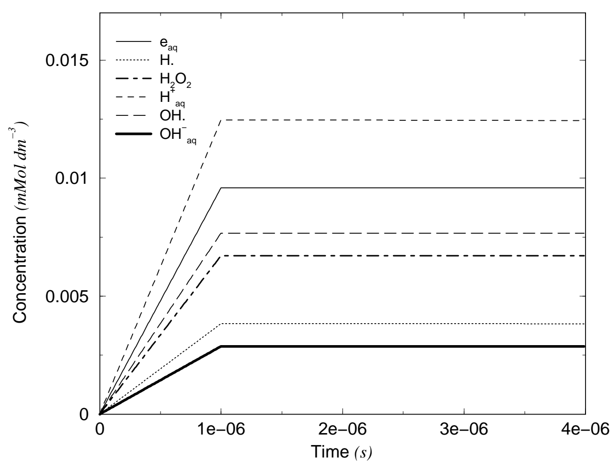

Figure 5.6: Early stages of radiolysis: all species increase linearly with time, in accordance with their G-values (table 5.3). 25 keV, dwelltime = $10^{-6}s$

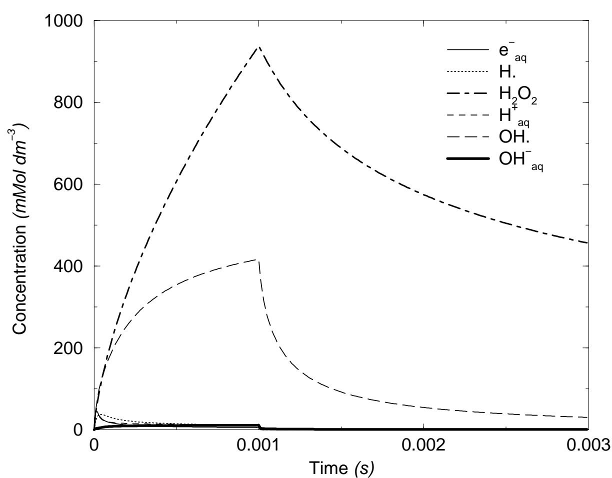

Figure 5.7: For the same dwelltime as figure 5.3 ($10^{-3}s$), the 5keV system appears markedly different. Central concentrations are dominated by $\cdot$OH *and* H_2O_2.

5.8 *(a)* and *(b)*. These plots show similar generic behaviour to figures 5.3 and 5.4, although the dwelltime is much shorter. The peaks for e^-_{aq}, H• and H^+_{aq} are again apparent, along with higher concentrations of H_2O_2 and •OH. Apart from the dwelltime, there are two main differences:

(1) The central concentration for 5keV is around 50 times higher.

(2) Total quantities produced are far higher in the 25 keV case.

In fact, all these effects are the consequences of the main difference between the 5keV and 25keV systems, the mean PE range. $\langle R \rangle$ is around fifteen times longer for 25 keV PE, (table 5.1). This means that the interaction volume is around 3400 times larger in the 25 keV case, since in our Gaussian approximation it goes as $\langle R \rangle^3$. So the primary yield is spread over a much greater volume, and the concentrations are far lower for 25 keV, although this is offset to some extent since five times as many species are created overall, from the increased energy absorption. The increased concentration for 5keV is then a direct result of the shorter mean PE range as shown in figures 5.4 and 5.8 *(a)*.

The concentration for 5keV (figure 5.8*(a)*) is very much higher when we consider the fact that the dwelltime is only $\frac{1}{10}th$ of the 25 keV dwelltime (figure 5.3). However when scanning a sample, the dwelltime is related to the time taken to for the beam to pass across the interaction volume. Since the 25 keV interaction volume is 15 times as wide (table 5.1), we expect much longer effective dwelltimes in this case.

A low concentration regime also means that it takes far longer for annihilation and diffusion to exceed creation, as we have already noted above. That annihilation is effectively suppressed for 25 keV means that the total quantities present are far greater, and the concentrations peak far later. The effect of the reduction in mean PE range is extreme indeed. Excepting the central region, we expect the 25 keV environment to be far more hostile.

Diffusion

It is not easy to decouple the effects of diffusion and annihilation. Both tend to reduce regions of high concentration with respect to those of low concentration. However we can

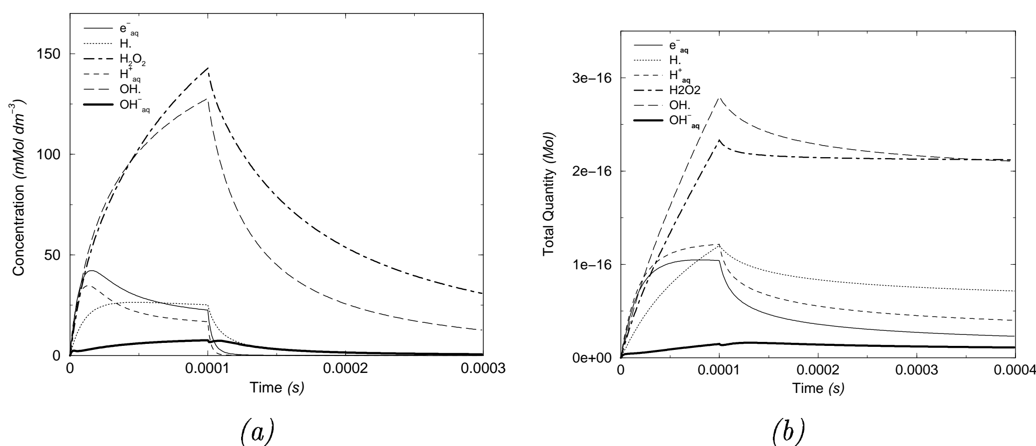

Figure 5.8: The 5keV system exhibits the same general behaviour as the 25 keV system, if the dwelltime is reduced by an order of magnitude. Central concentrations, (a) *and total quantities,* (b)*, both for a dwelltime of* 10^{-4}*s.*

solve equation 5.13 without a contribution from diffusion for comparison. Figure 5.9 shows lateral profiles for 5 keV *(a)* and 25 keV *(b)* after 10^{-4}s of irradiation with and without the contribution of diffusion.

The central concentration of ·OH has fallen by a factor of two as a consequence of diffusion in the 5 keV case (figure 5.9*(a)*). There is only a small reduction in central concentration from diffusion in the 25 keV case (figure 5.9*(b)*). Furthermore, we see that the e^-_{aq} is the most abundant species for 25 keV. The hydrated electron is produced at a greater rate than the other species shown, the fact that it remains the most abundant at this time suggests that annihilation reactions are not yet significant, and that the system is still in the range of linear increase with time (figure 5.6). The apparent increase in e^-_{aq} concentration in the diffusing 5keV system (figure 5.9*(a)*) is taken to be a result of decreased rates of reaction caused by lower concentrations of other species (eg H· and ·OH).

The variation here also stems largely from the different system sizes in each case. The 5keV system has a change in concentration two orders of magnitude greater than that in the 25 keV system over $\frac{1}{15}$th of the distance. This enormous change in concentration gradient is responsible for the different effects of diffusion.

Diffusion can also be followed with the time-evolution of hydrogen peroxide. Figure 5.10 shows the characteristic broadening and flattening of the concentration profile as

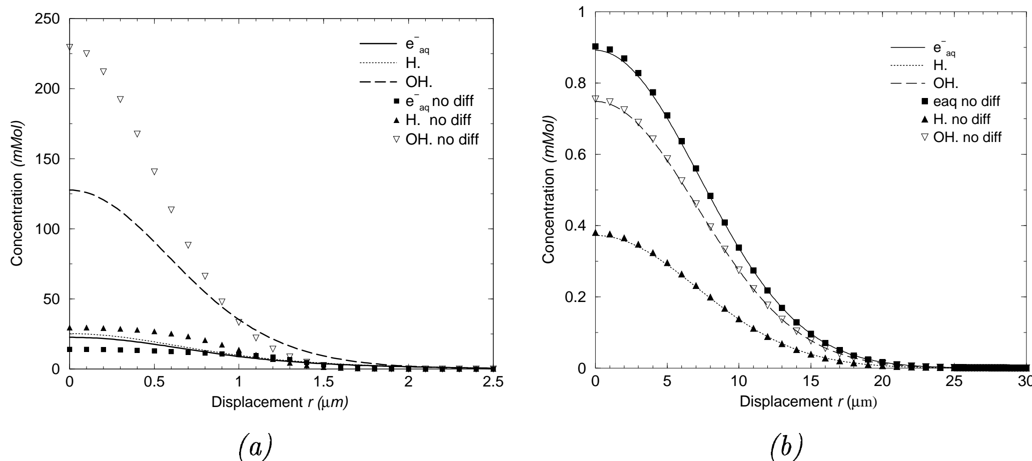

Figure 5.9: Lateral concentration profiles after a dwelltime of 10^{-4}s (5 keV, (a)*, 25 keV,* (b)*). The thicker lines represent simulations with diffusion. No diffusion is plotted as a series of data points.*

a result of diffusion. Here the dwelltime was 10^{-3}s. Since we have already noted that annihilation is not too significant for H_2O_2, this behaviour can be taken as evidence of diffusion.

Dominance of the hydroxyl radical

We now turn our attention to the different species. The behaviour of e^-_{aq}, H· and H^+_{aq} is straightforward enough. All are highly reactive, so the fact that they quickly reach a concentration where annihilation exceeds creation is not surprising (figures 5.3, 5.4, 5.8 *(a)* and *(b)*). Likewise OH^-_{aq}. This species is reactive, but produced in fairly small quantities (table 5.3) so it is quickly annihilated, mainly through reaction with the more abundant H^+_{aq}. Recombination between these two species has a high reaction rate (table 5.2).

Hydrogen peroxide is not very reactive on this timescale (table 5.2), so its high concentration and slow decay is entirely reasonable. Indeed, in the reaction scheme of Hill and Smith [80], it only reacts with the hydrogen radical (reaction 7, table 5.2). Since it is also the product of ·OH self annihilation (reaction 1, table 5.2), we expect to find H_2O_2 present in large quantities (figures 5.3, 5.4, 5.7, 5.8 *(a)* and *(b)*).

More interesting is the hydroxyl radical, which has a similar behaviour to hydrogen

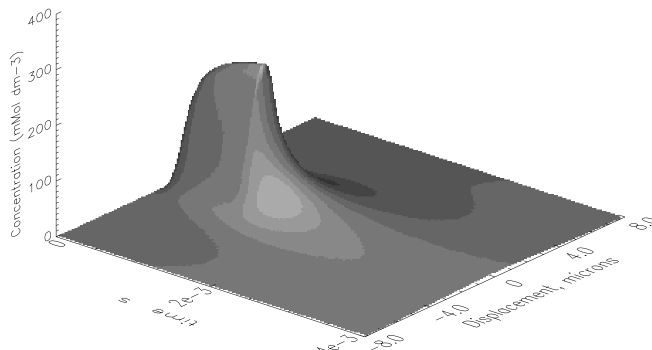

Figure 5.10: Time-evolution of lateral profile of H_2O_2 *5keV, dwelltime=*10^{-3}*s showing diffusion at times longer than the dwelltime.*

peroxide, although it is far more reactive, and so would be expected to react away. However, ·OH is produced in significant quantities (table 5.3), and the routes of annihilation are limited by the low concentration of other species. Self annihilation is possible but the rate is rather slow, at $0.45 \times 10^{10} M^{-1} s^{-1}$ (equation 1 in table 5.2). This lack of annihilation routes means that ·OH has a high concentration, and is expected to be the dominant damage-causing species. It is also relatively long-lived in water, again from lack of annihilation routes, further increasing the potential for damage.

The Approach to Equilibrium

For longer dwelltimes, the system tends towards a steady state in the $r = 0$ region (figure 5.11). After the concentration peaks, annihilation is dominant but in a regime of falling concentration rates of reaction are also reduced, so the concentrations tend towards an equilibrium value. Diffusion also becomes more and more significant for hydrogen peroxide and the hydroxyl radical by the time they have reached high concentration. Eventually, the competition between annihilation and diffusion, and radiolysis tends towards equilibrium, as shown in figure 5.11. The central concentrations are all largely constant after a dwelltime of 10^{-2}s for the 5keV system.

The system as a whole does not approach equilibrium, as diffusion continues to spread

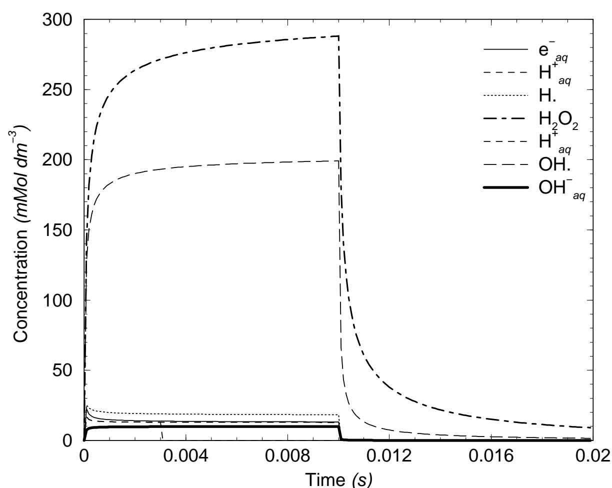

Figure 5.11: After sufficient dwelltime, the central concentration tends towards a steady state (5keV), dwelltime = 10^{-2}s.

the concentration profiles at all times. Additionally, far from the centre, we expect the concentrations to simply increase at all times, and not to exhibit clear maxima, as annihilation is less effective at lower concentrations (figures 5.5 and 5.10).

5.7

Conclusions

This simple first-order approach can determine the concentrations of reactive species in an ESEM water sample. The environment is clearly a hostile one, so increased radiation damage in the presence of water as found by Kitching [100] and Jenkins [99] is not surprising. We expect and find that our PBMA latex is highly beam-sensitive. This is because PBMA as a saturated polymer has limited mechanisms for energy loss [73] and the polymer-water interfacial area is extremely large in the case of a latex suspension. We have seen that water is a source of small, mobile reactive species, so latices will be especially sensitive to beam damage.

The high concentration of the hydroxyl radical suggests that this is the dominant species for sample degradation via free radical attack. The high concentration of ·OH

appears to be due *(i)* to its high primary yield and *(ii)* to the shortage of decay routes available in the absence of other reactive species. Hydrogen peroxide is also present in large quantities, but is relatively stable on the timescales considered here.

There is significant transport of the hydroxyl radical beyond the interaction volume for 5keV PE. Although diffusion is much reduced in the 25 keV system, much more of the sample is damaged in any case, because of the longer PE range. Not only does a 25 keV beam penetrate further into the sample, it also delivers five times as much energy as a 5 keV beam, producing fives times as many reactive species. However, the reactive species are more widely spread in the 25 keV case. This reduces annihilation, which is concentration dependent. The reactive species thus have longer lifetimes in the 25 keV system.

In practice, the beam current (set to 5nA here) is typically larger for 25 keV than 5keV, increasing the effect of beam energy further. It is clear that radiation damage is much reduced with a lower beam energy, if the damage is due to *quantity* of species, rather than *concentration*. As already noted, dwelltimes are also longer in the case of 25 keV, as the beam takes longer to scan across the larger interaction volume, so the decrease in damage by reduction in beam energy is expected to be very considerable.

This is in accord with the experimental results in figure 5.1, which show a significant effect from a relatively modest change in beam energy. In our subsequent ESEM work, we therefore minimise beam energy where possible. However we can only do this at the expense of our signal to noise ratio. This is reduced in two ways: *(i)* beam current is reduced at lower energies, as already noted, so we have a reduction in signal, although we can counteract this to some extent with a longer scan-time. *(ii)* In ESEM, the increased scattering cross-section at lower PE energies [80] [106] increases the electron density of the probe beam skirt (see chapter 4). This reduces the signal-noise ratio considerably as 5keV is approached.

5.8

Appendix: Diffusion Algorithm

We seek an expression for $D\nabla^2\phi_\alpha(r,t)$, to satisfy the right-hand side of the diffusion equation (equation 5.11) where we have the $\phi_\alpha(r,t)$ discreetly defined for a number of elements.

In Cartesian co-ordinates,

$$\nabla^2\phi_\alpha(x,y,z) = \frac{\partial^2}{\partial x^2}\phi_\alpha(x,y,z) + \frac{\partial^2}{\partial y^2}\phi_\alpha(x,y,z) + \frac{\partial^2}{\partial z^2}\phi_\alpha(x,y,z). \quad (5.14)$$

The finite difference scheme considers the sample as a number of cubic elements, of separation h along the x-axis. $\frac{\partial^2}{\partial x^2}\phi_\alpha(r,t)$ for the nth element is found from the central difference theorem [109], [107],

$$\frac{\partial^2}{\partial x^2}\phi_\alpha(nh,0,0) \approx \frac{1}{h^2}\left(\phi_\alpha((n+1)h,0,0) - 2\phi_\alpha(nh,0,0) + \phi_\alpha((n-1)h,0,0)\right). \quad (5.15)$$

Boundary conditions are taken as a mirror at $r = 0$ through which no diffusion is permitted. For large r (typically 100 μm) an equilibrium concentration is used. This is set to 10^{-7} Mol for H^+_{aq} and OH^-_{aq}, and 10^{-42} Mol for other species. The values for H^+_{aq} and OH^-_{aq} are taken for pH 7. Other values take the equilibrium concentration of $\cdot OH$ as a guide to typical values of reactive species.

Considering cells adjacent to the x-axis (figure 5.12), the central difference method yields $\frac{\partial^2}{\partial y^2}\phi_\alpha(x,y,z)$ for the nth element along the x-axis,

$$\frac{\partial^2}{\partial y^2}\phi_\alpha(nh,0,0) \approx \frac{1}{h^2}\Big(\phi_\alpha(nh,h,0) - 2\phi_\alpha(nh,0,0) + \phi_\alpha(nh,-h,0)\Big). \quad (5.16)$$

The values for $\phi_\alpha(nh,\pm h,0)$ are found from linear interpolation (figure 5.12) of $\phi_\alpha((n+$

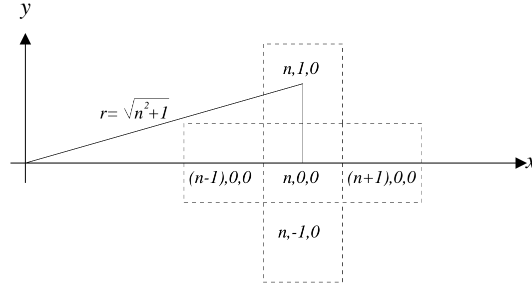

Figure 5.12: Adjacent elements to the nth element along the x-axis. Approximate values of $\phi(r,t)$ are found for the elements above and below the x-axis by linear interpolation along the x-axis.

1)$h,0,0)$ and $\phi_\alpha((n-1)h,0,0)$ to give

$$\phi_\alpha(nh,h,0) = \phi_\alpha(nh,-h,0) \approx \frac{1}{2h}\Big(\phi_\alpha((n+1)h,0,0) - \phi_\alpha(h(n-1),0,0)\Big)\left(\sqrt{n^2+1}-n\right)h + \phi_\alpha(nh,0,0). \quad (5.17)$$

Substitution into equation 5.16 gives

$$\frac{\partial^2}{\partial y^2}\phi_\alpha(nh,0,0) \approx \frac{1}{h^2}\left(\phi_\alpha((n+1)h,0,0) - \phi_\alpha(h(n-1),0,0)\right)\left(\sqrt{n^2+1}-n\right). \quad (5.18)$$

Since from symmetry,

$$\frac{\partial^2}{\partial y^2}\phi_\alpha(x,y,z) = \frac{\partial^2}{\partial z^2}\phi_\alpha(x,y,z), \quad (5.19)$$

the contribution from diffusion is

$$\frac{\partial}{\partial t_{diff}}\phi_\alpha(r,t) \approx \\ -\frac{D}{h^2}\Big(\phi_\alpha((n+1)h,0,0) - 2\phi_\alpha(nh,0,0) + \phi_\alpha((n-1)h,0,0)\Big) \\ -2\frac{D}{h^2}\Big(\phi_\alpha((n+1)h,0,0) - \phi_\alpha(n(h-1),0,0)\Big)\left(\sqrt{n^2+1}-n\right) \quad (5.20)$$

For the case $n = 0$, the x, y and z components are all equal by symmetry, and all three axes are treated as a mirror. Although linear interpolation is only accurate to first order, it requires only one-dimensional arrays for the $\phi_\alpha(r,t)$, allowing a smaller element size to be used.

Chapter 6

Image Analysis

So far we have considered scanning microscopes as a source of images. We have regarded these images as spatial variations of some signal, from which we can determine structure. In fact we can go further than this, using numerical image analysis. Here we aim to compare images quantitatively, and find means to probe the predictions of our model in chapter 3.

Image analysis has essentially two facets [110]. Image processing, where we seek to enhance the appearance of an image in some way, for example by increasing the contrast, and numerical analysis, the extraction of the quantitative information we are interested in. This numerical data requires the segmentation of each image, to isolate regions of interest. Segmentation is applied via the use of a threshold, which selects pixels according to certain criteria. Here we seek to explain each threshold, and to maintain the same values throughout our analysis.

We consider image analysis for each microscopy technique in turn, explaining how and why we invoke different methodologies in each case. We begin by considering silica structures in confocal microscopy, before moving on to surface silica measurements in ESEM and surface roughness in AFM. We also examine a method for correcting attenuation in confocal microscopy.

Since this image analysis is computational, representing images as arrays, extension from a 2D to 3D analysis is relatively straightforward. Therefore we can easily handle 3D CLSM images. Here all CLSM image analysis is three dimensional, whereas AFM and

ESEM is 2D. The main problem with 3D analysis is 2D rendering. Here we typically print out xy and xz planes.

6.1

Deconvolution in Confocal Microscopy

We have already considered image formation as a convolution of the specimen and the point spread function (PSF) which describes the blurring introduced by the microscope in chapter 4. Clearly in the case where this blurring is significant, it would be highly desirable to reconstruct the original specimen function $s(x_0)$ from the image function $i_(x_i)$ which are related by the imaging equation, page 54, [95],

$$i(x_i) = h(x_0) \oplus s(x_0) = \int_0 h(x_i - x_0)s(x_0)dx_0, \tag{4.3}$$

where $\oplus$ represents the convolution operation. The blurring is governed by $h(x_0)$, the point spread function (PSF) which is described by diffraction [14]. As the silica has structure below the resolution of the CLSM, we are extremely interested in reconstructing the specimen function $s(x_0)$ to reveal these fine details. We label the silica with fluorescein isothiocyanate (FITC) as described in chapter 8, page 136, which produces a bright signal when adsorbed onto silica.

Since $i(x_i)$ is the image obtained, we seek to 'deconvolve' it with $h(x_0)$ to yield $s(x_0)$. We can obtain the PSF with a sub-resolution object, which we treat as a point source, effectively a δ-function [14]. This δ-function then returns the PSF as its image, as shown in figure 6.1 *(a)* and *(b)* for the Zeiss LSM510 used with a 63$\times$ planapochromat objective lens fitted. The blurring is evident in the xy image by comparison with the scale bar. We also note the difference between the xy and xz images, with a reduced axial resolution.

Unfortunately this deconvolution is not trivial. Conceptually the most straightforward method is to Fourier transform the image function and divide this by the Fourier transform of the PSF to obtain the Fourier transform of the specimen function [95] [112]. However

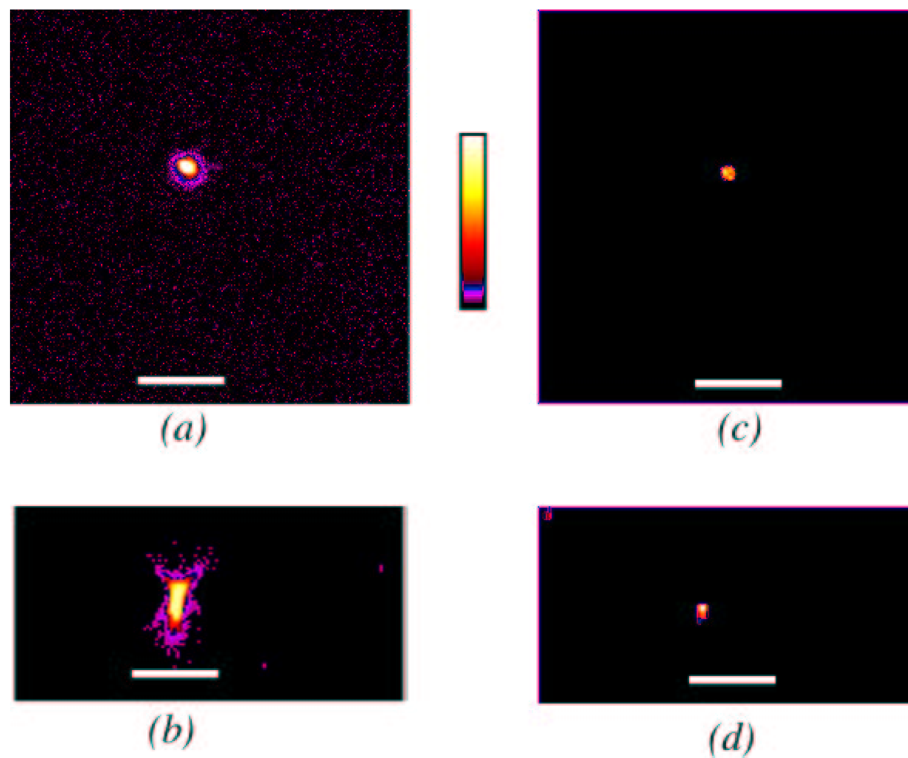

Figure 6.1: The point spread function obtained from sub-resolution polystyrene beads obtained from Molecular Probes [111]. (a) *xy image and* (b) *xz image. EM restored images* (c) *xy and* (d) *xz Bars=4 μm. Here we have employed the artificial colour table shown between* (a) *and* (c) *to enhance the contrast at low brightness.*

this linear approach is severely limited by the noise inherent in any measured PSF (which we can see in figure 6.1*(a)*) and also in the image function $i(x_i)$ [14] [95]. Rather better results are obtained using Conchello *et al.*'s application [94] [113] of the expectation maximisation (EM) algorithm of Dempster *et al.* [114]. This iterative approach takes trial specimen functions which approximate the true specimen function ever more closely. It is described below.

We want to find the specimen function which is most likely to have produced the image observed, given the PSF. The PSF can be determined numerically avoiding the noise inherent in measurement [96] [97]. We can take a log-likelihood [1]

$$\mathcal{L}[s(x_0)|i(x_i)] = -\int_I \left[\int_0 h(x_i - x_0)s(x_0)dx_0 - i(x_i)log\left\{ \int_0 h(x_i - x_0)s(x_0)dx_0 \right\} \right] dx_i, \tag{6.1}$$

where we seek to maximise the likelihood of $s(x_0)$ given $i(x_i)$. This leads to the iterative relation

$$\hat{s}_{EM}^{(k+1)} = \frac{\hat{s}_{EM}^{(k)}(x_0)}{H_0} \int_I h(x_i - x_0) \frac{i(x_0)}{\hat{i}^{(k)}(x_0)} dx_i. \tag{6.2}$$

Here $\hat{s}_{EM}^{(k)}(x_0)$ is the estimate of the specimen function at the kth iteration and $\hat{i}^{(k)}(x_i)$ is the image of $\hat{s}_{EM}^{(k)}(x_0)$ given by

$$\hat{i}^{(k)}(x_i) = \int_0 h(x_i - x_0)\hat{s}_{EM}^{(k)}(x_0)dx_0, \tag{6.3}$$

and the normalisation factor

[1] Since $log(f(x))$ increases monotonically with $f(x)$, the value of x which maximises $f(x)$ also maximises $log(f(x))$ [109].

$$H_0 = \int_0 h(x_0)dx_0. \tag{6.4}$$

The iterative relation equation 6.2 works via a comparison of the real and estimated images. If a pixel in the estimated image $\hat{i}^{(k)}(x_i)$ is darker than the corresponding pixel in the true image $i(x_i)$, we assume that that same pixel in the estimated specimen function $\hat{s}_{EM}^{(k)}(x_0)$ is also too dark. The pixel brightness in the specimen function is raised for the next iteration. This is reasonable as in general, dark regions in the specimen function lead to dark regions in the image.

In other words, if $\frac{i(x_0)}{\hat{i}^{(k)}(x_0)} > 1$, $\hat{i}^{(k)}(x_0) < i(x_0)$, so the value of $\hat{s}_{EM}^{(k)}(x_0)$ is too low for a given x_0. The new $\hat{s}_{EM}^{(k+1)}(x_0)$ is weighted with the factor $\frac{i(x_0)}{\hat{i}^{(k)}(x_0)}$ greater than unity, so the new specimen function value is increased and the new $\hat{i}^{(k)}(x_0)$ is closer to $i(x_0)$. In this way the EM algorithm proceeds towards the optimum specimen function. Figure 6.1 *(c)* and *(d)* shows the effect of 100 iterations of the EM algorithm in the PSF in *(a)* and *(b)*. Both horizontal and vertical sections show a very considerable reduction in blurring and noise. Figure 6.2 *(a)* (raw image) and *(b)* (EM restored image) shows the improvement in resolution on dried lacquer with silica obtained by using the EM algorithm for 100 iterations.

However the EM method tends to introduce noise eventually [94], as we can see in figure 6.2 *(c)*, after 1000 iterations. It tends to accentuate small bright regions at the expense of neighbouring darker structure. This reduces the signal to noise ratio, as noise produces bright pixels which are then emphasised [94] [113].

We can make use of two methods to reduce this problem. These are referred to as penalties, as they constrain each iteration. Equation 6.1 is then re-written to include a new term,

$$\mathcal{M}[s(x_0)|i(x_i)] = \mathcal{L}[s(x_0)|i(x_i)] - \alpha R(s(x_0)) \tag{6.5}$$

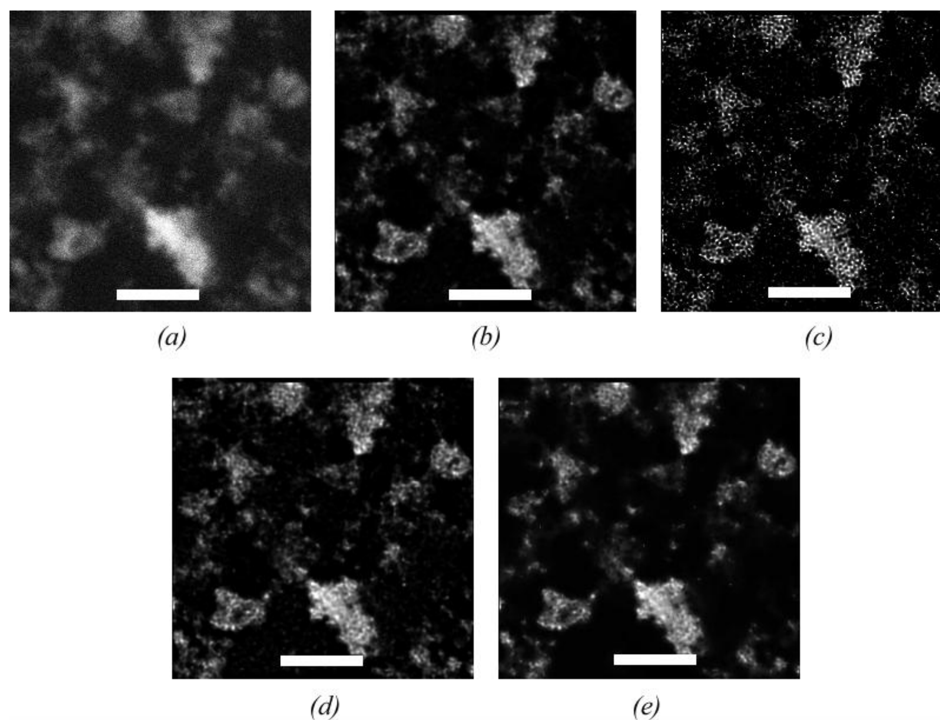

Figure 6.2: xy images of dried lacquer with AFS. (a) *unreconstructed image,* (b) *EM with 100 iterations,* (c) *EM with 1000 iterations,* (d) *EM with 1000 iterations and a 0.01 roughness penalty and* (e) *EM with 1000 iterations and an intensity penalty of* 10^{-7}*. The background in the original image* (a) *is blue, corresponding to a value rather greater than 0, whereas the black background in the other images corresponds to a value of 0. In other words, the EM algorithm tends to darken the background of the images. In fact, it darkens the entire image, but here we have used contrast expansion (see section 6.3) for printing, Bars=4* μ*m.*

where $\mathcal{M}$ is the new log-likelihood functional, R is the penalty functional, and α is a constant weighting factor. The Good's roughness penalty has

$$R(s(x_0)) = R_r(s(x_0)) = \int_0 |\nabla s(x_0)|^2 \, dx \tag{6.6}$$

which penalises rapid changes in $s(x_0)$, such as those introduced by noise. This tends to blur the image. The effect of 1000 EM iterations with Good's roughness is shown in figure 6.2 *(d)*. The image shows some blurring at low light intensities compared to *(b)*, with the loss of fine structure. Since the Good's roughness is essentially a blurring filter, this is not surprising. We discuss the use of blurring filters in section 6.3.

A penalty which reduces very bright pixels in $s(x)$ without blurring is Conchello's intensity penalty [94],

$$R(s(x_0)) = R_i(s(x_0)) = \int_0 [s(x_0)]^2 \, dx \tag{6.7}$$

1000 iterations with the intensity penalty are shown in figure 6.2 *(e)*.

This image shows slightly more fine structure at low intensities than figure 6.2*(b)*, although the images are very similar. Given the similarity in the results between *(b)*, *(d)* and *(e)*, and the tenfold reduction in computer time for *(b)*, we conclude that 100 EM iterations is the most appropriate for this work, where we compare relatively similar images under very similar experimental conditions.

6.2

Numerical Analysis

Having obtained $s(x_0)$, we now wish to identify the silica within the image. Since the silica is bright as we have labelled it with fluorescein isothiocyanate, we regard bright pixels as silica, and dark as polymer matrix.

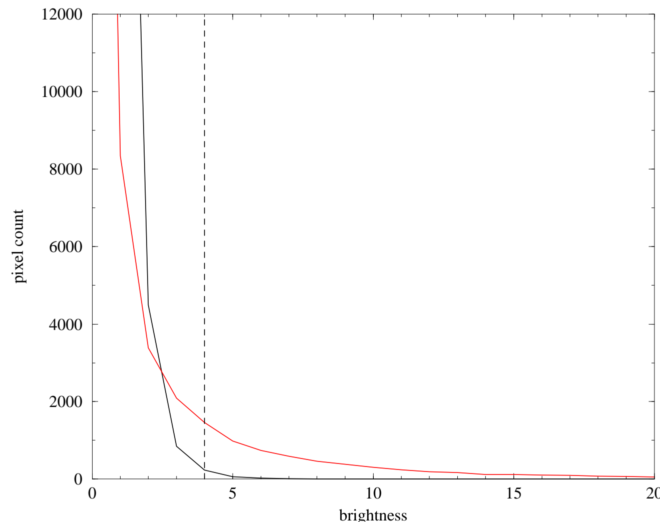

Figure 6.3: Image histograms for images without silica (black line) and with silica (red line). The threshold is shown for a value of four (dotted line). Clearly these image histograms have a very large number of pixels with grey scale values of 0 and 1, suggesting saturation. This is a result of the EM analysis, which biases pixels to low intensities. The original image had a range of pixel values from 0-255, like figure 6.2 (a).

Thresholding

So we must select the bright pixels by choosing some threshold value of brightness in the range 0-255. All pixels with brightness greater than the threshold are then treated as silica, all below or equal to the threshold are taken to be polymer. The most straightforward way to obtain a threshold is extract the *image histogram* [110]. This plots the number of pixels as a function of brightness, as shown in figure 6.3, from a silica-free sample (black line) and one line from a silica-containing sample (red line).

We see that the silica-containing sample has many more bright pixels. In fact without silica, there are almost no pixels with a brightness greater than four, which we take as our threshold. The pixels of brightness greater than four we then interpret as silica.

Thresholding is shown rather more quantitatively in figure 6.4. Here we plot the fraction of 'bright' pixels as a function of threshold. We can see that the no silica (noise) image has values in the range $5 \times 10^{-3} - 10^{-4}$ for a threshold of four. We discuss further noise reduction methods below. For now we require that the bright pixel fraction fraction of a silica-free image should be $< 10^{-3}$. This we take as the residual noise in the system.

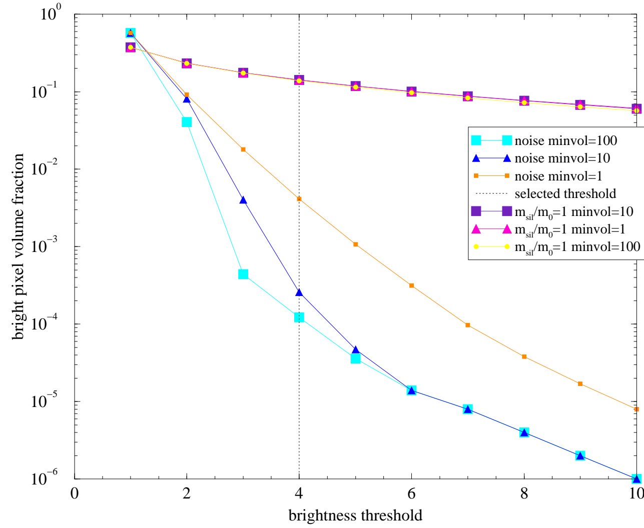

Figure 6.4: The threshold is the black dotted line, at a brightness of 4 The fraction of bright pixels as a function of brightness threshold. Lines are plotted for images of a silica-containing specimen, and for a specimen without any silica (noise). The minimum cluster volume to be treated as a silica particle is set to 1, 10 and 100 pixels in each case.

Having selected our threshold, we then *segment* the image into bright (white) and dark (black) regions. The resulting two-level image is termed a binary image. The EM-restored images in figure figure 6.5 *(a)* and *(c)* are segmented to produce the binary images in *(b)* and *(d)*, with the percolating structure (see below) are shown in red.

Cluster counting and percolation

To go further, we must identify the individual silica particles in an image. At this point, it is important to distinguish silica particles and clusters. A silica particle is a real piece of silica, and a single object. A cluster is a number of neighbouring white pixels in an image, and may correspond to one or more silica particles which lie close together. Since the silica particles are irregular in shape, it is not possible in principle to determine how many particles contribute to each cluster.

We therefore deal with clusters in image analysis, and identify them by labelling each one with a counting algorithm which is implemented as follows (figure 6.6). The image is scanned, and if a white pixel (corresponding to a silica particle) is found, a new particle is recorded. Neighbouring pixels are tested, and the algorithm moves to the first new white

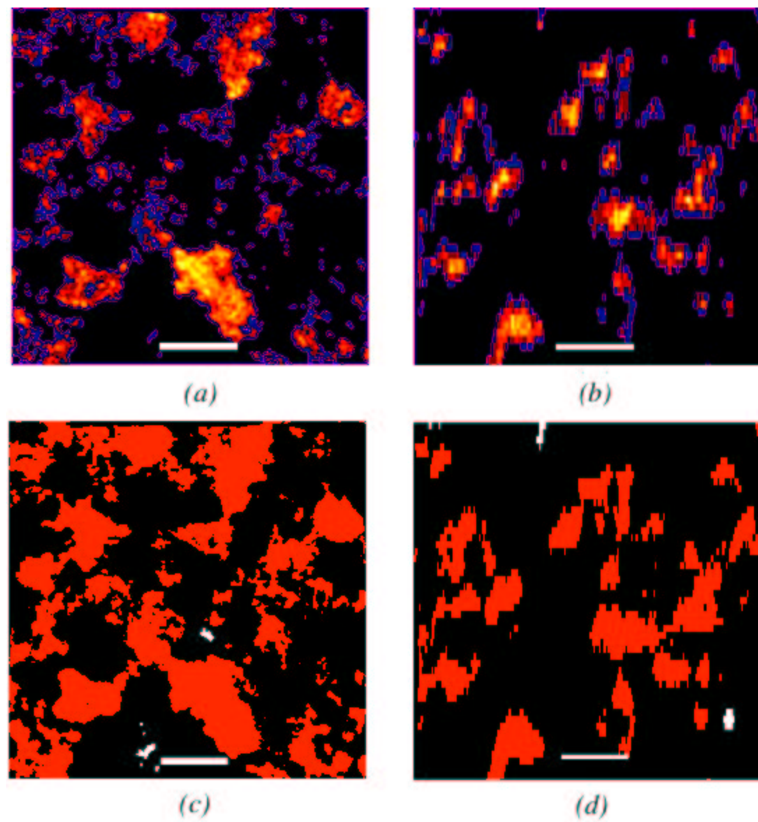

Figure 6.5: EM-reconstructed CLSM images of a lacquer containing AFS, (a) *xy and* (b) *xz, with binary images* (c) *xy and* (d) *xz. Although the red regions appear separated in 2D, our percolation algorithm reveals connectivity in 3D, as all red pixels are part of one cluster. Bars=4 μm.*

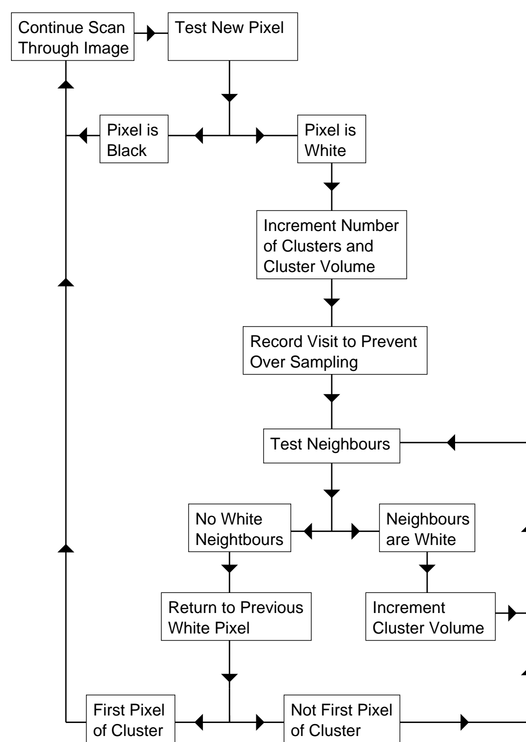

Figure 6.6: Algorithm for counting and sizing clusters in a binary image where white corresponds to silica, and black corresponds to polymer.

pixel found. Here we define neighbouring pixels as those which share a face, an edge *or* a corner, such that each pixel has 26 neighbours, which corresponds to 8-fold connectivity in 2D. The algorithm tests again for neighbours, and moves on if successful. Upon reaching the edge of a cluster of white pixels where no white neighbours are found, the algorithm returns to the previous site visited, and moves to the first previously unvisited white neighbour, if possible. Eventually all possibilities are exhausted and the algorithm returns to the first pixel visited and finds no new neighbours. In this way, all the pixels are found, and by incrementing the cluster size for every pixel counted, the volume of each cluster is determined. By labelling each cluster, the number of clusters in a given image may be found.

Since we know the size of each cluster, we can further reduce noise. As noise manifests itself as isolated bright pixels [110], then if we remove these we expect to reduce the noise. By selecting different size for this minimum cluster volume (labelled as 'minvol' in figure 6.4), we can determine a volume-threshold. From figure 6.4, we see that imposing a minimum volume of 10 pixels reduces the noise by more than an order of magnitude for a threshold of four. Increasing our minimum cluster volume to 100 pixels has little effect on the bright pixel volume fraction, but we can significantly reduce the noise contribution to the *number* of clusters, so we use 100 as our cluster volume threshold. The advantage of this method of noise reduction is that it is non-blurring so does not reduce the resolution of the image at all (see below). Clusters treated as silica particles are unaffected by this noise reduction.

We test for percolation by comparing cluster labels on opposite sides of the image. If two planes on opposite sides of the image share the same cluster label, then that cluster must span the image. One such cluster is shown in red in figures 6.5*(c)* and 6.5*(d)*. Our cluster labelling enables us to investigate a number of percolation phenomena [58]. Since we have counted the clusters, we can explore this count as a function of silica concentration. We can also determine the volume of the largest cluster, which we expect to increase sharply at the percolation threshold.

To get an idea of the lengthscale of the largest (percolating) cluster, we turn to the approach of Doi and Edwards for polymer chains [115]. We assume clusters to be entirely disordered, so we take the radius of gyration R_g as our lengthscale. We have

$$R_g^2 = \frac{1}{N} \sum_{i=1} N \langle (R_i - R_{COG})^2 \rangle, \tag{6.8}$$

with R_i the location of the ith pixel in the cluster, N the number of pixels and the centre of gravity R_{COG} defined by

$$R_{COG} = \frac{1}{N} \sum_{i=1}^{N} \langle R_i \rangle. \tag{6.9}$$

6.3

Silica extraction for ESEM

We now turn to ESEM. The contrast mechanisms in ESEM (see chapter 4, section 4.1) propose some key challenges for quantitative image analysis. Specifically these are the difficulties of segmenting images and achieving reproducibility, and require a different approach.

Contrast in ESEM, predominantly via the secondary electron cascade [78] is highly sensitive to working distance, chamber pressure, detector bias and primary beam characteristics. We can control the first three, with *some* degree of accuracy, but the variation in the electron beam (spot size, beam current) is hard to control or measure routinely [70]. Together, these mean that images of the same sample are not necessarily the same. Important differences are often apparent in the image histograms.

Contrast enhancement

The most obvious way rectify differences in ESEM image acquisition is to use contrast expansion [110]. This involves rescaling the image histogram such that the values lie throughout the range from 0-255. This is done in figure 6.7*(a)*, and we see the original

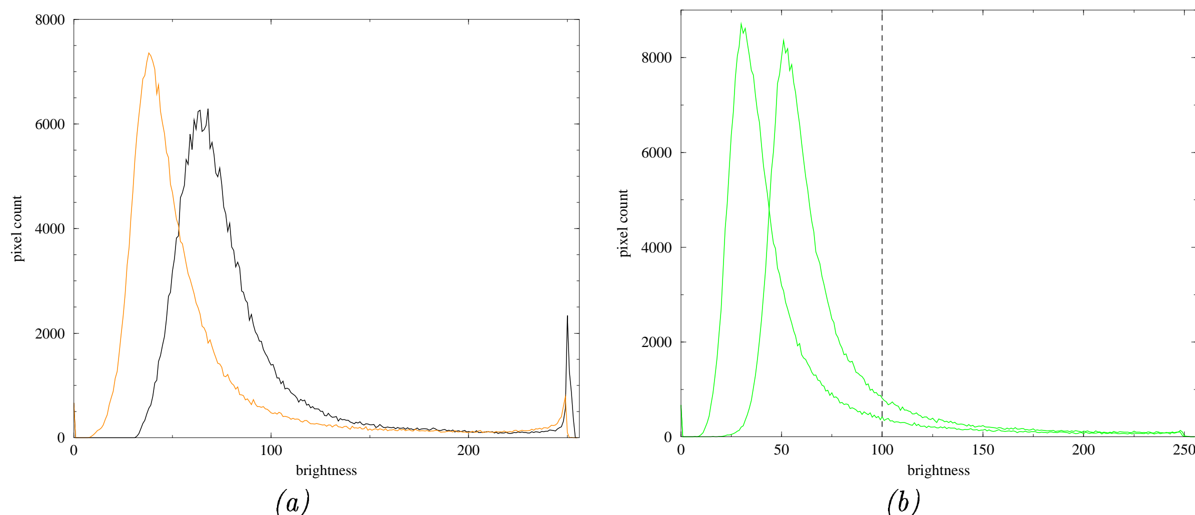

Figure 6.7: (a) *ESEM Contrast enhancement. The original image histogram (black line) is stretched to fill all available brightness levels (orange line).* (b)*Limitations of brightness thresholding for ESEM. These two image histograms were taken from identical regions of the same sample, under almost the same imaging conditions. The use of a brightness threshold here will give different fractions of bright pixels.*

(black) line is stretched (red line) to lie along the whole range. This can increase the noise, as we are constrained to integer values for the pixels.

Unfortunately contrast expansion does not always resolve differences in ESEM image histograms. Figure 6.7*(b)* shows image histograms from two similar regions of the same sample under similar imaging conditions. Both histograms have had contrast expansion applied. The differences between the histograms are clear, with the whole line bodily shifted along the x-axis. So were we to impose the same brightness threshold here, we would expect different proportions of white pixels in each binary image, for identical experimental conditions.

The numerical accuracy of a brightness threshold for ESEM images, is thus extremely limited. Despite these considerations, contrast expansion provides a useful starting point for processing ESEM images.

Gaussian noise reduction

Before considering other means of thresholding we discuss an important means of noise reduction: Neighbourhood averaging [110]. We have already noted that noise is found as isolated bright pixels. By modulating the brightness of each pixel with its surroundings we can remove these bright pixels and reduce the noise in the image.

Naively we can sum the eight neighbours (in 2D) with the pixel we are interested in and normalise by dividing by nine. This simple technique of neighbourhood averaging is the equivalent of applying the kernel

$$\hat{W}_{ij} = \begin{pmatrix} 1 & 1 & 1 \\ 1 & 1 & 1 \\ 1 & 1 & 1 \end{pmatrix}. \tag{6.10}$$

This means modulating each pixel in the image $I_{(x,y)}$ to

$$I_{(x,y)} \stackrel{i,j}{=} \frac{\sum_{i,j}^{m} W_{ij} I_{(x+i,y+j)}}{\sum_{i,j}^{m} W_{ij}} \tag{6.11}$$

where the denominator is simply the sum of the kernel elements (nine in this case). m the dimension of the kernel is here equal to three.

A variety of noise-reduction kernels have been developed [110]. Here we use a Gaussian kernel of side five. There is some physical basis for using a Gaussian kernel, as we expect noise to enter the system normally, although the standard deviation (0.625 pixels in this case) and magnitude are not defined [110]. The Gaussian kernel used here is

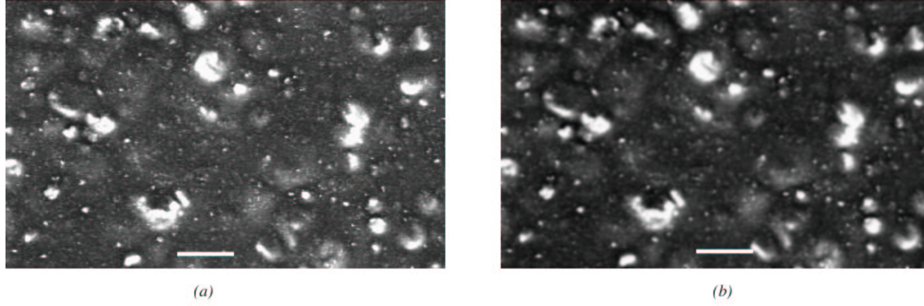

Figure 6.8: Original ESEM image of dried lacquer containing silica (a) *and* (b) *following Gaussian blur noise reduction and contrast enhancement. Bars=20 μm*

$$\hat{W}_g = \begin{pmatrix} 1 & 2 & 3 & 2 & 1 \\ 2 & 7 & 11 & 7 & 2 \\ 3 & 11 & 17 & 11 & 3 \\ 2 & 7 & 11 & 7 & 2 \\ 1 & 2 & 3 & 2 & 1 \end{pmatrix}. \quad (6.12)$$

The effect of this operator is shown in figure 6.8. We apply a Gaussian noise reduction and contrast expansion to figure 6.8*(a)* to form *(b)*. Crucially, this spatial filter approach to noise reduction implies some blurring (for example the Good's roughness penalty in deconvolution). This is because fine structure and noise are impossible to distinguish as both have high spatial frequency. So we eliminate noise and inevitably some fine structural details [110]. Note that we ignore the edges of the image following noise reduction, setting a two-pixel boundary to 0, as we can not apply this Gaussian blur kernel at the edge of an image.

Edge enhancement

Examination of figure 6.8*(b)* shows us that silica is associated with *variations* in brightness. Moving along the image from dark polymer to bright silica we would expect to encounter a brightness gradient. Within the silica particles there are also changes in brightness, so there should be a brightness gradient here too.

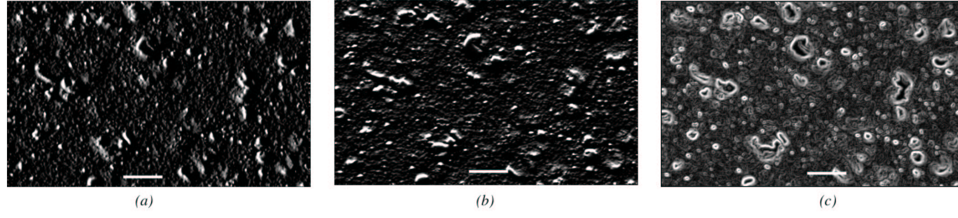

Figure 6.9: The effect of gradient and Sobel operators. $\frac{\partial}{\partial x}$ (a)*and* $\frac{\partial}{\partial y}$ (b) *gradient images and Sobel image* (c) *from figure 6.8*(b). *Bars=20 μm*

If we could differentiate the image function $I_{(x,y)}$, we would expect silica to be associated with non-zero values in a 'gradient image'. We can differentiate with respect to x and y, the kernels are shown below [110].

$$\hat{W}_{\frac{\partial I}{\partial x}} = \begin{pmatrix} 1 & 0 & -1 \\ 2 & 0 & -2 \\ 1 & 0 & -1 \end{pmatrix} \tag{6.13}$$

$$\hat{W}_{\frac{\partial I}{\partial y}} = \begin{pmatrix} 1 & 2 & 1 \\ 0 & 0 & 0 \\ -1 & -2 & -1 \end{pmatrix} \tag{6.14}$$

Gradient images of figure 6.8*(b)* are shown in figure 6.9 *(a)* and *(b)* for $\frac{\partial I}{\partial x}$ and $\frac{\partial I}{\partial y}$ respectively. Here y is defined as increasing down the page; we start differentiating from the top left-hand corner of the image.

Comparison between the original and gradient images show that bright areas in the gradient images correspond to regions where the brightness is increasing in the x direction (figure 6.9*(a)*) and in the y direction *(b)*. Decreasing image brightness produces a negative value in the gradient image. Consequently in figure 6.9*(a)* we find the left-hand edges of the silica particles and in *(b)* we have the top sides.

We can combine the $\frac{\partial I}{\partial x}$ and $\frac{\partial I}{\partial y}$ images, and make use of the negative values for the right-hand and bottom sides of the silica particles by taking the square root of the sum of

the squares of the two gradient images with the Sobel operator [110]. This is defined as

$$\hat{S}[I(x,y)] = \sqrt{\left(\frac{\partial}{\partial x}I(x,y)\right)^2 + \left(\frac{\partial}{\partial y}I(x,y)\right)^2}. \tag{6.15}$$

The Sobel operator produced the image shown in figure 6.9*(c)*. Comparison with figure 6.8*(b)* shows that we have indeed found the edges of the silica particles.

Gradient thresholding

This Sobel image gives us a new means to detect silica, and hence a new form of segmentation, gradient thresholding. Of course the Sobel image is brightest around the silica particle edges, as that is where the gradient is largest. So just taking the brightest (greater than 100) pixels produces the image shown in figure 6.10*(a)*. Here we have only the edges of the silica particles. Reducing the threshold to 50 increases the number of pixels identified as silica. However the holes at the centres of silica particles remain (6.10*(b)*).

Examination of figure 6.8*(b)* shows that although the centres of the silica particles show little brightness variation, they are typically very bright. So by selecting a stringent brightness threshold (of 245) that eliminates all polymer, we can identify the centres of the silica particles (figure 6.10*(c)*).

Combining the white pixels in figure 6.10 *(b)* and *(c)* in *(d)* we have our final binary image. Although there are some residual 'holes' in the silica particles, the vast majority of the silica in figure 6.10 is identified successfully. By obtaining the fraction of white pixels, we can obtain a measure of the proportion of surface occupied by the silica.

It is possible to use a 'dilation' operator where we add extra white pixels around the edges of clusters to fill in the holes in the gradient threshold image only (figure 6.10 *(b)*). Having filled in the holes, we can then use an 'erosion' operator to perform the reverse [110]. However it was hard to distinguish the white regions that 'should' be joined together and those which should not. We have found that our gradient and brightness thresholding method gives the best results.

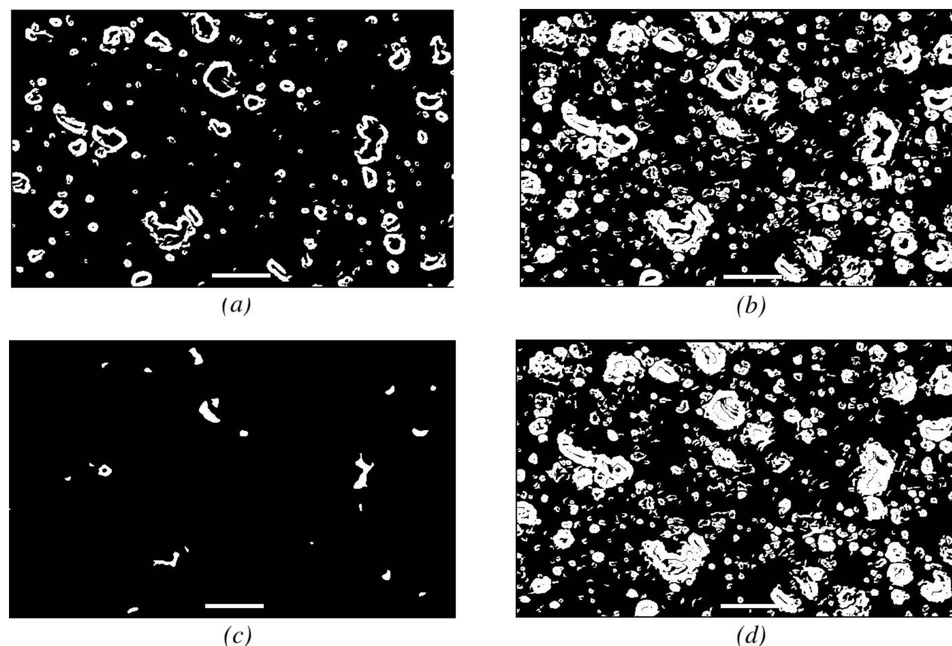

Figure 6.10: Thresholding methods to isolate silica from the polymer background to produce binary images from figure 6.8(b)*: Gradient threshold (100)* (a), *Gradient threshold (50)* (b), *Brightness threshold (245)* (c), *and brightness and Sobel* ((a)∪(c)), (d). *Bars=20 μm*

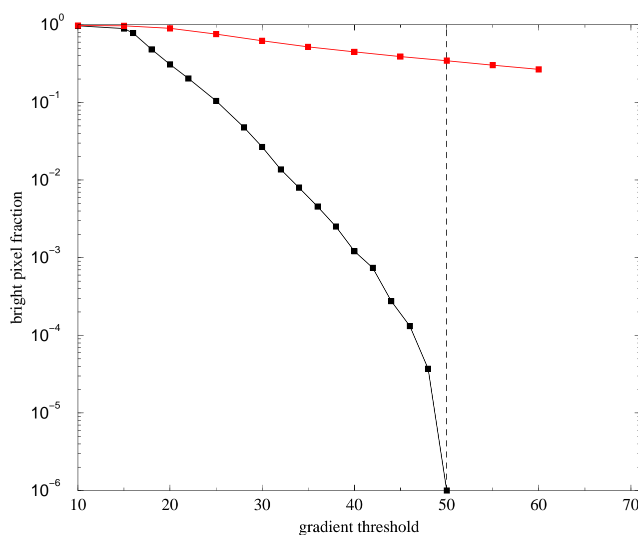

Figure 6.11: ESEM gradient thresholding, comparison between polymer background (black line) and silica-containing lacquer (red line). The dotted line is the threshold employed (figure 6.10(d))

We determine the optimal gradient threshold in a similar way to our brightness threshold for CLSM above. Plotting the proportion of bright pixels as a function of gradient threshold for images with and without silica, we find that the polymer background image (black line in figure 6.11) falls rapidly at a gradient threshold of 50. The silica-containing image (red line) is rather less affected. As above, noise is further reduced by requiring a minimum cluster size, this time of 10 pixels. This technique produces consistent repeatable and quantitative results, as we will see in chapters 7 and 8.

6.4

Contrast enhancement in CLSM

In confocal microscopy we transmit light through the specimen. Highly transparent specimens produce images of constant intensity with depth, subject to the constraints of spherical aberration (chapter 4, page 55).

Here we consider images of specimens labelled with rhodamine, as discussed in chapter 9 page 172. Unlike FITC, rhodamine labels both silica and polymer, although there is contrast between them. Less transparent specimens exhibit attenuation. For example figure 6.12*(c)* shows decreasing brightness towards the bottom of the image.

We can quantify this by finding the mean pixel brightness as a function of depth (figure 6.13). Without silica, the brightness increases around the surface, as we begin to image the fluorescently labelled film (black line in figure 6.13). Further into the film, there is slight attenuation, but the mean brightness is fairly constant. By contrast with silica in the lacquer the transparency may be reduced, as is the case here. The brightness now falls off within the film, by a factor of ~30 in 22μm, although the increase to the surface is retained (orange line)

We can correct for this by linearly scaling each pixel such that each xy plane has the same mean brightness, in a similar way to the contrast expansion above. Of course above the surface of the film, the intensity is small. To avoid using contrast expansion here, we determine the gradient of the mean brightness, as shown in figure 6.13. A positive gradient shows that the brightness increases with depth, corresponding to an xy plane above the

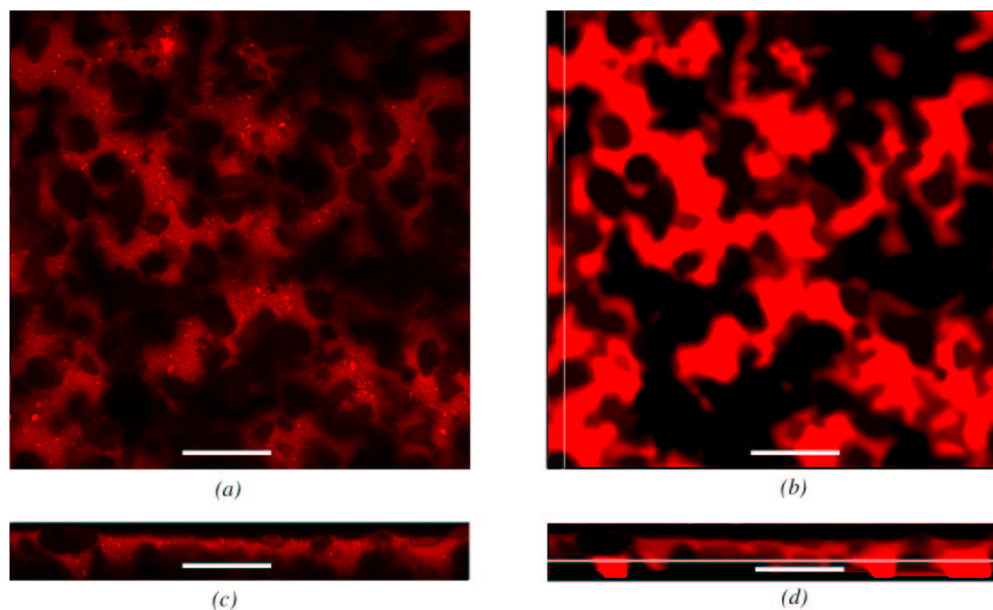

Figure 6.12: Contrast expansion for attenuation in CLSM. (a) *xy original image,* (b) *xy contrast enhanced image,* (c) *xz original image and* (d) *xz enhanced image. The darkening towards the bottom of the xz* (c) *image is alleviated in* (d)*. The white line in* (b) *shows the location of the plane in* (c)*and* (d)*, the line in* (d) *shows the plane in* (a) *and* (c)*. Bars=40 μm*

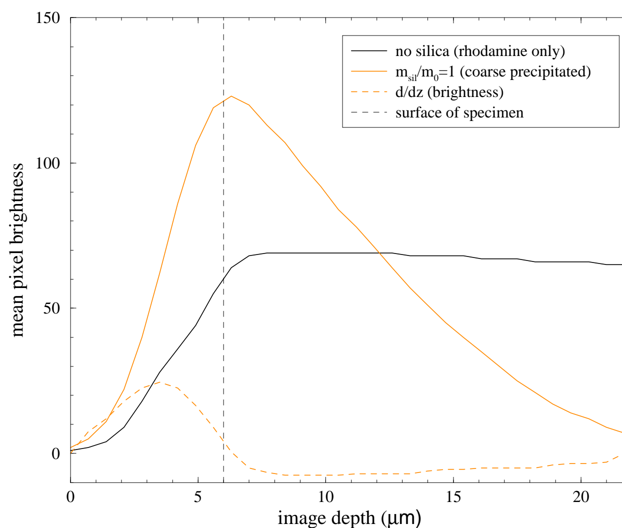

Figure 6.13: Attenuation in films containing large amounts of silica (orange line), and no silica (black line). The mean brightness is differentiated with respect to depth, to determine the location of the surface (orange dotted line).

surface.

So we require a negative gradient before we expand the contrast. This technique is particularly effective for very rough surfaces, where the surface roughness exceeds the vertical spacing between pixels. In these images it is hard to find the surface by inspection.

This contrast expansion is shown in figures 6.12*(b)* and 6.12*(d)*. *(b)* is rather brighter than *(a)*, but the xz image *(d)* shows much more brightness towards the bottom of the film, compared to *(c)*. In the printing, some saturation is evident, as there are many pixels with brightness greater than 255. Although this structure is lost in printing, it is retained computationally by extending the range of pixel values beyond 0-255. We shall return to the interpretation of these images in chapter 9.

6.5

Surface Roughness in AFM

Compared to ESEM and CLSM, AFM height images are relatively straightforward to analyse. At the resolution we use here, the image is assumed to be an absolute map of the surface, as the dimensions of the tip are well below the lengthscales we are interested in here (figure 6.14). Every value in the image is the height at that location.

As noted in chapter 2 page 20, R_a the surface roughness is given by

$$R_a = \frac{1}{N} \sum_{i=0}^{i=N} |h_{(i)} - \bar{h}| \tag{2.7}$$

with N the number of pixels in the image, $h_{(i)}$ the height of each pixel and $\bar{h}$ the mean image height. R_a is found using the proprietary software developed by Digital Instruments [56].

Our major error here is the non-planar scanning, the cross-coupling, as mentioned in chapter 4, page 50. This we can quantify using a single crystal of silica as a flat surface. The R_a in this case was 6nm for a 60 μm scan, which we take as our error. The cross-

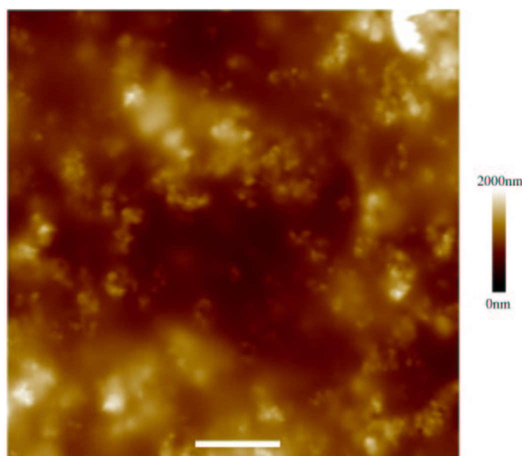

Figure 6.14: AFM surface map, of silica-containing lacquer with 2 μm total vertical range. R_a=196nm. Bar=6 μm.

coupling is largely rectified by the Digital Instruments Nanoscope III software [56].

Although it might be supposed that there is much more to extract from AFM than surface roughness, as we shall see later there is a wealth of qualitative information available from the technique. We could in principle construct a means of extracting the silica pixels, but there are further considerations concerning 'surface silica' which we will address in chapter 8.

6.6

Summary

We have developed a variety of analysis techniques to quantify microscope images, and will return to these parameters in subsequent chapters. We have introduced the parameters used in chapters 7, 8 and 9, of silica volume and surface fraction (confocal microscopy and ESEM).

We demonstrated the ability of image reconstruction via expectation maximisation to significantly enhance resolution in the confocal microscope. From the CLSM, we can determine silica structure and observe percolation phenomena, such as cluster count and maximum cluster size.

Repeatable techniques have been developed for segmentation of ESEM images to find the surface silica content. Using contrast expansions, we can offset some of the negative effects of ESEM imaging and attenuation in thick samples in confocal microscopy, and we have found a means of determining the sample surface in CLSM.

From AFM we can extract the surface roughness parameter R_a with a high degree of precision. As noted in chapter 4 page 50 we do not interpret AFM phase images quantitatively.

Chapter 7

ESEM characterisation

In this our first results chapter, we describe the use of ESEM for the study of matt water-based lacquers. We begin by describing sample preparation and mounting before pulling together the ideas of chapter 4, section 4.1 and chapter 5 to ESEM optimisation. We pay special attention to the optimised pumpdown for matt lacquers, discussing our parameters and the potential for water loss during pumpdown, extending the work of Cameron *et al.* [72].

This leads on to the techniques used in the experiments to image the lacquer film-forming *in-situ*. We also consider the use of ESEM to determine some key properties of the dried film, in particular the effect of film thickness.

We interpret our results in terms of the silica structure model of chapter 3, and use the image analysis techniques developed in chapter 6 to extract quantitative information. However this chapter is not meant to test the silica structure model. Its aim is to demonstrate the unique abilities of ESEM in characterising matt water-based lacquers. We focus on the silica structure model in the next chapter.

Component	Function	% by weight in formulation	Supplier
Glascol C47	80nm PBMA† Latex Binder	71.4	Allied Colloids [59]
Water		16.8	
Tegofoamex 1488	Defoamer	0.1	Tego Chemie [116]
Degussa TS100*	Matting Agent	variable	
Dowanol PnB	Coalescing aid	3.81	Dow Chemical [117]
Dowanol DPnB	Coalescing aid	1.90	Dow Chemical [118]
Tegofoamex 1488	Defoamer	0.05	[116]
Troysol LAC	Anti Cratering Agent	0.5	Troy Chemical Co [119]
Glaswax E1	Surface enhancer	2.14	Allied Colloids[120]
Henkel DSX 1514	Rheology Modifier	0.8	Henkel [121]

*Table 7.1: Formulation Recipe. The components are added in the order and amounts shown. † Poly butyl methacrylate. * The silica is varied between samples.*

7.1

Sample preparation

The lacquers used have been produced according to a formulation described in the Allied Colloids literature [59]. The ingredients are listed in table 7.1. Suppliers and further information are given in the appendix, page 216. We pre-mix silica and water, also the two coalescing aids. The components are then mixed together with a Cowles head rotating at 1500 rpm.

We mix in the order and quantities given in table 7.1, with one minute separation between the addition of each component. The silica is dispersed in the water prior to addition to the mix. The formulation is then mixed for a further 15 minutes after the addition of the last ingredient. Typically we produce 50 cm^3 of lacquer, so we halve the percentages in table 7.1 to obtain the desired weight in grammes. The density of all the components (except the silica) is close to 1 gcm^{-3}. The values given by the suppliers are quoted in the appendix, page 217.

The work presented here pre-dates the silica structure model, so rather than adding silica by volume, we used 2.5% silica by weight. Using equation 3.8 we have different values

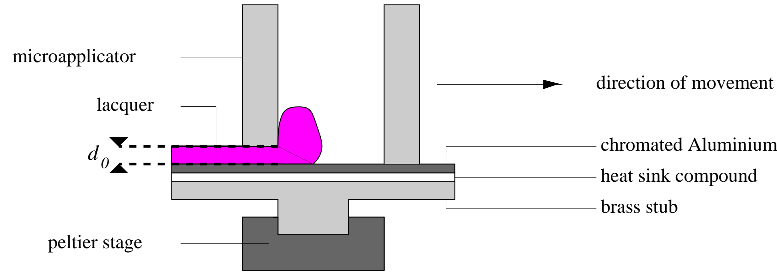

Figure 7.1: Schematic experimental set-up. Movement of the microapplicator leaves a wet film of thickness d_0 on the substrate. The Chromated Aluminium substrate is mounted on a brass stub. Heat sink compound is used between the stub and Chromated Aluminium to ensure good thermal contact

of the parameter $\frac{m_{sil}}{m_0}$ for the (unsieved) precipitated silica and agglomerated fumed silica (AFS) studied here, of 0.480 (< 1) and 1.13 ($\gtrsim 1$) respectively. This point is crucial to consider when we come to interpret the effects of the film thickness variation.

ESEM requires almost no sample preparation [72]. However, good thermal contact is important between the sample and Peltier stage. For repeatable results, we use a *microapplicator* (figure 7.1). The microapplicator has a groove in the trailing edge. We draw the film out by moving the applicator as shown in the figure. The nominal thickness of this film is then d_0 as shown in figure 7.1, but capillary forces tend to reduce the film thickness somewhat [122]. The microapplicator is 25 mm across, so a stub with a flat top 25 mm square was made, the base was machined to fit snugly into the ESEM Peltier stage (figure 7.1).

Adhesion to smooth metal surfaces is poor in the case of the lacquers studied, so after some work with an uncoated aluminium stub, we switched to a chromated aluminium substrate. The chromate treatment is described in Wernick [123]. For our purposes, the micro-roughness in the chromated aluminium surface promoted adhesion between the lacquer and substrate. A brass stub was made, and the chromated aluminium attached to it by a small bolt in each corner. This bolt also provided electrical earthing for the sample, which (despite the ability of ESEM to image insulating samples) improves contrast. RS heat sink compound was used to improve thermal contact (figure 7.1). We used applicators with nominal thicknesses of 37, 75, 100 and 200 μm to vary the thickness of the films. For *in-situ* film formation, we used a nominal thickness of 200 μm.

7.2

ESEM Experimental

In ESEM we are concerned primarily with optimising three independent parameters: Beam energy, chamber pressure and magnification. Our selection of pressure then gives us the operating temperature by reference to the saturated vapour pressure (SVP) line for water (figure 7.2). We now consider each parameter in turn.

The key result from chapter 5 was that we should seek to minimise the beam energy to reduce beam damage, especially for repeated scans of the same area. Unfortunately we are limited by the loss of signal at low beam energy (less than 5keV), by probe beam scattering in the gas, so here we use 8keV. We have shown in figure 5.1 that this energy reduces damage significantly, compared to 12 keV.

Our next consideration is the chamber pressure and temperature. Clearly the temperature must exceed the minimum film-forming temperature (MFT) of the latex, or we will not observe film formation. This is listed by the supplier as 0°C [59]. However the MFT is not necessarily enough, as we shall see when we discuss the results of this work.

The lacquer is designed for use in ambient conditions, and ideally we would like to replicate these in the ESEM. Of course this is not possible, as we have seen in chapter 4 section 4.1 that the probe beam scattering limits ESEM to a maximum pressure of around 10 torr. Above around 10 torr, so many electrons are scattered into the skirt that the signal to background ratio is too low to produce images of sufficient quality.

Therefore we use a pressure of 7.5 torr, which gives a temperature of around 7.0°C from the saturated vapour pressure line (figure 7.2). As we intend to use quite a high chamber pressure we require a small working distance. This minimises the loss of signal associated with the beam skirt. In practice we have typically 1mm between the sample and the detector.

We select the magnification such that the largest features are well below the image size. The largest silica particles are typically around 10 μm across, so an image of side 140 μm is used. We therefore expect each image to be representative of the whole sample, so that

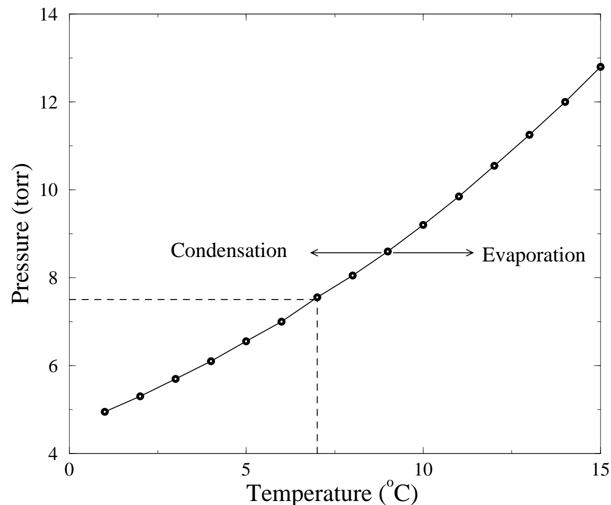

Figure 7.2: Saturated Vapour Pressure Line for water, reproduced from chapter 4. The condensing and evaporating regimes are shown. Dotted lines show our conditions: 7.0° C and 7.5 torr.

images from different locations are similar. This corresponds to an original magnification of 800×, which we use for all ESEM work, unless otherwise stated.

Here we describe our experimental technique for drying experiments, applying the considerations above. It should be stressed that drying in ESEM was experimentally difficult to reproduce. The lacquer frequently dried too rapidly, leading to shrinkage and cracking. The cool conditions required (7°C) also tended to promote cracking. We begin by developing our optimised pumpdown.

Optimised pumpdown

We have not yet considered the effect of the pumpdown, the initial removal of air from the sample chamber. During this period, the partial pressure of water vapour (around 12 torr at room temperature and 50% relative humidity) [124] is reduced by a factor of around 100 during the pumpdown from 760 torr to 7.5 torr. In this analysis we draw heavily on previous work by Cameron *et al.* [72].

This initial pumpdown can be very important in the case of latex suspensions, as the low water vapour pressure causes a high evaporation rate. In fact there is a risk of

all the water evaporating prior to imaging in thin latex suspensions. We can offset this evaporation in two ways. Reducing the sample temperature by around 0.5° C decreases the evaporation rate, and ensures that the total chamber pressure (air and water vapour) does not fall below the sample SVP, which would result in boiling.

Secondly, if we add a drop of water on a part of the stage which is not chilled, then this will evaporate preferentially to the sample during pumpdown due to its higher temperature. The increased partial pressure of water vapour will then help to reduce evaporation from the sample. Since Cameron *et al.* did not consider this additional source of water vapour, we extend their work to include it, applying our values of chamber pressure and sample temperature to their model.

Extending the model of Cameron *et al.*

Here we review the main features of the approach of Cameron *et al.*[72]. ESEM pumpdown consists of three stages. Initial pumpdown, flooding with water vapour and further pumpdown. The last two stages are repeated several times. Here we use eight flood/pumpdown cycles. Finally the chamber is left in equilibration mode, where residual air is gradually replaced with water vapour.

The pressure regime in each stage was described as follows. In pumpdown, the air pressure P_a and water vapour pressure P_w in the chamber reduce exponentially at the same rate, so

$$\frac{d}{dt}P_a(t) = -k_1 P_a(t) \tag{7.1}$$

$$\frac{d}{dt}P_w(t) = -k_1 P_w(t) \tag{7.2}$$

where k_1 is the time constant of the pumping system. In the flood mode, there is a residual pumping, with time constant k_3, such that

$$\frac{d}{dt}P_a(t) = -k_3 P_a(t). \tag{7.3}$$

The change in water vapour pressure is given by

$$\frac{d}{dt}P_w(t) = -k_3 P_w(t) + k_2 \left(X(T_r) - P_w(t) - P_a(t)\right), \tag{7.4}$$

where $X(T_r)$ is the SVP of water at the water vapour temperature, which we take as room temperature T_r, k_2 is the flooding time constant.

During equilibration, the overall chamber pressure, $P_c(= P_a + P_w)$ is constant, but the residual pumping continues to remove the air, so

$$\frac{d}{dt}P_a(t) = -k_3 P_a(t). \tag{7.5}$$

To maintain a constant chamber pressure, this removal of air is compensated for by introduction of water vapour,

$$\frac{d}{dt}P_w(t) = k_3 P_a(t). \tag{7.6}$$

The time constants k_1, k_2 and k_3 clearly depend on the type of ESEM used. They also vary over time, depending on the efficiency of the pumps, flooding water temperature and a number of other parameters. Changes in ambient relative humidity also effect this pumpdown behaviour. Therefore we seek to determine a typical behaviour, rather than an absolute prediction. Here we set relative humidity to 50%, room temperature to 25°C, and use the k values determined by Cameron *et al.* [72]. These are listed below.

$k_1 = 0.07\ \mathrm{s}^{-1}$

$k_2 = 0.02152\ \mathrm{s}^{-1}$

$k_3 = 0.00097\ \mathrm{s}^{-1}$.

Cameron *et al.* determined the rate of water evaporation by a sample, according to the following relation,

$$\frac{d}{dt}m_e = \left(\frac{k_B T_s}{2\pi m}\right)^{\frac{1}{2}} \rho_w exp\left(-\frac{\epsilon}{k_B T_S}\right) \tag{7.7}$$

where $\frac{d}{dt}m_e$ is the change in the mass of the water sample, k_B is Boltzmann's constant, m is the mass of a single water molecule, ρ_w the density of water, ϵ the latent heat of vaporisation of a single water molecule and T_s the sample temperature. We calculated the value of $\frac{\epsilon}{k_B}$ to be around 3180 at 7.5° C for values listed in Kaye and Laby [124]. We assumed a surface area of 1cm^2 to determine mass lost from the sample.

Equation 7.7 allowed us to determine the effect of a water source on water vapour pressure during pumpdown. By assuming a surface area of 1 cm^2 and a specimen chamber volume of 8×10^{-3} m^3, we could determine the contribution to the partial water vapour pressure from the evaporating water source. We assumed that the water drop evaporated throughout the initial pumpdown, but had no effect thereafter. In effect the drop had totally evaporated at the end of the initial pumpdown. We assumed the surface area and temperature (T_r) of the water source were constant.

Optimised pumpdown with a water source

The total chamber pressure is shown in figures 7.3*(a)* and *(b)* as a thick dotted black line in each case. Comparison with the water vapour shows that with the water drop, we need only three flood and pumpdown cycles until the chamber atmosphere is almost entirely water vapour (figure 7.3*(a)*). Without the water source, we need rather more cycles to achieve a satisfactory fraction of water vapour, as found by Cameron *et al.* [72] (figure 7.3*(b)*). We also see a strong decrease in water vapour pressure during the initial pumpdown without a water source. The pumpdown is slowed when we have a water source, as the pumps must remove the additional water vapour from the sample chamber.

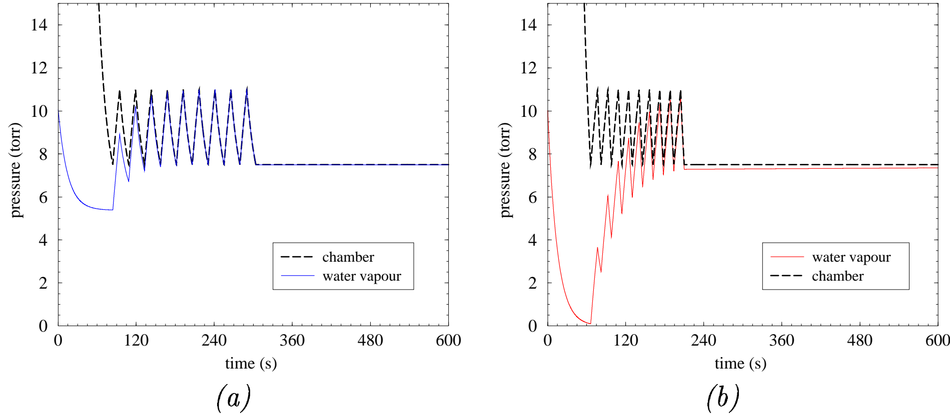

Figure 7.3: Pressure as a function of time during our optimised pumpdown with (a)*, and without* (b) *a water source in the sample chamber*

The rate of flooding is also slowed, due to the reduced rate of water evaporation in the flooding process at higher water vapour pressure.

In practice the behaviour is somewhere in between these two regimes, as it is very hard to put such an exact amount of water into the sample chamber. It is important to ensure that the additional water source evaporates completely during pumpdown. Any residual water will alter the equilibration rates, because it continues to evaporate in equilibrate mode due to its higher temperature. This forces the pumps to work harder to maintain the equilibrium, which can result in the main rotary pumps being activated, altering the chamber pressure significantly. Such pressure fluctuations effect the imaging process through the SE cascade and can cause sample boiling in extreme cases.

The two pressure regimes are reflected in the evaporation rates, figures 7.4*(a)* and 7.4*(b)* with and without a water source respectively. We see that the initial pumpdown results in the highest rate of evaporation in both cases, but that this is very much reduced with a water source in the sample chamber. It is clear that much less of the sample will evaporate if we have a water source. Note that the suppressed sample temperature (6.5° C) results in condensing water ($\frac{dm_e}{dt} > 0$) at long times.

To remove the condensed water, we gently increase the temperature of the sample until we identify silica in our images. It is very hard to image our latex spheres, because they are both film-forming and relatively small. Film-forming latices do not exhibit much

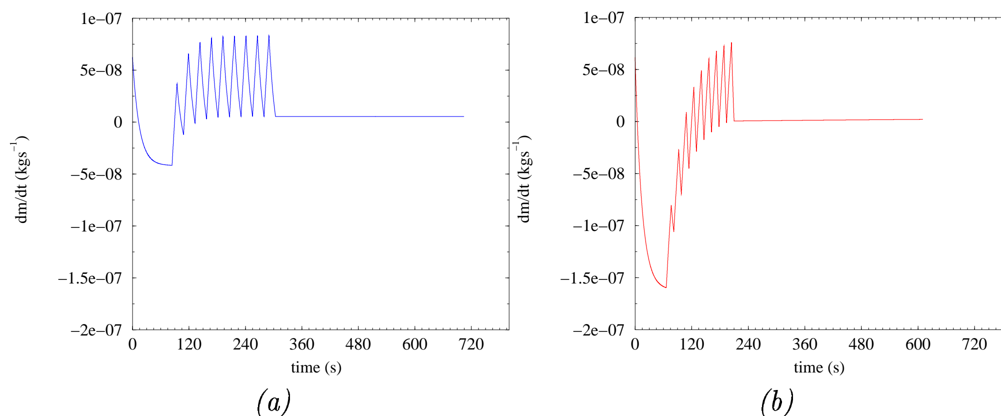

Figure 7.4: Rate of change of sample mass (equation 7.7) as a function of time with (a), *and without* (b) *a water source. This assumes a sample area of 1cm*^{2}.

surface topography, because they deform concurrently with water evaporation (see chapter 2, figure 2.1 and page 10) so there is little contrast in ESEM. So we record the drying sequence from the first image in which we can detect silica, which gives us a somewhat arbitrary starting point.

Our rate of temperature increase is important. We need to raise the sample temperature, because at the end of our pumpdown procedure the sample is on the condensing side of the SVP line (figure 7.2). There is a time lag between the set-point and the actual sample temperature, so we risk overheating the sample and causing boiling if we heat it too quickly. If we increase temperature very slowly, we will simply condense large amounts of water, diluting the latex enormously. This entirely changes the formulation! Typically we increase the temperature by around 0.1°C per minute until we can detect silica, and then leave the temperature unchanged.

Drying outside the ESEM

The films of varying thickness were all dried prior to imaging. These samples were dried at ambient temperature in a dessicator with phosphorous pentoxide dessicant. We used a chromated aluminium substrate. The lacquer was left for 24 hours to dry. Although interdiffusion (stage IV) was unlikely to be complete by this time, it occurs below the lengthscales we are interested in ($\gtrsim 1\mu$m), so for our purposes it is reasonable to regard

the film as formed after this time. Here we use the same imaging conditions as for the drying experiments, 8keV beam energy and 7.5 torr chamber pressure, and as small a working distance as is practical, typically 7mm which corresponds to ~1mm from the detector to the sample. As the films were already formed, we did not need an optimised pumpdown procedure. The chamber was simply pumped to 1 torr and flooded to 10 torr twice, and then set to 7.5 torr for imaging.

All samples for subsequent experiments have been prepared in this way, unless otherwise stated. All ESEM work in this chapter has been carried out on an Electroscan 2010 fitted with a tungsten filament and GSED detector.

7.3

Film formation results

Here we discuss the results from film formation experiments carried out as described above. Selected images from two drying experiments are shown in figures 7.5 and 7.6 for precipitated silica and AFS respectively. In both cases we see the transition from a rather featureless aqueous dispersion to a film which we regard as 'dry', where silica appears as bright compared to the polymer background. Upon removal from the ESEM, the film was indeed dry as we discuss below. There is a significant difference between the precipitated and fumed silicas (figures 7.5 and 7.6 respectively). The AFS has a more uniform appearance, whereas the precipitated silica has a wider particle size distribution.

We see that individual silica particles in both sequences become easier to distinguish with time. For example the particle marked as *(a)* in figure 7.5 grows larger and brighter at longer drying times. Examination of this region shows some movement between the frames in figure 7.5 taken at 15 and 59 minutes. This is a result of non-uniform drying leading to shrinkage and/or specimen drift. This sample was cast on non-coated aluminium, so we would expect the adhesion to be relatively poor.

In figures 7.5 and 7.6, the polymer background becomes darker with time. We attribute this to water loss. Recall that in chapter 4 we associated a bright signal with the high band-gap electronic structure of water [74].

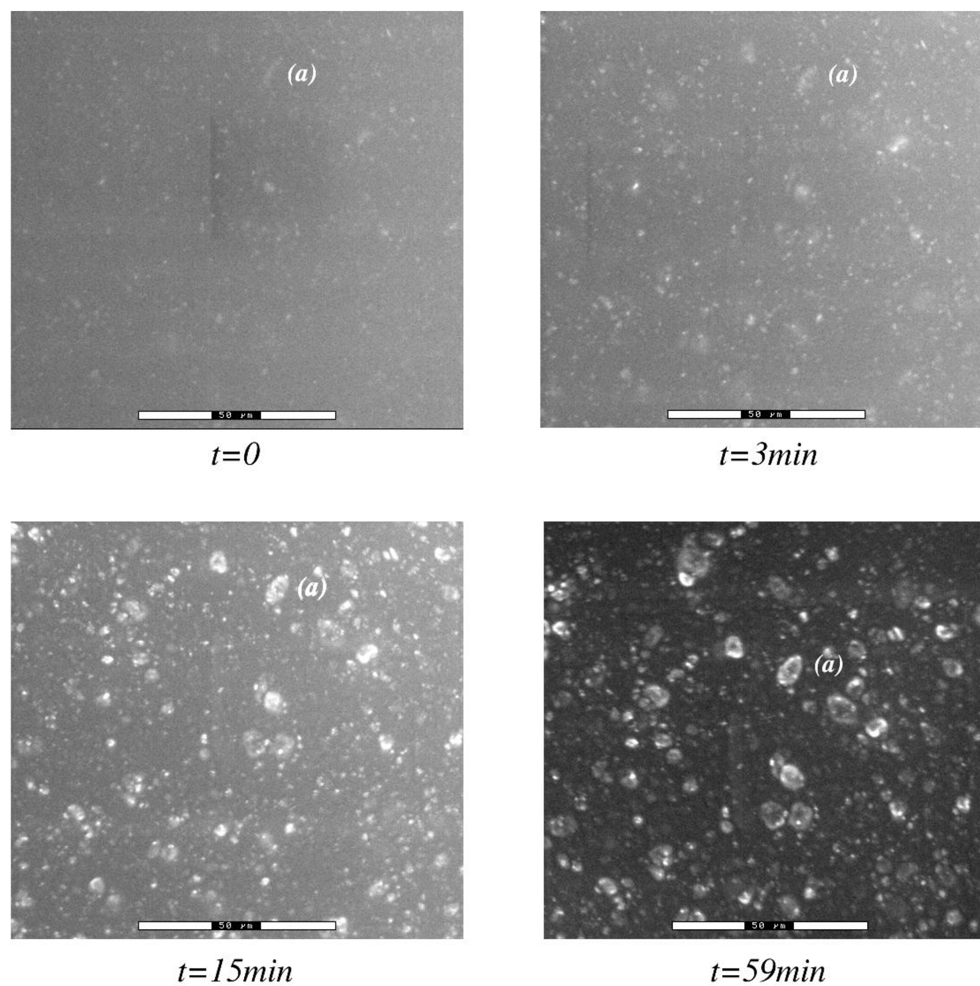

Figure 7.5: Film containing precipitated silica drying in-situ *in the ESEM. From an aqueous dispersion, the film dries to reveal silica particles. The area* (a) *shows how an individual particle is revealed with time.*

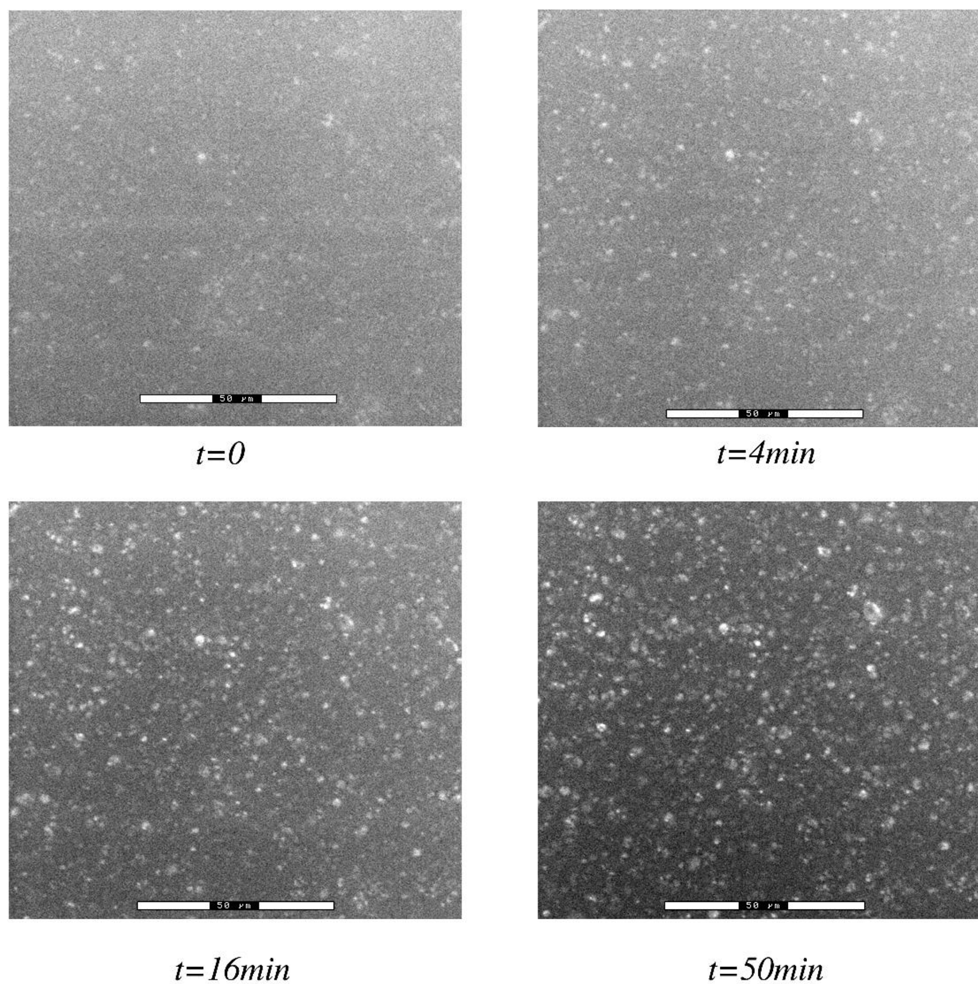

Figure 7.6: Film containing AFS drying in-situ *in the ESEM. Like figure 7.6 there is a general darkening with time, which is interpreted as loss of water.*

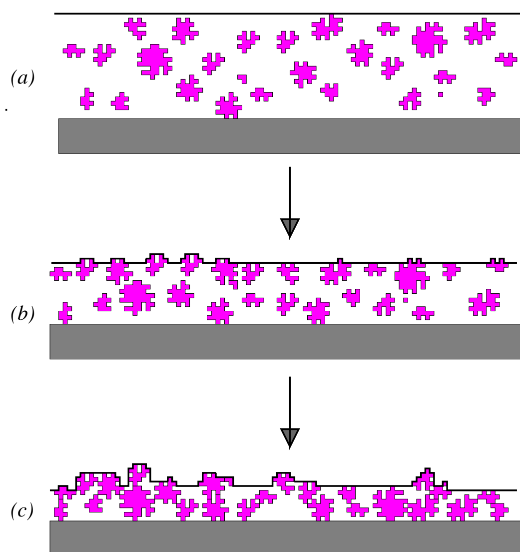

Figure 7.7: Schematic of silica in film forming aqueous lacquer. Stage I of latex film formation corresponds to (a)*, where the silica is dispersed throughout the aqueous latex suspension.* (b) *and* (c) *are the results of volume loss from water evaporation, and correspond to stages II and III or II* of latex film formation (figure 2.1)*

A schematic of this film formation process is shown in figure 7.7. Film formation is here driven by volume reduction from water evaporation. Initially in figure 7.7*(a)*, we have an aqueous suspension with no structure accessible to ESEM. As water evaporates, silica begins to perturb the surface and we expect to be able to image this structure with the ESEM (figure 7.7*(b)*).

Finally all the water is removed and we have the dried film, in the sense that the volume reduction due to water evaporation is complete. This process covers the latex film formation process of chapter 2 section 2.1 from stage I to stage III or II*. In fact (and here lies a key weakness of the ESEM method) we believe the films dried only to stage II* inside the ESEM. Upon removal, the samples were not transparent. Where dried at ambient temperatures, these samples were transparent (this topic is further discussed in chapter 9).

An opaque latex is characteristic of stage II*, where the voids between latex particles have not had time to close as we discussed in chapter 2 page 10 [18] [19] [33]. It is reasonable that this reduction in temperature to 7°C could slow the rate of deformation enough that our latex could change from being film-forming at room temperature to non

film-forming at ESEM temperature at least on a timescale of one hour. Although the MFT is quoted as 0°C, this may assume a longer film formation time than we used. However since the lengthscale of the latex and its interstitial voids is less than that of the silica, we nonetheless proceed with our analysis.

Numerical Analysis

In this section we extract numerical information from our images, enabling further analysis. We have explained in chapter 6, section 6.3 our procedure for obtaining the fraction of pixels in an image corresponding to silica from an ESEM image.

Here we use a gradient threshold of 15 and our standard brightness threshold of 245. To re-cap, this means that any pixel of brightness greater than 245 is taken to be silica along with any pixel in the Sobel gradient image with a value greater than 15. We use one pass of the Gaussian blur kernel (chapter 6, page 100) to reduce noise.

The fraction of pixels identified as silica (silica surface fraction) is plotted against film formation time in figures 7.8*(a)* and *(b)* for AFS and precipitated silica respectively. In all cases we see an increase in silica surface fraction with time, as we would expect, although the precipitated silica shows large variation between the two data sets. We assume that this results from slightly different experimental parameters. Here solid data points correspond to an uncoated aluminium substrate, unfilled points to a chromated substrate.

The different slopes of the data in figure 7.8*(a)* are indicative of variation in evaporation rates. The evaporation rate is hard to control precisely in ESEM. The drop in the two data points marked as *(h)* in figure 7.8*(b)* is assumed to be sample movement. This data set was produced from the sequence of images shown in figure 7.5 and we have already noted some movement in this data.

We can also determine the number of clusters corresponding to silica particles in an image as figure 7.9*(a)* and *(b)* show for AFS and precipitated silica respectively. In all cases, this number increases with time, rather more quickly than the surface silica fraction. In other words, all the silica particles present on the surface are identified quite early, after around 10min. Further drying tends to expose more of these same particles, so the number of clusters in the image stays roughly constant, but the total area of silica continues to

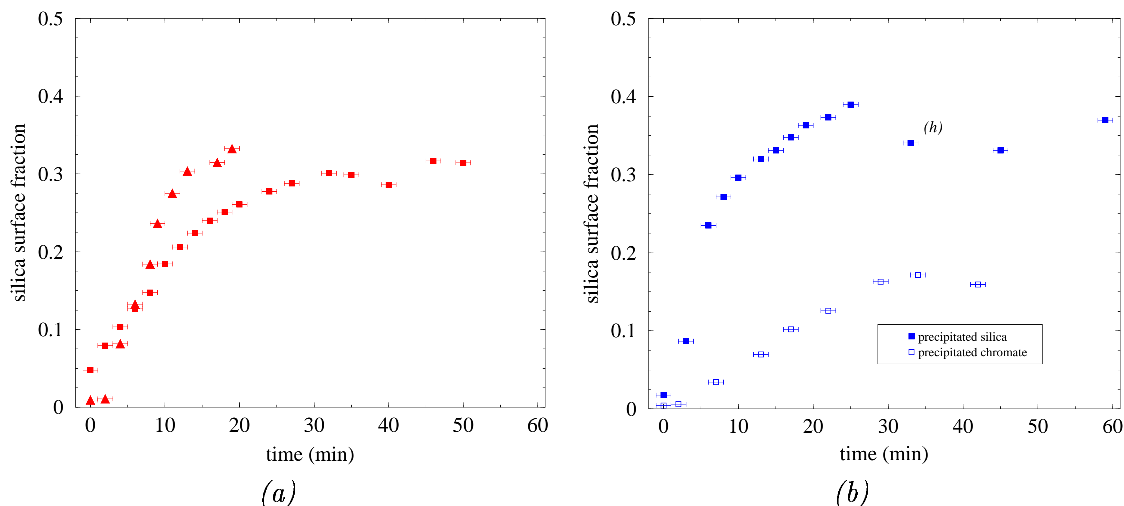

Figure 7.8: Silica surface fraction as a function of drying time (a) *AFS and* (b) *precipitated silica, on uncoated aluminium (filled symbols) and chromated aluminium (unfilled symbols) substrates.*

increase.

The small peak marked *(h)* in figure 7.9*(a)* gives an example of the difference between silica *particles* and *clusters*. When more of the particles are revealed, it can occur that what were once identified as separate clusters are in fact part of the same particle, so the total number of clusters falls off with time. We interpret the small peak *(h)* in 7.9*(a)* in this way.

7.4

Film thickness results

ESEM images of films prepared with differing thicknesses are shown in figure 7.10. These images are similar to those in figures 7.5 and 7.6 for long times. Again silica is bright contrasting with darker polymer background. Precipitated silica is shown in *(a)* and *(c)*, AFS in *(b)* and *(d)*. In the case of the precipitated silica, the change from a wet film thickness d_0 of 37 μm (figure 7.10*(a)*) to $d_0 = 200$ μm *(c)* is not too significant.

By contrast the AFS has a very different appearance between $d_0 = 37$ μm (figure

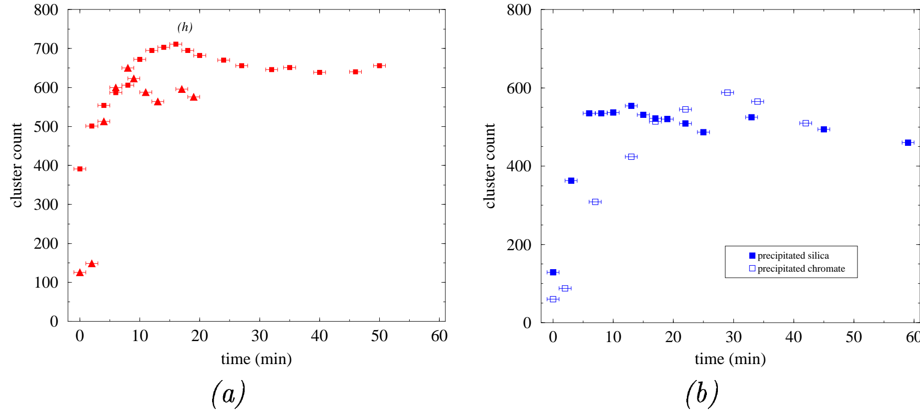

(a) *(b)*

Figure 7.9: Cluster count as a function of drying time (a)*AFS and* (b) *precipitated silica, on uncoated aluminium (filled symbols) and chromated aluminium (unfilled symbols) substrates.*

7.10*(b)*) to $d_0 = 200\ \mu m$ *(d)*. Large regions of silica are evident in figure 7.10*(b)*, which are absent in the case of a thicker film which also has a more uniform appearance. This difference is due to the fact that in figure 7.10*(b)*, the dry thickness of the film is of order $10\ \mu m$, since the wet thickness is $\sim 37\ \mu m$. Given the solids content of 0.35, we expect a roughly threefold weight reduction during film formation, from the similar density of the wet and dry films. Now this $10\ \mu m$ thickness is comparable to the size of the silica particles, so they may be squeezed between the film surface and the substrate during drying. Conversely in the thicker film, the silica particles have rather more space in which to pack during film formation, and so need not perturb the surface of the dried film as much.

Here we recall that the precipitated silica sample has $\frac{m_{sil}}{m_0} = 0.480 < 1$ and the AFS has $\frac{m_{sil}}{m_0} = 1.13 \gtrsim 1$ in these experiments. This interpretation is shown schematically in figure 7.11. Figure 7.11*(a)* corresponds to figure 7.10*(a)*. 7.11*(b)* to 7.10*(b)* and so on. In the case of the low silica concentration (figure 7.11*(a)* and *(c)*), we see that in both cases there are isolated silica particles perturbing the surface, and that there is little change in the *surface* between the thin and thick films. This is borne out in figure 7.10*(a)* and *(c)* where there is little film thickness effect on the surface.

Conversely in the higher silica concentration, figure 7.11*(b)* and *(d)* we may have the network disrupted because the silica is not uniformly distributed. Instead, some regions

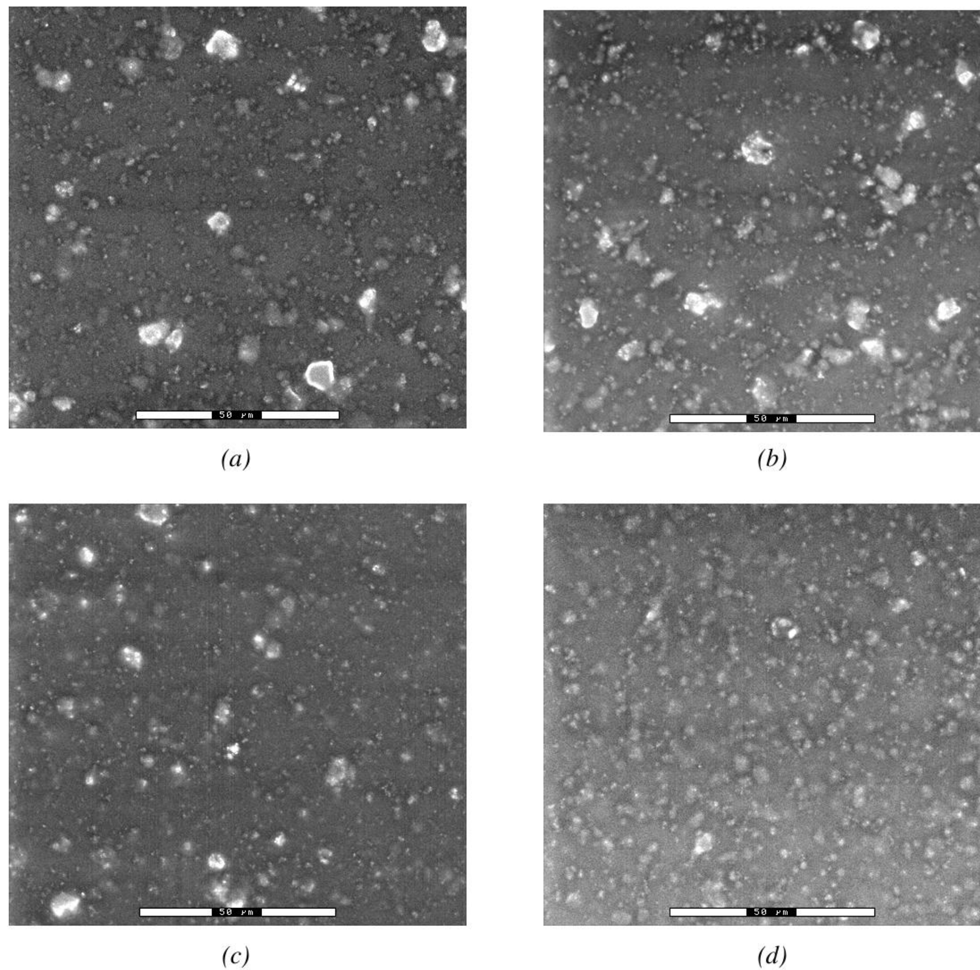

(a) *(b)*

(c) *(d)*

Figure 7.10: Film thickness variation in the ESEM. Precipitated silica (a) $d_0 = 37\mu m$ *and* (c) $d_0 = 200\mu m$ *and AFS* (b) $d_0 = 37\mu m$*and* (d) $d_0 = 200\mu m$. *Although the precipitated silica shows little change, the AFS surface is strongly influenced by film thickness. Bar =* $50\ \mu m$

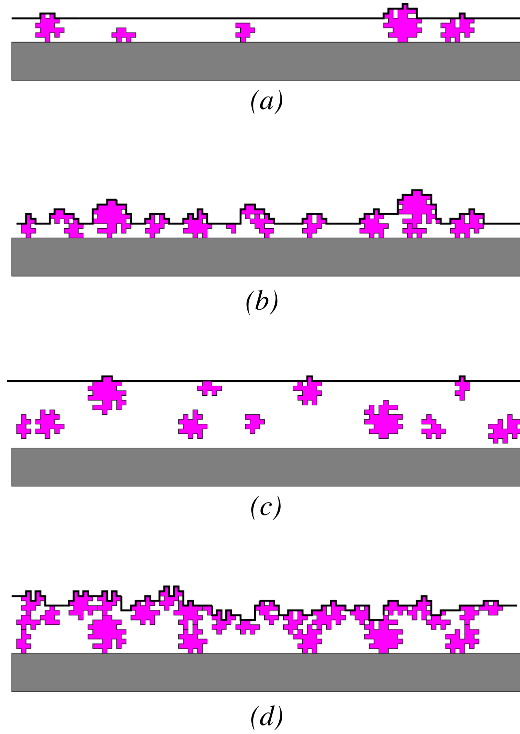

Figure 7.11: Schematic of film thickness variation. (a) *'thin' film for* $\frac{m_{sil}}{m_0} < 1$, (b) *'thin' film for* $\frac{m_{sil}}{m_0} \sim 1$, (c) *'thick' film for* $\frac{m_{sil}}{m_0} < 1$ *and* (d) *'thick' film for* $\frac{m_{sil}}{m_0} \sim 1$

are silica-rich, whereas others are devoid of silica. We expect this to happen if the size of the silica particles is comparable to, or exceeds, the film thickness. So the thin films have large silica particles and spaces between them, and the thicker film have a more uniform structure as shown in figure 7.11*(b)* and *(d)*.

A further argument relating to this work is the mechanical behaviour of the silicas. Precipitated silica is quite robust, but we expect AFS to collapse rather than break the surface during its film formation. This stems from the mechanical properties of the silicas, AFS aggregate particles are only loosely held through hydrogen bonding, whereas precipitated silica is more firmly bound through covalent bonding (chapter 2 section 2.3). So the surface of the thicker AFS film (figure 7.11*(d)*) is quite uniform due to the collapsed silica structure, but in the thin film case *(b)* collapse may be limited by strong local fluctuations in concentration. Specifically, silica-rich regions may be too concentrated for complete collapse, so we see the partially collapsed particles perturbing the film surface.

We also note that these large particles in figure 7.10*(b)* are typically quite bright.

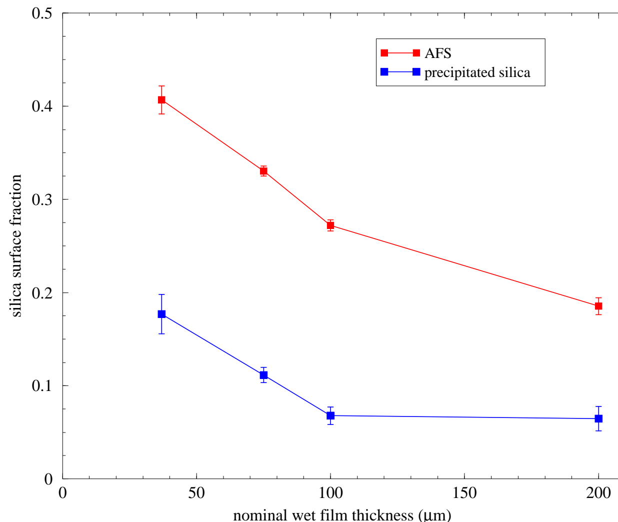

Figure 7.12: Silica surface fraction as a function of film thickness. The increased value for AFS reflects its higher $\frac{m_{sil}}{m_0}$ *value*

This suggests that there is increased surface roughness in these regions, in contrast to the collapsed, polymer-covered structure in *(d)* which has comparatively few bright features. We develop these concepts further and present evidence for polymer coverage of 'surface' silica in the next chapter.

Numerical Analysis

Here we extract our quantitative measures from the images in figure 7.10. We use the same parameters as above for the film formation data. Numerical analysis shows us some interesting trends. Each point on these plots is the mean from typically six samples, with the error bars the standard error.

The surface silica fraction falls off for both AFS and precipitated silica with increasing film depth (figure 7.12). At all depths the AFS has a higher silica surface fraction than the precipitated silica. This we relate to the higher value of $\frac{m_{sil}}{m_0}$, corresponding to a greater bulk volume of silica, which we discuss in detail in the next chapter. In thicker films, the silica particles have more freedom to pack so that they remain within the film and do not perturb the surface. So the decrease in silica surface fraction with increasing film depth is not unreasonable. We also note that the error bars in surface silica fraction are quite

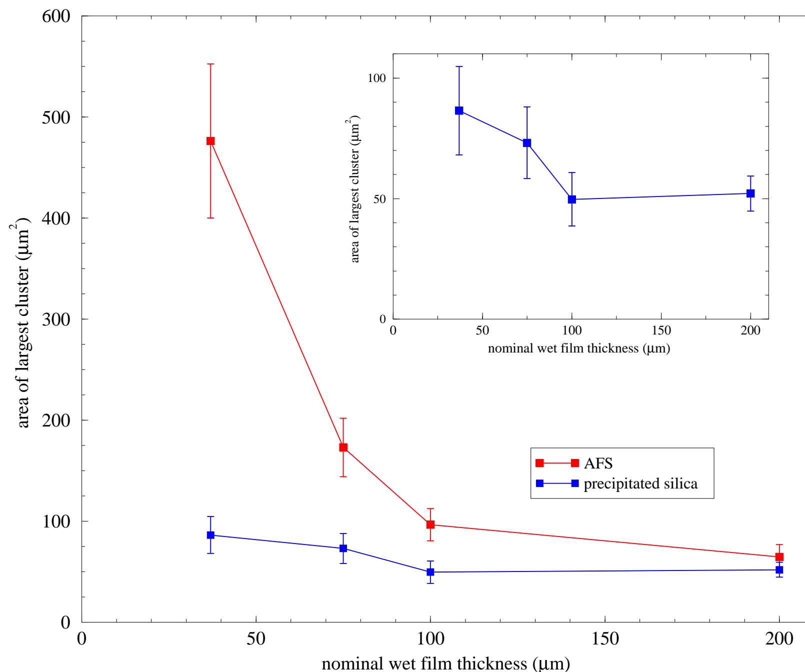

Figure 7.13: Maximum cluster area as a function of film thickness. Inset re-plots the precipitated silica data with an expanded vertical scale.

small, showing little variation in the data. This suggests that the film surface is fairly uniform, as each image is taken from a different area. So a single scan may be taken as representative of the sample, although we typically take six scans per sample.

We can also determine the area of the largest cluster in each image (figure 7.13). We see the dramatic decrease in large cluster area for AFS, in accord with the images and our discussion on surface perturbation in thin films. However the very large AFS particles could be neighbouring particles treated as one single particle by the image analysis software. The expanded scale shows that precipitated silica also exhibits the same trend, although rather less dramatically.

If we count the clusters, we have two competing trends. The cluster area (at least for large clusters) reduces with increasing film depth, so we expect the number of clusters to rise for a given surface silica fraction. However the surface silica fraction falls as a function of film depth, reducing the number of clusters, for a given cluster size. In the case of AFS, the size reduction dominates, so the count rises with depth, as shown in figure 7.14. In precipitated silica however, it is the other way around, as the cluster size reduction is

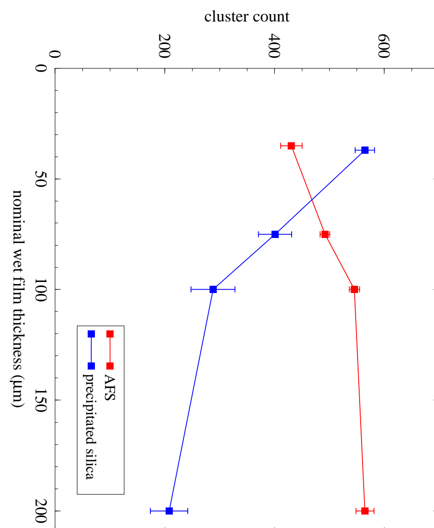

Figure 7.14: Cluster count as a function of film thickness. The competition between cluster area and surface silica fraction leads to different behaviour between the two silicas.

much less marked. Consequently the number of clusters falls off with film thickness.

7.5

Conclusions

In this chapter we have seen how ESEM may be used to image the lacquer drying *in-situ*. These experiments required a special pumpdown procedure, which minimises sample evaporation in the initial pumpdown. We have shown that the inclusion of a water source in the sample chamber significantly reduces evaporation during pumpdown.

Our results show that film formation is a gradual process from an aqueous suspension, producing little contrast in ESEM (stage I in latex film formation) to a dry film in which we can distinguish silica. However we do not believe that the film formation process is complete, as the samples were opaque upon extraction from the ESEM. This is indicative of stage II*, which we put down to the cool film-formation conditions in the ESEM. We have interpreted the results in terms of the silica structure model developed in chapter 3. We have also analysed our results numerically. Although these numbers can only really

be treated as semi-quantitative due to variation in experimental parameters, they provide good insight into film formation for matt water-based lacquers. In particular we see that the number of silica particles on the surface rises quickly, with further increase in drying tending to reveal more of these same particles.

We have also investigated the effect of film thickness. The quantitative results here are rather more accurate, and we will see that they are consistent with further work. The surface silica fraction reduces with increasing film depth, suggesting that in deeper films, more of the silica is concealed as it has more space in which to arrange itself.

In thin films, we see that the silica distribution is less uniform, leading to local fluctuations in concentration. This occurs when the film thickness falls below the size of the large silica particles, and is much more marked in the case of AFS. So we see large particles in the thin film, which are hidden in thicker films. This means that we actually see a greater number of distinct clusters in thicker films with AFS.

From this chapter, we conclude that

(1) We have improved the optimised pumpdown procedure of Cameron *et al.* [72] for hydrated samples sensitive to water evaporation.

(2) ESEM can follow one region of lacquer throughout film formation, although it is limited to stage II* here.

(3) During film formation the tops of silica particles are revealed first by the receding latex matrix.

(4) Film formation can be interpreted in terms of the silica structure model.

(5) Reducing the film depth to a lengthscale similar to the silica particles strongly influences their packing.

(6) despite generic similarities, AFS and precipitated silica show different surface morphologies.

Chapter 8

Testing the Silica Structure Model

In this chapter we discuss the verification of our silica structure model (chapter 3). We re-cap on the main predictions of the model, and explore how the microscopy techniques may be used to probe various properties of the model.

We then describe the results and, where appropriate, the methodology of each experimental technique. Particular attention is paid to fluorescent labelling of silica for confocal microscopy and image analysis techniques for percolation phenomena, as discussed in chapter 6, section 6.4.

8.1

Model Predictions

So what are the key predictions of the model and how may we access them? The fundamental assumption is that at some critical mass fraction of silica (which we denoted by m_0), the bulk volume of silica powder equals the volume of dried lacquer (polymer and silica). We would expect to find a percolating silica structure at our critical silica loading, where $\frac{m_{sil}}{m_0} = 1$. This is shown schematically in 2D in figure 8.1*(b)* (reproduced from chapter 3). In reality, we have percolation in 3D so our 2D representation is schematic.

Percolation is necessary but not sufficient for the self-supporting structure, which exists in the dry powder and corresponds to $\frac{m_{sil}}{m_0} = 1$. In other words, the packing at the

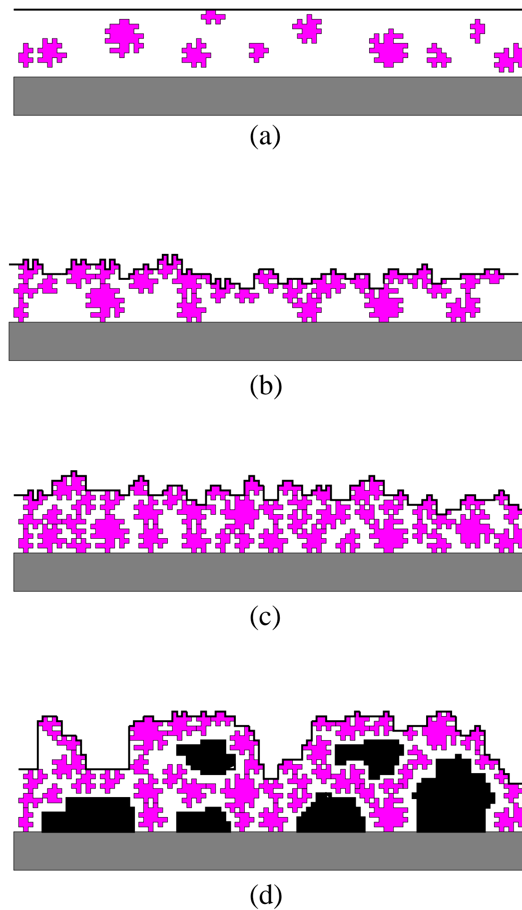

Figure 8.1: Schematic of the model of silica structure within dried lacquer reproduced from chapter 3. The low concentration regime (a) ($\frac{m_{sil}}{m_0} < 1$), critical mass of silica (b) ($\frac{m_{sil}}{m_0} = 1$), and two possibilities for $\frac{m_{sil}}{m_0} > 1$, with silica densification from a collapsing silica structure (c), or increased surface roughness and possible void formation with more robust silica (d).

percolation threshold need not be as dense as in the dry powder. So we may see the percolation threshold at a lower silica loading than the critical mass, $\frac{m_{sil}}{m_0} = 1$.

Below the percolation threshold, we expect the silica particles to be isolated, as shown in figure 8.1*(a)*. In this regime, and for $\frac{m_{sil}}{m_0} \lesssim 1$, we have

$$\phi \approx p\frac{m_{sil}}{m_0}, \tag{3.10}$$

where ϕ is the silica volume fraction, corresponding to silica particles and internal pores, and p is a packing fraction.

At high $\frac{m_{sil}}{m_0}$, we have two extremes. Densification (figure 8.1*(c)*) occurs when the silica structure collapses during film formation. Here we expect equation 3.10 to hold for $\frac{m_{sil}}{m_0} > 1$, but of course $\phi \leq 1$, so the linear behaviour of ϕ with respect to $\frac{m_{sil}}{m_0}$ will be limited. Alternatively the silica may have sufficient mechanical strength that above $\frac{m_{sil}}{m_0} \approx 1$ no collapse occurs, figure 8.1*(d)*. This second case corresponds to a transfer from silica supported by the film (figure 8.1*(a)*) to polymer adhering to a robust silica structure. Here we expect a dramatic increase in surface roughness, which may be accompanied by air voids (shown in black in figure 8.1*(d)*) on the scale of the silica particles. This surface roughness behaviour and void formation correlates with the critical pigment volume concentration (CPVC) model of Asbeck and van Loo [48].

Accessing the model

We now consider how the various predictions may be accessed using microscopy. The bulk technique of CLSM is central to verifying our model. By finding the silica volume fraction ϕ as a function of $\frac{m_{sil}}{m_0}$ we can test equation 3.10. Here we expect a uniform increase in ϕ with $\frac{m_{sil}}{m_0}$, given that $\phi \leq 1$. ϕ is simply the fraction of pixels identified as silica in a given image, so it is easy to obtain through segmentation. By segmenting each horizontal slice separately, we can also obtain the depth profile of the silica volume fraction, $\phi(z)$. In particular this will tell us if the silica is randomly distributed, as we have assumed or if there is some surface segregation.

We can also explore percolation phenomena. Using the cluster labelling methods discussed in chapter 6, page 93, we can determine whether a single cluster spans the image, by comparing different cluster labels on each side of the image. Testing for percolation at different $\frac{m_{sil}}{m_0}$ allows us to identify the threshold.

We also investigate percolation by counting the labelled clusters. At low silica volume fraction, ($\frac{m_{sil}}{m_0} < 1$) we expect isolated particles and that the number of clusters should be linear in $\frac{m_{sil}}{m_0}$. As the silica volume fraction increases we find clusters correspond to two or more silica particles. The number of clusters thus rises more slowly as a function of $\frac{m_{sil}}{m_0}$, eventually reaching a peak. At high $\frac{m_{sil}}{m_0}$, almost all the silica particles are joined, so the count should approach unity [58].

We now consider the cluster with most pixels. Here we expect a dramatic increase in the number of pixels around the percolation threshold. As we work at constant magnification, we can evaluate this number of pixels in μm^3 as the pixel volume is $1.7 \times 10^{-3} \mu\text{m}^3$ for the set-up chosen. We can also determine the radius of gyration, R_g, of the largest cluster. Like the volume of the largest cluster, the radius of gyration should increase sharply at the percolation threshold. R_g should be limited by a value characteristic of the system size.

These percolation phenomena can be simulated, by randomly populating a cubic lattice. Treating this lattice as an image, we can determine cluster counts and maximum cluster size, and then compare with the experimental data. Of course we expect some differences, as we randomly populate the lattice with single pixels, whereas the silica particles occupy many pixels and are not cubic in shape.

At first glance it may seem that we only need confocal microscopy to test our model. Not so. The surface techniques of AFM and ESEM each have vital contributions to make. First, we expect surface roughness to increase sharply around the point where the silica structure is formed. Compare the flat surface of figure 8.1*(a)* and the roughened surface in *(b)* along with that in *(d)*. We expect to differentiate this behaviour with ESEM and particularly AFM.

A further and more subtle consideration requires the use of surface techniques. Confocal microscopy requires highly transparent samples. Franklin's work showed that this certainly depended on the type of silica used, with agglomerated fumed silica (AFS) being

especially transparent (low haze in the parlance of Franklin)[17]. Now silicas exhibiting lower transparency produce poorer quality images with confocal microscopy, which is especially apparent at high silica concentrations, so it is hard to extract the silica structure for these samples. We explore the optical properties in more detail in chapter 9.

ESEM by contrast can image almost any sample, so we can analyse the surface of any dried film containing silica. Analysis of ESEM images gives us a measure of the surface silica fraction. As we have based our model on bulk silica volume fraction, we can see if silicas of differing densities have the same behaviour and test this volume dependence assumed in the silica structure model.

8.2

Confocal Methodology

To image silica in the confocal microscope, we need to label it with a fluorescent dye. We have worked with two dyes and tested a variety of labelling techniques, which we discuss here.

We noted in chapter 2, page 16 that the silica surface is negatively charged in aqueous suspension. This would suggest labelling with rhodamine 6G, a cationic dye in the form of a chloride salt. Rhodamine is readily soluble in water, which has two effects: *(i)* labelling the silica is trivial, as we simply disperse the silica in rhodamine solution instead of water prior to mixing, *(ii)* the dye leaches into the aqueous solution, so when the film is formed, the polymer is also labelled. Although the silica and polymer are easy to distinguish, the labelled polymer creates an undesirable background signal. However we use this labelling of both silica and polymer to our advantage in the next chapter.

Here we instead use fluorescein iso-thiocyanate (FITC) obtained from Molecular Probes, which labels only silica [125]. FITC in the polymer matrix does not produce a strong fluorescent signal. Since FITC is only sparingly soluble in water, a variety of methods were investigated to introduce enough FITC to the lacquer to give a strong signal. FITC dissolves readily in alkaline solution and a variety of organic solvents so we prepared samples by dissolving FITC in dilute sodium hydroxide, ethanol and acetone. In each case, the

silica was mixed with the FITC solution prior to incorporation in the formulation. The remainder of the preparation was the same as that described in chapter 7. As expected, all three solvents showed brightly labelled silica against a dark polymer background, with the acetone and alkaline solution producing a somewhat stronger fluorescent signal than the ethanol.

Of course we seek to use a labelling technique which affects the lacquer as little as possible. For example, it would not be desirable to incorporate acetone in the formulation, as it may interact with the latex binder during storage. To this end, we choose the alkaline solution as a vehicle for FITC labelling. As noted in chapter 2, page 12, acrylic latices can be formulated in alkaline conditions [39], which is the case here. The pH of the lacquer is around 10, so the inclusion of 1 drop of 0.1 molar NaOH containing the FITC label should have little effect in a 50cm^3 sample.

However care must be taken with labelling such that any changes observed are due to the silica and not the dye. Furthermore, we must ensure that *all* the silica is labelled and that the structure we observe is real and not artifact. To do this, we work almost exclusively at one FITC concentration. We add 1.5mg of FITC per 50cm^3 sample, dissolving the FITC in one drop of NaOH solution. In this way, any changes are related to the silica and not the FITC.

We test our labelling by varying the dye concentration while the rest of the components, especially the silica, are fixed. The results for agglomerated fumed silica (AFS) with $\frac{m_{sil}}{m_0} = 0.94$ are shown in figure 8.2. It is clear that a variation in dye concentration of two orders in magnitude does not enormously affect the fraction of pixels identified as silica, determined using a gradient threshold of 40. The gradient threshold technique used here is relatively insensitive to the widely varying amounts of noise in the images, due to the different labelling strengths. So using a FITC concentration of 1.5 mg per 50cm^3, we are confident that any variations we measure are a function of silica, not FITC.

Unfortunately FITC adsorption is sensitive to the surface chemistry, and does not interact with fumed and precipitated silicas in the same way, as we see from figure 8.2, for fine precipitated silica $\frac{m_{sil}}{m_0}$=0.92. This limited our approach in the case of fine precipitated silica (FPS). We endeavoured to ensure that all the silica was labelled by increasing the FITC concentration to 5 mg per 50 cm^3 sample. Treating FPS images in the same way

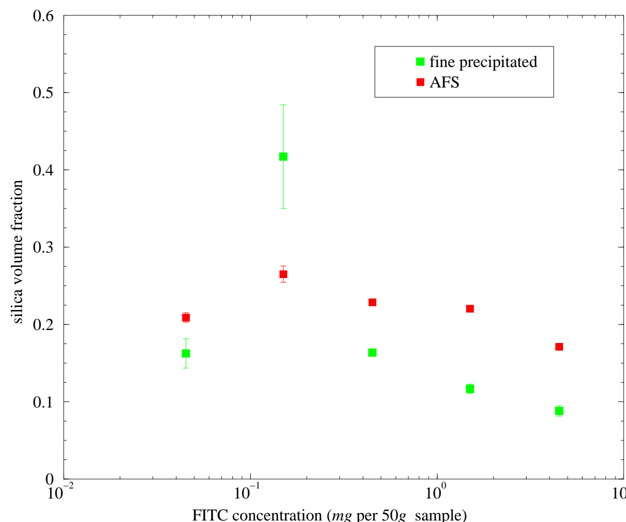

Figure 8.2: Silica volume fraction as a function of FITC concentration. The variation in AFS is quite small, given the large range of FITC concentration. The high FPS value at quite low FITC concentration is assumed to be noise.

as AFS, we looked for a similar behaviour in the analysis.

Further evidence of differing surface chemistry was found when we attempted to label the soft precipitated silica (SPS). We prepared a FITC labelled sample as described above, but the signal produced in the confocal microscope was very weak indeed, so that the images were of a poor quality yielding little structural information. Any numerical analysis was swamped by artifacts. We return to CLSM images of SPS in the next chapter. This different surface chemistry may be related to the fact that SPS is around 1% alumina [12].

The samples were laid down on chromated aluminium and dried in a dessicator as described in chapter 7. All films were produced with a 200 μm wet depth. They were imaged on a Zeiss LSM 510 confocal microscope, using a 488nm laser with a 505nm low pass filter to reject reflected light. Full experimental parameters are given on page 218. The CLSM work in this chapter is at constant magnification, which afforded easy comparison between images. We used a pixel size of $0.07\mu\text{m}\times0.07\mu\text{m}\times0.35\mu\text{m}$ or $1.7\times10^{-3}\mu\text{m}^3$. Our pixel size was limited by considerations of photobleaching and sampling rate. A desirable smaller pixel size would increase photobleaching for a given sampling rate, and a high sampling rate was required for a high signal to noise ratio. However our pixel size is close to the minimum size set by the Nyquist criterion (see chapter 4, page 58). We sampled

$512 \times 512 \times 64$ images, which corresponded to a region of $38.4\mu m \times 38.4\mu m \times 22.4\mu m$. The $22.4\mu m$ image thickness is less than the total film thickness, typically 40-50μm, so we image the top section of the film to minimise any attenuation and spherical aberration, typically the top of the image was 1μm below the film surface.

All images were then reconstructed using the expectation maximisation (EM) method of chapter 6 [95]. Here we use 100 iterations, with no penalties. The memory limitation of the computer used (Silicon Graphics workstation) required that each image of $512\times512\times64$ pixels was split into four $256\times256\times64$ images for EM reconstruction. These four images were then recombined into a $512\times512\times64$ image for analysis. This larger image size gave better statistics.

8.3

Results of confocal microscopy

The general structure assumed by silica in the bulk of the dry lacquer is shown in figure 8.3 for lateral xy *(a)* and vertical xz *(b)* slices. To enhance contrast, we have applied the colour table used in chapter 6, page 87. Recall that the data for these images have differing lateral and axial sampling rates of 0.07μm pixel^{-1}, and 0.35μm pixel^{-1} respectively. Here we expand the z pixels by a factor of five, so that magnification is the same in the x and z directions.

Notwithstanding the differing pixel size between the two images, the appearance is very similar, with small particles of silica appearing randomly distributed, both laterally and vertically. The resolution enhancement from the EM reconstruction is significant, as we can see structure well below the micron scale.

The effect of varying silica concentration is shown in figure 8.4 for AFS. All of these images are xy planes, taken around 7μm from the surface The total film depth is typically 40-50μm, so these images are well within the bulk. At low concentrations the silica particles are isolated, figure 8.4*(a)* ($\frac{m_{sil}}{m_0}$=0.47), corresponding to the schematic in figure 8.1*(a)*.

The image shown in figure 8.4*(b)* has $\frac{m_{sil}}{m_0} = 0.94$. Although the silica particles are isolated in two dimensions, we can test for percolation in three dimensions by comparing

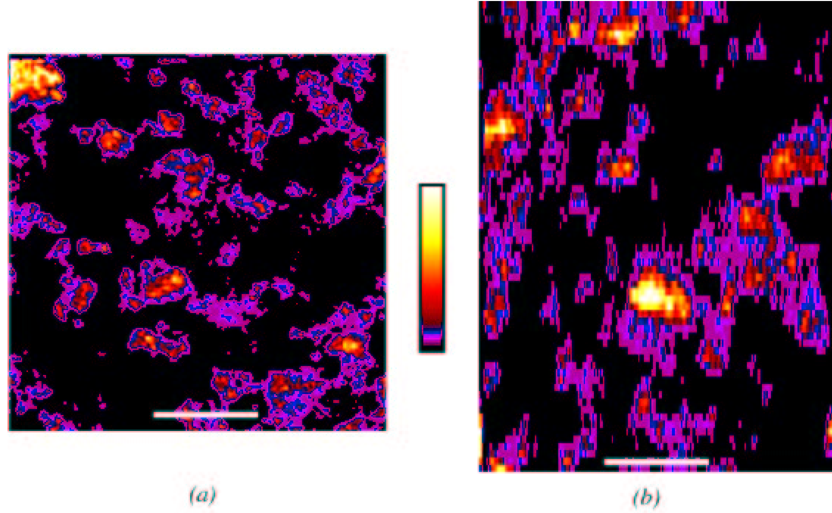

Figure 8.3: Confocal microscopy images of lacquer with AFS, $\frac{m_{sil}}{m_0} = 0.94$*. Both xy and xz slices are shown in* (a) *and* (b) *respectively. The xy slice is taken around 7μm below the surface. These images have been restored using EM deconvolution. Bar = 5μm. The slice in* (a) *is* 256×256 *pixels, whereas* (b) *is* 256×64 *pixels with the z pixels expanded such that x and z magnifications are the same. The contrast is enhanced with the colour bar shown.*

cluster numbers on different sides of the image (see chapter 6, page 93), and we find that this structure does indeed percolate in 3D. This image then corresponds to figure 8.1*(b)*.

Increasing the silica concentration to $\frac{m_{sil}}{m_0} = 1.87$ (figure 8.4*(c)*) we see percolation in two dimensions. There is rather more silica present than in the previous image which is indicative of silica densification associated with structural collapse. So this image corresponds to figure 8.1*(c)*, since a robust structure *(d)* would not be expected produce a higher silica volume fraction beyond $\frac{m_{sil}}{m_0} \approx 1$. At higher loading still ($\frac{m_{sil}}{m_0} = 2.81$, figure 8.4*(d)*), we see more densification, with silica present throughout the image.

We have also been able to produce high-quality images of other silicas, as shown in figure 8.5. Like figure 8.4, these are xy scans at around 7 μm depth. Coarse precipitated silica (CPS) (8.5*(a)* $\frac{m_{sil}}{m_0} = 0.72$) shows a number of distinct, brightly labelled particles, although with a typical size of 5 μm, these are not significantly larger than fine precipitated silica. We expect that the very large particles which we also find in coarse precipitated silica (see next section) are too thick for the confocal microscope to successfully image through, so we can only image the regions of the film from which the larger particles are

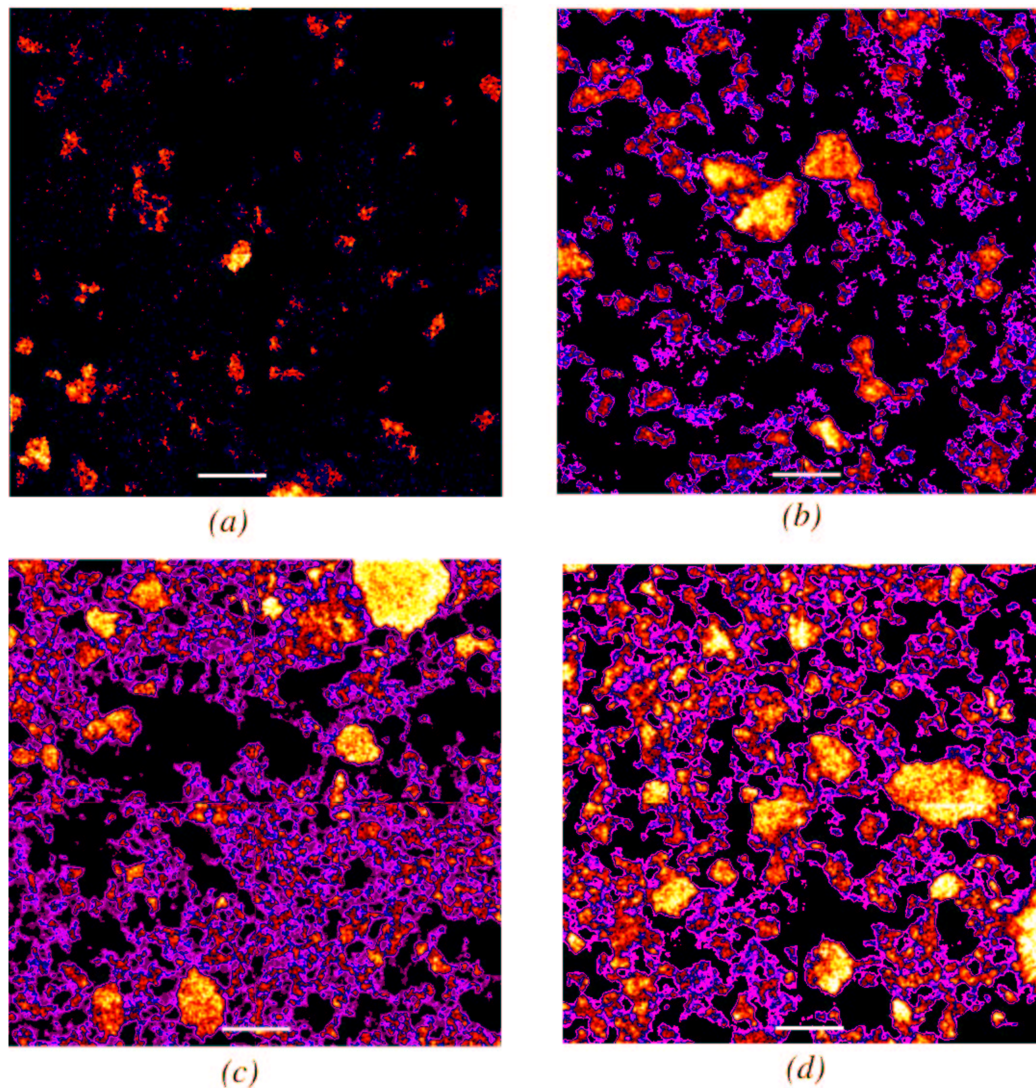

Figure 8.4: EM-restored confocal images of film with AFS at a range of concentrations. (a) $\frac{m_{sil}}{m_0} = 0.47$, (b) $\frac{m_{sil}}{m_0} = 0.94$, (c) $\frac{m_{sil}}{m_0} = 1.87$ *and* (d) $\frac{m_{sil}}{m_0} = 2.81$. *All images are* 512×512 *xy slices taken at a depth of 7μm from the surface of the film. Faint horizontal and vertical lines in each image are artifacts of EM restoration of each image in four sections, which are then recombined. Bars=5μm.*

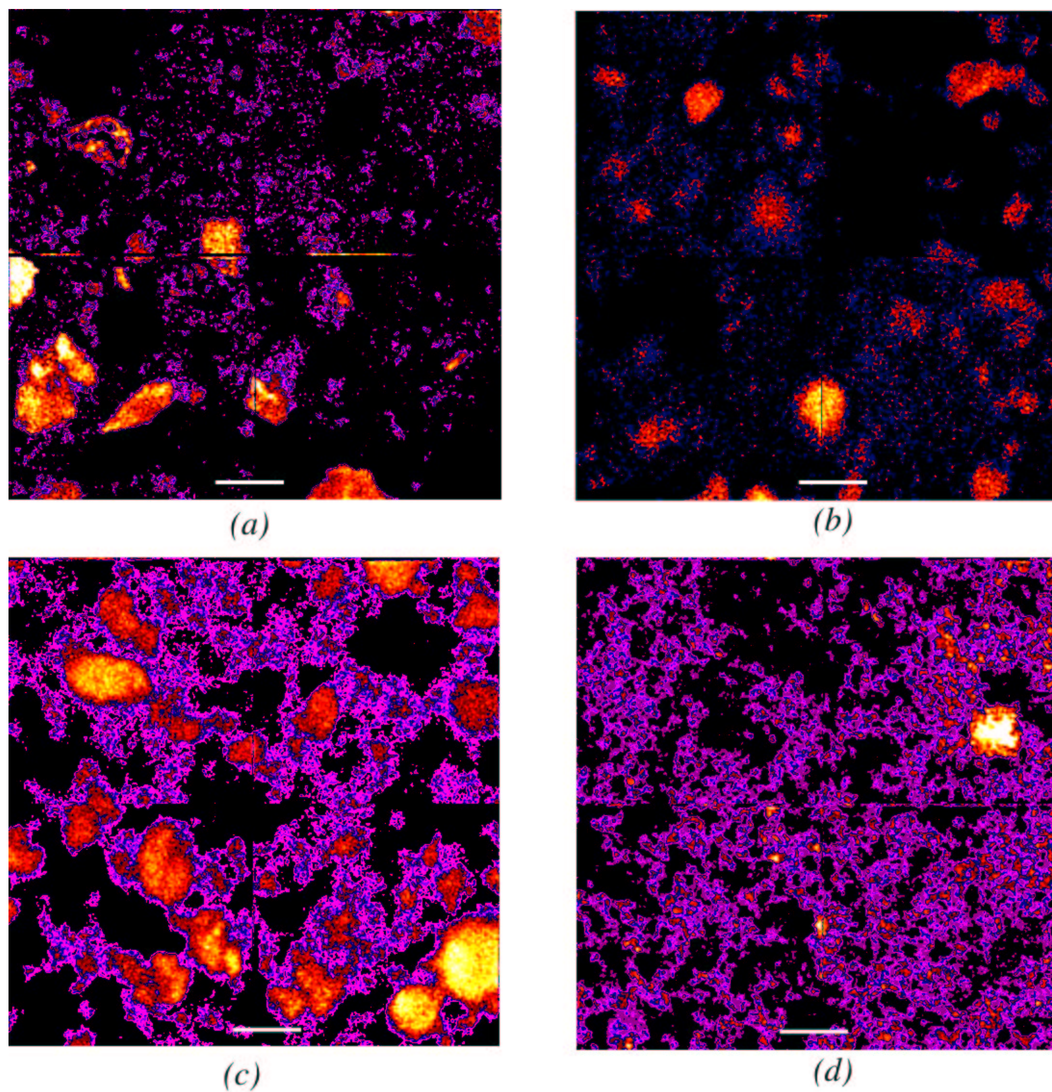

Figure 8.5: EM-restored confocal images of film with CPS ((a) $\frac{m_{sil}}{m_0} = 0.72$) *FPS* ((b) *and* (c) $\frac{m_{sil}}{m_0}$ =*0.93 and 1.84 respectively) and fumed silica* (d) $\frac{m_{sil}}{m_0} = 0.93$. *These are xy slices from* $512 \times 512 \times 64$ *pixel images, around 7μm from the surface of the film. Again the effects of image recombination can be seen. Bar = 5μm.*

absent. The effect of large silica particles on CLSM image quality is considered in chapter 9. For now we treat our analysis of CPS with some caution.

Fine precipitated silica (FPS) (figure 8.5 *(b)* and *(c)* $\frac{m_{sil}}{m_0} = 0.92$ and 1.84 respectively) is somewhat similar to AFS. At $\frac{m_{sil}}{m_0} = 0.92$ the silica structure does not percolate in two dimensions (but it does in three) and the $\frac{m_{sil}}{m_0}$ value is almost identical to figure 8.4*(b)*. At higher concentrations (figure 8.5*(c)* we again see densification similar to the AFS case. However the appearance is somewhat different, especially between figures 8.4*(b)* and 8.5*(b)*. The AFS has a large number of $\sim 1\mu$m particles, whereas in FPS we have both $\sim 5\mu$m particles and very small particles which may be residual noise or fragments of larger particles introduced through mixing.

A different structure again is shown for (non-agglomerated) fumed silica for $\frac{m_{sil}}{m_0} = 0.93$ in figure 8.5*(d)*. This is largely comprised of rather dim regions filled with small silica particles, and is entirely consistent with fumed silica consisting of small, weakly bound ultimate particles, although the structure seen here is rather larger than the ultimate particle lengthscale of 20nm. However we recall that 20nm ultimate particles aggregate spontaneously [10]. As can be seen from the image fumed silica percolates in two dimensions at $\frac{m_{sil}}{m_0} = 0.93$.

Quantitative Results

We now consider quantitative analysis of these images. Implementing the technique discussed in chapter 6, section 6.2, we use a brightness threshold of four to separate pixels corresponding to silica from the polymer background. In the case of fine precipitated silica with higher FITC concentration, we use a brightness threshold of nine. Clusters with a volume of less than 100 pixels (0.17 μm^3) are rejected as noise. The total proportion of white pixels is then the silica volume fraction, ϕ.

Silica volume fraction ϕ is plotted as a function of $\frac{m_{sil}}{m_0}$ in figure 8.6. Each point in the plot is the mean of 1-6 images (typically 4). Error bars are the standard error. From the plot we see that ϕ is clearly a linear function of $\frac{m_{sil}}{m_0}$ whose slope depends upon the silica used. Note that we do not extend coarse precipitated or fumed silica beyond $\frac{m_{sil}}{m_0} \approx 1$. The images in both cases are of sufficiently poor quality that any information gleaned is

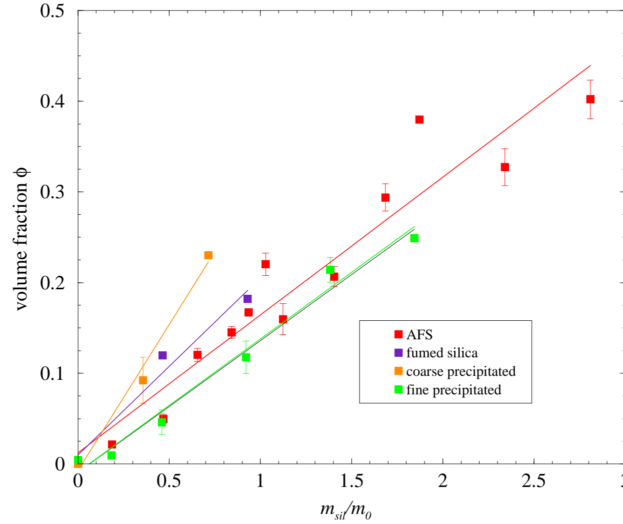

Figure 8.6: Silica volume fraction as a function of $\frac{m_{sil}}{m_0}$, determined from confocal images. This plot is a direct realisation of equation 3.10. For each silica, we have applied a regression fit to find the value of the packing fraction p.

Silica	p	intercept	percolation threshold $(\frac{m_{sil}}{m_0})$
AFS	0.152 ± 0.013	0.012 ± 0.019	0.94
FPS	0.146 ± 0.010	-0.009 ± 0.010	0.92
Fumed silica	0.195 ± 0.036	0.010 ± 0.021	0.46
CPS	0.322 ± 0.037	-0.007 ± 0.017	0.72

Table 8.1: Values of the packing fraction p obtained from regression fits of the lines in figure 8.6

swamped by artifacts and noise.

However we can determine the value of the packing fraction p, which is the slope of the graph from equation 3.10. Of course, this straight line behaviour is limited in extent, because we must have $\phi \leqslant 1$. Nonetheless the behaviour we see is fairly linear and provides good agreement with equation 3.10.

The values obtained from regression fits of the data in figure 8.6 are listed in table 8.1. All the intercepts are equal to zero within error bounds, as expected from equation 3.10. The packing fraction is rather higher in the case of the CPS. This is not too surprising, given the increased bulk density of CPS we might expect a higher packing fraction (table 3.1). Note however, that the absence of large silica particles from our CLSM images may well influence the packing fraction measurement.

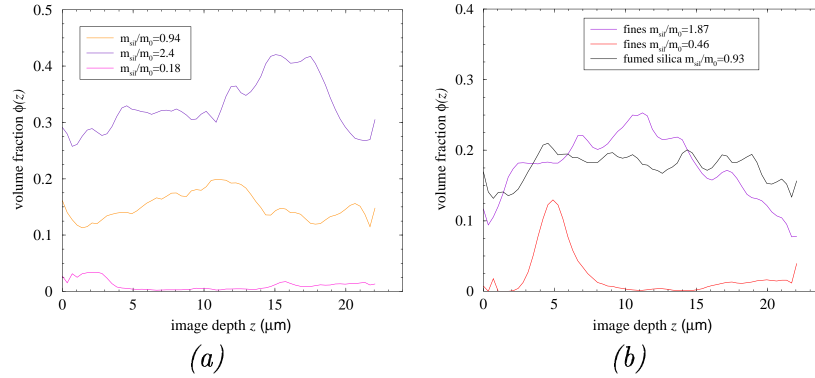

Figure 8.7: Silica volume fraction as a function of depth for AFS (a) *and fumed and fine precipitated silicas* (b). *Various silica concentrations are shown. Apart from local fluctuations, the lines are fairly uniform, with no tendency for surface segregation.*

The silica volume fraction can also be plotted as a function of depth. In particular this should reveal whether or not there is more silica present on the surface than in the bulk. Some of the data is plotted in figure 8.7, and we see that there is generally little consistent variation with depth for AFS and FPS. However the FPS $\frac{m_{sil}}{m_0} = 0.42$ line shows a large local increase in silica concentration at a depth of around 5μm. We discuss the interpretation of these local fluctuations below.

We can also determine the percolation threshold of the silica structure for each case, table 8.1. Recall that we expect a percolation threshold for $\frac{m_{sil}}{m_0} \lesssim 1$. These data however come with a health warning: our system is very small for observing percolation, relative to the size of the silica particles. We are treating it as a semi-infinite system, when in fact we have an image size of $512 \times 512 \times 64$ pixels ($35\mu\text{m}\times35\mu\text{m}\times24\mu\text{m}$). Nonetheless, we test for percolation in three dimensions and find that in the case of FPS and AFS, the threshold occurs at $\frac{m_{sil}}{m_0} = 0.92$ and 0.94 respectively. This is remarkably close to the value of unity where we expect the silica structure to resemble that of the dry powder.

Interestingly (non-agglomerated) fumed silica can exhibit percolation for $\frac{m_{sil}}{m_0}$ as low as $\frac{m_{sil}}{m_0} = 0.47$, which is well below the critical mass. In fact Kleinschmidt [16] notes that fumed silica can form a network in solution at low concentration, which appears to be the case here. As we noted in chapter 3, there is no reason why a percolating structure should occur at the critical mass. So in the case of fumed silica, the dry powder is approximately

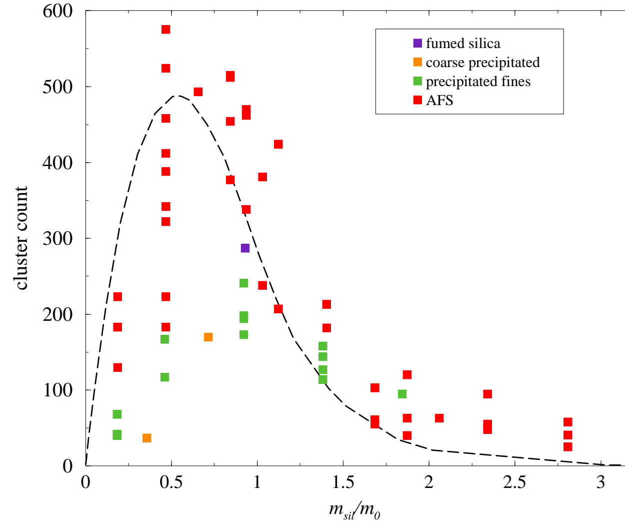

Figure 8.8: Cluster count as a function of $\frac{m_{sil}}{m_0}$. The broad peak for FPS and AFS is evidence for percolation. Each data point corresponds to a single image. Dotted line is the count on a randomly populated $256 \times 256 \times 64$ cubic lattice, normalised to the AFS peak.

twice as dense as the percolating structure formed here at $\frac{m_{sil}}{m_0} = 0.47$.

CPS seems to percolate at $\frac{m_{sil}}{m_0} = 0.72$, although we do not have enough data to properly support this figure. In fact, all these percolation thresholds are limited in accuracy by the number of samples produced. For simplicity, we take these as the sample with lowest $\frac{m_{sil}}{m_0}$ exhibiting consistent percolation.

We can also examine percolation through the variation in the number of clusters as a function of $\frac{m_{sil}}{m_0}$. At low silica concentration the count increases with $\frac{m_{sil}}{m_0}$, until enough particles touch that it starts to fall. This occurs before percolation [58]. Ultimately at high silica volume fraction, the number declines to a low value as eventually all the silica in the image is part of the same large cluster.

Both FPS and AFS exhibit this peak behaviour, figure 8.8. Each point corresponds to a single image and we see a large variation in the data for AFS, which is interpreted as a result of the small system size.

The count on a randomly populated $256 \times 256 \times 64$ cubic lattice is also shown in figure 8.8 (dotted line). This shows good agreement with the AFS data, also peaking well below the percolation threshold, which we have scaled to $\frac{m_{sil}}{m_0} = 0.93$. The random lattice percolated at a volume fraction of 0.091, below the percolation threshold of AFS, which

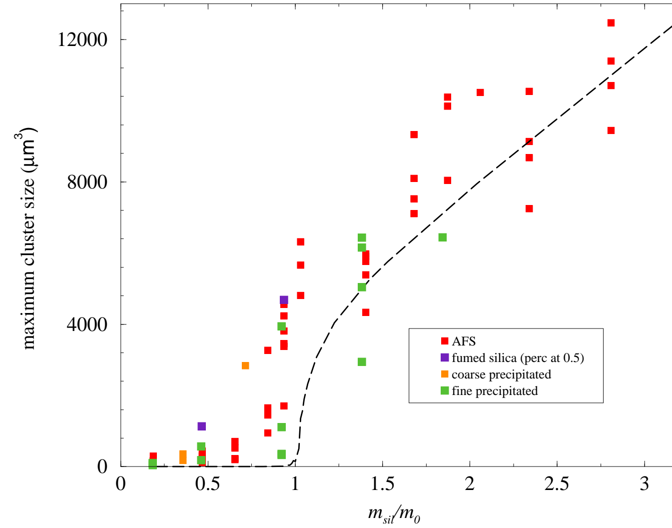

Figure 8.9: Maximum cluster size as a function of $\frac{m_{sil}}{m_0}$. *At the percolation threshold, the maximum cluster size increases discontinuously. Further increase in cluster size is the result of densification. Each data point corresponds to a single image. Dotted line is the maximum cluster size on a* $256 \times 256 \times 64$ *lattice.*

occurs at a volume fraction of 0.14. We therefore rescaled the random lattice x values by a factor of $\frac{0.091}{0.14 \times p}$. The packing fraction p (=0.152 for AFS) is required to determine a value of $\frac{m_{sil}}{m_0}$ for the random lattice. We justify this scaling by noting that the cluster count is a function of percolation behaviour, rather than absolute volume fraction. A differing percolation threshold between the cubic lattice and irregularly shaped particles is not unreasonable. The y-values from the random lattice simulation are normalised to fit the AFS data.

The count for AFS is higher in all cases than FPS. Since this includes low $\frac{m_{sil}}{m_0}$ values where we expect a single cluster to typically correspond to a single particle, this trend may be due to the more discrete nature of the FPS particles. For the fine precipitate we expect fewer larger well-defined particles, whereas for the more diffuse and weakly bound AFS rather more, smaller, less well-defined particles will be seen. Results for the coarse precipitate and fumed silica are also plotted. Although they follow the trends, there is not enough data to determine location of any peak.

Percolation is also evident through the size of the largest cluster, figure 8.9. Here we measure size as the number of pixels comprising the largest cluster, which we explicitly

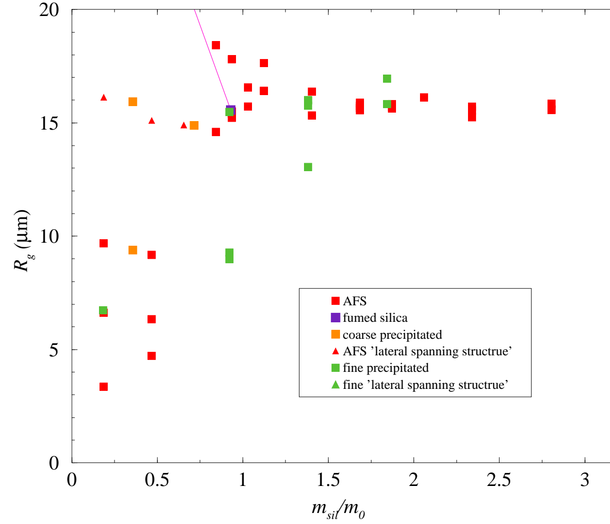

Figure 8.10: Radius of gyration of the largest cluster r_g as a function of $\frac{m_{sil}}{m_0}$. r_g increases to a size characteristic of the system. Each data point corresponds to a single image.

evaluate to μm^3. This size is clearly limited to the volume of specimen sampled to form the image, 28800 μm^3. Below the percolation threshold, the clusters are small, corresponding to isolated silica particles. The volume then increases sharply around the percolation threshold as the largest cluster now corresponds to many silica particles. This increase would be discontinuous in a large system [58]. Further increase with densification is seen at high $\frac{m_{sil}}{m_0}$ values, as the volume of the largest cluster increases with rising silica volume fraction.

Again AFS and FPS show good agreement with the random lattice simulation. We scaled the x-values as above, and normalised the y-values in accordance with AFS. Although there is the same general behaviour as the experimental data, the larger size of the silica particles compared to the single pixels of the random lattice is particularly apparent at low $\frac{m_{sil}}{m_0}$.

Another measure of the size of the largest cluster is R_g (figure 8.10). We recall from chapter 6 page 97 that

$$R_g^2 = \frac{1}{N} \sum_{i=1} N \langle (R_i - R_{COG})^2 \rangle, \tag{6.8}$$

with R_i the location of the ith pixel in the cluster, N the number of pixels and R_{COG} the centre of gravity. This physical parameter gives the lengthscale of the largest cluster. At the percolation threshold, we expect a sharp increase in R_g to a value the same order of magnitude as the system size. This we see, as almost all R_g values for $\frac{m_{sil}}{m_0} \gtrsim 1$ are close to 16μm, which is the same order as the image size, of $35 \times 35 \times 22\mu\text{m}^3$. Recall that the $(R_i - R_{COG})$ contribution should be around half of these values, so $R_g = 16\mu$m is very reasonable for the image size. However we are again limited by the system size: the R_g values for $\frac{m_{sil}}{m_0} \lesssim 1$ are not very much less than 16μm, although with AFS in particular, the increase to R_g is considerable.

Key exceptions to this trend are the data points marked as triangles in figure 8.10. These exhibited a lateral spanning structure. In other words the silica tended to be found in a layer in the images, which percolated laterally but not vertically. The $\phi(z)$ profile for such an image is shown by the red line in figure 8.7*(b)*. The peak at a depth of $\sim 5\mu$m shows that here the silica is not evenly distributed. This rather two-dimensional structure then gave a large value of R_g. This is presumably due to a very diffuse cluster having no pixels near its centre of gravity. Without any low $(R_i - R_{COG})$ values, the R_g is disproportionately high. Since R_g is related to the moment of inertia, this is equivalent to saying that material away from the centre of gravity contributes strongly to the moment of inertia.

We believe these flat silica structures (which are found predominantly at $\frac{m_{sil}}{m_0} \lesssim 0.5$) are silica-rich regions in the wet lacquer which are 'smeared out' as the film is laid down.

8.4

Atomic force microscopy

Here we describe how we applied the AFM technique to matt water-based lacquers. We then consider the results in terms of our silica structure model, focusing on surface roughness as a function of $\frac{m_{sil}}{m_0}$. To prepare the samples, we laid out the film on a 1cm^2 piece of glass, which provided a flat transparent surface, easy to align in the AFM. The films were laid out using a piece of sheet aluminium with a groove of depth 200μm and width 7mm cut in it. This replicated the microapplicator (chapter 7, page 111) on a scale appropriate to AFM.

We used a Digital Instruments multimode AFM with a Nanoscope III controller [56]. The cantilever was oscillated 5% below its resonant frequency, at typically 300 khz, as discussed in chapter 4, section 4.2. Two lines were scanned per second for 5μm scans and one line per second for 30 μm scans. We recorded images both in the topographic and phase imaging modes. Topographic mode records the height of the surface, whereas phase mode is sensitive to viscoelastic properties as described in some detail in chapter 4 section 4.2.

AFM Results

We begin our discussion of AFM work by looking at some particularly revealing small-scan images. By virtue of its high resolution, AFM can access certain key features that are beyond the resolution of the other techniques.

Figure 8.11*(a)* shows a topographic image of the latex without any silica. Comparison with the scale bar shows that the latex particles are around 80nm in diameter and that they do not appear to form a regular array on lengthscales more than 500nm.

However the particles in figure 8.11*(a)* are not spherical. The width is around 80nm

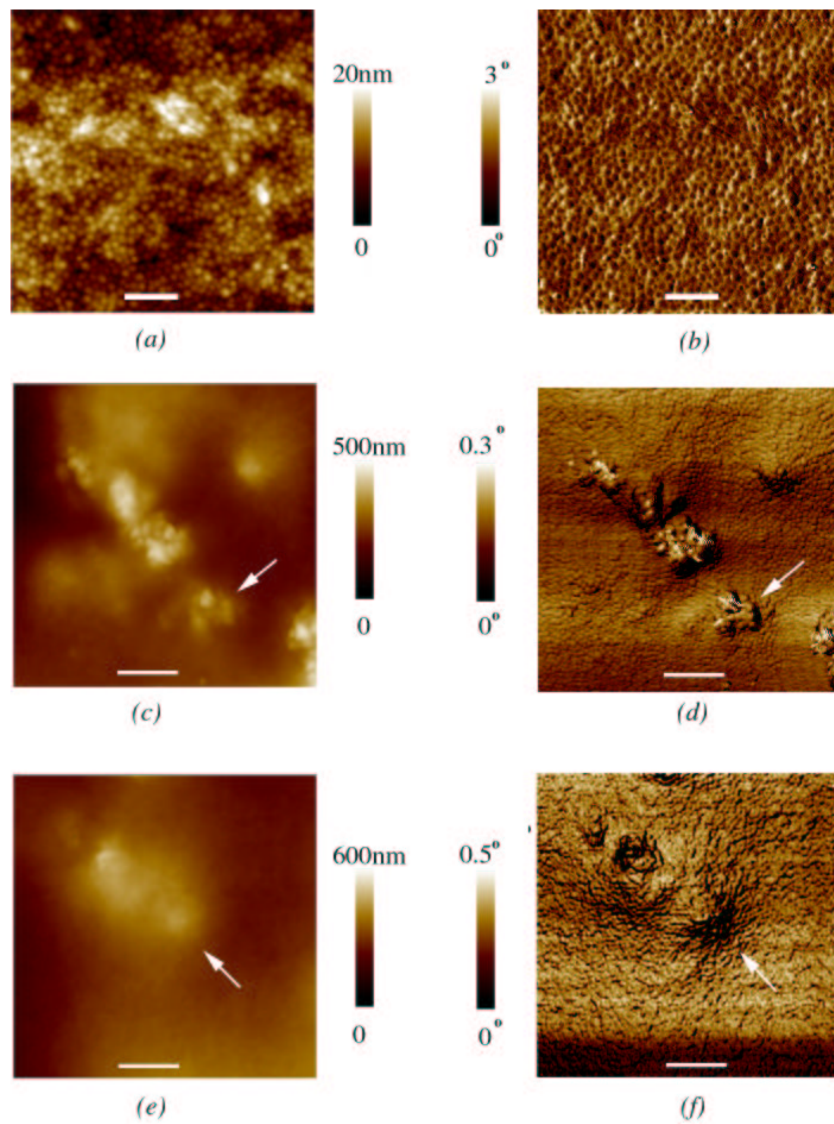

Figure 8.11: AFM images of dried films. Images without silica (a) *height and* (b) *phase reveal latex particles (Bars=500 nm), precipitated silica* $\frac{m_{sil}}{m_0} = 1.8$ *height* (c) *and phase* (d) *along with AFS* $\frac{m_{sil}}{m_0} = 1.31$ *height* (e) *and phase* (f). *Bars=1* μm.

but the height variation around each particle is only 6nm. We interpret this small height variation in terms of latex deformation, and conclude that the film is at stage III-IV in latex film formation (figure 2.1). Why then is the surface not entirely flat, as figure 2.1 suggests? Well residual viscoelastic forces tend to resist deformation, and the surface energy of a slightly undulating surface such as we see here is very similar to that of an absolutely flat surface. Therefore the rate of deformation slows considerably at these longer timescales, as found by Lin and Meier [29]. These workers found that a 250nm diameter PBMA latex tended towards a 30nm 'corrugation height' (broadly equivalent to our 6nm height, considering the smaller 80nm latex diameter) after around 200 hours of drying time.

The phase contrast image in figure 8.11 also reveals the latex particles from viscoelastic variations between the centres and edges of these deformed particles. Phase contrast is not sensitive to larger-scale height variation.

Raised regions, such as that in figure 8.11*(c)* marked with an arrow are interpreted as silica (precipitated silica, $\frac{m_{sil}}{m_0} = 1.75$). This topographic image shows a huge increase in surface roughness compared to the silica-free film, as the vertical scale bar here is 500nm, a 25-fold increase. The accompanying phase image 8.11*(d)* again shows the latex particles. The latex particles are 'washed out' in the height image, as the lengthscales of height variation are too great to reveal them. Crucially, on careful comparison with the topographic image (figure 8.11*(c)*), we see that the high regions (silica) appear to be covered in latex particles (marked by arrow in both topographic and phase images). This has significant implications: here we have a fairly robust silica of moderate density, at fairly high $\frac{m_{sil}}{m_0}$. Yet the silica is covered in latex particles, with very little silica present on the surface.

The situation is similar for AFS ($\frac{m_{sil}}{m_0} = 1.31$) in figures 8.11*(e)* and *(f)*. Again we associate the increase in surface roughness in the height image with silica. Here the phase image 8.11*(f)* shows a change in the viscoelastic properties of the latex close to the silica particle in the marked region. This suggests stresses introduced during drying around the silica particle (recall that phase imaging measures the viscoelastic properties of the surface), so non-uniform drying and the presence of silica could influence the mechanical properties of the dried film. The latex particles can again be distinguished.

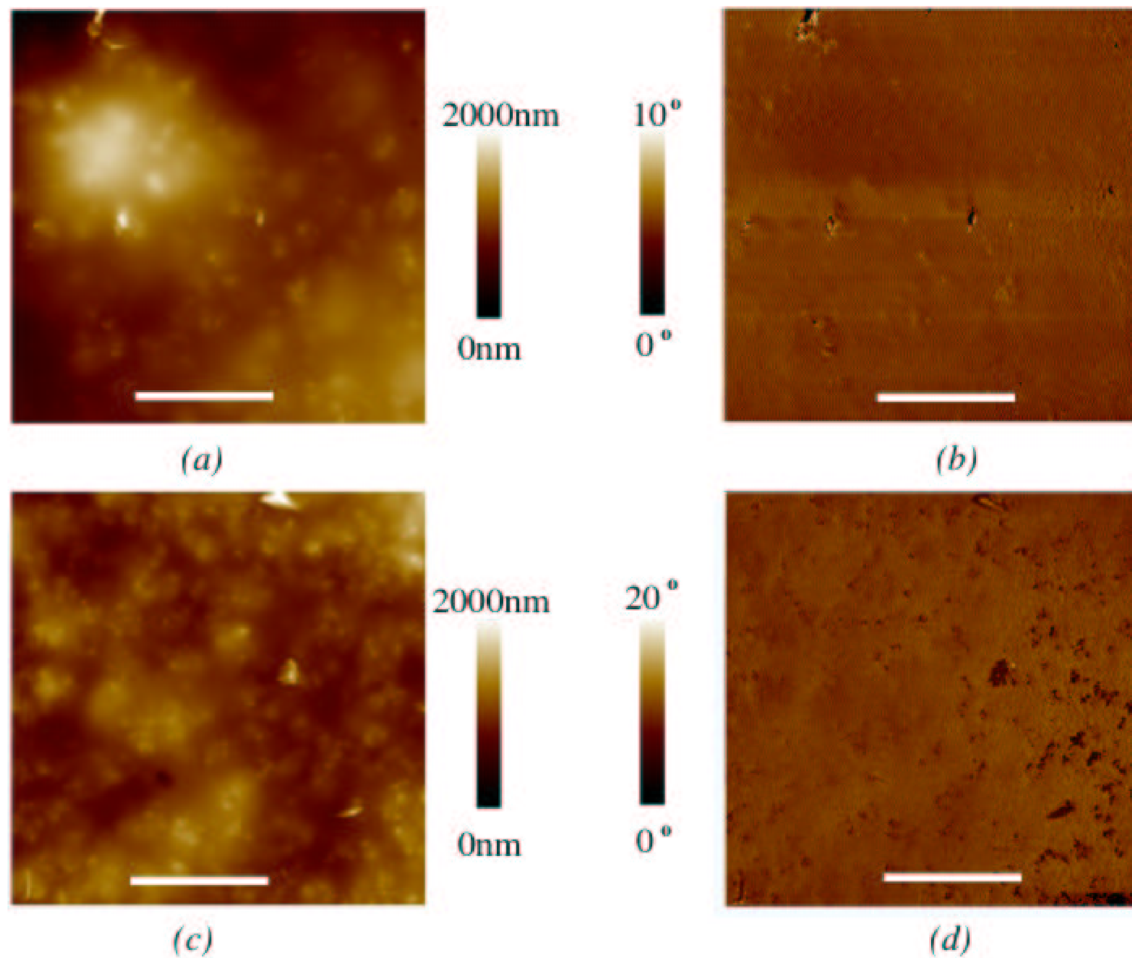

Figure 8.12: AFM images of film with AFS $\frac{m_{sil}}{m_0}$ = 0.94 *(*(a) *height and* (b) *phase)* $\frac{m_{sil}}{m_0}$ = 2.34 *(*(c) *height and* (d) *phase). No substantial increase in surface roughness is seen in the height images. Bars=10μm.*

These small area scans are useful in the detail they reveal, but to go further we again need to ensure that our image size exceeds the silica lengthscale. Such images are shown for AFS in figure 8.12, with a larger scan size of 30 μm. Figures 8.12*(a)* and *(c)* show topographic images which are fairly similar despite the increase in silica concentration ($\frac{m_{sil}}{m_0}$=0.94 and 2.34 in *(a)* and *(c)* respectively). Certainly these images have the same variation in height as the scale is unchanged. This similarity is consistent with AFS undergoing structural collapse at high silica concentration, as noted from the confocal data.

The corresponding phase images show relatively little contrast, especially in the $\frac{m_{sil}}{m_0}$=0.94 case (figure 8.12*(b)*). With these larger scans, we can no longer resolve individual latex particles. The lack of phase contrast further supports the idea that the silica is covered in deformed latex particles, as we saw from figure 8.11. We would expect to distinguish silica and polymer in the phase images on account of the different viscoelastic properties. This observation that the silica is covered in polymer will have a significant implication when we discuss interpretation of ESEM images in the next section.

In the case of the precipitated silicas, typical topographic images are shown in figure 8.13. The CPS (figure 8.13*(a)*, $\frac{m_{sil}}{m_0}$=0.72) is immediately distinguished by the large particles, of around 10 μm in size, and large variation in height. The other images are all rather flatter with smaller particles. Although the FPS (figure 8.13*(b)* $\frac{m_{sil}}{m_0}$=0.92) seems particularly flat, the large vertical scale (4000nm) shows that the peak marked with an arrow is particularly high, compared to the soft and unseived silicas.

The lateral structure of the SPS (figure 8.13*(c)* $\frac{m_{sil}}{m_0}$=0.89) is on a similar lengthscale to the FPS, well below the image size, with features typically a few μm in size. As we will see, this is also shown up in the ESEM work. The image does not show a huge vertical variation, compared to the CPS (2500nm compared to 5000nm). We see that the unseived precipitated silica (UPS) (figure 8.13*(d)* $\frac{m_{sil}}{m_0}$=1.31) has a larger particle size compared to the fine and soft precipitates. As this silica is quite hard and has not been sieved, these larger particles are expected.

The R_a surface roughness measure was determined from 30 and 60 μm scans and the results are plotted in figure 8.14. No difference in R_a was found between the two scan sizes, so no differentiation is made in the plot. Recall that R_a is defined as

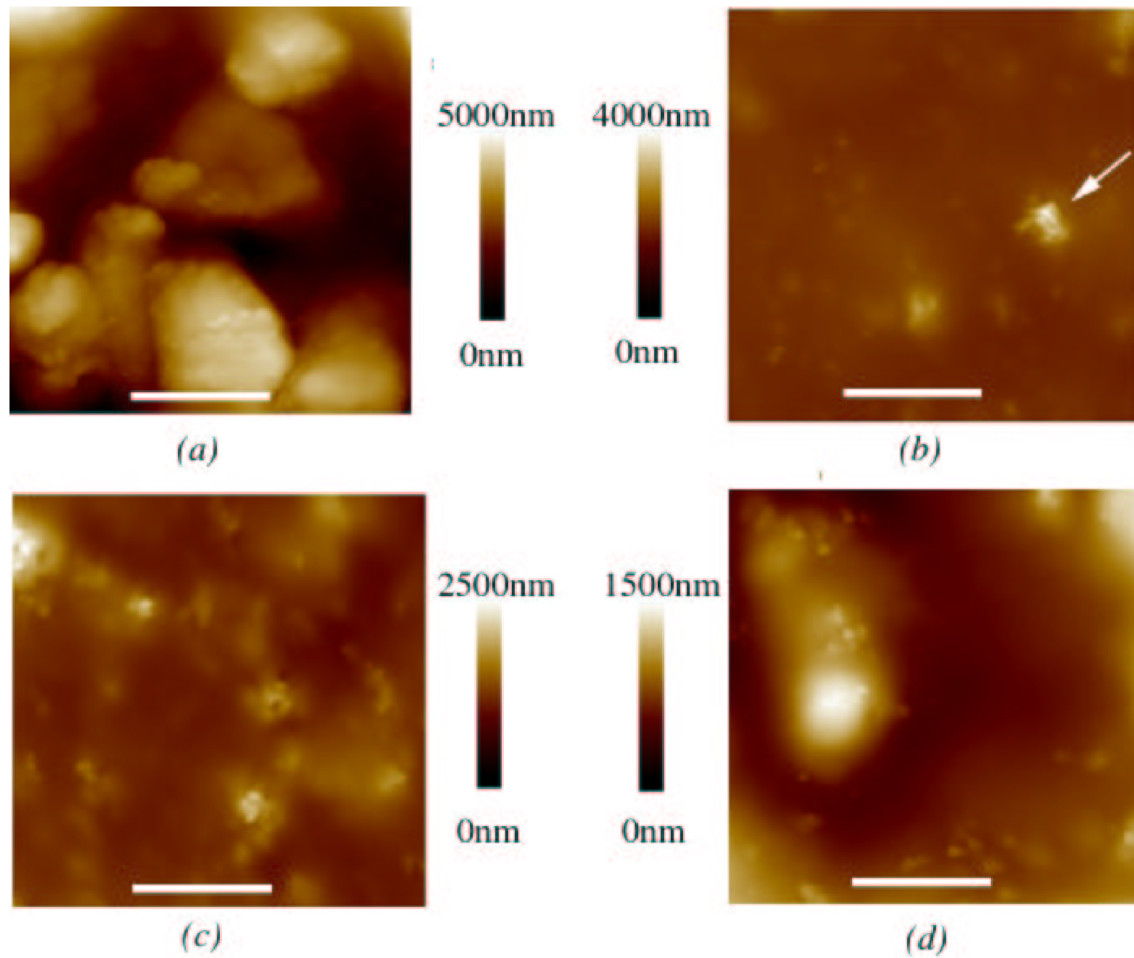

Figure 8.13: AFM height images of film with precipitated silicas. (a) *coarse precipitated* $\frac{m_{sil}}{m_0} = 0.71$ (b), *fine precipitated* $\frac{m_{sil}}{m_0} = 0.92$ (c), *soft precipitated* $\frac{m_{sil}}{m_0} = 0.89$ (d) *and unseived precipitated* $\frac{m_{sil}}{m_0} = 1.31$. *Bars=10μm.*

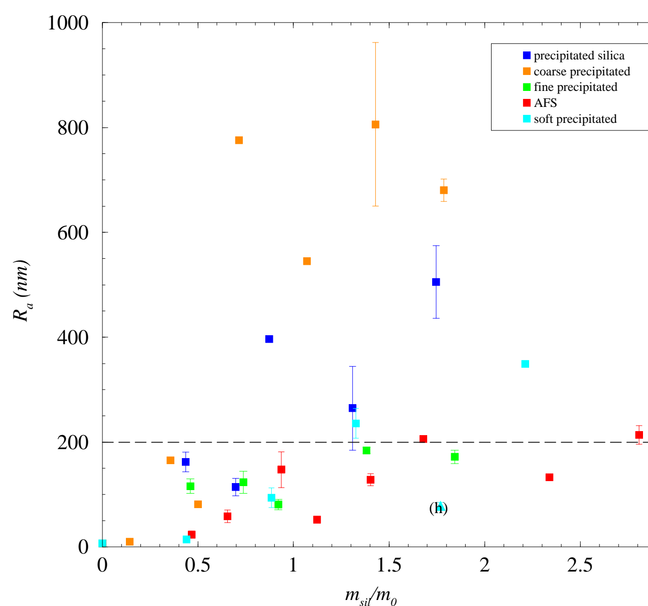

Figure 8.14: R_a as a function of $\frac{m_{sil}}{m_0}$. The coarse and unsieved precipitated silicas with larger more robust particles have a far greater surface roughness (for $\frac{m_{sil}}{m_0} \gtrsim 1$) than the other silicas. AFS and FPS data points fall below $r_a \approx 200$ nm (black dotted line). The low SPS point marked (h) is from a sample with poor silica distribution, which was a problem of the AFM preparation technique.

$$R_a = \frac{1}{N}\sum_{i=1}^{i=N} |h_i - \bar{h}| \tag{2.7}$$

with N the number of pixels in the image, h_i the height of each pixel and $\bar{h}$ the mean height. The error bars in figure 8.14 are the standard errors taken from 1-4 images. In the case where we have a single image, the error is taken as 6nm, the error introduced from the cross-coupling in 60 μm AFM scans (see chapter 4 page 50 and page 106).

Although we do not have a large number of data points (due to the relatively slow rate of image acquisition in AFM and lack of time on the instrument) we can draw some conclusions from figure 8.14. The R_a above $\frac{m_{sil}}{m_0} \approx 0.7$ appear to be banded according to particle size. The larger coarse precipitated silica particles have high $R_a \gtrsim 500$nm whereas the unsieved precipitated silica particles lie in the range 200nm$\lesssim R_a \lesssim 500$nm. Amongst the silicas with smaller aggregate particles, AFS and FPS have $R_a \lesssim 200nm$ for all $\frac{m_{sil}}{m_0}$, although SPS can reach 400nm at high $\frac{m_{sil}}{m_0}$. From this data it is clear that R_a is strongly influenced by the silica particle size.

However silica volume fraction is important as well. At low $\frac{m_{sil}}{m_0}$, $R_a < 200$nm for all silicas. Although the $\frac{m_{sil}}{m_0} = 0.72$ point is high for CPS, recall that we found percolation at $\frac{m_{sil}}{m_0} = 0.72$ in CLSM work. So with a percolating silica structure, there is a large rise in surface roughness, which is in keeping with the model. This is due to the transition between isolated silica particles embedded in the film to a more robust silica structure which perturbs the surface very significantly (figure 8.1*(d)*). A similar behaviour is seen for unsieved precipitated silica.

There is no change in R_a at $\frac{m_{sil}}{m_0} \sim 1$ for AFS and FPS. The inclusion of any silica increases the R_a from $\sim$ 20nm (no silica) to $100 - 200$nm. So the silica structure would need to produce an R_a significantly more than 200nm to be apparent. Since we do not see this, we conclude that AFS and FPS aggregate particles are too small to influence R_a enough whether or not a robust structure is formed. However the fact that both AFS and FPS exhibit densification at $\frac{m_{sil}}{m_0} > 1$ in CLSM work strongly suggests some structural collapse in any case.

At high $\frac{m_{sil}}{m_0}$ SPS also perturbs the surface significantly, despite the absence of large

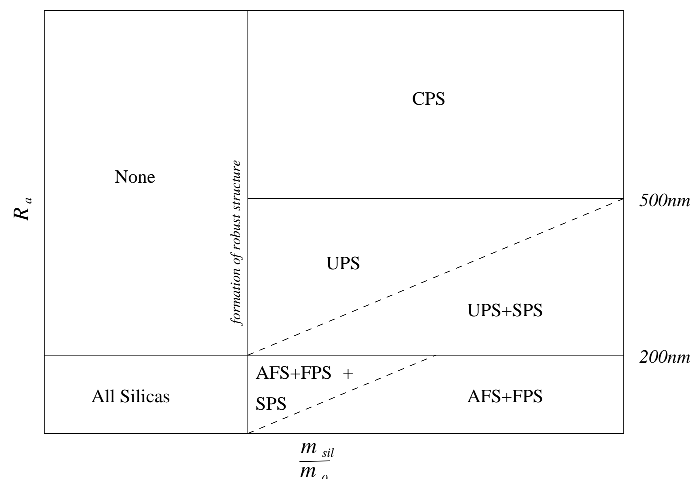

Figure 8.15: Schematic of figure 8.14, summarising R_a behaviour for different silicas. The range of R_a of each silica is shown, for different $\frac{m_{sil}}{m_0}$ regimes.

particles. We return to our consideration of this silica following the ESEM section. The R_a behaviour is summarised in figure 8.15, a schematic of figure 8.14. We see that different silicas populate the various regions of this $R_a/\frac{m_{sil}}{m_0}$ diagram.

8.5

Environmental SEM

We now turn to the contribution from ESEM in determining the silica structure. Recall from chapter 7 that it was hard to carry out truly quantitative experiments with ESEM, on account of a number of difficult to control operating parameters. In particular, the electron beam properties vary over time.

We have largely circumvented this problem by using an Electroscan E3 ESEM fitted with a lanthanum hexaboride (LaB_6) filament. This electron source is much more stable than the tungsten source used in chapter 7. For the work carried out here we left the beam on overnight before conducting the experiments. To produce the results shown here, two experiments were carried out, two days apart.

Our operating parameters were: 12keV beam voltage, 4 torr chamber pressure and

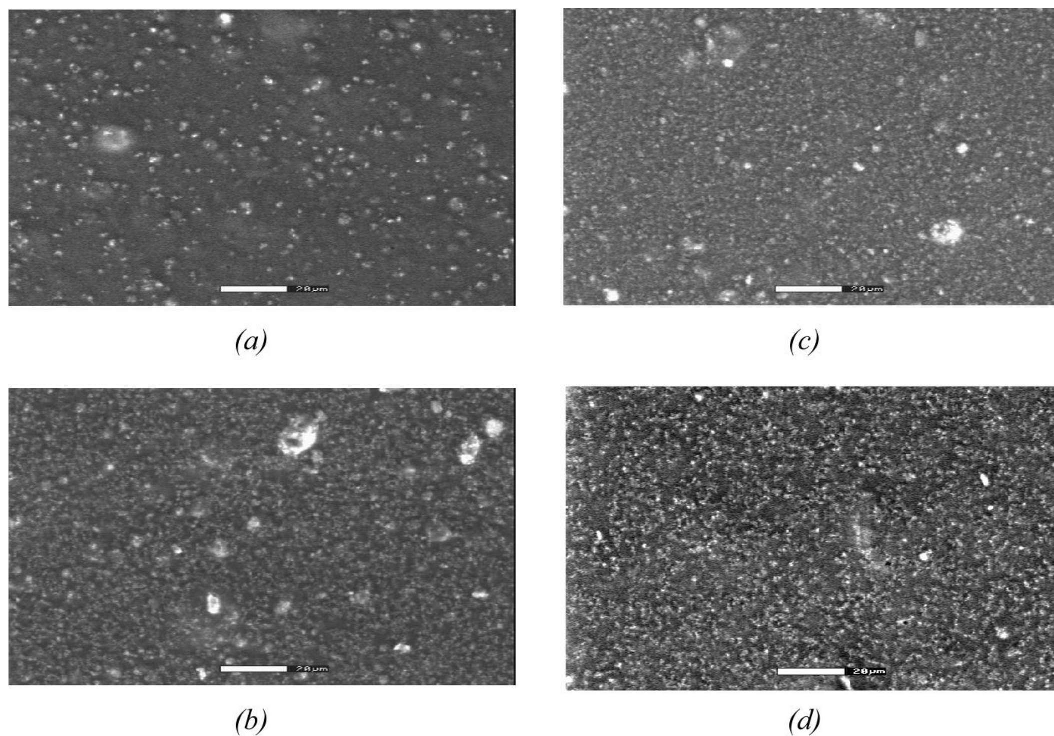

Figure 8.16: ESEM images of dried lacquer with fumed silicas. (a), (b) *and* (c) *show AFS at* $\frac{m_{sil}}{m_0}$ *= 0.47, 0.94 and 2.81 respectively.* (d) *is fumed silica* $\frac{m_{sil}}{m_0}$ *= 0.93. Bar=20μm.*

7mm working distance, which corresponds to a detector-sample distance of around 1mm. We used a scantime of 17s, again the original magnification was 800×. The samples were prepared in a dessicator overnight as before (chapter 7), except that we ensured that the sample was electrically earthed, with silver dag between the chromated aluminium substrate and the ESEM stub. The films were prepared with a wet depth of 200μm. As the films were already formed, we did not need an optimised pumpdown procedure. The chamber was simply pumped to 1 torr and flooded to 10 torr twice, before imaging at 4 torr.

ESEM Results

The discussion of ESEM results centres on three main areas: first we identify features of interest in the images. We then move on to the quantitative data, before putting our

ESEM work in context with the confocal and AFM results above. Finally we investigate image interpretation and the relationship between silica and image contrast.

Dried lacquer containing AFS is shown in figures 8.16*(a)-(c)* for a variety of silica concentrations, $\frac{m_{sil}}{m_0}$ =0.47, 0.94 and 2.81 respectively. As usual we associate silica with bright regions. There is a considerable increase in the surface silica between figures 8.16*(a)* and *(b)*, but there is very little difference at all between figures 8.16*(b)* and *(c)*. This fits well with our idea of a collapsing silica structure at high $\frac{m_{sil}}{m_0}$. As the structure collapses, adding more silica to the formulation need not alter the surface. Fumed silica is shown in figure 8.16*(d)* for $\frac{m_{sil}}{m_0} = 0.93$. The appearance is similar although not identical to the AFS. In particular we note the absence of larger regions of silica, like the confocal image (figure 8.5*(d)*), as the silica is not agglomerated.

Figure 8.17 shows fine *(a-c)* and unsieved *(d-f)* precipitated silica for a variety of silica concentrations. The two silicas show rather similar behaviour, at low silica concentration (*(a)* $\frac{m_{sil}}{m_0}$=0.46, *(d)* $\frac{m_{sil}}{m_0}$=0.43) the silica particles are rather isolated. More silica is apparent as we increase the silica concentration for both the fine and unsieved precipitates (figure 8.17 *(b)* $\frac{m_{sil}}{m_0}$=0.94, *(e)* $\frac{m_{sil}}{m_0}$=0.87). Interestingly, the contrast is rather better than the AFS and the surface does appear rather different. The AFS morphology is relatively homogeneous throughout the image (figure 8.16*(b)*), whereas UPS in particular (figure 8.17*(e)*) has regions of a few μm from which silica is absent.

At high silica concentration (figure 8.17 *(c)* $\frac{m_{sil}}{m_0}$=2.30, *(f)* $\frac{m_{sil}}{m_0}$=2.18) we see a further increase in surface silica, unlike the AFS. This suggests that the UPS and FPS present at least some resistance to collapse during film formation. Figure 8.17 *(f)* (unsieved precipitate) shows some large silica particles which are clearly absent from the fine precipitate analogue *(c)*, as we would expect from the sieving.

We now turn to the soft and coarse precipitates. At $\frac{m_{sil}}{m_0} \lesssim 1$ the SPS aggregate particles appear rather small (figure 8.18 *(a)-(b)*), as with the AFM image (figure 8.13*(c)*). In fact the particle lengthscale is not that far above the ultimate particle size of 100nm. This suggests that larger aggregate particles may be broken down during the mixing and film formation processes, in a similar way to AFS. The similarity is not altogether surprising when we recall that the soft precipitate aggregate particles are weakly bound, almost like the AFS aggregate particles. However, at high silica concentration (figure

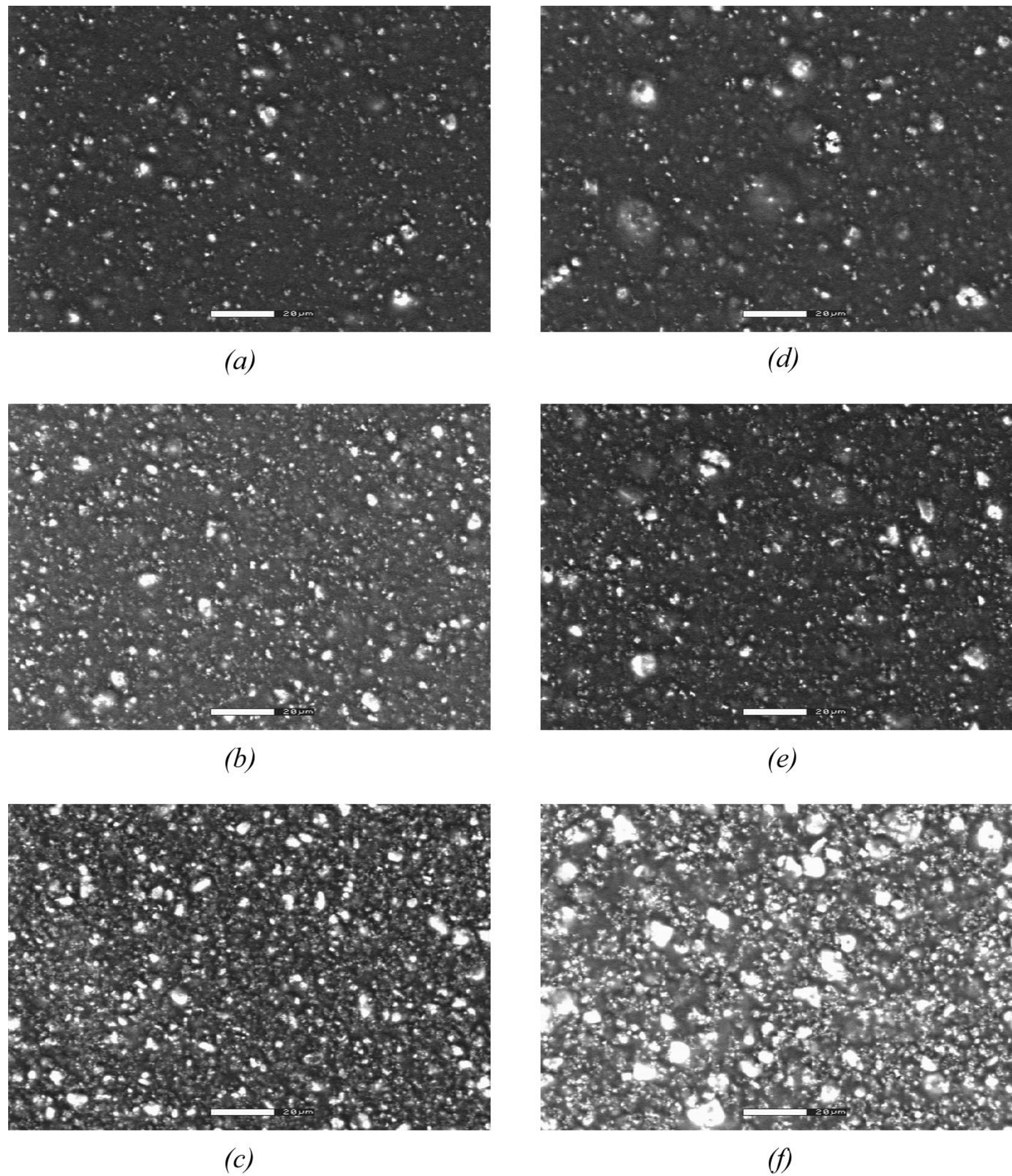

Figure 8.17: ESEM images of dried lacquer with fine ((a), (b), (c), $\frac{m_{sil}}{m_0}$*=0.46, 0.92 and 2.30 respectively) and unsieved (*(d), (e), (f), $\frac{m_{sil}}{m_0}$*=0.43, 0.87 and 2.18 respectively) precipitated silica. Bar=20µm.*

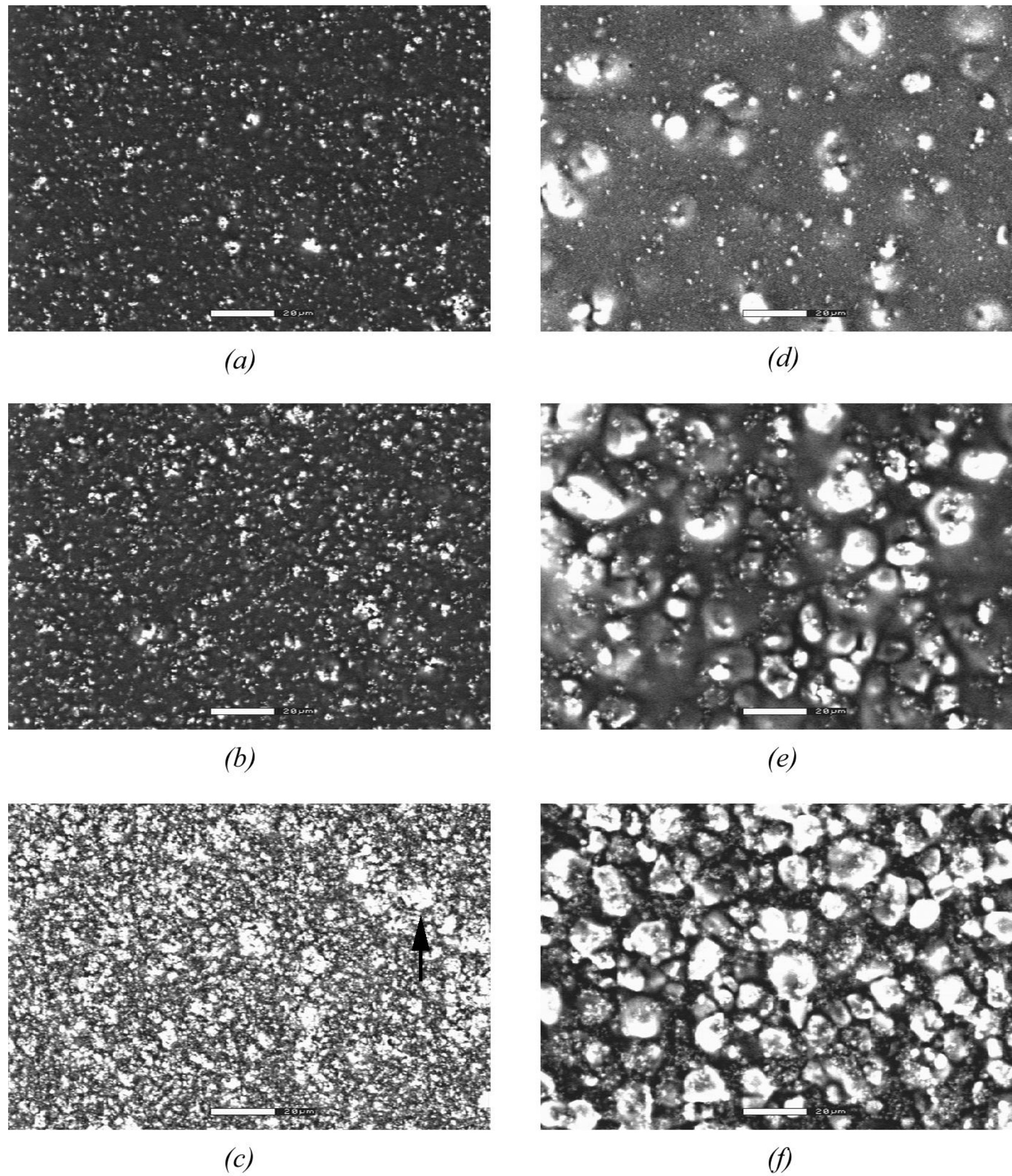

Figure 8.18: ESEM images of dried lacquer with soft ((a), (b), (c), $\frac{m_{sil}}{m_0}$=0.41, 0.82 and 2.05 respectively) and coarse precipitated silicas. ((d), (e), (f), $\frac{m_{sil}}{m_0}$=0.36, 1.07 and 1.79 respectively). Bar=20μm.

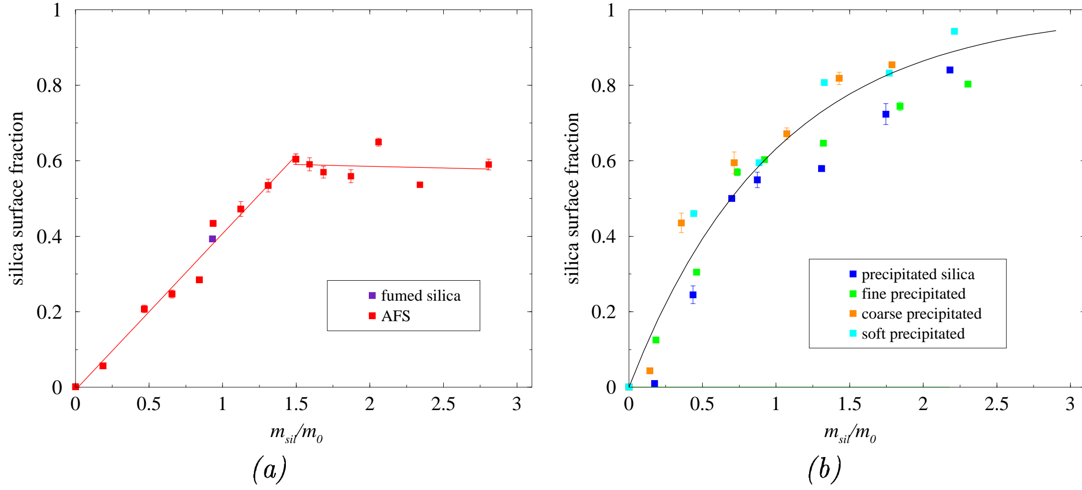

Figure 8.19: Silica surface fraction as a function of $\frac{m_{sil}}{m_0}$. (a) *fumed silicas and* (b) *precipitated silicas. The surface silica fraction ceases to rise beyond* $\frac{m_{sil}}{m_0} \approx 1.5$ *in the AFS case whereas for all precipitated silicas it increases to approach unity.*

8.18*(c)* $\frac{m_{sil}}{m_0}$=2.05) we see more silica, unlike the AFS behaviour.

At high $\frac{m_{sil}}{m_0}$ we also see some larger regions of silica, such as that marked with an arrow in figure 8.18*(c)*. There are a number of these, but they are absent from the images at lower $\frac{m_{sil}}{m_0}$. It seems that higher silica loading could result in 'piling up' of this silica. This piling up then explains why SPS can exhibit an R_a of around 400nm at high $\frac{m_{sil}}{m_0}$, which is significantly higher than we would expect for a silica with such small particles, compared to AFS and FPS.

Coarse precipitated silica, in figure 8.18 (*(d)*-*(f)*) clearly shows some large particles, as expected. In particular these images show a strong resemblance to the AFM image (figure 8.13*(a)*). Again the surface silica increases markedly with $\frac{m_{sil}}{m_0}$. The structure in figure 8.18*(e)* $\frac{m_{sil}}{m_0} = 0.72$ is very reminiscent of figure 8.1*(d)*. Interestingly, small particles are also present, presumably from fragmentation during sieving, mixing or film formation.

Image Analysis

We can determine the surface silica fraction for each image using the analysis technique described in chapter 6. Here we have a gradient threshold of 35 and a brightness threshold of 245. We use a different gradient threshold from chapter 7 because the Electroscan E3

	Slope	Intercept
$\frac{m_{sil}}{m_0} \lesssim 1.5$	0.4142 ± 0.023	-0.0071 ± 0.021
$\frac{m_{sil}}{m_0} \gtrsim 1.5$	-0.0094 ± 0.034	0.604 ± 0.070

Table 8.2: Regression data from fits to AFS surface silica fraction. After an initial linear increase, the data appears to flatten off. Standard errors are given here.

ESEM has slightly different imaging characteristics to the Electroscan 2010 used previously.

The fraction of pixels corresponding to silica is plotted as the silica surface fraction in figure 8.19*(a)* for the fumed silicas and *(b)* for precipitated silicas. Each point is the mean of typically six images with errors Bars the standard error. The difference between AFS and the precipitated silicas is clear. Surface silica fraction does not increase beyond $\frac{m_{sil}}{m_0} \approx 1.5$ for AFS, as we expect from the images, but up to this silica loading, there is a linear increase in surface silica fraction as a function of $\frac{m_{sil}}{m_0}$. We have applied regression fits to both regimes as shown in the plot. The results from the fit are given in table 8.2.

The precipitated silica all appear to fall broadly on the same line. This is plotted as surface silica fraction $= 1 - exp\left(-\frac{m_{sil}}{m_0}\right)$. Curiously both the coefficients in this function are unity. The functional form is required because the surface silica fraction must not exceed unity, but has no further physical meaning.

It is interesting that all the points fall on the same line, for silicas of widely differing bulk density (table 3.1 in chapter 3). This clearly shows that the surface silica is dominated by the bulk *volume* rather than the mass of silica added to the formulation. Recall that our confocal results were largely based on AFS and FPS, both of which had similar bulk densities, so it was hard to show conclusively that the structure depended upon silica bulk volume rather than mass. Figure 8.19*(b)* provides strong evidence for a structure dependent on silica bulk volume.

We can also determine a cluster count for the surface silica, in a similar way to that employed for the bulk silica in the confocal microscopy section, only here we work in 2D. Cluster counts are shown in figure 8.20 as a function of $\frac{m_{sil}}{m_0}$. Again we see a peak, and also at a broadly similar value of $\frac{m_{sil}}{m_0} \sim 1$ to the CLSM data. Is this indicative of percolation as well? Perhaps, but recall that in ESEM we have 2D images and confocal

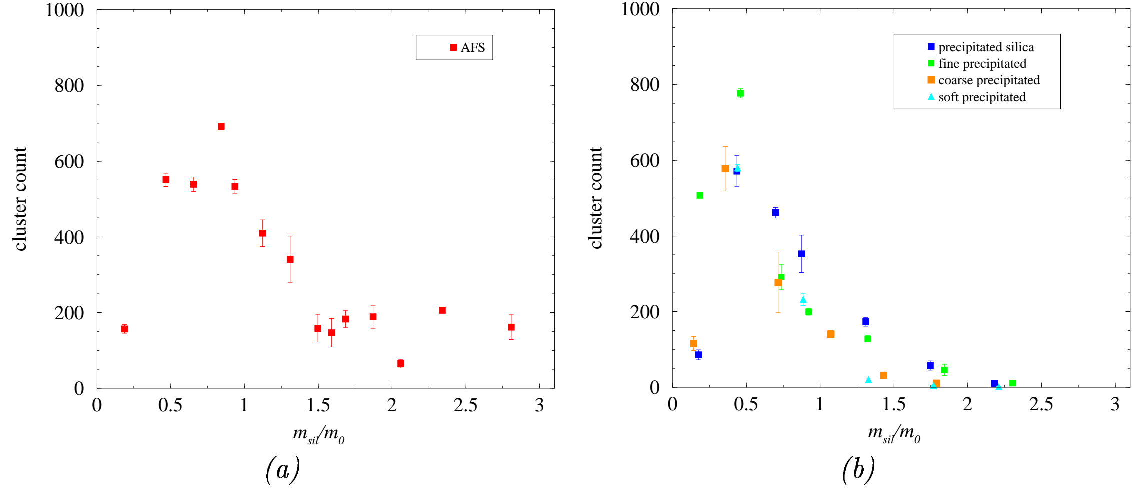

Figure 8.20: Cluster count as a function of $\frac{m_{sil}}{m_0}$. (a) *AFS and* (b) *precipitated silicas. There is again a peak number of clusters, suggesting percolation. However this is taken to be an artifact of ESEM image formation.*

images do not show 2D percolation until $\frac{m_{sil}}{m_0} \sim 2$. Although in all cases percolation is a geometric property of the image, we must explain this apparent discrepancy in 2D percolation between confocal microscopy and ESEM.

The percolation threshold on a square (2D) lattice is 0.407 for 8-fold connectivity as we have assumed here (each square has 8 neighbours) [58]. So if our surface silica fraction significantly exceeds this value, we might expect percolation. Comparing figures 8.6 and 8.19, we see that the surface silica fraction exceeds the silica volume fraction, which explains why we have 2D percolation on the surface of samples which do not exhibit 2D percolation in the bulk. We have no evidence for silica migrating to the surface during film formation (figure 8.7) so why is the 'surface silica fraction' higher than the silica volume fraction?

To answer this question we discuss the contrast mechanism in ESEM in more detail. Consider the scenario in figure 8.21. We know from AFM that the silica is generally covered in polymer. So strictly there is hardly *any* surface silica. It appears to reside just below the surface, but well within the lengthscale of the ESEM interaction volume, around 1-2μm at the 12keV beam energies used here [70]. The surface roughness, along with the silica itself, accounts for the ESEM signal. Since this topography can extend

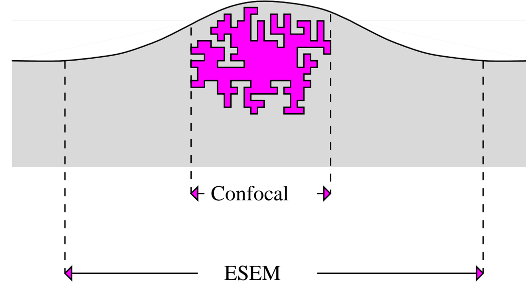

Figure 8.21: The difference between ESEM and confocal microscopy contrast mechanisms. ESEM is sensitive to both surface roughness and silica, whereas confocal microscopy will detect only FITC-labelled silica. So ESEM can overestimate the silica surface fraction.

beyond the bounds of the silica particles, the ESEM signal is strong over a wide area and we gain a rather high measure of 'surface silica', compared to CLSM which is not sensitive to surface topography.

One further observation can be made from figure 8.20. At high $\frac{m_{sil}}{m_0}$, the count for precipitated silicas tends towards a low value, but the AFS count levels off at around 200, at $\frac{m_{sil}}{m_0} \approx 1.5$. This lack of variation at high $\frac{m_{sil}}{m_0}$ is further evidence for structural collapse in AFS at high $\frac{m_{sil}}{m_0}$.

8.6

Conclusions

We have seen that the central predictions of our model are upheld.

(1) A percolating silica structure is formed at a silica volume fraction somewhat below $\frac{m_{sil}}{m_0} = 1$.

(2) The silica volume fraction in the bulk of the film is a linear function of $\frac{m_{sil}}{m_0}$, at the concentrations we have studied.

The following observations reveal behaviour consistent with our model, along with the different geometric and mechanical properties of the silicas studied:

(1) AFS undergoes structural collapse above $\frac{m_{sil}}{m_0} \sim 1.5$. This results in silica densification in the bulk of the film.

(2) FPS undergoes some structural collapse, but also perturbs the surface more at high $\frac{m_{sil}}{m_0}$.

(3) Surface roughness is characterised by both aggregate particle size and silica volume fraction, and increases markedly around the critical mass in CPS and UPS.

(4) There is a unique behaviour for all precipitated silica surface fractions, dependent solely upon silica volume.

Percolation has been demonstrated directly for fumed silica, AFS, CPS and FPS with confocal microscopy. Percolation occurs somewhat below $\frac{m_{sil}}{m_0} = 1$, but we note that in fact it is a necessary but not sufficient condition to produce a self-supporting structure as in the dry silica powder.

AFM work shows that coarse and unsieved precipitated silicas perturb the surface in a way consistent with the model for robust silicas. We have shown with AFM that the latex undergoes substantial deformation, and that the silica is largely covered by latex particles. Since we know that AFS collapses, a high R_a is not expected. In FPS the particle size must be too small to significantly influence the R_a, although we see a high silica surface fraction in ESEM at high $\frac{m_{sil}}{m_0}$, corresponding to a fairly robust silica structure.

There are different behaviours between the precipitated and fumed silicas, which we deduce with ESEM. AFS we know undergoes densification and apparently complete structural collapse at high values of $\frac{m_{sil}}{m_0}$. The precipitated silicas are more robust and do not totally collapse, as we see the increasing surface silica fraction at high $\frac{m_{sil}}{m_0}$. However the CLSM shows some densification for FPS, which is indicative of at least some structural collapse. So we conclude that the FPS behaviour lies somewhere between figures 8.1*(c)* (total collapse like AFS) and *(d)* (entirely robust structure). From ESEM work we see that all precipitated silicas behave similarly, with the possible exception of SPS. The main difference is their aggregate particle size which is shown also by AFM. We therefore extend this idea of partial structural collapse to UPS and CPS as well. This is further explored in the following chapter.

SPS is more curious and warrants special attention. The aggregate particle size is small, as we have noted from AFM and ESEM, yet unlike the other silicas with small particles, AFS and FPS, it can have $R_a \gtrsim 200$nm at high $\frac{m_{sil}}{m_0}$. We suggested that SPS might 'pile up' such that large regions of silica perturbed the surface, leading to high R_a. In fact SPS has the highest surface silica fraction of any silica (figure 8.19*(b)*). Why does SPS 'pile up' whereas silicas with apparently similar aggregate particle sizes, FPS and AFS, do not?

One key difference between SPS and AFS/FPS is its bulk density. SPS is approximately three times as dense, requiring a proportionate increase in silica mass fraction for a given $\frac{m_{sil}}{m_0}$ (table 3.1 in chapter 3). This suggests that the mass of silica added to the lacquer may be important, in addition to the bulk volume. So in the case of SPS, more of the bulk volume is in fact silica so at high $\frac{m_{sil}}{m_0}$, there will be less space in the silica structure accessible to the polymer. This may reduce the degrees of freedom of the silica to pack in the drying film compared to the lighter silicas. Note that we distinguish this 'piling up' of SPS from the surface roughening of CPS and UPS. These larger particle size silicas show a sharp rise in R_a at the $\frac{m_{sil}}{m_0} \approx 0.72$ for CPS and $\frac{m_{sil}}{m_0} \approx 0.8$ for UPS. The rise in R_a is more gradual in the case of SPS, although more data would be desirable to clarify this point. This accounts for the sloping dotted lines in figure 8.15. Recall also that SPS is structurally weak, and we do not expect a robust network like CPS and UPS. We explore this point further in the next chapter.

Chapter 9

Optical properties

We have seen that the structure assumed by the silica is described by our model of chapter 3. This chapter is devoted to understanding how the optical properties of the system are related to the silica structure. Matt lacquers are distinguished by their low specular reflection. Here we investigate the dependence of reflection on the silica structure. By measuring specular reflection, it is also possible to follow film formation in ambient conditions. At constant temperature and humidity, we can compare drying of different lacquers more quantitatively than our ESEM work allowed.

As reflection is primarily a surface phenomenon, we relate the measurements to the AFM surface roughness measurements. We recall that Franklin [17] found that the surface roughness parameter R_a was linearly related to the reduction in specular reflection. We compare our measurements of R_a to reflection in order to compare with his result. Using reflection-mode CLSM, we can also investigate reflection on the microscopic lengthscale. In particular, we should be able to determine whether reflection is a surface or bulk phenomenon.

Franklin [17] noted that different silicas exhibited more or less wide-angle light scattering (haze, defined in figure 2.12). This scattering is associated with changes in refractive index (RI) in the bulk of the film. Since the silica and polymer are RI-matched, we associate this RI mismatch with the introduction of air voids. We investigate possible mechanisms for hazing with CLSM and freeze-fracture ESEM with reference to our silica structure model.

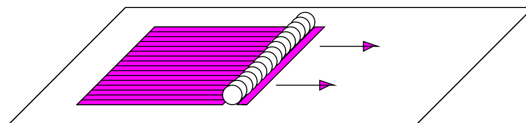

Figure 9.1: A bar coater. The lacquer is drawn out in the grooves of the bar. Surface forces then level the film to a calibrated thickness (100 μm here).

Sample Preparation

Here we introduce our experimental procedures for reflection and haze measurements, as defined in figure 2.12. We describe sample preparation and experimental procedure, paying special attention to the fact that here we are dealing with *clear* lacquers, as distinct from pigmented, opaque lacquers. The absence of pigment introduces haze as a property of the film, as a pigmented system clearly has a very high proportion of light scattered by more than 2.5°.

The differing scales of the reflection and haze apparatus compared to microscopy necessitate a different sample preparation method (figure 9.1). Instead of the micro-applicator, we use a bar coater. Essentially, this is a metal rod wrapped in wire. Upon application, the lacquer is forced through the grooves of the bar coater. Surface forces then level the film, whose thickness is determined by the grade of wire wrapped around the bar. We use a bar which produces a wet nominal film thickness of 100 μm. The sample area is typically 100mm square.

9.1

Light scattering: Hazing

We now consider the bulk optical properties in the form of 'haze'. Recall that haze is light scattered through more than 2.5° (figure 2.12). This is strongly related to microstructural properties accessed via confocal microscopy. Here we label the lacquer with rhodamine instead of FITC to reveal further structure. We then analyse our microscopy results and compare them with the macroscopic property of haze.

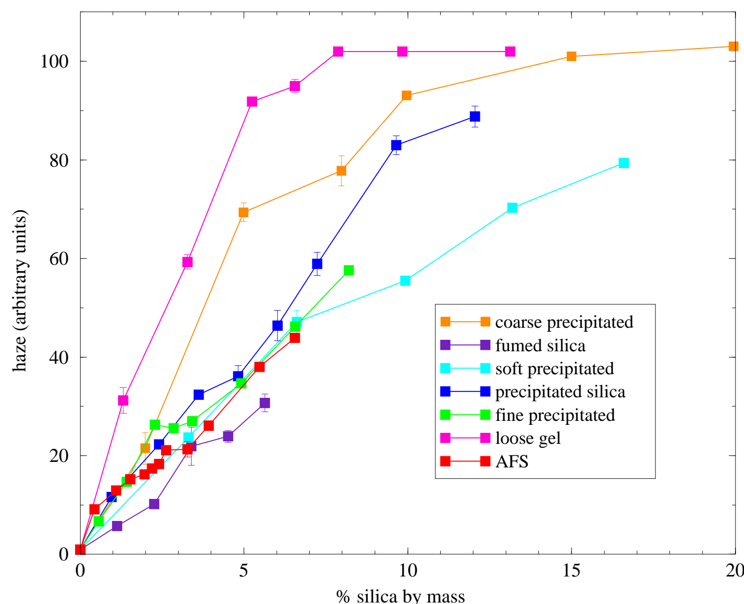

Figure 9.2: Haze as a function of % silica mass. Haze appears to be a function of silica mass added. Note however that silica gel, coarse, unsieved and soft precipitated exhibit successively lower haze values for a given mass of silica added.

Aside from the CLSM work, we measure haze by transmitting light through the substrate. We laid a single layer of lacquer on glass, using the bar coater with a wet depth of 100μm. We then measured the fraction of light scattered away from the normal. In the units of the haze meter used [126], the maximum value was 103. This was assumed to correspond to all normal light scattered by more than 2.5°. The results for haze as a function of % silica mass of the (wet) lacquer formulation are shown in figure 9.2.

Haze appears to be a function of silica mass (figure 9.2) rather than volume added to the lacquer. However, there is some evidence for the increased haze behaviour of some silicas suggested by Franklin [17]. Here we have repeated his measurements on a silica gel, which was found to have a rather high haze value as a function of the per cent mass of silica in the lacquer. Coarse precipitated silica also has a high haze behaviour, suggesting that these larger precipitate particles may behave in a similar way to a gel. Soft precipitated silica has a rather lower haze value. We investigate the reasons for this haze behaviour in the next section.

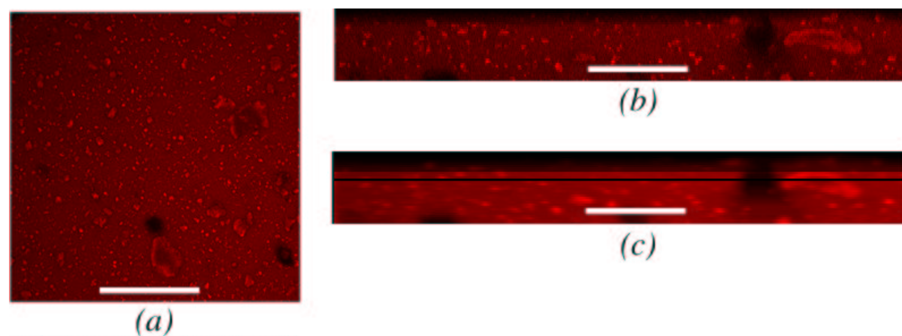

Figure 9.3: Confocal images of dried film with AFS labelled with rhodamine ($\frac{m_{sil}}{m_0}$=0.94). (a)*: xy image Bar=50µm,* (b) *xz image,* (c) *contrast enhanced xz image, Bars=25µm. Some larger silica particles can be seen, along with 'dark regions'. The dark line in* (c) *locates the xy plane in* (a).

9.2

Confocal Microscopy: Hazing

We can examine the origins of hazing using confocal microscopy. By labelling the samples with rhodamine instead of FITC as before, we can determine the optical properties in more detail. Rhodamine labels both silica and polymer background, so we obtain rather different information than from FITC labelled images. Our experimental procedure is identical to that described in chapter 7, page 110 except that we mix the silica with a 1% by mass aqueous solution of rhodamine 6G (obtained from Sigma). We use a 543 nm laser to excite the rhodamine with a 560nm low frequency filter to select only the fluorescent light emitted. Further details are given in the appendix, on page 218.

Typical images are shown in figures 9.3 to 9.8 for AFS ($\frac{m_{sil}}{m_0}$=0.94), fine ($\frac{m_{sil}}{m_0}$=0.92), soft ($\frac{m_{sil}}{m_0}$=0.89), unsieved ($\frac{m_{sil}}{m_0}$=0.88), calcined ($\frac{m_{sil}}{m_0}$ = 0.90) and coarse precipitated silica ($\frac{m_{sil}}{m_0}$=0.72) respectively.

All of these images except the soft precipitated silica reveal dark regions. Since rhodamine labels both silica and polymer, it seems reasonable to interpret these dark regions as air voids. The dark regions correlate quite well with our haze measurements, as we see that the CPS has a large amount of dark regions, compared to unsieved and particularly

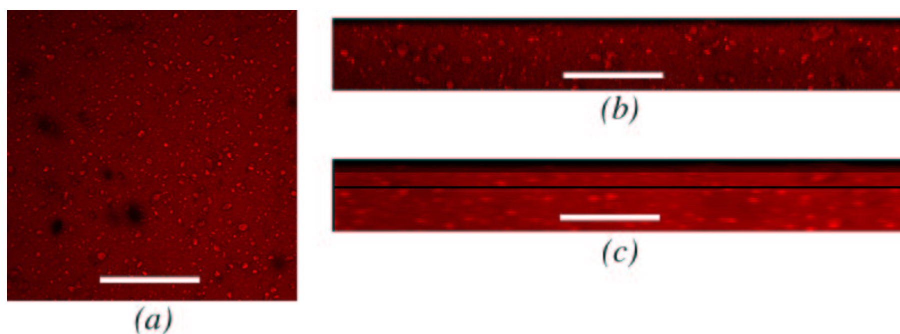

Figure 9.4: Confocal images of dried film with fine precipitated silica labelled with rhodamine ($\frac{m_{sil}}{m_0}$=0.92). (a)*: xy image Bar=50μm,* (b) *xz image,* (c) *contrast enhanced xz image, Bars=25μm. The dark line in* (c) *locates the xy plane in* (a).

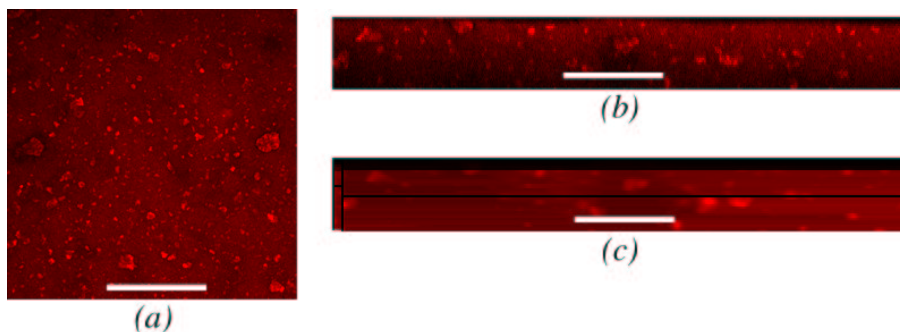

Figure 9.5: Confocal images of dried film with soft precipitated silica labelled with rhodamine ($\frac{m_{sil}}{m_0}$=0.89). (a)*: xy image Bar=50μm,* (b) *xz image,* (c) *contrast enhanced xz image, Bars=25μm. The dark line in* (c) *locates the xy plane in* (a).

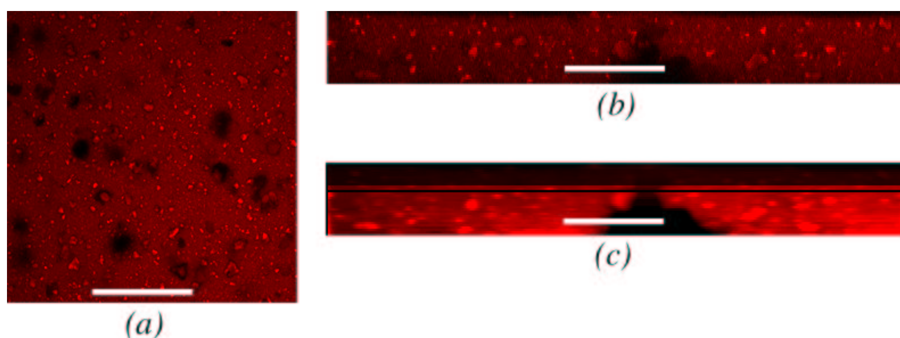

Figure 9.6: Confocal images of dried film with unsieved precipitated silica labelled with rhodamine ($\frac{m_{sil}}{m_0}$=0.88). (a)*: xy image Bar=50μm,* (b) *xz image,* (c) *contrast enhanced xz image, Bars=25μm. The dark line in* (c) *locates the xy plane in* (a).

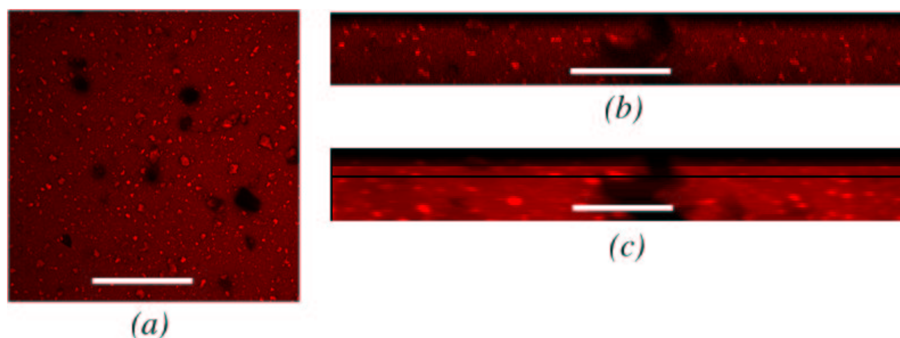

Figure 9.7: Confocal images of dried film with calcined precipitated silica labelled with rhodamine ($\frac{m_{sil}}{m_0}$=0.90). (a)*: xy image Bar=50μm,* (b) *xz image,* (c) *contrast enhanced xz image, Bars=25μm. The dark line in* (c) *locates the xy plane in* (a).

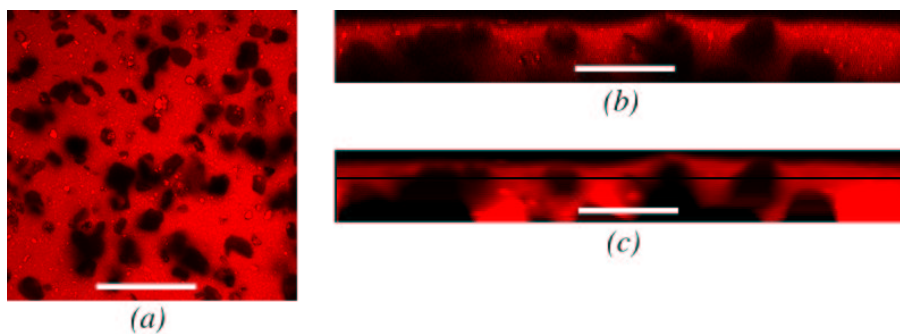

Figure 9.8: Confocal images of dried film with coarse precipitated silica labelled with rhodamine ($\frac{m_{sil}}{m_0}$=0.72). (a)*: xy image Bar=50μm,* (b) *xz image,* (c) *contrast enhanced xz image, Bars=25μm. The dark line in* (c) *locates the xy plane in* (a).

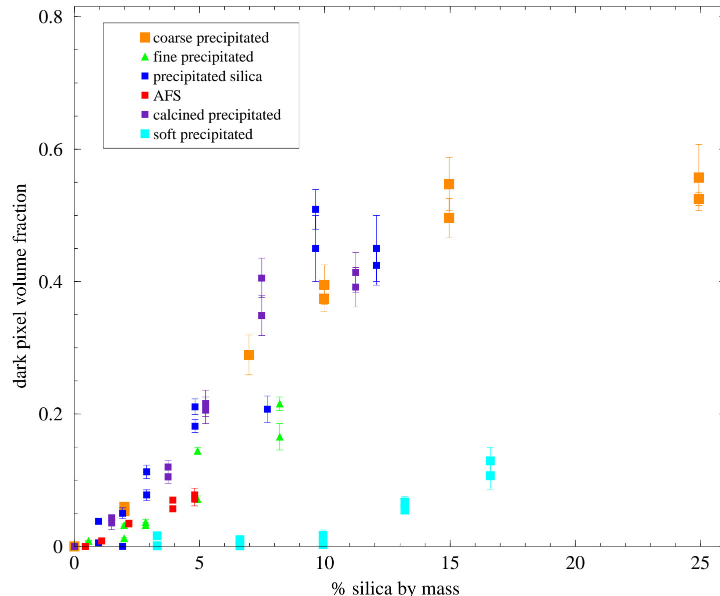

Figure 9.9: Dark pixel fraction as a function of silica per cent by mass. We see a similar behaviour to figure 9.2, although the soft precipitated silica has exceptionally few dark pixels.

soft precipitated silica.

Here we consider the heat-treated (calcined) precipitated silica (figure 9.7). This silica expected to have surface chemistry similar to AFS, but mechanical properties similar to the unsieved precipitated silica (chapter 2 section 2.3). The calcined precipitated silica is shown in figure 9.7, but there is no significant difference compared to the untreated precipitated silica (figure 9.6), suggesting that calcination has little effect.

Using the contrast enhancement method discussed in chapter 6 section 6.4, we can partially correct for attenuation. The corrected images are shown in figures 9.3*(c)*-9.8*(c)*. Using a brightness threshold, we can then obtain a value for the 'dark pixel' volume fraction from the corrected image. This is simply the fraction of pixels with brightness of less than 80. Recall from chapter 6 section 6.4 that we can identify the surface in these images, so we consider only 'dark pixels' below the surface.

Plotting this 'dark pixel' volume fraction against per cent mass of silica added, we see a fairly similar behaviour for all silicas, except the SPS (figure 9.9). The data in figure 9.9 show the same trends as those in 9.2, although CPS and UPS behave more similarly. The dark pixel fraction is a function of silica mass, with all points falling roughly on the same

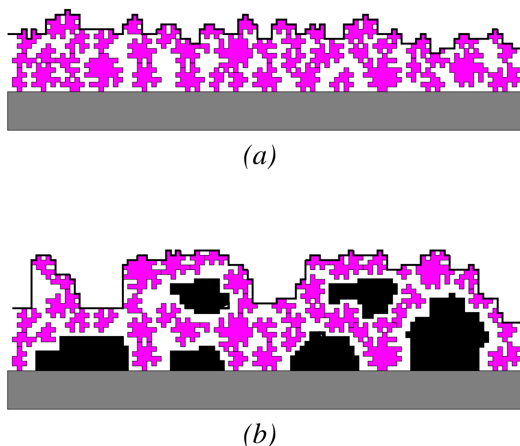

Figure 9.10: Schematic of the model of silica structure within dried lacquer reproduced from chapter 3. Here we illustrate the two possibilities for $\frac{m_{sil}}{m_0} > 1$, with silica densification from collapse (a), or void formation with more robust silica (b).

line, excepting soft precipitated silica. The plateau at a volume fraction of around 0.5 is taken to be saturation introduced via the contrast enhancement process.

The correlation between haze and dark pixel measurements is interesting. UPS, FPS and AFS have similar behaviour as a function of mass in both cases. CPS exhibits high haze, but most interesting is SPS. This has lower haze, but near-zero dark pixel volume fraction, which suggests that there are two components to haze. One is related to 'dark pixels' and one is more intrinsic to the silica-polymer system, and dependent upon silica mass fraction.

9.3

Mechanisms for Hazing

So how may we interpret these 'dark regions' in figures 9.3 to 9.8? The most obvious solution, in terms of our silica structure model is to regard these dark regions as large air voids. This is consistent with the fact that the more robust silicas seem to form more of these 'voids' than for example, the AFS, as we see from figure 9.3 and figure 9.8. Thus we may identify two regimes, with AFS and possibly SPS forming a structure similar to

figure 9.10*(a)* and other precipitated silicas behaving as shown in *(b)*.

However, in chapter 8 we argued that FPS showed signs of both structural collapse, and increased surface silica fraction at high $\frac{m_{sil}}{m_0}$. Adopting this idea for the other precipitated silicas, as they behave similarly in ESEM work, we suggested that some form of partial collapse best explained our behaviour. Here we seek to determine whether this idea of partial collapse is valid. The crucial point is that without *any* collapse, there must be a high volume fraction of air voids at $\frac{m_{sil}}{m_0} \sim 2$, which should be possible to detect. The absence of these air voids will show that partial collapse, a mix of the behaviours of figures 9.10*(a)* and *(b)* provides the best explanation.

One possible way to test for air voids might be the film thickness, which would increase in the case of a non-collapsing silica structure, but remain fixed around the $\frac{m_{sil}}{m_0}$=1 value for a collapsing structure. However the thickness is influenced by viscosity [122], which is itself dependent on silica type and concentration. Film thickness will not be a good measure of any void formation.

Freeze-fracture ESEM

We begin this investigation with freeze-fracture ESEM. For freeze fracture ESEM, we base our approach on that which Sutanto *et al.* [127] developed for conventional SEM. This technique allows ESEM to access the bulk of the material, by cleaving the dried film to reveal the interior. Here we use a film which was dried overnight, in ambient conditions. This film was then dipped in liquid nitrogen, to render it sufficiently brittle to cleave easily. The samples were laid down on a glass coverslip, which was fractured during to cleave the film.

Having fractured the film, we placed it edge-up in the ESEM, to reveal the interior. We hoped to image a vertical section through the film, which would reveal a structure similar to that in figure 9.10*(b)*. We used coarse precipitated silica, with $\frac{m_{sil}}{m_0}$=0.72, as this silica was known to produce large amounts of 'dark regions' (figure 9.8).

As the images in figures 9.11 and 9.12 show, there is little evidence for these 'dark regions' from freeze-fracture ESEM. Air voids on the scale of 20 μm and above would have been easy to detect as the surface topography at the edge of the void would give a strong

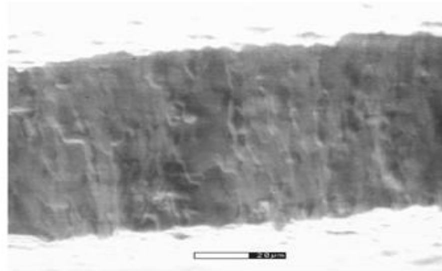

Figure 9.11: Freeze-fracture ESEM image film containing coarse precipitated silica $\frac{m_{sil}}{m_0}$*=0.72. The structure is not what we would expect from figure 9.10*(b)*. Bar=40*μ*m.*

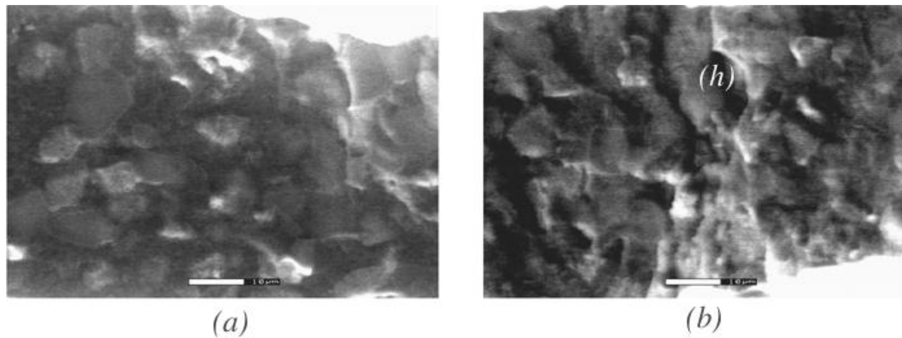

Figure 9.12: The same sample as figure 9.12, at higher magnification. Although (a) *does not show anything which resembles a void, the region marked as* (h) *in* (b) *may be interpreted as an air void. Bar=10*μ*m.*

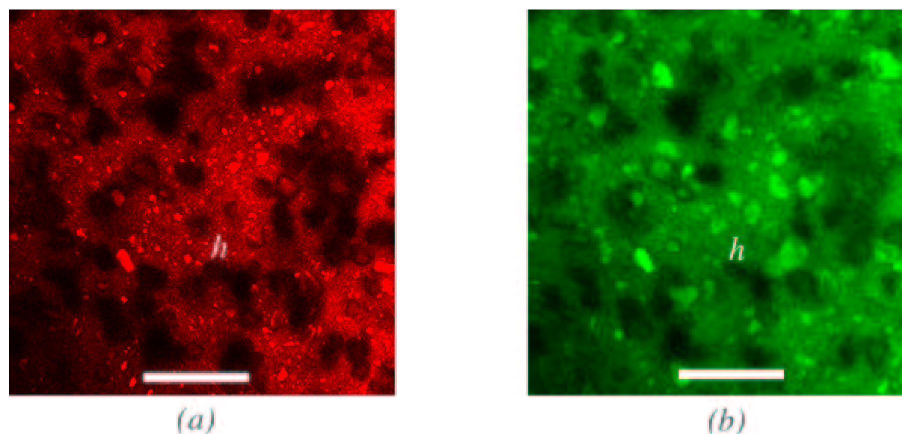

Figure 9.13: CLSM xy images of coarse precipitated silica ($\frac{m_{sil}}{m_0}$=0.72) labelled with both rhodamine (a) *and FITC* (b). *The FITC image shows some bright (silica) regions, which are dark in the rhodamine image, especially around the region marked* (h). *Bars=40μm.*

secondary electron signal. A possible void is marked as *(h)* in figure 9.12*(b)*, but there are not enough of these structures to explain our 0.5 'dark pixel' volume fraction of figure 9.9.

Dual labelling in confocal microscopy

To further investigate these 'voids', we used the confocal microscope. By labelling a sample with both FITC and rhodamine, it was possible to see if the 'dark regions' in a rhodamine image were in fact silica particles. We labelled a sample with FITC as described in chapter 8 page 136. Rhodamine was then added to the formulation in aqueous solution. We used 2cm^3 of a solution of 0.1% rhodamine by mass in the 50 cm^3 sample.

We prepared a sample of coarse precipitated silica, $\frac{m_{sil}}{m_0}$=0.72, for comparison with the freeze-fracture ESEM work. Two xy images produced from this work are shown in figure 9.13, with rhodamine *(a)* and FITC *(b)* labelling. Some of the 'dark regions' in figure 9.13*(a)* are in fact revealed to be silica particles in *(b)*, particularly around the region marked *(h)*. So at least a proportion of these 'dark regions' are silica.

There is a considerable amount of 'cross-talk' between the rhodamine and FITC signals. Although the dyes were excited at different wavelengths (533nm and 488nm) for rhodamine and FITC respectively, the 488nm excitation appears to produce some rhodamine signal,

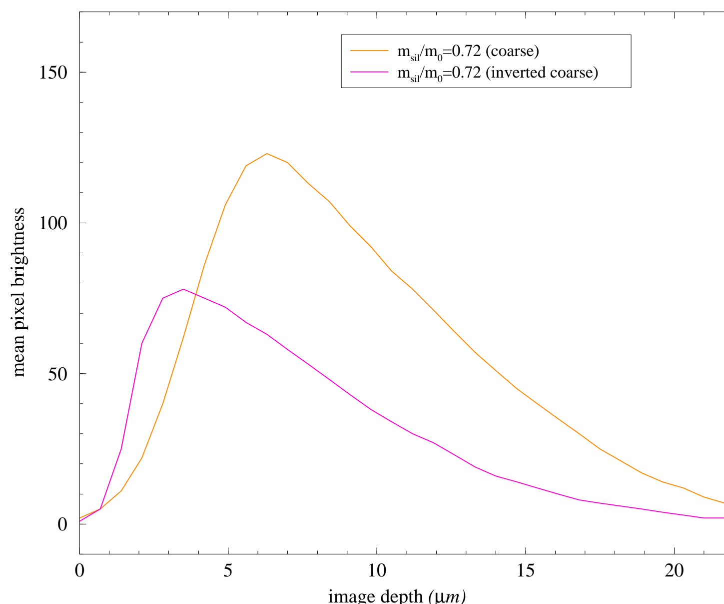

Figure 9.14: Mean pixel brightness as a function of depth for inverted (red line) and non-inverted (orange line) films. Since both plots show the same trends, the decrease in brightness must be an artifact of the confocal microscope, rather than an intrinsic property of the sample.

by comparison with earlier FITC images (chapter 8, section 8.3). This is not surprising, as the emission and absorption spectra of these dyes extend across a considerable wavelength range [14].

Sample inversion

Another test for the occurrence of voids was to invert some samples in the confocal microscope. These were prepared with a glass coverslip as a substrate. Imaging was then through the coverslip, so the 'top' surface for the confocal microscope was the film-substrate interface. We used samples prepared with rhodamine as described above.

The results were analysed by determining the mean pixel brightness as a function of depth. As we noted above and in chapter 6 section 6.4, after an initial rise to the top surface of the film, the mean pixel brightness decreased with increased penetration into the film, which we associated with the 'dark regions'.

The mean brightness of images of films with coarse precipitated silica ($\frac{m_{sil}}{m_0}$=0.72) is

shown as a function of depth in figure 9.14. While not identical, we see that the signal produced from inverted and non-inverted samples show the same trends.

These dark regions then, are simply artifacts of the confocal microscope. We interpret them as 'shadowing' by large silica particles. These silica particles will not in general have all their pores filled by the latex, as a fair proportion are significantly less than 80nm, the latex diameter, recall (chapter 3 table 3.2) that the mean pore diameter for coarse precipitated silica was 42nm. So the space occupied by these silica particles is assumed to be a combination of silica with the a significant fraction of pores filled with air. Light passing through such a particle will encounter a number of interfaces and changes in refractive index, so we expect light scattering to be very strong in the locality of these large particles. This strong scattering will clearly reduce the transparency and increase the haze in the film. We return to the property of haze in our analysis of reflection mode CLSM, but note that this investigation supports our idea of partial collapse in the case of the precipitated silicas.

If the silica structure structure did not undergo collapse at all (figure 9.10*(b)*) then we would have seen a very different structure with the freeze-fracture ESEM, with many more air voids. In the absence of a high volume fraction of these air voids, we conclude that the silica structure must collapse, in agreement with our arguments in chapter 8 page 167.

Returning to figure 9.2 we can now understand haze behaviour rather better. *All* silicas show increasing haze with silica mass, as adding more silica of any type adds to the number of interfaces within the film which promote light scattering. Now mass appears to be more important than bulk volume here, for if we look at low values of silica by mass ($\lesssim 5\%$), we see than all silicas excepting the silica gel lie roughly on the same line, despite their very different densities (and hence bulk volumes, table 3.1).

However there seems to be a second factor at work here, as the difference between silica gel, CPS, UPS and SPS, for silica mass fraction $\gtrsim 7\%$ shows. We know from our confocal work that in shadowing terms, CPS and UPS exceed SPS, for a given mass fraction of silica. This shadowing presumably contributes to the haze, which is why we see a different behaviour, particularly at high silica loadings. We return to this argument in the conclusion to this chapter. For now we note that we have identified two factors which

influence the haze: silica mass fraction and the degree of shadowing.

9.4

Reflection

We now turn to reflection, the defining property of matt water-based lacquers. Here we seek to relate it to the silica and our structure model. We draw heavily on AFM measurements of surface roughness (chapter 8, section 8.4) as this is closely linked to reflection.

Experimental

A typical experimental set-up for determining specular reflection is shown in figure 9.15. The light source is white on the Byk-Gardner gloss meter used [128]. We see from the figure that in the case of clear, transparent lacquers, the reflection from the film-substrate interface may contribute to our signal. We know that this is the case, as different substrates consistently give varying results.

Ideally we would like to use a matt black substrate, which would have a negligible reflection. However this has its own drawbacks. Matt black surfaces are (unsurprisingly) very rough and porous. So even without any silica in the film, we end up with a roughened surface and decreased reflection. Here we use placquettes [129]. These are sheet aluminium with a matt coating, which has been sealed to limit porosity. To further seal the substrate, we used a film of silica-free lacquer with a wet depth of 100 μm. In this way, the substrate did not contribute significantly to the reflection, nor did it effect the surface of the film. We then laid the film to be measured on top of this layer.

Film Formation

Using our reflection technique, we can follow film formation. Unlike the ESEM work, we can work in ambient temperature and humidity. Not only does this result in properly

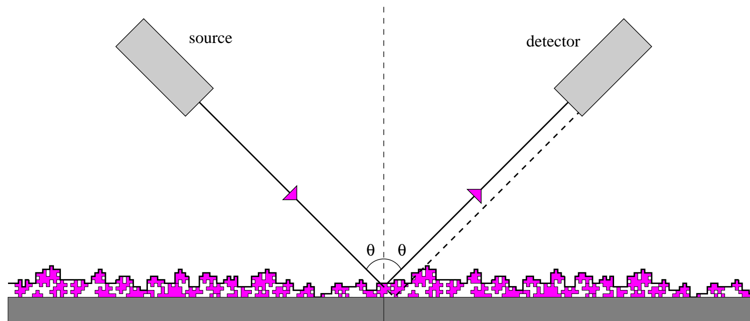

Figure 9.15: A typical experimental set-up for determining the spectral reflectance. It is clear that, if the lengthscale of the film is small compared to the detector, then we can have an additional signal from the film-substrate interface in the case of clear *lacquers.*

formed films (recall that in chapter 7 film formation ceased at stage II*), but the conditions are relatively stable. So successive experiments may be compared with one another. The film formation was carried out at a temperature of 26°C and a relative humidity of 40%. We used a white light source and an incident angle of 60°, measured on a Byk Gardner gloss meter [128]. The films were laid down with a bar coater as described above, on the aluminium placquettes with a wet depth of 100 μm.

We then measured the specularly reflected light as a function of time from the moment at which the film was laid down. The results for various silicas are given in figure 9.16. Typically we see a 2 minute period when the surface is smooth, corresponding to high reflection. Here the lacquer is still in stage I of film formation. After volume reduction following water removal silica begins to perturb the surface, which continues until the majority of water has evaporated, which in this case corresponds to a transparent film of stage III. Since volume reduction is now complete the reflection is constant over time.

We see that without any silica, our reflection actually increases during film formation. Initially, when the latex spheres are in an aqueous suspension, there is a large polymer-water interface, resulting in a large degree of light scattering and absorption. Removing the water produces a more transparent film, so a residual contribution from the film-substrate interface can boost the reflection. AFS (figure 9.16 *(a)*) also shows a small increase in reflection at longer times, presumably for the same reason.

There is another possible reason for this slight hump in the AFS system (figure 9.16 *(a)*). The structural collapse in AFS may have an associated time lag, during which

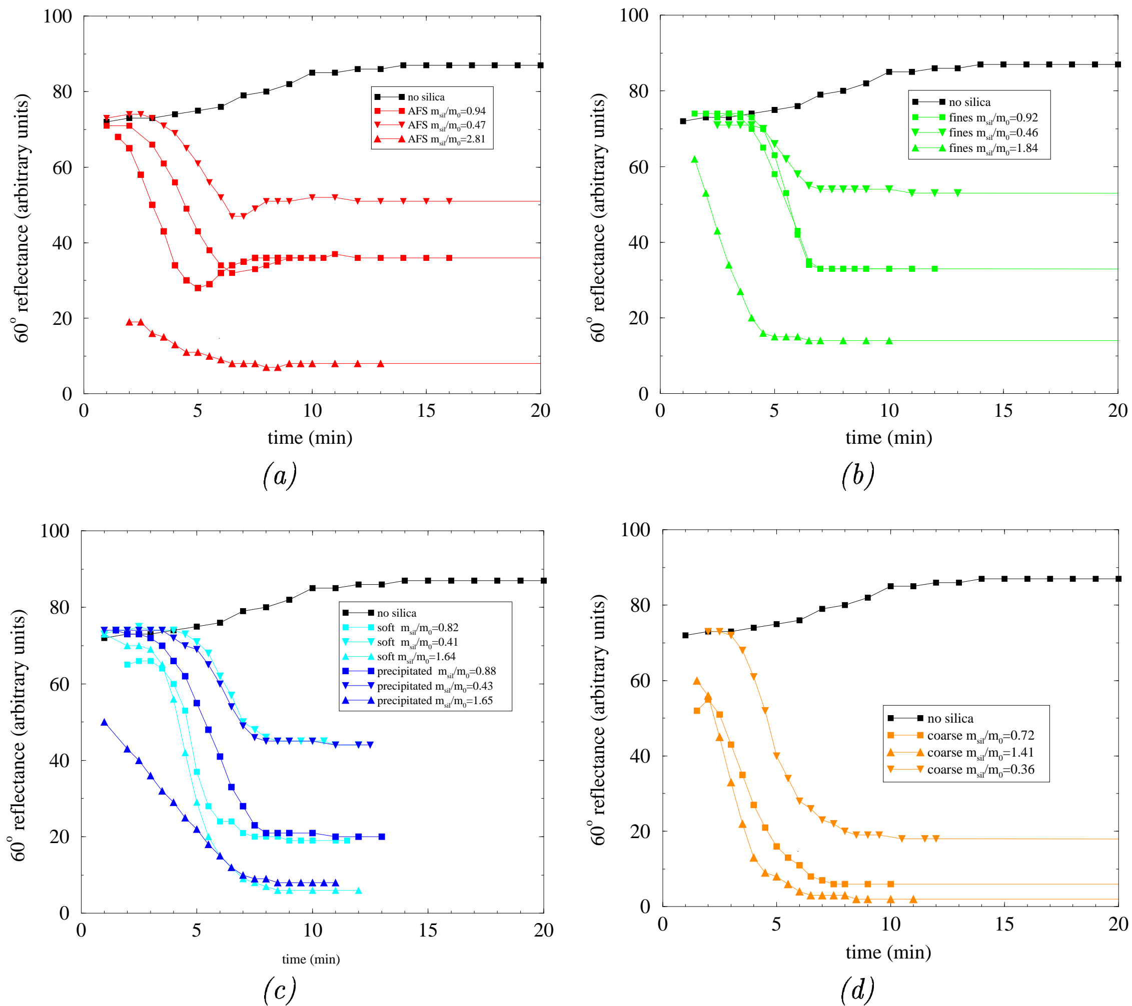

Figure 9.16: Reflectance as a function of time, during film-formation. A variety of silica concentrations ($\frac{m_{sil}}{m_0}$) *are used for AFS* (a), *fine* (b), *soft and unsieved* (c) *and coarse precipitated silica* (d). *The wet film is shiny, as expected. Reflectance reduces as silica perturbs the surface, higher* $\frac{m_{sil}}{m_0}$ *causes a more rapid loss of reflection. (Incident angle = 60°).*

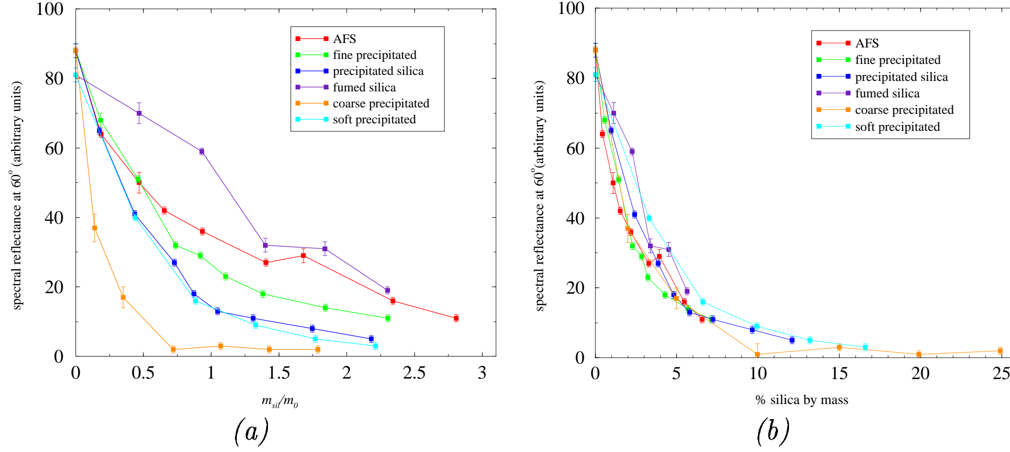

Figure 9.17: Reflectance as a function of $\frac{m_{sil}}{m_0}$ (a) *and per cent silica by mass added to the formulation* (b). *It is clear that plotting reflection as a function of silica mass produces a similar behaviour for silicas. Error bars are the standard deviation. (Incident angle = 60°).*

surface forces act to flatten the surface of the film. This flattening would tend to increase the reflection, resulting in the 'hump'.

We have varied the the silica concentration in each case. From our interpretation of drying in chapter 7 page 122, we expect that with a higher silica concentration, less volume reduction is needed for the surface to become rough due to the silica network. For example, if $\frac{m_{sil}}{m_0}$=1, we have a network when all the water has evaporated and volume reduction is largely complete. By contrast, for $\frac{m_{sil}}{m_0}$ ∼3, since the solids fraction C_{sol} = 0.35 the silica should form a network in the wet lacquer. Here we have again assumed that the density of the water and the latex are equal (see appendix, page 217). With a silica network in the wet lacquer, we would expect an instant reduction in reflection without the need for any volume loss from water evaporation. This we see for $\frac{m_{sil}}{m_0}$=2.8 in figure 9.16*(a)*. This trend holds for all the silicas, in that at high $\frac{m_{sil}}{m_0}$, the time taken before there is some loss of reflection is reduced. Data points denoted by squares (■) correspond to moderate $\frac{m_{sil}}{m_0}$, triangles pointing down (▼) to low $\frac{m_{sil}}{m_0}$ and triangles pointing up (▲) to high $\frac{m_{sil}}{m_0}$. The final values of reflectance here correlate well with those in figure 9.17*(a)*.

Reflection and surface roughness

Here the samples were dried in ambient conditions. We plot our reflection measurements as a function of $\frac{m_{sil}}{m_0}$ (figure 9.17*(a)*) and the per cent mass of silica added to the formulation (figure 9.17*(b)*). The angle to the normal was again 60°. It is clear from these plots that although adding more silica causes a decrease in reflection, the absolute reflection is dominated by the silica *mass*. All silicas produce a fairly similar behaviour as a function of silica mass fraction.

This is not what we would expect, since our model predicts a marked increase in surface roughness at $\frac{m_{sil}}{m_0} \approx 1$, which would be expected to lead to a decrease in reflection around this value (figure 9.10). This rapid reduction in reflection is in fact seen at the critical pigment volume fraction (CPVC) for pigmented lacquers [48]. Indeed our AFM measurements showed that at $\frac{m_{sil}}{m_0} \gtrsim 1$, the more robust coarse and unsieved precipitated silica exhibited much greater surface roughness. How do we reconcile these reflection measurements with AFM work and the predictions of our model?

In fact, a close look at figure 9.17*(a)* shows that CPS has reflection dropping sharply to $\frac{m_{sil}}{m_0} \approx 0.7$ (the percolation threshold). For higher values of $\frac{m_{sil}}{m_0}$ the reflection is constant and small. Similarly, unsieved precipitated silica has reflection falling quickly to $\frac{m_{sil}}{m_0} \approx 1$, after which the decline is slower. So as in AFM, these two silicas behave as we would expect if they form a roughened surface around the critical mass. Further decline in the UPS case is not unreasonable. Recall that ESEM work shows the surface becoming more silica-rich at higher $\frac{m_{sil}}{m_0}$ (chapter 8, section 8.5).

If we plot the AFM surface roughness measurements as a function of silica mass, we see that only the soft, coarse and unsieved precipitate have a mass per cent of $\gtrsim 7\%$ (figure 9.18*(a)*). We also note that there is a trend for a large percentage of silica by mass to produce a high degree of surface roughness.

Crucially, CPS and UPS have a high bulk density (table 3.1), but they also have a number of larger aggregate particles as we saw from the AFM and ESEM work, boosting surface roughness (figure 8.15). So we see that an increase in aggregate particle size (and bulk density) will result in a mass-dependence in the surface roughness plot in figure 9.18*(a)*.

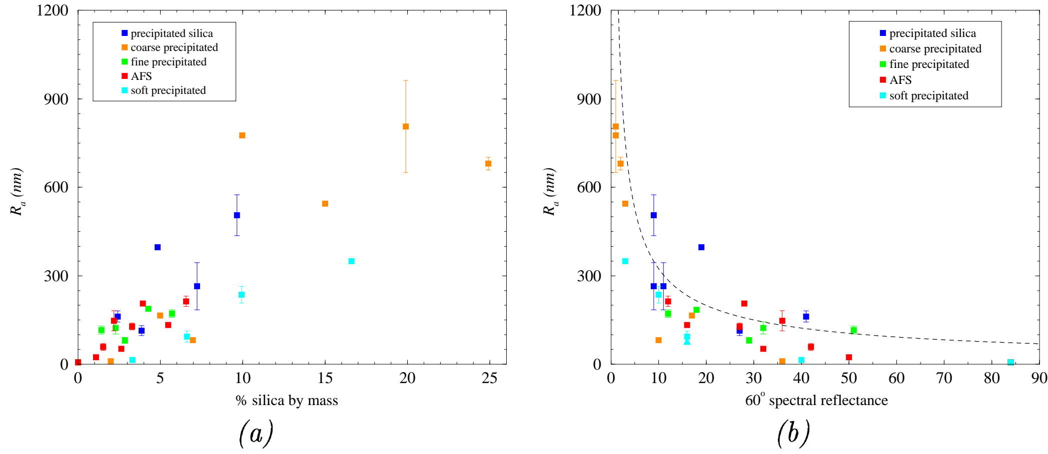

Figure 9.18: AFM measurements of R_a as a function of silica mass per cent (a) *and reflection* (b)*.* (a) *shows a continuous increase in R_a with mass %, excluding soft precipitated silica. In* (b) *we see that low reflection need not require large surface roughness.*

By plotting the R_a results against reflection, the mass-dependence of reflection and R_a is reproduced (figure 9.18*(b)*). We see that there there is a broad hyperbolic trend, as shown by the black line. In particular, high R_a values are always accompanied by low reflectance. At this point we note that these high R_a values are of the order of the wavelength of light. It seems reasonable that if $R_a \sim \lambda_{light}$ then we would expect some considerable decrease in reflection.

This hyperbolic trend must however be treated with caution. It is consistent with our ideas that at very high surface roughness, we expect essentially no reflection, and at low roughness we expect high reflection. However we can see from the plot that a significant number of data points lie well away from the fitted line, but we have already noted in chapter 8, section 8.4 that our AFM results come from a statistically small sample. Although this data does not exactly agree with Franklin's finding of a linear dependence between reflection and R_a, the trend is in the same direction, and presents a unifying relation for all silicas [17].

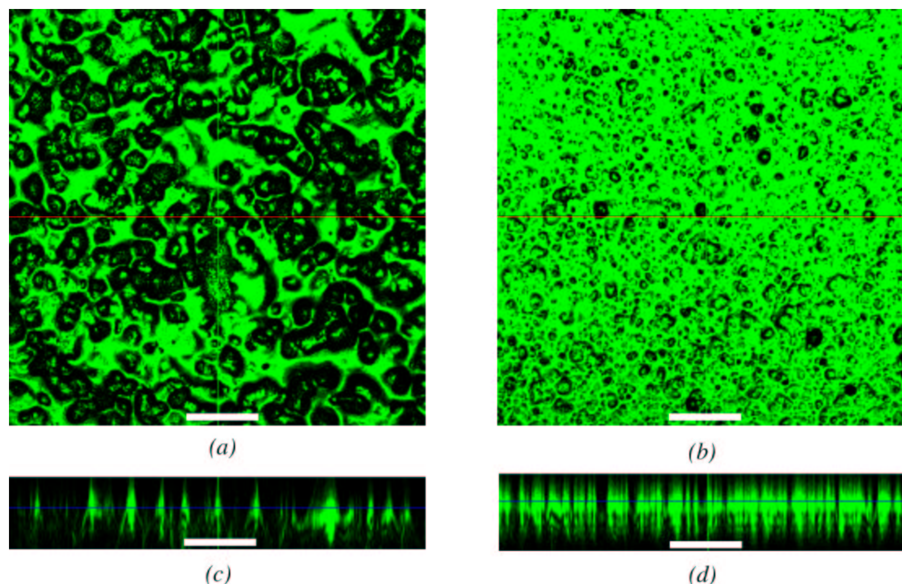

Figure 9.19: Reflection mode CLSM images with a non oil-immersion lens. (a) *xy,* (c) *xz, CPS* $\frac{m_{sil}}{m_0}$*=0.72;* (b) *xy,* (d) *xz, AFS,* $\frac{m_{sil}}{m_0}$*=0.93. The reduction in intensity from the coarse precipitated silica surface image is clear compared to the AFS sample. Blue lines in xz images show xy location, red lines in xy vice versa. Bars=50µm.*

9.5

Reflection Mode CLSM

We can unite the optical properties with our microscopy techniques by using the CLSM in reflection mode. Here, instead of light emitted by a fluorescent dye, we investigate light that is simply reflected. Rather than mapping the distribution of the fluorophore, the source of contrast is refractive index variation. In practice this is straightforward to implement, as we simply remove the filter which discriminates against reflected light. We avoid fluorescent signals by using a laser source of a significantly different wavelength to the fluorescent absorption of the dye.

To begin with, we investigated the film-air interface. Since we wanted the surface reflection in air, we did not use an immersion oil, so a suitable Zeiss LD achroplan 32× lens

was chosen. This lens has a lower axial resolution than the usual Zeiss 63× Planapochromat. We used a 633nm HeNe laser source to avoid any fluorescent signal which might have been contributed at an excitation wavelength below ∼540nm, as the sample was labelled with rhodamine to enable dual-mode imaging.

Figure 9.19 shows reflection mode images, for coarse precipitated silica (*(a)* and *(c)*, $\frac{m_{sil}}{m_0}$=0.72) and AFS (*(b)* and *(d)*, $\frac{m_{sil}}{m_0}$=0.94). The reduced axial resolution is apparent in the streaking of figures 9.19*(c)* and *(d)*. On scanning in the z direction, the lacquer-air interface forms a plane of maximum brightness. This one plane produces the bulk of the reflection, and is smeared out due to the poor axial resolution. So reflection is strongest around the surface, as we expected from our work above.

Recall that coarse precipitated silica has around 10.0% silica by mass for $\frac{m_{sil}}{m_0}$=0.72, around five times that of the AFS (table 3.1). Now this suggests that we may expect to interpret the dark regions in figures 9.19*(a)* and *(b)* as silica. The lengthscale is appropriate in each case, and we know from AFM work and the silica structure model that the key differences between these samples are the mass of silica added and increased surface roughness in the CPS case.

So if these dark regions of silica reduce the normally reflected light, then we can understand why the reflection is related to R_a. Although close inspection of figure 9.19*(b)* suggests that silica is present throughout the surface, in accord with the silica structure model, the AFS is much more strongly reflecting than the CPS. Clearly the rougher CPS surface would be expected to produce more of these dark areas, where the (normally) incident light is reflected away the normal.

Since we know from our AFM work that the CPS surface is much more rough, the darker regions in figure 9.19*(a)* are taken to be the sloping sides of silica particles, which reduce the specular reflection. This idea is further supported by the fact that within each dark (sloping) region is a bright feature which we interpret as the (flat) top surface of the silica particle. So the AFS is simply flatter and consequently has a higher specular reflection, although dark regions here also have bright reflecting central plateaux.

By using an oil immersion lens (a Zeiss Planapochromat 63×), we can do two things. The RI mismatch at the film surface is reduced from around 1 : 1.45 to 1.515 : 1.45, lowering the reflection at the surface. The second effect is the increase in xz image quality

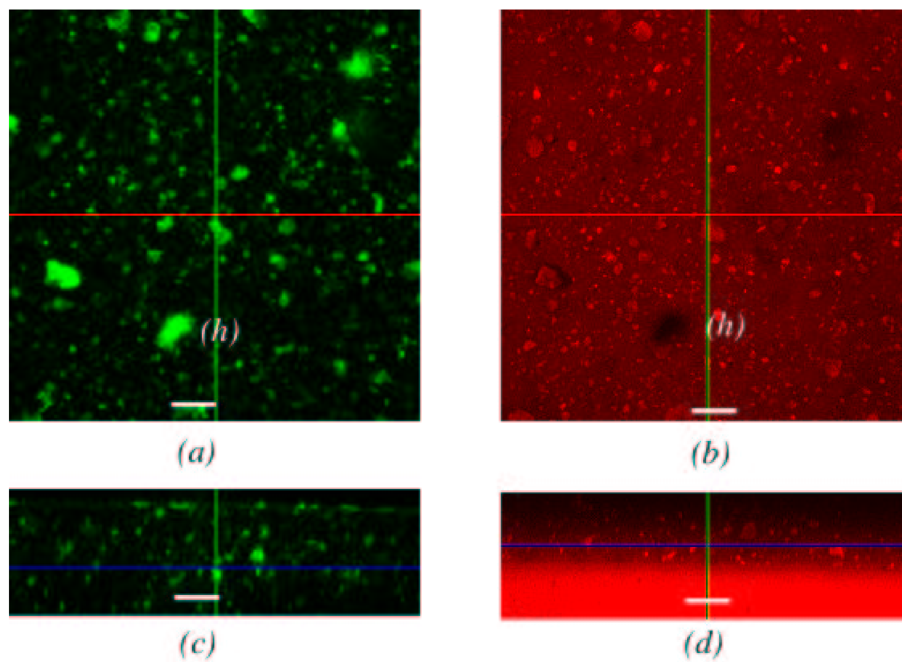

Figure 9.20: CLSM images of AFS $\frac{m_{sil}}{m_0}$*=0.94 using an oil-immersion lens.* (a) *(xy)*, (c) *(xz), reflection mode images ,* (b) *(xy)*, (d) *(xz) rhodamine fluorescent labelling. The xz images in the same plane, although not at exactly the same height. The blue line which indicates the location of the xy planes is at the same height in each image. Red lines in xy images show xz location. Bars=20μm.*

from the improved lens resolution and reduction in spherical aberration.

These two factors allow us to image sub-surface silica, it is related to RI mismatch within the bulk of the film. For the reflection work, we again used the 633nm laser, but with a rhodamine-labelled sample, we were also able to image the same area in fluorescence mode in the usual way.

The subsurface silica is clearly seen in figure 9.20 *(a)* xy and *(c)* xz, for AFS $\frac{m_{sil}}{m_0}$=0.94. Comparison with the rhodamine image of the same region, figure 9.20 *(b)* xy and *(d)* xz, it is clear that both silica and 'dark regions' such as that marked *(h)* cause strong reflection. That the 'dark regions' and silica are indistinguishable in reflection mode further supports the idea that they are simply silica with air-filled pores.

The xz image, figure 9.20*(c)* reveals some residual surface reflection. The rhodamine xz image *(d)* shows a lower layer of film with a higher concentration of rhodamine giving a stronger signal. For reflection CLSM work, we used a matt substrate with two layers of silica-free lacquer, which produced a stronger rhodamine signal.

The CPS system (figure 9.21) interacts far more strongly with normally incident light. In figures 9.21*(a)* and *(c)* we reduced the CLSM detector gain enormously compared to figure 9.20, but the large silica particles are still very bright. The bright regions of strong reflection in figure 9.21*(c)* correlate very well with the dark regions in *(d)*.

We see that using an oil immersion lens removes the main source of reflection, the surface. This subsurface behaviour we would expect to be related to the haze. Clearly the CPS film which interacts more strongly with normally incident light will produce higher haze than AFS, as previously noted.

9.6

Conclusions

Here we discuss the findings of this chapter, and how we may build an understanding of the parameters which determine the optical properties.

Following film formation with reflected light shows that surface roughness forms gradually during drying, following an initial period during which the surface remains strongly

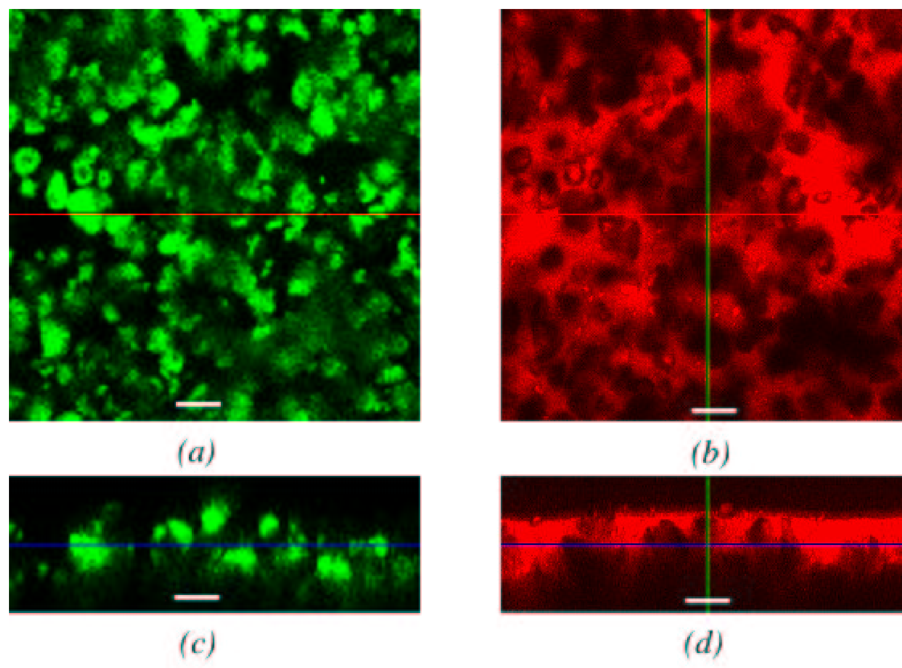

Figure 9.21: CLSM images of coarse precipitated silica $\frac{m_{sil}}{m_0}$*=0.72 using an oil-immersion lens.* (a) *(xy),* (c) *(xz), reflection mode images ,* (b) *(xy),* (d) *(xz) rhodamine fluorescent labelling. Blue lines in xz images show xy location, red lines in xy vice versa. Bars=20µm.*

reflecting. This first stage (I-II) in film formation is dominated by the volume reduction from water evaporation. At some point, the silica structure begins to perturb the surface. The point at which this occurs depends on the volume occupied by the silica, as given by $\frac{m_{sil}}{m_0}$.

At high $\frac{m_{sil}}{m_0}$, the greater volume occupied by the silica structure perturbs the surface at earlier times, as less volume reduction driven by water evaporation is required. Along with the gradual loss of reflection, this work correlates well with our volume-driven film formation interpretation of chapter 7 (figure 7.7), where silica is gradually exposed during film formation in stages I-II*.

In the dried film, we find that both haze and reflection are related to silica *mass* rather as well as volume as we have assumed in our structure model. We begin this discussion by considering haze, before moving on to reflection.

Haze is regarded as a bulk property, dependent upon sources of light scattering within the film, *ie* refractive index mismatch. Figure 9.2 showed that haze is a function of silica *mass* (not bulk volume), although at higher loadings, different haze behaviour was seen for silica gel, CPS, UPS and SPS. We now explain this different haze behaviour in terms of porosity.

We have seen from reflection mode CLSM that coarse precipitated silica interacts with normally incident light far more strongly than AFS. Of course, between the samples we looked at, there is five times as much silica by mass in the film with the CPS. Much of this extra mass of silica is found in larger, denser particles. The CPS pore diameter here is below smaller than the latex (typically 42nm (table 3.2) chapter 3, table 3.2), so the pores are assumed to be filled with air. This air-silica medium has a structure below the lengthscale of light, so it may be regarded as having a single RI, which differs from that of the surrounding polymer.

It is this difference in RI on a 10μm lengthscale which we believe is responsible for the very strong interaction between CPS and incident light. This causes shadowing in CLSM ('dark regions') and high haze. So the shadowing in CLSM need not be interpreted as air voids on the 20 μm scale, as in figure 9.10*(d)*. The silica gel particles are a similar size to coarse precipitated silica particles, and the pores are even smaller at 19nm (table 3.2 in chapter 3). So it is reasonable to associate the high haze behaviour here with

small, unfilled pores in relatively robust aggregate silica particles. Recall from chapter 2 section 2.3 that in silica gels the ultimate particles are more strongly bound. We also note that unseived and calcined precipitated silica both had some large silica particles, which were associated with dark regions and haze. In particular, no effect was seen from the calcination, so we conclude that hazing is driven by physical properties rather than the surface chemistry between the silica and polymer.

Contrast this haze behaviour with soft precipitated silica. Here there is less hazing and none of the 'dark regions' in CLSM work. We have also seen from ESEM studies that SPS particles tend to be rather small. This absence of large aggregate particles then reduces the light scattering for soft precipitated silica, as incident light does not encounter such large regions of refractive index mismatch.

Another reason to expect low haze behaviour with SPS is its low pore volume, just 0.1 $\mathrm{cm^3g^{-1}}$ of which is inaccessible to the latex, only $\frac{1}{5}$ of the other silicas. With SPS, therefore, very little air is introduced and we see a corresponding drop in haze.

We have shown with AFM work (chapter 8, section 8.4) that the latex is highly deformed in our film formation conditions. So if the there is *some* pore penetration, then smaller aggregate silica particles such as SPS, FPS and AFS would have relatively fewer air-filled pores. This in turn would reduce the extent of the RI mismatch and therefore the haze.

Finally we turn to reflection. We know that reflection is surface dominated through reflection mode CLSM. This agrees with the fact that R_a and reflection are inversely related. This second point is the key to our model. Reflection decreases sharply up to $\frac{m_{sil}}{m_0} \sim 0.7$ for CPS, and also for UPS up to $\frac{m_{sil}}{m_0} \sim 1$. This correlates with the observation that these silicas have high R_a values which increase sharply near the critical mass. Moreover these silicas which have larger aggregate particles are also rather dense. So by adding more silica by mass, we decrease the specular reflection as we will typically add more larger particles which boost the surface roughness.

The smaller aggregate particle silicas, AFS and FPS have higher reflections for a given $\frac{m_{sil}}{m_0}$. However while the R_a is fairly constant for these silicas at all loadings, reflection decreases with increased silica mass fraction. The denser SPS also with small aggregate particles extends this mass dependence, as a greater mass of silica is added to the formu-

lation for a given $\frac{m_{sil}}{m_0}$.

From reflection mode CLSM we associated low contrast with the sides of silica particles. Although we have only looked at one mass of CPS and AFS in reflection mode CLSM, it is reasonable to suppose that adding more silica would result in more dark sides of silica particles, and hence loss of reflection.

This dependence of reflection upon silica mass fraction in AFS and FPS suggests that R_a should also vary as a function of silica mass for these silicas. However we have a statistically small number of samples in our R_a measurements, and the hyperbolic nature of the reflection-R_a relation would require very precise determination of R_a in the AFS/FPS mass fraction range of less than about 6% silica. As previously noted, at a higher mass fraction SPS produced $R_a \approx 400nm$ and a corresponding loss in reflection in any case.

From this chapter we conclude that:

(1) Reflection and R_a are inversely related.

(2) Reflection is a surface phenomenon, dependent on silica mass through surface roughness introduced by larger, denser silica particles.

(3) Haze is a function of silica mass but is influenced by silica particle porosity.

(4) CPS and UPS have large silica particles which act as sources of scattering and light shadowing in CLSM.

(5) Smaller aggregate silica particles reduce light scattering in AFS, FPS and particularly SPS which may be related to pores being partially filled with deformed latex.

(6) Air voids on the lengthscale of silica particles are not significant, so the precipitated silicas must undergo some form of partial structural collapse at high $\frac{m_{sil}}{m_0}$.

Chapter 10

Summary and Conclusions

The conclusions from this work fall broadly into two categories: our improved understanding of matt water-based lacquers, and the developments in experimental and analytical techniques we have made along the way. In this chapter we therefore summarise the main results, beginning with developments in methodology. We also consider possible further work, and sum up with a list of key conclusions.

10.1

Developments in methodology

This work has encompassed a range of microscopy techniques. Here we consider the key developments made in applying the two principle techniques, ESEM and confocal microscopy to matt water-based lacquers.

Beam damage in ESEM

The study of beam damage via radiolysis (chapter 5) gives some interesting results. Although Kitching *et al.* [100] noted an increase in damage with high beam energy, it is only now that the reason has become clear. The quantity of reactive species present in a water sample increases dramatically at higher beam energies. We see a very non-linear

dependence, as the volume in which the species are formed goes (in our approximation) as the cube of the mean primary electron (PE) range. The PE range is itself a non-linear function of beam energy, increasing with electron energy [106]. Given the second-order annihilation reaction rates between reactive species, we have far higher annihilation at the lower beam voltages where the shorter PE range leads to vastly higher concentrations of reactive species. This annihilation between the reactive species reduces their potential to damage the sample. In addition, at low beam energies, the species are produced in smaller quantities.

Therefore we expect that reducing the beam voltage will drastically lessen the beam damage, as more of the reactive species produced will annihilate with each other. This correlates with our practical work, where we saw a significant drop in damage from 12keV to 8keV beam energy and the work of Kitching [100].

Another key finding of this work was to identify the most significant free radical: $\cdot$OH. The hydroxyl radical is present in far greater quantities than other species, except the relatively stable hydrogen peroxide. Hydrated samples which are especially sensitive to $\cdot$OH will suffer particularly high beam damage in ESEM.

The increased mobility from liquid water, rather than ice in *cryo*-SEM was harder to quantify. However we see a significant broadening of the concentration profile from self-diffusion when reactive species are confined to a small region, as is the case at lower beam energies. At higher beam energies the reactive species are more spread out, so the concentration gradient is rather small. Diffusion here is not tremendously important. We therefore conclude that the increase in damage in the presence of water as found by Kitching may be related to water as a source of small, highly mobile free radicals, similar to Talmon's [73] discussion for *cryo*-SEM.

In-situ **film formation in ESEM**

Previous work by Meredith *et al.* focussed on acquiring images of film formation [18] [19] [68]. These workers found that latices could be hard to follow during film formation, as the transition from stage I to stage III often presented little contrast in ESEM due to the concurrent particle deformation and water evaporation of latex particles above the

minimum film-forming temperature (MFT) [5]. The latex particles were either covered in a layer of water (stage I) or had deformed to produce a layer of polymer too smooth to produce enough contrast for the ESEM (stage III).

Although Meredith *et al.* were in fact able to image most stages of film formation despite these difficulties, the small lengthscale necessitated by the latex diameter (< 0.5 μm) meant a high magnification. This resulted in significant beam damage, so to follow the same area throughout film formation was very hard indeed.

By contrast, here we have followed film formation from the silica inclusions. These aggregate silica particles are up to 10 μm in size, so we need only use 800$\times$ original magnification, whereas Meredith *et al.* worked at 4-6000$\times$. The 25 fold reduction in electron density on the sample vastly reduced the beam damage, which in turn was critical in enabling us to follow film formation.

From the work of Cameron *et al.* we have developed a modified optimised pump-down. By lowering the sample temperature and adding a water source, the evaporation during initial pumpdown was much reduced. This means we are confident that the images produced correspond to *in-situ* film formation, rather than simply the evaporation of condensed water from a previously dried film. Unlike a purely latex system, the silica gives sufficient contrast to follow film formation closely, despite the fact that the latex itself is not accessible to ESEM.

We have developed image analysis for ESEM. Recall that ESEM images are hard to treat systematically, due to fluctuating conditions. Our combination of gradient and brightness thresholds is shown to work well. We can quantify surface (or near surface) silica. The cluster counting algorithm allows further quantitative information to be extracted.

Confocal microscopy and image analysis

In confocal microscopy we have developed techniques for labelling the silica in matt lacquers. Using fluorescein iso-thiocyanate, only the silica is labelled, whereas rhodamine 6G labels both silica and polymer, revealing further structure.

We adopted the methods of Conchello *et al.* [94] [95] [113] to reconstruct our images

via the expectation maximisation algorithm. This significantly improved the resolution and we were able to image the sub-micron silica structure throughout the bulk of the film.

These reconstructed images presented new challenges for our image analysis. Although silica extraction via brightness threshold segmentation was straightforward, there was a wealth of information to be tapped. The crucial development was to label and distinguish clusters, working in 3D. We could then count and size clusters, and also investigate the percolation behaviour of the system.

10.2

Matt lacquers

We now turn to the matt lacquer system. Here there are two phenomena which we have investigated. The microscopic structure assumed by the silica, and how it correlates with the model we proposed. The latex suspension is treated as a continuous medium, except for some particular considerations. Secondly we have studied the optical properties which distinguish matt lacquers. In particular we have looked at spectral reflection and light scattering in the bulk of the film, and related them to the silica structure model. First we consider the silica microsctructure.

Silica structure

The central assumption of the silica structure model is that the silica does not interact strongly with the other components of the lacquer. From this assumption, we determined a critical silica mass fraction of the lacquer formulation. At this mass fraction, the bulk volume of the silica equalled the volume of film-formed lacquer (silica and polymer binder). In other words, at the critical mass, the process from mixing the lacquer though to film formation is equivalent to replacing the air between the silica particles with polymer. Above the critical mass we have two possibilities. The silica structure can collapse or may be robust enough enough to resist the compressive forces introduced through water evaporation during film formation. In this second case we expect a sharp rise in surface

roughness at the critical mass along with void formation.

There are some similarities between our approach and that of Asbeck and van Loo [48] with their critical pigment volume concentration (CPVC). However they make no relation between CPVC and the dry pigment powder. Instead CPVC is defined in terms of pigment wetting by polymer binder. Our silica structure is not related to having sufficient binder to fully wet the silica. We implicitly assume that there is enough polymer available. We find no evidence of the large scale air voids implied by Asbeck and van Loo.

We imaged the silica structure in the bulk of the film using 3D confocal microscopy. Our silica structure model assumed percolation, which was demonstrated by image analysis of space-spanning clusters. This focussed on cluster counting and geometric properties of the largest cluster in the image. These measurements support our model of randomly distributed silica particles, which form a percolating network a little before a critical mass corresponding to the self-supporting dry powder. A key exception here was (non-agglomerated) fumed silica, which forms a spanning structure well below the critical mass. This correlates with Kleinschmidt's observation that in suspension, fumed silica reversibly forms spanning networks at low concentrations [16].

CLSM image analysis gives us the silica packing fraction according to our model. The packing fraction is the volume fraction of silica particles and internal pores at the critical mass. It is around 0.15 for agglomerated fumed silica (AFS) and fine precipitated silica (FPS), but rather higher at 0.19 for fumed silica and higher still for coarse precipitated silica (CPS) at 0.32. The larger CPS particles must therefore pack more closely than the smaller FPS ones, which correlates with the higher CPS bulk density.

CLSM shows structural collapse for AFS and also for FPS. When the bulk silica volume exceeds that of the dried film, we see densification for these silicas, so the silica structure collapses as the volume of the lacquer reduces during film formation.

This is backed up by ESEM. AFS shows no surface change beyond a silica loading of around 1.5 times the critical mass, so additional silica simply collapses in the bulk. By contrast, all precipitated silicas show a characteristic increase in silica surface fraction at high silica volume fraction, suggesting some resistance to collapse. This is in keeping with the more robust nature of precipitated silica. Interestingly the surface silica fraction has the same value for all precipitated silicas for a given $\frac{m_{sil}}{m_0}$, regardless of their bulk density.

This provides strong evidence that the silica structure depends upon the bulk volume of silica added, as we have assumed. However, despite some resistance, there is at least partial collapse for precipitated silica. Certainly FPS shows some densification at high silica loading in CLSM and we present evidence for other precipitated silicas below.

AFM work contributes three further key pieces of information. The latex deforms strongly during film formation, corresponding to stage III. This is consistent with a high-quality film. Secondly, the silica is covered in these deformed latex particles, at all silica loadings used. So strictly there is very little surface silica. Thirdly the surface roughness parameter R_a is not solely dependent upon silica volume fraction, although it does exhibit a strong increase around the critical mass for UPS and CPS as expected. Above the critical mass, the R_a tends to band according to the size of the aggregate silica particles, so for the smaller FPS and AFS no significant change is seen in R_a at the critical mass. AFS collapses in any case, so no change in R_a is expected.

SPS exhibits gradually rising surface roughness at high silica loading. We interpret this as a 'piling up' of silica within the bulk of the film. Although SPS is structurally weak (so collapse is expected), its high bulk density is thought to reduce the freedom to pack efficiently at high silica loading. These 'piles' of silica then protrude through the surface of the film, and raise the surface roughness.

We understand ESEM results of *in-situ* film formation in terms of the silica structure model. To extend the model to describe film formation, we interpret stages I to II* or III as volume reduction from water evaporation. The receding lacquer surface exposes the tips of silica particles first, before revealing more and more as the film formation progresses. The was determined using image analysis to count the silica particles and to find the surface silica fraction as a function of time. However we note the limitations of the ESEM operating temperature, as film formation did not proceed past stage II* during our experiments.

The silica structure model predicts that for high silica loadings, only a small reduction in lacquer volume from water evaporation is required before the silica perturbs the surface. Since smaller quantities of water take less time to evaporate, we expect to see this time dependence in reflection measurements. Reflection is sensitive to silica as it is inversely related to surface roughness. The characteristic decrease in reflection that occurs when

the silica structure first perturbs the surface during film formation happens at a shorter time at higher silica loadings. This is simply because the smaller water volume required evaporates more quickly.

Optical properties

The key aspect of clear matt lacquers is their optical behaviour. Low specular reflection is crucial to a successful product. Previous work by Schneider [11] and Franklin [17] defined matt lacquers in terms of their optical properties.

In clear matt lacquers, we have considered both reflection and the bulk light scattering property haze. Both show a dependence on silica mass fraction. In the case of haze, silica within the film acts as a source of light scattering, so a greater mass fraction of silica can produce more scattering. The mass dependent behaviour was backed up when we found through reflection mode CLSM that denser CPS interacted far more strongly with light than did AFS in the bulk of the film.

Moreover Franklin's suggestion that some small pores are not filled by latex particles seems entirely reasonable. We find that silicas with smaller pores produce somewhat more haze, for the same mass fraction, whereas in the absence of pores, SPS produces little haze, for a given mass of silica added.

One possible extension of our silica structure model to high silica loading suggested that a very robust silica structure might resist the capillary pressure of film formation, and produce very large air voids on the lengthscale of the silica particles, similar to the CPVC of Asbeck and van Loo [48]. This has been found not to be the case, from freeze-fracture ESEM and dual-labelling CLSM. The dark regions in some CLSM images are merely shadowing from large, dense, silica particles with pores filled with air. This absence of air voids confirms that precipitated silica undergoes partial collapse during film formation, although there is some resistance, which promotes surface roughness.

Reflection is dependent on silica mass fraction like haze. It is dominated by the interface at the top of the lacquer, as we have shown with reflection mode CLSM. We find that reflection is inversely related to R_a, but unlike Franklin we do not find a negative linear correlation. Now reflection is related to silica mass fraction through R_a, which increases

strongly at the critical mass for UPS and CPS. In reflection we see a sharp drop to the critical mass before some levelling off once the very rough structure is formed above the critical mass.

Increased surface roughness is expected to reduce reflection. What is more interesting is the fact that these parameters depend on silica mass. However the larger, denser silica particles of CPS and unseived precipitated silica (UPS) promote surface roughness and correspond to a large mass of silica being added. Nonetheless this doesn't fully explain why we have a near universal behaviour for reflection as a function of mass for both fumed and precipitated silica over a wide density range, and from silicas such as FPS from which large dense particles are absent. For example for AFS and FPS reflection decreased with silica mass even when no change in R_a was found with AFM. This may be due to insufficient data, or possibly an effect of more silica-polymer interfaces in the film, at higher silica loading. These could act to reduce the reflection through more light absorption, as we know from reflection mode CLSM that some reflection occurs below the surface.

10.3

Future work

Although we have extracted much of what our techniques have to offer on this system, there are still some questions. The mass-dependence of reflection still seems a little curious. The obvious way to investigate this more fully is more reflection mode CLSM. More AFM work to improve the R_a statistics would also help us to pin down whether reflection varies for an apparently constant R_a, particularly for AFS and FPS.

More samples would enable a more accurate determination of percolation thresholds, and how closely these correspond to the critical mass. This would also tell us how steep the increase in surface roughness in the case of CPS and UPS around the critical mass is.

CLSM could also be used to image film formation *in-situ* in ambient conditions. Our attempts at this were confounded by the low axial resolution encountered when an oil immersion lens is not used. However we have already inverted a dry sample. It is not beyond the bound of possibility to image an inverted sample in stage I-II, laid on a

coverslip. Although inverted, this technique would allow in-situ imaging during drying. We could also use reflection-mode CLSM to image in-situ film formation, which would also be sensitive to water content, as the aqueous latex has a great deal of RI mismatch.

Given our extensive image analysis techniques, it should be possible to track the location of individual particles during drying, where we could determine whether drying is, as assumed, essentially a vertical contraction in the majority of the film.

One key aspect of a silica structure which we have not considered is the effect on film porosity. Asbeck and van Loo [48] note a significant increase in porosity at their critical pigment volume concentration, which is associated with the formation of small air voids. Clearly our silica structure may well affect the porosity.

10.4

Conclusions

.

We now present our key conclusions for technique development:

(1) ESEM can follow *in-situ* film formation of a specific region.

(2) Beam damage of hydrated specimens in ESEM is very strongly dependent on beam energy, increasing at high beam energies.

(3) The dominant reactive species in water samples is ·OH, the hydroxyl radical.

(4) Diffusion is more significant at lower beam energies.

(5) We can separate silica from the polymer/water matrix for both ESEM and CLSM images.

(6) CLSM images of matt lacquers are highly accessible to reconstruction of the specimen function via deconvolution.

(7) Percolation phenomena can be accessed via CLSM image analysis.

Matt water-based lacquers:

(1) Silica forms a structure in dried lacquer similar to that in the absence of polymer, at a certain critical mass.

(2) The silica structure percolates as expected, close to (but before) the critical mass.

(3) The packing fraction is related to the silica density.

(4) All precipitated silicas have a unique surface silica fraction as a function of bulk volume of silica added.

(5) AFS collapses totally at high silica loading.

(6) UPS and CPS structures undergo partial collapse, but these more robust covalently bound particles produce a sharp increase in surface roughness at the critical mass.

(7) FPS behaves similarly to UPS/CPS although there is no surface the roughness increase at the critical mass.

(8) SPS ‘piles up’ above the critical mass, so surface roughness increases relatively gradually.

(9) The film surface is largely covered in deformed latex particles, including the silica regions.

(10) Haze is characterised by the silica mass fraction.

(11) Light scattering is accentuated by large silica particles with air-filled pores.

(12) Reflection is inversely related to surface roughness.

(13) Both reflection and surface roughness are related to silica mass fraction through the presence of large, dense silica particles in CPS and UPS.

(14) The silica behaviour is dominated by the physical properties: despite similar surface chemistry, AFS and calcined precipitated silica still behave very differently.

Bibliography

[1] G.P.A. Turner. *Introduction to Paint Chemistry.* Chapman and Hall, London, 3rd edition, 1991.

[2] J.C. Padget. Additives for water-based coatings - a polymer chemist's view. *Royal Society of Chemistry Special Publication*, (76):1–29, 1988. Editor: D. R. Karsa.

[3] D.C. Blackley. *Emulsion Polymerisation.* London, 1975.

[4] L.A. Matheson R.E. Dillon and E.B. Bradford. Sintering of synthetic latex particles. *jcs*, 6:108–117, 1951.

[5] G.L. Brown. Formation of films from polymer dispersions. *jps*, 12:423–434, 1956.

[6] M.C. Jenkins J.W. Vanderhoff, H.L. Tarkowski and E.B. Bradford. Theoretical consideration of the interfacial forces involved in the coalescence of latex particles. *Journal of Macromolecular Chemistry*, 1(2):361–367, April 1966.

[7] D.P.Sheetz. Formation of films from drying of latex. *japs*, 9:3759–3773, 1965.

[8] J.L. Keddie. Film formation of latex. *Materials Science and Engineering R*, 21(3):101–170, December 1997.

[9] M.A. Winnik. *The Formation and Properties of Latex Films.* John Wiley and Sons Ltd, 1997.

[10] R.K. Iler. *The chemistry of silica.* John Wiley and Sons Ltd, 1979.

[11] H. Schneider. Matting of modern surface coatings. *Surface Coatings International*, 77:376–385, 1994.

[12] G. Morea-Swift. Personal communication.

[13] G.D. Danilatos. Introduction to the esem instrument. *Microscopy Research and Technique*, 25:354–361, 1993.

[14] J.B. Pawley. *Handbook of Biological Confocal Microscopy.* Plenum Press: New York and London, 2nd edition, 1995.

[15] D. Sarid. *Scanning force microscopy, with applications to electric, Magnetic and Atomic Forces.* Oxford series in optical and imaging sciences. Oxford University Press, Oxford UK, 1991.

[16] P. Kleinschmidt. Silicas and related materials. *Royal Society of Chemistry Special Publications*, (40):196–225, 1981.

[17] K. R. Franklin and A. Small. Optical properties of water-based lacquer coatings containing silica matting agents. Crosfield Group Internal Publication, 1996.

[18] R.A.L. Jones J.L. Keddie, P. Meredith and A.M. Donald. *Rate-limiting steps in film formation as elucidated with ellipsometry and environmental scanning electron microscopy*, pages 332–348. Number 648 in ACS Symposium Series. American Chemical Society, Washington DC, December 1996.

[19] R.A.L. Jones J.L. Keddie, P. Meredith and A.M. Donald. Kinetics of film formation in acrylic latices studied with multiple-angle-of-incidence ellipsometry and environmental sem. *ACS Symposium Series*, 28(8):2673–2682, 1995.

[20] F. Dobler and Y. Holl. *Mechanisms of particle deformation during latex film formation*, pages 22–43. Number 648 in ACS Symposium Series. American Chemical Society, Washington DC, December 1996.

[21] S.S. Voyutskii. Ammendment to the papers by bradford, brown and coworkers:"concerning mechanisms of film formation from high polymer dispersions. *jps*, 17(125):528–530, 1958.

[22] H. Schuller K. Hahn, G. Ley and R. Oberthur. On particle coalescence in latex films. *Colloid and Polymer Science*, 264:1092–1096, 1986.

[23] G. Ley K. Hahn and R. Oberthur. On particle coalescence in latex films ii. *Colloid and Polymer Science*, 266:631–639, 1988.

[24] Z. Hruska C-L Zhao, Y. Wang and M.A. Winnik. Molecular aspects of latex film formation: An energy-transfer study. *Macromolecules*, 23(18):4082–4087, 1990.

[25] M.A. Winnik. Latex film formation. *Current Opinion in Colloid and Interface Science*, 2:192–199, 1997.

[26] J. Frenkel. Viscous flow of crystalline bodies under the action surface tension. *Journal of Physics of the Academy of Sciences, USSR*, 9(5):385–391, 1945.

[27] G. Mason. Formation of films from latices: A theoretical treatment. *British Polymer Journal*, 6:101–108, 1973.

[28] S.T. Eckersley and A. Rudin. Mechanism of film formation from polymer latexes. *Journal of Coatings Technology*, 62(780):332–348, 1990.

[29] F. Lin and D.J. Meier. A study of latex film formation by atomic force microscopy. 1. a comparison of wet and dry conditions. *Langmuir*, 11(7):2726–2733, 1995.

[30] M. Lambla F. Dobler, T. Pith and Y. Holl. Coalescence mechanisms of polymer colloids 2: coalescence with evaporation of water. *Journal of Colloid and Interface Science*, 152(1):12–21, 1990.

[31] M. Lambla F. Dobler, T. Pith and Y. Holl. Coalescence mechanisms of polymer colloids 1: coalescence under the influence of particle-water interfacial tension. *Journal of Colloid and Interface Science*, 152(1):1–11, 1990.

[32] K. Kendall and J.C. Padget. Latex coalescence. *International Journal of Adhesion and Adhesives*, pages 149–154, July 1982.

[33] M.L. O'Dowd P.R. Sperry, B.S. Snyder and P.M. Lesko. Role of water in particle deformation and compaction in latex film formation. *Langmuir*, 10(8):2619–2628, 1994.

[34] J.C. Hwa. Mechanism of film formation from latices. phenomenon of flocculation. *Journal of polymer science: A*, 2:785–796, 1964.

[35] A.F. Routh and W.B. Russel. A process model of latex film formation: particle deformation. In *Proceedings of the American Chemical Society Division of Polymeric Materials: Science and Engineering*, volume 81, pages 209–210, 1999.

[36] J.B. Clarke. Additives for water-based coatings: A review. *Polymer Paint Colour Journal*, 181:496, 1992.

[37] F.J.J. Riesthuis J.H. Bieleman and P.M. van der Velden. The application of urethane-based thickeners to polymeric systems. *Royal Society of Chemistry Special Publication*, (76):156–180, 1988. Editor: D. R. Karsa.

[38] L.J. Calbo, editor. *Handbook of Coatings Additives*. Marcel Dekker, New York, 1987.

[39] J.I. Amalvy and B. del Amo. Flow properties of acrylic latices. *Surface Coatings International*, (2):78–81, 1997.

[40] W. Scholz. Additives for aqueous coatings. *J. Oil and Colour Chemists Assoc.*, 184(4354):172–174, 1994.

[41] D. Clarke. Foam control agents for surface coatings. *Royal Society of Chemistry Special Publication*, (76):243–255, 1988. Editor: D. R. Karsa.

[42] C. Isenberg. *The science of soap films and soap bubbles*. John Wiley and Sons Ltd, 1979.

[43] K.R. Walker. Role of coalescing aids in latex paints. *Royal Society of Chemistry Special Publication*, (76):90–105, 1988. Editor: D. R. Karsa.

[44] H. Fratzscher and Associates. pages 167–187. John Wiley and Sons, 1988.

[45] L.T. Zhuravlev. The surface chemistry of silica. the zhuravlev model, 1998.

[46] V. Buttingnol and H.L. Gerhardt. Polymer coatings. pigment dispersion. *Industrial and Engineering Chemistry*, 60(8):68–79, 1968.

[47] G.D. Parfitt. Dispersion. *Journal of the Oil and Colour Chemists Association*, 50:822–843, 1967.

[48] W.K. Asbeck and M. van Loo. Critical pigment volume relationships. *Industrial and engineering chemistry*, 41:1470–1475, 1949.

[49] B. Lu and S. Torquato. Local volume fraction fluctuations in heterogeneous media. *Journal of Chemical Physics*, 93(5):3452–3459, 1990.

[50] R.S. Fishman, D.A. Kurtze, and G.P. Bierwagen. The effects of density fluctuations in organic coatings. *Polymer*, 36(23):4397–4403, 1995.

[51] V. Granier and A. Sartre. Ordering and adhesion of latex particles on model inorganic surfaces. *Langmuir*, 11:2179–2186, 1995.

[52] C.R.Walker. Personal communication, 1997. Allied Colloids.

[53] E. Bourgeat-Lami, Ph. Espiard, and A. Guyot. Poly(ethyl acrylate) latexes encapsulating silica: 1. functionalization and dispersion of silica. *Polymer*, 36(23):4385–4389, 1995.

[54] Ph. Espiard and A. Guyot. Poly(ethyl acrylate) latexes encapsulating silica: 2¿ grafting process onto silica. *Polymer*, 36(23):4390–4396, 1995.

[55] Ph. Espiard, A. Guyot, J. Perez, G. Vigier, and L. David. Poly(ethyl acrylate) latexes encapsulating silica: 3. morphology and mechanical properties of reinforced films. *Polymer*, 36(23):4397–4403, 1995.

[56] Digital Instruments, 112 Robin Hill Road Santa Barbara, CA 93117, URL = www.di.com. *Nanoscope III manual.*

[57] J. Boxall and J.A. von Fraunhofer. *Concise Paint Technology.* Paul Elek (Scientific Books) Ltd, London, 1977.

[58] D. Stauffer and A. Aharaony. *Introduction to Percolation Theory.* Taylor and Francis, London, Washington DC, 2nd edition, 1992.

[59] Allied Colloids, Coatings and Specialities Division, Allied Colloids Ltd, PO Box 38, Low Moor, Bradford, west Yorkshire, BD12. 0JZ. *Glascol C47, Technical and Processing Data.*

[60] J.S. Blakemore. *Solid State Physics.* Cambridge University Press, Cambridge, England, 2nd edition, 1985.

[61] P.A. Webb and C. Orr. *Analytical Methods in Fine Particle Technology.* Micrometrics, 1997.

[62] S.J. Gregg and K.S.W. Sing. *Adsorption, surface area and porosimetry.* Academic Press, London and New York, 1967.

[63] Colton, Engel, Frommer, Gaud, Gewirth, Guckenberger, Heckl, Parkinson, and Rabe, editors. *Procedures in Scanning Probe Microscopes.* Wiley , Chichester, UK, 1998.

[64] C.J.R. Sheppard and D.M. Shotton. *Confocal Laser Scanning Microscopy.* Microscopy Handbooks 38. BIOS Scientific Publishers; Oxford, England, 1997.

[65] V.N.E. Robinson D.A. Moncreiff, P.R. Barker. Charge neutralisation of insulating surfaces in the sem by gas ionisation. *Journal of Physics D: Applied Physics*, 11:2315–2325, 1978.

[66] A.M. Donald. Environmental scanning electron microscopy for the study of 'wet' systems. *Current Opinion in Colloids and Interface Science*, 3:143–147, 1998.

[67] A.M. Donald and B.L. Thiel. *: ESEM image contrast and applications to wet organic materials*, pages 415–444. Kluwer academic publishers, The Netherlands, 1999.

[68] P. Meredith and A.M. Donald. Study of 'wet' polymer latex systems in environmental scanning electron microscopy: Some imaging considerations. *Journal of Microscopy*, 181:23–35, 1996.

[69] *Environmental Scanning Electron Microscopy*, 1996.

[70] J.I. Goldstein *et al. Scanning Electron Microscopy and X-ray Microanalysis.* Plenum Press, New York, 2nd edition, 1992.

[71] L.B. Harris D.A. Moncreiff, V.N.E. Robinson. Electron scattering by gas in the scanning electron microscope. *Journal of Physics D: Applied Physics*, 12:481–488, 1979.

[72] R.E. Cameron and A.M. Donald. Minimising sample evaporation in the environmental scanning electron microscope. *Journal of Microscopy*, 173:227–237, 1994.

[73] eds: R.A.S. a. K. Zierold Y. Talmon. *Electron beam damage to organic and biological cryospecimens*, pages 61–84. Springer-Verlag, Berlin, Germany, 2nd edition, 1987.

[74] B.L. Thiel D.J. Stokes and A.M. Donald. Direct observation of water-oil emulsion systems by environmental scanning electron microscopy. *Langmuir*, 14:4402–4408, 1998.

[75] G.D. Danilatos. A gaseous detector device for an environmental sem. *Micron and Microscopica Acta*, 14(4):307–318, 1983.

[76] B.L. Thiel A.L. Fletcher and A.M. Donald. Amplification measurements of alternative imaging gases in environmental sem. *Journal of Physics D: Applied Physics*, 30:2249–2257, 1997.

[77] A.L. Fletcher. *Cryogenic developments and signal amplification in environmental scanning electron microscopy.* PhD thesis, University of Cambridge, 1997.

[78] B.L. Thiel, I.C. Bache, A.L. Fletcher, P. Meredith, and A.M. Donald. An improved model for gaseous amplification in the environmental sem. *Journal of Microscopy*, 187:143–157, 1996.

[79] A. von Engel. *Ionised Gases.* Clarendon Press, Oxford, England, 1955.

[80] M.A.Hill and F.A. Smith. Calculation of initial and primary yields in the radiolysis of water. *Radiation Physics and Chemistry*, 43(3):265–280, 1994.

[81] C.F. Quate. The afm as a tool for surface imaging. *Surface Science*, 299:980–995, 1993.

[82] C.C. Williams Y. Martin and H.K. Wickramasinghe. Atomic force microscopy-force mapping and profiling on the sub 100-åscale. *Journal of Applied Physics*, 61(10):4723–4729, 1987.

[83] Thermomicroscopes, URL = www.thermomicro.com/. *A Practical Guide to Scanning Probe Microscopy.*

[84] M. Marth *et al.* A unifying view on some experimental effects in tapping-mode atomic force microscopy. *Journal of Applied Physics*, 85(10):7030–7036, 1999.

[85] G. Bar and R. Brandsch. Effect of viscoelastic properties of polymers on the phase shift in tapping mode atomic force microscopy. *Langmuir*, 14(26):7343–7347, 1998.

[86] V. Elings S.N. Magonov and M-H Whangbo. Phase imaging and stiffness in tapping-mode atomic force microscopy. *Surface ScienceLetters*, 375:L385–L391, 1997.

[87] R. Brandsch G. Bar and M-H Whangbo. Effect of tip sharpness on the relative contributions of attractive and repulsive forces in the phase imaging of tapping mode atomic force microscopy. *Surface ScienceLetters*, 422:L192–L199, 1999.

[88] G. Meyer and N.M. Amer. Novel approach to atomic force microscopy. *Applied Physics Letters*, 53(24):2400–2402, 1988.

[89] M. Minsky. United states patent 3013467, 1961. filed 1957.

[90] A.E. Ribbe. Laser scanning confocal microscopy. *Trends in Polymer Science*, 5:333–337, 1997.

[91] J.S. Villarrubia. Algorithms for scanned probe microscope image simulation, surface reconstruction and tip estimation. *Journal of Research of the National Institute of Standards and Technology*, 102(4):425–453, July-August 1997.

[92] E. Hecht. *Optics*. Addison-Wesley Publishing Co.; Reading, Massachusetts, 2nd edition, 1987.

[93] C.J.R. Sheppard and A. Choudbury. Image formation in the scanning microscope. *Optica Acta*, 24(10):1051–1073, 1977.

[94] J-A. Conchello and J.G. McNally. Fast regularisation technique for expectation maximisation algorithm for optical sectioning microscopy. *SPIE*, 2655:198–208, 1996.

[95] J.G. McNally, T. Karpova, J. Cooper, and J-A. Conchello. Three-dimensional imaging by deconvolution microscopy. *Methods*, 19:373–385, 1999.

[96] J.G. McNally, C. Preza, J-A. Conchello, and L.J. Thomas Jnr. Artifacts in computational optical-sectioning microscopy. *Journal of the Optical Society of America*, 11(3):1056–1067, 1994.

[97] S.F. Gibson and F. Lanni. Experimental test of an analytical model of aberration in an oil-immersion objective lens used in three-dimensional microscopy. *Journal of the Optical Society of America*, 8(10):1601–1613, 1991.

[98] S. Hell, G. Reiner, C. Cremer, and E.H.K. Stelzer. Aberrations in confocal fluorescence microscopy induced by mismatches in refractive index. *Journal of Microscopy*, 169:391–405, 1993.

[99] L.M. Jenkins and A.M. Donald. Use of the esem for the observation of the swelling behaviour of cellulosic fibres. *Scanning*, 19:92–97, 1997.

[100] S. Kitching and A.M. Donald. Beam damage of polypropylene in the environmental scanning electron microscope: An ftir study. *Journal of Microscopy*, 190:357–365, 1998.

[101] S.M. Pimblott, M.J. Pilling, and N.J.B. Green. Stochastic models of spur kinetics in water. *Radiation Physics and Chemistry*, 37(3):377–388, 1991.

[102] S.M. Pimblott, J.A. LaVerne, and A. Mozumder. Monte carlo simulation of range and energy deposition by electrons in gaseous and liquid water. *Journal of Physical Chemistry*, 100(20):8595–8606, 1996.

[103] M. Terrissol and A. Beaudre. Simulation of space and time evolution of radiolytic species induced by electrons in water. *Radiation Protection Dosimetry*, 31:175–177, 1990.

[104] C.D. Jonah, M.S. Matheson, J.R. Miller, and E.J. Hart. Yield and decay of the hydrated electron from 100 ps to 3 ns. *Journal of Physical Chemistry*, 80(12):1267–1270, 1976.

[105] C.D. Jonah and J.R. Miller. Yield and decay of the oh radical from 100 ps to 3 ns. *Journal of Physical Chemistry*, 81(21):1974–1976, 1977.

[106] J.A. La Verne and A. Mozumder. Penetration of low-energy electrons in water. *Radiation Research*, 96:219–234, 1983.

[107] W.H. Press, S.A.Teukolsky, W.T. Vetterling, and B.P. Flannery. *Numerical Recipes in C*. Cambridge University Press, Cambridge, UK, 1988.

[108] F. Reif. *Fundamentals of statistical and thermal physics*. McGraw-Hill, New York, international edition, 1985.

[109] E. Kreysig. *Advanced engineering mathematics*. John Wiley and Sons Ltd, New York, 7th edition, 1993.

[110] J.C. Russ. *The image processing handbook*. CRC Press, Boca Raton, USA, 2nd edition, 1995.

[111] Microscope point source kit p-7220. Yellow-green fluospheres 505-515nm.

[112] C. Preza, M.I. Miller, L.J. Thomas Jr, and J.G. McNally. Regularised method for reconstruction of three-dimensional microscopic objects from optical sections. *Journal of the Optical Society of America*, 9:219–228, 1992.

[113] J. Markham and J-A. Conchello. Tradeoffs in regularised maximum likelihood image restoration. *SPIE*, 2655:18, 1997.

[114] A.P. Dempster, N.M. Laird, and D.B. Rubin. Maximum likelihood from incomplete data via the em algorithm. *Journal of the Royal Statistical Society B*, 39(1):1–38, 1977.

[115] H. Doi and S.F. Edwards. *The theory of polymer dynamics.* Number 73 in International series of monographs on physics. Clarendon Press, Oxofrd, UK, 1985.

[116] Tego Chemie Service, Th Golschmidt Ltd, Chippenham Drive, Kinston, Milton Keynes, Bucks, MK10 0AE, UK. *Safety Data Sheet, TEGO Foamex 1488.*

[117] Univar PLC, Suffolk House, George St, Croydon, CR9 3QL, UK. *Dowanol PNB glycol ether safety data sheet.*

[118] Univar PLC, Suffolk House, George St, Croydon, CR9 3QL, UK. *Dowanol DPNB glycol ether safety data sheet.*

[119] Troy Chemical Co, 3rd floor Adelphi Mill, Grimshaw Lane, Bollington, Macclesfield, UK. *Technical Data, Troysol LAC.*

[120] Allied Colloids, Coatings and Specialities Division, Allied Colloids Ltd, PO Box 38, Low Moor, Bradford, west Yorkshire, BD12. 0JZ. *Glaswax E1, Technical and Processing Data.*

[121] Henkel Performance Chemicals, Material Safety Data Sheet, Nopco House, Kirkstall Road, Leeds, West Yorkshire, LS3 1JN, UK. *Material safety data sheet DSX 1524.*

[122] D. Ward D. Aldcroft, A.R. Minnihan. A modern approach to matting paint films. Crosfields internal report, Crosfield Group, Warrington, Cheshire, WA5 1AB, UK, 1994.

[123] S. Wernick and R. Pinner. *Surface Treatment of Aluminium.* Clare o' Moseley Ltd, Moseley, Surrey, UK, 4th edition, 1972.

[124] G.W.C. Kaye and T.H. Laby. *Tables of physical and chemical constants.* Longman, Harlow, England, 16th edition, 1995.

[125] *Fluorescein isothiocyanate isomer II cat. no F-144.* URL = www.probes.com.

[126] Byk Gardner, url=www.byk.com. *Byk Gardner 'Haze-Gard Plus' haze meter.*

[127] E. Sutanto, Y. Ma, H.T. Davis, and L.E. Scriven. *Cryogenic Scanning Electron Microscopy of Early Stages of Film Formation in Drying Latex Coatings*, volume 81, pages 181–182. American Chemical Society, 1999.

[128] Byk Gardner, url=www.byk.com. *Byk Gardner Gloss meter.*

[129] Placquettes for reflection work, obtained from chatel, le curtillet, 73590 flumet, france.

[130] M. and I. Ash. *Handbook of Paint and Coating Raw Materials.* Gower Publishing,Aldershot, Hants, UK, 1996.

Component	Function	% by weight in formulation	Supplier
Glascol C47	Latex Binder	71.4	(1)
Water		16.8	
Tegofoamex 1488	Defoamer	0.1	(2)
Degussa TS100*	Matting Agent	variable	(3)
Dowanol PnB	Coalescing aid	3.81	(4)
Dowanol DPnB	Coalescing aid	1.90	(4)
Tegofoamex 1488	Defoamer	0.05	(3)
Troysol LAC	Anti Cratering Agent	0.5	(5)
Glaswax E1	Surface enhancer	2.14	(1)
Henkel DSX 1514	Rheology Modifier	0.8	(6)

Table 10.1: Formulation Recipe. The components are added in the order and amounts shown. * the silica is varied between samples.

Appendices

List of Suppliers

(1): Allied Colloids Ltd, PO Box 38, Low Moor, Bradford, west Yorkshire, BD12 0JZ
Telephone: (+44) (0)1274 417000

(2): Tego Chemie Service, A division of Th Golschmidt Ltd, Chippenham Drive, Kinston, Milton Keynes, Bucks, MK10 0AE.
Telephone (+44) (0)1908 582250

(3): Degussa A.G., Postfach 1345, D-6450 Hanua I, Germany.

(4): Dow Chemical Company Ltd, Lakeside House, Uxbridge, Middlesex, UB11 1BE

(5): Troy Chemical Co, 3rd floor Adelphi Mill, Grimshaw Lane, Bollington, Macclesfield

(6): Henkel Performance Chemicals, Nopco House, Kirkstall Road, Leeds,

West Yorkshire, LS3 1JN
Telephone (+44) (0)1332 457471

Component	Supplier	Chemical nature	Specific Gravity gcm^{-3}
Glascol C47	(1)	PBMA 80nm latex [52]	1.04 [59]
Water			1.0
Tegofoamex 1488	(2)	dimethicone copolyol emulsion [130]	0.1 [116]
Degussa $TS100^*$ (3)		Measured	
Dowanol PnB	(4)	3-Butoxypropan-2-ol[130]	0.9 [117]
Dowanol DPnB	(4)	Dipropyleneglycol n-butyl ether [130]	0.922 [118]
Troysol LAC	(5)	28% propylene glycol [130]	1.04-1.07 [119]
Glaswax E1	(1)	polyethylene wax [120]	0.995 [120]
Henkel DSX 1514	(6)	23% 2(2-Butoxyethoxy))ethoxy ethanol [121]	1.068 [121]

Table 10.2: Silicas used in this work. Characteristic primary particle size is determined from ESEM work (chapter 8 8.5) except silica gel from light scattering [12] and fumed silica (where we quote typical *ultimate* particle size [10]).

Appendices

Parameter	FITC Setting	Rhodamine
Laser	Argon ion 15mW	HeNe 0.5mW
Power	$0.25 \times 2.5\%$	10 %
Fluorescent filter	505-560nm band pass	560nm low pass
Lens	Zeiss Planapochromat 63×	Zeiss Planapochromat 63×
Pixel size xy	0.07 μm	0.28 μm
Pixel size z	0.35 μm	0.7 μm
Detector gain	935-940	700-800
Amplitude offset	set such that a few pixels of value	were present in each image
Amplitude gain	1.0	1.0
Scan time (per pixel)	22.8 μs	22.8 μs

Table 10.3: Experimental parameters for confocal microscopy of FITC and rhodamine labelled film. These paramters are taken from a Ziess lsm510 CLSM.